

UNDERSTANDING AND OVERCOMING
LIMITATION MECHANISMS IN Nb_3Sn
SUPERCONDUCTING RF CAVITIES

A Dissertation

Presented to the Faculty of the Graduate School
of Cornell University

in Partial Fulfillment of the Requirements for the Degree of
Doctor of Philosophy

by

Samuel Elliott Posen

January 2015

© 2015 Samuel Elliott Posen
ALL RIGHTS RESERVED

UNDERSTANDING AND OVERCOMING LIMITATION MECHANISMS IN
NB₃SN SUPERCONDUCTING RF CAVITIES

Samuel Elliott Posen, Ph.D.

Cornell University 2015

Nb₃Sn has the potential to significantly improve cryogenic efficiency and maximum fields in superconducting RF cavities, structures that impart energy to charged particle beams in large accelerators. Previous experiments demonstrated excellent cryogenic efficiency at small accelerating fields, producing cavities with surface resistance R_s on the order to 10 n Ω , but it consistently increased strongly as the peak surface magnetic field exceeded the first critical field $\mu_0 H_{c1} \approx 30$ mT. This dissertation describes results from a new research program to investigate whether this behavior is fundamental and to determine what mechanisms ultimately limit RF superconductivity in this material. A chamber was designed and built for coating niobium substrates with a thin layer of Nb₃Sn via high temperature vapor deposition. After commissioning with samples, many coatings of single cell 1.3 GHz cavities were carried out. Several RF tests showed that small R_s could be maintained up to fields significantly higher than H_{c1} , showing that it is not a fundamental limitation. The field limitation encountered in these experiments was primarily quench, likely due to surface defects, based on results that include temperature mapping and high power pulsed measurements. Measurements of the temperature dependence of R_s and microscopic investigations of the surface indicate that low tin content regions cause R_s degradation, especially after material removal. A theoretical investigation showed that thick films have only slightly lower maximum fields

than alternating layers of thin film superconductor and insulator on a bulk superconductor, and only for a small parameter range. The highest fields reached by a Nb₃Sn cavity in these experiments corresponds to an accelerating gradient of 17 MV/m, with a quality factor of 8×10^9 at 4.2 K. Cavities with this performance would significantly reduce costs in many applications, including large high duty factor linear accelerators and small-scale industrial accelerators. Additional development aided by increased understanding is expected to push performance even further.

BIOGRAPHICAL SKETCH

Sam was born and raised in Ottawa, Ontario, Canada. In 2005, he began undergraduate studies in Engineering Physics at Queen's University, graduating in 2009. In 2007, he developed a passion for particle accelerators during an internship at CERN through the University of Toronto. Sam joined the Cornell University SRF group in summer 2009 as he began PhD studies. He graduated in 2014.

I dedicate this work to my parents, who have dedicated so much to me.

ACKNOWLEDGEMENTS

The work in this thesis was made possible by the help, mentorship, and friendship of the people I have been fortunate enough to have gotten to know and be a part of my life.

I am deeply grateful to my advisor Matthias. I am extremely fortunate to have worked with an advisor who possesses genuine concern for his students, a kind personality, and an expansive knowledge of his field. He is encouraging and supportive when experiments go as expected; he is patient and helpful when they don't. I have benefited greatly from his wisdom and friendship.

I have had the distinct pleasure of working with Jim Sethna, a brilliant theorist, over many meetings discussing SIS' films, holes in dykes, and metastability. I owe him a great thanks for developing my intuition for superconductivity and for demonstrating how a skilled physicist can apply a vast array of tools to approach a complex problem.

I would like to thank Hasan Padamsee, Maury Tigner, Don Hartill, Georg Hoffstaetter, and Ritchie Patterson for their insight, advice, and support. Thank you for believing in me and for giving me opportunities to represent Cornell and present my research to the scientific community.

Learning the hands-on aspects of SRF requires a skilled and experienced teacher willing to take on an apprentice. In my first year at Cornell, Zack Conway taught me everything there is to know about working in a clean room, about hardware, and about living in Ithaca. Then Curtis Crawford came and taught me about electropolishing, using the right tool for the job, and how to endear yourself to machinists through insults. Along the way, I was given lessons on mechanical problem solving from James Sears and instrumentation from Peter Quigley. Thank you all for taking me under your wing.

My day-to-day life in grad school was made immeasurably more enjoyable by my fellow SRF grad students Yi Xie, Nick Valles, Dan Gonnella, Daniel Hall, and James Maniscalco. Whether we were discussing new results, working together in the clean room, debating, or playing Glory to Rome, I was always grateful for your help and your friendship. I also consider myself extremely fortunate to have gotten to know the Liepe, Valles, and Xie families.

I have been lucky to get the chance to collaborate with some excellent researchers. This includes Gianluigi Catelani, Mark Transtrum, Thomas Proslir, Bob Laxdal, Sergey Belomestnykh, and Sarah Aull.

I would also like to express my humble gratitude to many members of the laboratory who have made important contributions to my education and my research: my special committee members Dave Rubin and Jim Sethna; RF experts Vadim Veshcherevich, Valery Shemelin, Vivian Ho, Ralf Eichhorn, and Sergey Belomestnykh; kindred SRF researchers Fumio Furuta and Mingqe Ge; chemistry room leaders Holly Conklin and Terri Gruber; cryogenics experts Dwight Widger, Dan Sabol, Colby Shore, and Eric Smith; master welder Brian Clasby; microscopy master John Kaufman; mechanical whizzes Brendan Elmore, Ben Bullock, and Paul Carriere; helium chief Andriy Ganshyn; outreach heroes Lora Hine and Erik Herman; machinists Mark Howser, Neal Alexander, Randy Miller, Dave Simmons, Henry Hansteen, Shawn Clark, and John Kaminski; drafters Dawn Sears, Matt Rifenburg, and Tom Kobela; the people who keep Newman Lab running, Monica Wesley, Katerina Malysheva, Peggy Steenrod, Jeanne Butler, and BJ Bortz; and the people who make sure that science can happen in the basement, Paul Bishop, Greg Kulina, and Don Heath. I would also like to express my thanks to CCMR microscopic analysis experts Mick Thomas, John Grazul, Jon Shu, and Don Werder.

A number of local community college students and Cornell undergraduates contributed to my research over the last five years. I'd like to thank Jihwan Oh, Rocco Cammarere, Justin Riley, Jordan Shields, Chris Wilson, Fiona Wohlfarth, and Sarah Meyers.

I am deeply thankful for the love, support, and encouragement of my parents and my family. My life is enriched as well by my friends both new and old, true grillers and those who don't BBQ in January. And I couldn't have made it to Cornell without Cameron Hurst, Ellen Schelew, Jordan Morelli, Richard Teuscher, and Andrew Zwicker.

TABLE OF CONTENTS

Biographical Sketch	iii
Dedication	iv
Acknowledgements	v
Table of Contents	viii
List of Tables	x
List of Figures	xi
List of Abbreviations	xiv
List of Symbols	xiv
1 Introduction	1
1.1 Organization of the Dissertation	3
2 SRF Background	4
2.1 General Introduction to Superconductivity	4
2.2 BCS Theory and Surface Resistance	6
2.3 Type I and Type II Superconductors	7
2.4 Critical Fields	9
2.5 Defects and the Metastable State	11
2.6 Introduction to SRF Cavities	13
2.7 Potential of Nb ₃ Sn for SRF Applications	16
2.8 Other SRF Materials	22
2.9 Enhancing Understanding of RF Superconductivity	24
2.9.1 Flux Penetration for a Defect Free Surface	24
2.9.2 Flux Penetration for a Surface With Defects	25
2.9.3 Sources of Spurious Surface Resistance	26
2.9.4 Closing of the Quasiparticle Spectral Gap	27
2.9.5 Optimal Geometry for Maintaining the Meissner State	29
3 Theoretical Investigation of the SIS' Geometry	31
3.1 Background: Maximum Fields	32
3.2 Critical fields in the London limit	33
3.3 Evaluation of Field Limits	39
3.4 Conclusions: Optimal Geometry for SRF Coatings	42
4 Nb₃Sn Background	44
4.1 General Properties of Nb ₃ Sn	44
4.2 Coating Method	48
4.3 Previous Results	51
4.4 Weak Link Grain Boundaries	55

5	Cornell Nb₃Sn Coating Apparatus	59
5.1	Design	59
5.2	Coating Procedure	64
5.3	Coating Evaluation	67
6	Experimental SRF Facilities	80
6.1	Preparation for Cavity Test	80
6.2	CW RF Cavity Testing	82
6.3	Slow Cool System	87
6.4	Temperature Map	88
7	Development of Nb₃Sn Surface Preparation via CW Testing	92
7.1	Overview of CW Testing	92
7.2	Effects of Preparation Parameters	97
7.2.1	Substrate Quality	98
7.2.2	Annealing Time	104
7.2.3	Surface Defects	111
7.2.4	Material Removal After Coating	117
7.2.5	Initial Chemistry	124
7.2.6	Cooldown Rate	124
7.2.7	Substrate Grain Size	129
7.3	Material Parameters	131
7.4	Flux Penetration at H_{c1}	141
7.5	Alloys with Low Tin Content	142
7.5.1	Weak Link Grain Boundaries	143
7.5.2	SEM/EDX	144
7.5.3	TEM	145
7.6	Thermal Stability	150
7.6.1	Thermal Instability for a Defect-Free Surface	150
7.6.2	Thermal Instability at a Defect	151
8	Experimental Probe of Maximum Field Limits	153
8.1	Pulsed RF Cavity Testing	153
8.2	DC Flux Penetration Field	160
9	Summary	165
9.1	Progress and Comparison to Previous Research	165
9.2	Comparisons between Coatings	168
9.3	Advances in Understanding	169
9.4	Evaluation of Nb ₃ Sn State-of-the-Art	172
9.5	Outlook and Next Steps	175
	Bibliography	177

LIST OF TABLES

2.1	Cavity shapes and parameters	16
2.2	Properties of alternative SRF materials	23
4.1	Maximum T_c of Nb-Sn phases	47
7.1	List of Nb ₃ Sn cavity tests	93
7.2	Measured and calculated properties of the Nb ₃ Sn film	135
7.3	Comparison of extracted parameters from five cavity tests	137

LIST OF FIGURES

2.1	Vortices in a type-II superconductor	9
2.2	Phase diagram and magnetization curve of a type II superconductor	12
2.3	RF fields in a pillbox cavity	14
2.4	Surface resistance of Nb ₃ Sn and Nb	19
2.5	Power dissipation in a Nb ₃ Sn and Nb cavity	20
2.6	Cryogenic plant efficiency	21
2.7	Density of states in the clean limit	27
2.8	Quasiparticle gap as a function of field	28
2.9	Q vs H including the gap.	30
3.1	Example of a SIS' structure	34
3.2	Gibbs free energy in a bulk and thin film	36
3.3	Gibbs free energy in a SIS' structure	37
3.4	Maximum fields for SIS' structures	39
3.5	Forces on a vortex in a homolaminate	40
3.6	Comparison of a SIS' to a bulk film	42
4.1	A15 crystal structure	45
4.2	Nb-Sn phase diagram	46
4.3	Thermal conductivity of Nb and Nb ₃ Sn	48
4.4	Vapor diffusion method	50
4.5	Vapor pressure of Sn and SnCl ₂	52
4.6	Siemens TM and TE cavity data	53
4.7	U. Wuppertal 1.5 GHz cavity data	54
4.8	Cracks in bent Siemens Nb ₃ Sn samples	58
5.1	Cornell Nb ₃ Sn coating chamber	61
5.2	Thermocouple locations	61
5.3	Pre-coating BCP	63
5.4	Accessories for Nb ₃ Sn coating	65
5.5	Nb ₃ Sn coating process	66
5.6	Nb ₃ Sn cavity and a Nb cavity	67
5.7	Inside surface before and after coating	68
5.8	Anodization of first Nb ₃ Sn samples	69
5.9	SEM images of first Nb ₃ Sn samples	69
5.10	Nb ₃ Sn EDX spectrum	70
5.11	Literature data for T_c versus tin content	71
5.12	XPS of first Nb ₃ Sn samples	72
5.13	FIB analysis	73
5.14	T_c measurement of first samples	74
5.15	RRR measurement of first samples	75
5.16	SEY measurement of Nb ₃ Sn sample	75

5.17	PCT analysis of Nb ₃ Sn sample	77
5.18	H_{c2} measurement	78
6.1	HPR and cavity assembly	81
6.2	Testing stand for CW RF measurements	83
6.3	Block diagram of RF system	84
6.4	Typical P_r trace	86
6.5	Slow cool apparatus	89
6.6	Temperature mapping system	89
6.7	Distribution of T-map sensors	90
6.8	Example of T-map plot	91
7.1	Plot of Nb ₃ Sn cavity tests	94
7.2	Inside surface of cavity 1	99
7.3	Q vs E curves for cavity 1	100
7.4	T-map of cavity 1 test 3	100
7.5	Effect of oxipolishing on Nb ₃ Sn surface	102
7.6	Anodized Nb ₃ Sn cavity	103
7.7	SEM images of Nb ₃ Sn grains	105
7.8	Variation of temperature ramp after nucleation	107
7.9	Q vs E curves for cavity 2	108
7.10	R_s vs E curves for cavity 2	109
7.11	Decomposed R_s vs E curves at 4.2 K	110
7.12	Decomposed R_s vs E curves at 4.2 K	110
7.13	Typical T-map for minimal Q -slope test	111
7.14	Comparison of T-map heating at different fields	113
7.15	T-map after quench and quench “video”	114
7.16	Quench locations for cavity 2	115
7.17	SEM image showing 3D features	116
7.18	Q vs E curves after material removal	118
7.19	Microscopic residue on HF-rinsed Nb ₃ Sn	120
7.20	Centrifugal barrel polishing	121
7.21	T-map after CBP	121
7.22	Temperature dependence of R_s vs E after material removal	122
7.23	Q vs T after material removal	123
7.24	Q vs E curves for BCP and EP initial chemistry	125
7.25	10 min/K cooldown	126
7.26	2 min/K cooldown	126
7.27	0.2 min/K cooldown	127
7.28	Comparison of different cooldown rates	128
7.29	Nb-Sn “Clumps” on large grain niobium	130
7.30	Grain growth observed in Nb substrate	131
7.31	Typical Q vs T curve	132
7.32	Contour plots of 1-parameter fits to Q vs T and f vs T	134

7.33	Combined material parameter contour plot	135
7.34	Material parameter fits for cavity 2 test 6	136
7.35	Ellipsoidal μ -SR sample	140
7.36	μ -SR measurement	140
7.37	Q vs B curves compared to $\mu_0 H_{c1}$	141
7.38	EDX line scan across a grain boundary	145
7.39	TEM image of region A	146
7.40	EDX of region A	147
7.41	TEM image of region B	148
7.42	EDX of region B	149
8.1	Setup for pulsed testing	154
8.2	Klystron pulse	154
8.3	Effect of varying klystron power	155
8.4	Pulsed quench field as a function of temperature	156
8.5	Pulsed quench field in a niobium cavity	158
8.6	Extrapolated pulsed quench field	159
8.7	DC flux penetration measurement setup	161
8.8	Example of DC flux penetration field measurement	162
8.9	DC flux penetration field vs temperature	163
9.1	Cornell Wuppertal CW cavity test comparison	166
9.2	Updated power comparison between Nb_3Sn	173
9.3	Comparison of Nb_3Sn maximum fields	175

LIST OF ABBREVIATIONS

AC	Alternating Current
ADC	Analog-to-Digital Converter
COP	Coefficient Of Performance
BCP	Buffer Chemical Polish
BCC	body center cubic
BCS	Bardeen, Cooper and Schrieffer
CAD	Computer-aided Design
CBP	Centrifugal Barrel Polish
CERN	Conseil Européen pour la Recherche Nucléaire
COP	Coefficient Of Performance
CW	Continuous-Wave
DC	Direct Current
EDX	Energy Dispersive X-ray
EP	Electro-polish
ERL	Energy Recovery Linac
FEL	Free Electron Laser
FIB	Focused Ion Beam
FOM	Figure Of Merit
HF	Hydrofluoric acid
HFQS	High Field Q-Slope
HPP	High Power Pulse
HPR	High-Pressure Rinse
HTSC	High Temperature Superconductor
ILC	International Linear Collider
KfK	Kernforschungszentrum Karlsruhe
LCLS	Linac Coherent Light Source
LINAC	Linear Accelerator
MFQS	Medium Field Q-Slope
PCT	Point Contact Tunneling
PLL	Phase-locked loop
RF	Radio Frequency
RLC	Resistor-Inductor-Capacitor

RRR	Residual Resistivity Ratio
RSS	Residual Sum of Squares
RTD	Resistive Thermal Device
SEM	Scanning Electron Microscope
SEY	Secondary Electron Yield
SIS	Superconductor-Insulator-Superconductor
SRF	Superconducting Radio Frequency
TE	Transverse Electric
TM	Transverse Magnetic
TEM	Transmission Electron Microscope
UHV	Ultra-High Vacuum
USD	United States Dollars
XFEL	X-Ray Free Electron Laser
μ -SR	Muon Spin Rotation

LIST OF SYMBOLS

A	Magnetic vector potential
B	Magnetic flux density
B_0	Applied magnetic field
B_i	Magnetic field in insulating film
B_M	Meissner-screened external magnetic field
B_{max}	Maximum magnetic field without flux penetration
B_q	Peak surface magnetic field at quench
B_V	Vortex magnetic field
B_{pk}	Peak surface magnetic field
d	Film thickness
E	Electric field intensity
E_{acc}	Accelerating electric Field
E_{pk}	Peak (maximal) surface electric field
f	Frequency
G	Geometry factor of RF structure
\mathcal{G}	Gibbs free energy
H	Magnetic field intensity
H_c	Critical magnetic field
H_{c1}	Lower critical magnetic field
H_{c2}	Upper critical magnetic field
H_{sh}	Superheating field
k	Thermal conductivity
k_B	Boltzmann constant
l	Electron mean free path
L	Cavity length
P_{AC}	AC power required
P_{diss}	Dissipated power in walls of cavity
P_e	Emitted RF power
P_f	Forward RF power
P_i	Incident RF power
P_r	Reflected RF power
P_t	Transmitted RF power
q	Charge of a particle
Q	Quality factor
Q_0	Intrinsic quality factor
$Q_{0,adj}$	Quality factor adjusted to 2 K

Q_{ext}	External quality factor for input power coupler
Q_L	Loaded Q of resonator and coupler
Q_t	External quality factor for transmitted power coupler
R_a	Shunt impedance
R_{BCS}	BCS surface resistance
R_{res}	Residual resistance
R_s	Surface resistance
T	Temperature
T_c	Critical temperature of a superconductor
T_{He}	Helium bath temperature
T_{rm}	Room temperature
U	Stored energy
V	Voltage
β	Coupling strength
β_e	Coupling strength calculated with P_e
β_r	Coupling strength calculated with P_r
Δ	Energy gap
ϵ	Quasiparticle energy
ϵ_g	Quasiparticle energy gap
κ	Ginzburg-Landau parameter
λ	Penetration depth
λ_0	Penetration depth offset
λ_b	Penetration depth of bulk
λ_f	Penetration depth of film
λ_L	London penetration depth
μ_0	Permeability of free space
$\nu(\epsilon)$	Normalized quasiparticle density of states
ξ	Coherence length
ξ_0	Intrinsic coherence length
ξ_f	Coherence length of film
τ_L	Cavity decay constant
ϕ	Cavity phase
ϕ_0	Flux quantum
ω	Angular frequency

CHAPTER 1

INTRODUCTION

Particle accelerators are devices that use electromagnetic fields to generate and manipulate energetic beams of charged particles. They are used in many applications, from high energy colliders that probe the fundamental laws of physics [Aea12, Cea12, Beh13], to light sources that provide unique analysis tools to biologists, chemists, and materials scientists [BEW05, Alt07, Gal14], to small-scale industrial applications [HS10, Sab13]. One of the most widely used methods for accelerating charged particle beams in larger applications is passing them through large electric fields produced in superconducting radiofrequency (SRF) cavities, specially shaped chambers made with a superconducting material that allows them to behave as extremely efficient electromagnetic resonators.

SRF cavities offer a relatively inexpensive way to accelerate particle beams, but the cost can be a limiting factor in large facilities. For example, high energy linear colliders can require thousands of cavities, operating at as high fields as they can reach, in order to reach their design energy, at a cost of approximately 100,000 USD per cavity (see for example the proposed International Linear Collider (ILC) [Beh13]). Another illustrative example is a large high duty factor linear accelerator, in which the near-constant RF heat load necessitates the use of a large cryogenic plant, which can cost on the order of 100 million USD, and require on the order of a megawatt of power to operate (see for example the planned Linac Coherent Light Source (LCLS) II [Gal14] or the Cornell ERL [HGT13]). These two examples show that increasing the maximum accelerating fields or the cryogenic efficiency of cavities could dramatically reduce

the cost of large-scale particle accelerators.

Alternative superconductors to niobium—the standard material used in state-of-the-art SRF accelerators—offer a way to push performance. One very promising material, Nb_3Sn , has a relatively high critical temperature, which allows it to have exceptionally high cryogenic efficiency at a given temperature, and it has a relatively high superheating field, which is predicted to allow it to reach exceptionally high maximum fields.

Previous research into Nb_3Sn cavities has shown that very high cryogenic efficiency can be achieved reliably, even at high temperatures. However, some limitations have been encountered in terms of the fields that these cavities can operate at with high efficiency. The nature of these limitations has not been well understood, and only limited resources have been devoted to this problem. Additional systematic studies correlating Nb_3Sn fabrication parameters, microscopic surface properties after coating, and cavity performance can be expected to produce a clearer picture of the mechanism behind these limitations to superconductivity. Further development to avoid these mechanisms can then allow this material to meet the demands of future accelerator facilities.

This dissertation presents new research into Nb_3Sn cavities. Following from the experiments of previous researchers, a new coating facility was developed at Cornell, and after commissioning, high quality Nb_3Sn cavities were produced. With these cavities, studies were performed investigating the effect of annealing time and grain size on RF performance. The influence of weak link grain boundaries in this material was studied. A conclusive test was performed of the hypothesis that strongly dissipative flux penetration may be unavoidable above the lower critical magnetic field. Insight was gained into the nature and

influence of defects in Nb₃Sn coatings. A theoretical discussion of the optimal geometry for screening large RF magnetic fields is also presented.

1.1 Organization of the Dissertation

The dissertation begins with an introduction to superconductivity and SRF, detailing the advantages of Nb₃Sn cavities for accelerator applications and the scientific questions that can be explored with the material ([chapter 2](#)). It continues with a discussion of the SIS' geometry, which are compared to the bulk films used in this research ([chapter 3](#)). Following this, the general properties of Nb₃Sn and its history in SRF applications are discussed ([chapter 4](#)). Next, Cornell's new Nb₃Sn coating facilities and first results on samples ([chapter 5](#)) are presented, as well as the general SRF experimental facilities ([chapter 6](#)). CW¹ cavity testing results are then presented in detail and interpreted, and associated microscopic investigations ([chapter 7](#)) are shown. Then experiments to probe the maximum field limits of the cavities ([chapter 8](#)) are presented, and the dissertation concludes with a summary and outlook for the future ([chapter 9](#)).

¹In continuous-wave (CW) operation, RF drive power is applied to the cavity continuously rather than in pulsed mode.

CHAPTER 2

SRF BACKGROUND

This chapter presents a general background necessary to understanding superconducting RF cavities and the SRF research performed in this dissertation. The chapter begins with an introduction to superconductivity, followed by a discussion of BCS theory and surface resistance, as well as a section on the differences between type I and type II superconductors. For additional information on the fundamentals of superconductivity, many excellent references are available, such as [Tin04, De 99]. In the next section, the various critical magnetic fields relevant to RF superconductors are introduced, and a brief overview of their relationship to the free energy in the superconductor is given; a more thorough discussion of this relationship appears in [chapter 3](#). The chapter continues with a note on the effect of dirt on superconductors and an introduction to SRF cavities. For a more in-depth introduction to SRF cavities, an excellent reference is [PKH08, Pad09]. Next, the interest of the SRF community in the alternative material Nb₃Sn is motivated by highlighting the demonstrated reduction in cryogenic costs and predicted increase in maximum accelerating gradient. Other superconductors are considered, and the choice of Nb₃Sn for this research is justified. Finally, the interest of the scientific community is motivated by showcasing important open questions about RF superconductivity that could be addressed by research on Nb₃Sn cavities.

2.1 General Introduction to Superconductivity

Superconductivity was discovered in 1911 by Kamerlingh Onnes [[Onn11](#)]. Onnes discovered that when a material is cooled below its critical temperature

T_c , it conducts DC electric current with zero resistance. This property makes superconductors useful in modern applications such as high efficiency power transmission and generation of persistent strong DC magnetic fields. As a result, superconductors have become very important in, for example, hospitals for magnetic resonance imaging machines, and in particle accelerators for manipulation of charged particle beams [SML04].

Superconductors react strongly to magnetic fields. If a weak magnetic field is applied to a superconductor, it will act as a diamagnet, generating screening currents on its surface which expel magnetic fields from the bulk, so that it remains in the flux free—also called Meissner—state. Stronger magnetic fields will penetrate the superconductor, causing localized regions to be driven normal conducting, and strong enough fields will drive the superconductor fully into the normal state. Different superconducting materials have different critical fields; those with higher critical fields can be exposed to higher magnetic fields before becoming normal conducting.

The earliest types of superconductors discovered were called Type I superconductors, generally elemental metals. Type II superconductors often are made of metallic alloys; the distinction between these and Type I superconductors will be described in the next sections. High temperature superconductors (HTSCs) are a special case of Type II superconductors with relatively high T_c , often made of complex ceramics. This dissertation primarily focuses on the low temperature Type II superconductors Nb and Nb₃Sn.

2.2 BCS Theory and Surface Resistance

The physics of superconductivity in low- T_c materials is described by BCS theory (proposed by Bardeen, Cooper, and Schrieffer) [BCS57]. In these materials, an attractive force between electrons is created as they pass through the crystal lattice and deform it, creating regions of locally intensified positive charge. At low temperatures, this phonon-mediated attraction causes free electrons to combine into Cooper pairs. The pairing process brings the electrons into a significantly lower energy state, such that an energy gap Δ exists between the superconducting and normal conducting states. In order to break a Cooper pair, an energy of 2Δ is required. When electrons in a Cooper pair encounter disorder in the lattice that would cause scattering and resistance in a normal conductor, the energy that the electrons would gain by scattering would not be enough to overcome the energy gap, so they do not scatter, and no resistance is caused by their DC transport current.

Under DC currents, Cooper pairs screen unpaired electrons, essentially short-circuiting them. However, under AC currents, because of the inertia of the pairs, the screening is imperfect, resulting in a small but finite resistance. This is generally described in terms of a surface resistance R_s , which can be used to calculate the dissipated power P_{diss} in the walls of a superconductor per unit area:

$$P_{diss} = \frac{1}{2} R_s \int_S |\mathbf{H}|^2 ds \quad (2.1)$$

The resistance decreases strongly with temperature as the fraction of paired electrons increases. The surface resistance of a superconductor predicted by

BCS theory is approximated by¹

$$R_{BCS} = A \frac{f^2}{T} \exp\left(\frac{-\Delta}{k_B T}\right) \quad (2.2)$$

where f is the frequency, T , is the temperature, k_B is the Boltzmann constant, and A is constant that depends on the material [PKH08].

When a superconductor is cooled far below T_c , R_{BCS} becomes exponentially small, but the total surface resistance R_s approaches a steady value. At this point, other sources of resistance become significant, such as trapped magnetic flux, moving flux lines, and impurity heating. This resistance that remains at low temperatures is called the residual resistance R_{res} . Noting that both can depend on the applied field, the two components of R_s can be summarized as follows:

$$R_s(T, B) = R_{BCS}(T, B) + R_{res}(B) \quad (2.3)$$

2.3 Type I and Type II Superconductors

There are two very important length scales in superconductivity: the coherence length ξ and the penetration depth λ . ξ is the characteristic length scale of the superconducting wavefunction. It describes the distance over which paired electrons interact. λ is the characteristic length scale of the interaction of the superconductor with magnetic fields. Magnetic fields decay exponentially into the bulk of the superconductor with decay constant λ .

The Type of a superconductor is determined by its dominant length scale. A

¹The temperature dependence of the prefactor before the exponential will depend on other parameters such as mean free path. Careful consideration should be taken when fitting to use the appropriate form of the BCS resistance equation.

material where ξ is dominant ($\xi > \sqrt{2}\lambda$) will be Type I, and a material where λ is dominant ($\xi < \sqrt{2}\lambda$) will be Type II. The difference can be understood in terms of energy. The energy of a superconductor is raised when an external magnetic field is applied to it, as it must apply screening currents to expel the flux from its bulk. If it were to allow a small volume with radius ξ within it to become normal conducting so that it could allow flux in, the free energy would be lowered in the region λ away from the normal conducting volume. However, in the volume that turned normal conducting, the energy would be raised by the condensation energy of the previously paired electrons. In Type I superconductors, where ξ dominates, the energy “cost” is larger than the “benefit,” but in Type II superconductors, the opposite is true, so at some external field it becomes energetically advantageous to create small normal conducting volumes in the superconductor. In these regions, called vortices (shown in [Figure 2.1](#)), current loops surround a flux-filled normal conducting core, with magnetic fields decaying exponentially into the superconducting regions around it. The magnetic flux in a flux line fully immersed in the bulk of a superconductor is quantized, with each vortex containing $\phi_0 \simeq 2.1 \times 10^{-15}$ Wb [[Nat](#)].

The Ginzburg Landau parameter $\kappa = \lambda/\xi$ is used to describe the Type of a superconductor. If a material has $\kappa < 1/\sqrt{2}$ it is Type I; otherwise it is Type II.

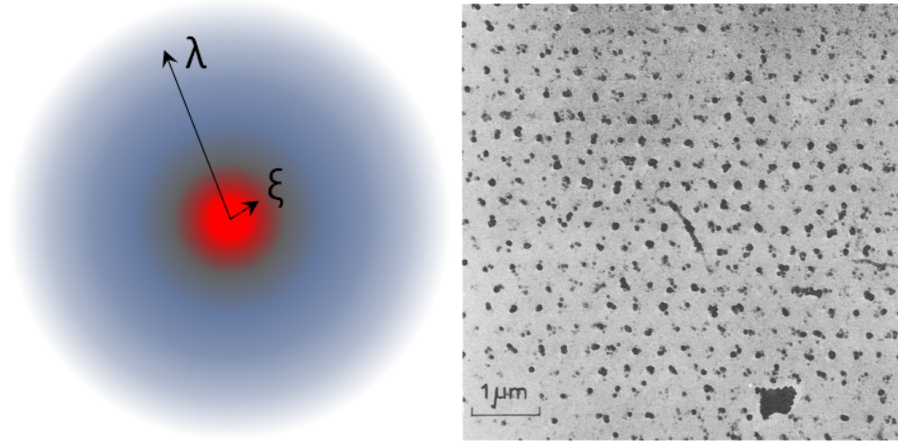


Figure 2.1: Left: diagram of a vortex in a type-II superconductor. The core with characteristic length ξ contains electrons that are excited out of the superconducting state, an energy “cost.” The penetration of magnetic fields with characteristic length λ acts as an energy “benefit.” Right: Array of vortices observed using Bitter decoration technique. Image from [ET67].

2.4 Critical Fields

In a Type II superconductor², the lowest applied field at which the free energy is lowered by having a vortex in the bulk rather than outside the superconductor is called the lower critical field H_{c1} ³. For a strongly Type II material ($\kappa \gg 1$), the low temperature H_{c1} is approximated by [Hei99]:

$$\mu_0 H_{c1} = \frac{\phi_0}{4\pi\lambda^2} (\ln \kappa + 0.5) \quad (2.4)$$

For materials with smaller κ , H_{c1} can be found numerically [HA63].

Even though it is energetically favorable for flux to be inside the superconductor at H_{c1} , it does not penetrate at this field. Just as water remains in the

²Type I superconductors are not focused on in this dissertation. Rather than having the two critical field H_{c1} and H_{c2} , they have only H_c , when it is energetically favorable for flux to be inside the superconductor, but as with Type II superconductors, a surface energy barrier allows a metastable state above H_c .

³In SRF applications, magnetic fields are generally measured in T or mT instead of A/m, so in this dissertation, values are given for $\mu_0 H$ instead of H .

liquid state above its boiling point, a superconductor can remain in the flux free state above H_{c1} . An energy barrier allows it to remain in this metastable state up to at most H_{sh} , the superheating field [MSJ67, BL64]. For defect-free Type II materials, the low temperature H_{sh} can be calculated from [TCS11]:

$$H_{sh} = H_c \left(\frac{\sqrt{20}}{6} + \frac{0.5448}{\sqrt{\kappa}} \right) \quad (2.5)$$

where H_c is the thermodynamic field, given by $\frac{\phi_0}{2\sqrt{2}\pi\mu_0\lambda\xi}$ [Tin04].

Flux penetration is generally acceptable in DC applications but extremely undesirable in RF applications, in which the direction of the magnetic field changes twice every RF cycle. If flux were to penetrate the superconductor billions of times per second, there would be a very large amount of heat dissipation due to the motion of the vortex cores through the material [BS65], and the superconductor would in most circumstances quench (be driven normal conducting). Therefore, H_{sh} is the ultimate limit for superconductors in RF fields.

Above H_{sh} , as the external field is increased, flux lines can continue to enter the superconductor, creating more and more normal conducting volume. In the vortex state, flux lines form a regular lattice, shown in Figure 2.1. H_{c2} is the ultimate limit of the superconducting state: above this field, the entire material will be normal conducting. The low temperature H_{c2} is given by [Tin04]:

$$\mu_0 H_{c2} = \frac{\phi_0}{2\pi\xi^2} \quad (2.6)$$

where ϕ_0 is the flux quantum.

The phase diagram of an ideal Type II superconductor (as a function of temperature and applied magnetic field H) is shown in Figure 2.2, with critical fields indicated⁴. The critical fields scale with temperature approximately as $1-(T/T_c)^2$

⁴The phase diagram assumes no transport current. To take current into account, another axis can be added, with superconductivity terminating at the critical current density J_c .

⁵. Also shown is the magnetization curve of an ideal type II superconductor increasing from zero field⁶.

2.5 Defects and the Metastable State

Impurities, voids, and other defects that can be present in a realistic superconductor may adversely affect the limit of the flux free state. When considering whether vortices can penetrate into a superconductor, calculations effectively take into account the energy “cost” from the normal conducting core and the energy “benefit” from the magnetic fields around it. However, defects near the surface can locally disrupt superconductivity, reducing the energy “cost” of the core, so that it is easier for flux to penetrate. Because vortex cores have size of approximately ξ , this sets the length scale at which defects become possible nucleation sites for flux penetration.

In contrast, defects are beneficial in DC magnet applications, where they can pin flux, preventing it from being moved by strong Lorentz forces. This increases the maximum current that can be sustained with zero resistance in a magnet, and therefore increases the maximum field it can create. Bulk pinning is not useful for RF applications, because of how strongly dissipative vortex core motion is. Even the motion of flux from the surface of the material to pinning sites nearby is likely to cause quench if it were happening billions of times per

⁵This dependence is approximate. The temperature dependence of H_c is close to this [Tin04] (as predicted for example by Gorter and Casimir’s early phenomenological two-fluid model [TT96, GC34]), but other critical fields have additional dependence on κ which will give an additional correction. For example, excellent summaries of the temperature dependence of H_{sh} and H_{c2} can be found in [CS08] and [God05] respectively. The impact of these corrections on the discussion in this dissertation would be small, so they are omitted.

⁶In the reverse direction, the magnetization curve will be quite different; e.g. the metastable superheated state will not be present.

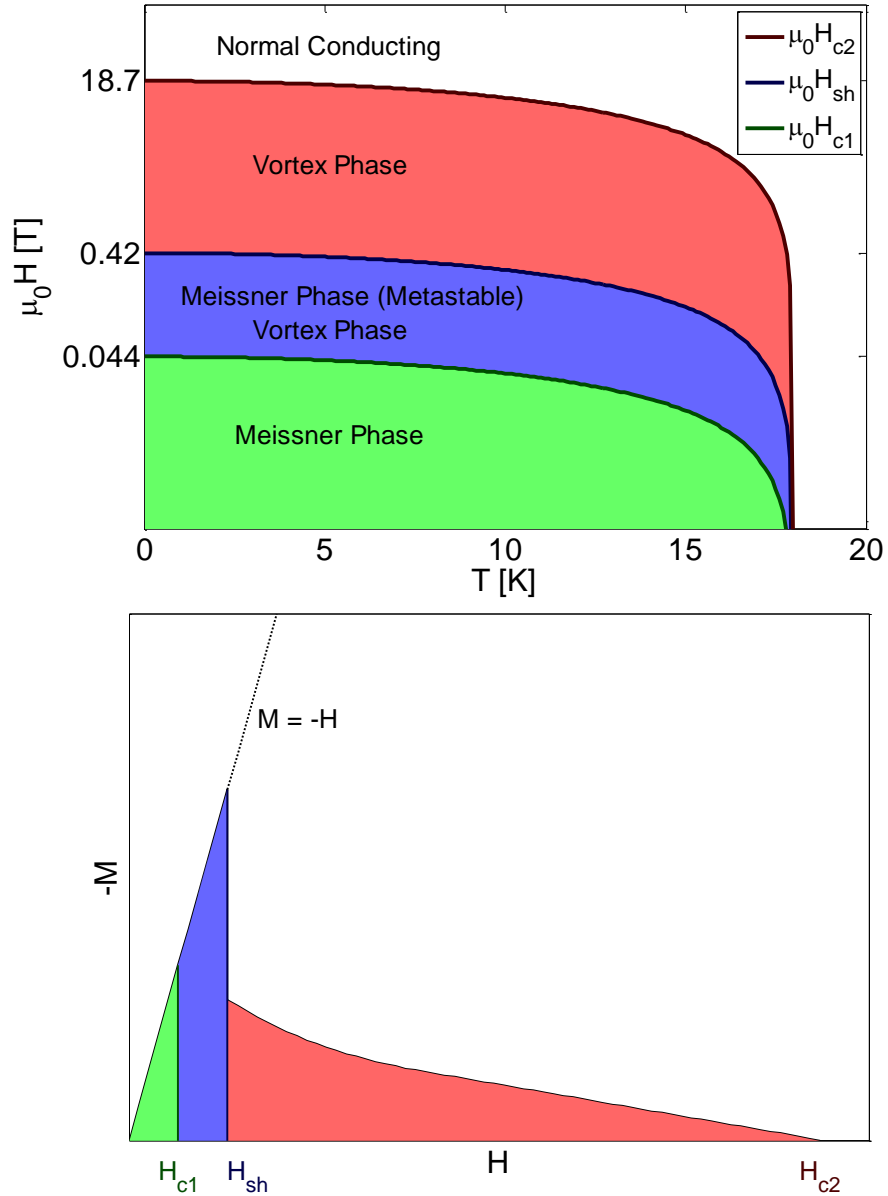


Figure 2.2: Phase diagram (top) and magnetization curve (bottom) of an ideal type II superconductor. For the phase diagram, critical fields of Nb_3Sn shown on log scale are calculated using material properties from Table 2.2.

second over the surface of the cavity.

The impurity content also affects ξ and λ of the superconductor. Very pure or “clean” materials will have ξ close to the intrinsic coherence length ξ_0 and λ close to the London penetration depth λ_L . For materials that are more “dirty,” the impurity content can be quantified by the electron mean free path l , and ξ and λ at $T = 0$ can be calculated from the following [Tin04,OMFB79]:

$$\lambda(T = 0) = \lambda_L \sqrt{1 + \frac{\xi_0}{l}} \quad (2.7)$$

$$\xi(T = 0) = 0.739 \left[\xi_0^{-2} + \frac{0.882}{\xi_0 l} \right]^{-1/2} \quad (2.8)$$

Generally, making a material more dirty will increase κ , making Type II superconductors act more strongly Type II: H_{c1} becomes smaller and H_{c2} becomes larger.

2.6 Introduction to SRF Cavities

RF cavities are electromagnetic resonators, meaning that they can build up a large electromagnetic fields from relatively small input RF amplitudes. If a cavity is driven at a frequency close to one of its resonant modes, it stores energy in electric or magnetic fields at different times during an RF cycle. A crude electrical model for an RF cavity is an RLC circuit, easily visualized by a pillbox cavity in the TM_{010} mode, as in [Figure 2.3⁷](#). At some point during the RF period (let us call this phase advance $\phi = 0^\circ$), there will be a buildup of charge on one of the endcaps of the cavity, a depletion of charge from the other endcap, and no

⁷The cavities used in experiments for this dissertation are not pillboxes, but they are very similar to this example in that they are single-cell cavities that operate in the TM_{010} mode.

charge motion. At this point, there will be a maximum in the longitudinally-oriented electric field in the cavity. In the RLC circuit model, the energy would now be stored in the capacitor. As the RF cycle progresses, the charge will be driven by the large electric field towards the charge-depleted region, causing a large current to flow longitudinally along the cylinder. This current will induce a radial magnetic field in the cavity, which will reach a maximum when the electric field is zero ($\phi = 90^\circ$). In the circuit model, now the energy would be stored in the inductor, and dissipation would be created as the current passes through the resistor (the walls of the cavity). The current will persist until the charge buildup (and electric field) is reversed ($\phi = 180^\circ$), and then the current will reverse and create a maximum in magnetic field in the opposite direction from before ($\phi = 270^\circ$).

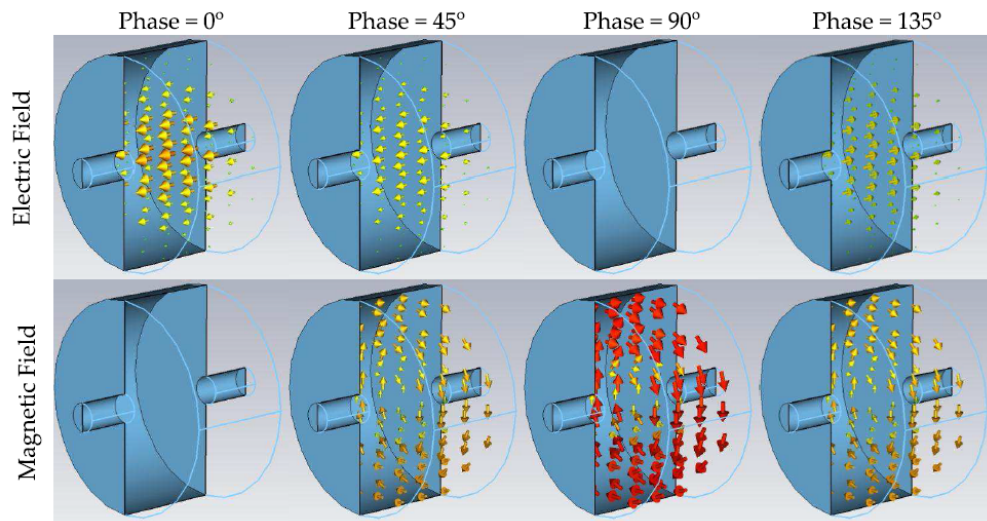


Figure 2.3: Illustration of the fields in a pillbox cavity as a function of time during the RF cycle. Energy is exchanged between the electric and magnetic fields, as in an RLC circuit. Image from [Val14].

The ultimate purpose of a cavity is generally to provide longitudinal acceleration to a beam of charged particles. The energy increase ΔE it imparts to a particle with charge q is described by the accelerating voltage $V = \Delta E/q$. It is of-

ten defined in terms of the accelerating gradient E_{acc} —this is the time-averaged longitudinal electric field seen by the beam as it passes through the cavity—according to $V = E_{acc}L$, where L is the length of the cavity. Other important fields are the peak surface magnetic field B_{pk} and the peak surface electric field E_{pk} , which are proportional to E_{acc} in a given cavity at a given field.

RF cavities are made from normal conducting materials (most commonly water-cooled copper operating near room temperature), or from superconducting materials (most commonly niobium operating at cryogenic temperatures cooled by liquid helium). Superconducting materials have the advantage of having much smaller surface resistance R_s , reducing the RF dissipation in the walls of the cavity by a factor of approximately 10^6 compared to similar normal conducting cavities. This allows SRF cavities to operate at high fields in continuous wave mode—meaning that the RF power is continuously applied with 100% duty factor—in a stable manner whereas similar copper cavities would overheat and melt if operating CW at these fields [PKH08].

A figure of merit used to evaluate the efficiency of an RF cavity is the quality factor Q_0 . Assuming that the surface resistance is constant over the surface of the cavity, Q_0 can be defined by $Q_0 = G/R_s$, where the constant G depends on the geometry of the cavity. The power dissipated in the cavity is given by

$$P_{diss} = \frac{V^2}{\frac{R_a}{Q_0} Q_0} \quad (2.9)$$

where R_a is the shunt impedance and R_a/Q_0 is a constant that depends on the geometry of the cavity⁸. The heat dissipated in the walls of an SRF cavity must be removed at cryogenic temperatures, where the thermodynamic efficiency is quite poor. Even taking this into account, the power consumption is still a factor

⁸Note that the accelerator definition of R_a/Q_0 is used in this dissertation, and not the circuit definition, which differs by a factor of 2.

of $10^2 - 10^3$ times smaller than the input RF power required to operate a normal conducting cavity at the same field in CW mode [PKH08].

The ratio of E_{acc} to E_{pk} and B_{pk} will depend on the cavity shape, as will G and R_a/Q_0 . Different cavity shapes are optimized for different applications. The shapes that will be discussed in this dissertation are given in Table 2.1⁹.

	TeSLA	Cornell ERL	CEBAF
f [GHz]	1.3	1.3	1.5
E_{pk}/E_{acc}	1.88	1.76	1.81
B_{pk}/E_{acc} [mT/MVm ⁻¹]	4.28	4.08	4.4
G [Ω]	278	272	255
R_a/Q_0 [Ω]	105	116	102
E_{pk}/\sqrt{U} [MVm ⁻¹ / \sqrt{J}]	15.1	14.7	17.6
Reference	[HMS92,Edw95]	[Vea14]	[KAK ⁺ 85,Kno97]

Table 2.1: Cavity shapes used in this dissertation and their parameters. Values were calculated by V. Shemelin for single cell cavities with long beam pipes using SLANS.

Generally, the two most important figures of merit for an SRF cavity are Q_0 and E_{acc} . The higher E_{acc} , the fewer cavities are needed to accelerate a beam to a given energy. The higher the Q_0 at that E_{acc} , the smaller the power dissipated into the walls of the cavity. Achieving high Q_0 at the design gradient in an SRF accelerator is important to keeping cryogenic costs reasonable.

2.7 Potential of Nb₃Sn for SRF Applications

The standard material in use today for SRF cavities is niobium, either in bulk form [PKH08], or as a relatively thin film on a copper substrate [Ben91]. Nio-

⁹The half-cells for the single cell cavities are formed using dies designed for multicell cavities, which generally consist of 2-3 different cup shapes. For these calculations, it was assumed that to make the single cell cavities, for TeSLA, endcup 2 was used, for the Cornell ERL, the main linac inner cell was used, and for CEBAF, the LE1 Mark III was used.

niobium has the highest T_c of the elemental superconductors, which is important to keeping R_s small. It also is relatively easy to fabricate particle accelerator cavities with—one can simply form sheets of purified niobium into the cavity shape and then weld them together, or else sputter pure niobium onto copper.

SRF researchers have been developing preparation methods for niobium cavities for several decades, and have found ways to avoid many non-fundamental limitation mechanisms. Examples of preparation methods developed relatively recently include high pressure rinsing (HPR) with purified water to clean surfaces and prevent field emission [BBF92,KLT93], electropolishing for extremely smooth surfaces [SK89], 120°C baking to avoid high field Q-slope (HFQS) [Vis98,Kne99], and nitrogen doping to increase Q_0 [GRS⁺13]. With these advances, state-of-the-art niobium cavities can reach very high accelerating gradients with accompanying B_{pk} close to the superheating field of niobium, the fundamental limit. They can also achieve very small R_s at operating temperatures, with minimal R_{res} . However, the material does have significant limitations. To illustrate this, let us consider two particle accelerator applications.

The first application is high duty factor (or CW), medium energy linacs, such as the Linac Coherent Light Source (LCLS) II [Gal14]. As Equation 2.2 shows, the R_{BCS} scales exponentially with $-\Delta/k_B T$, so these machines generally operate near 2 K to keep the R_s manageable. However, the high duty factor means that the dynamic load is quite large, necessitating the use of large cryogenic plants, which cost on the order of 100 million USD and require megawatts of power to operate. Because the heat dissipated by a cavity scales with E_{acc}^2 as shown in Equation 2.9, the cost optimum energy gradient tends to be relatively small, well below the H_{sh} limit [Lie09,Pow13]. An alternative material with a smaller

R_{BCS} at a given temperature than niobium could increase the cost optimum E_{acc} , allowing fewer cavities to be used. Alternatively, it could allow the cavities to be operated at a higher temperature, such as 4.2 K, the boiling point of liquid helium at atmospheric pressure. This would simplify the cryogenic plant, reducing its capital cost and its power requirements.

The second application to consider is low duty factor, high energy SRF linacs, which require many cavities operating at as high E_{acc} as possible. For example, the International Linear Collider (ILC) design calls for approximately 16,000 cavities in a 31 km linac [Beh13]. Since the maximum gradient of state-of-the-art cavities are limited by H_{sh} , the only way to reach significantly higher gradients—and thereby decrease the number of cavities needed in such an SRF linac—is to use an alternative material with a larger H_{sh} than niobium.

One promising alternative SRF material is Nb_3Sn . It has an energy gap of approximately 340 meV, compared to approximately 140 meV for niobium (from Table 2.2 later in the chapter). This allows it to have a far smaller R_{BCS} at a given temperature, as shown by the exponential term in Equation 2.2. To illustrate this strong improvement, in Figure 2.4, R_s is plotted as a function of temperature up to T_c for typical 120°C baked niobium and Nb_3Sn surfaces at 1.3 GHz. The curves were calculated using Halbritter’s SRIMP code [Hal70b, Hal70a, Val14]. Input material parameters for niobium are from [MM65, NM75] and for Nb_3Sn from [Hei99]. R_{res} of 3 n Ω was assumed for both materials. R_s of copper at 273 K (conductivity from [JTS+80]) is shown for comparison, to illustrate the benefit of superconducting materials in RF applications.

As a case study, let us consider a 1.3 GHz TeSLA cavity operating CW at 16 MV/m, similar to the specification for LCLS II or the Cornell ERL

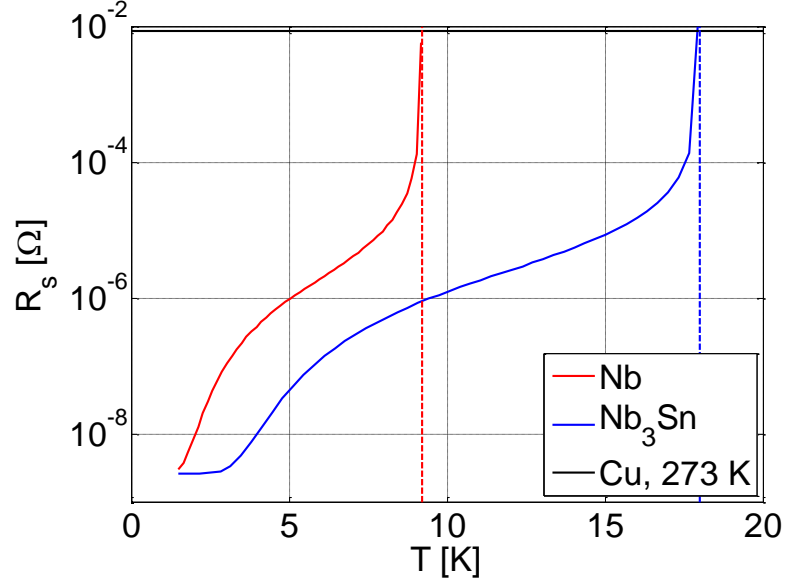


Figure 2.4: Significant improvement in surface resistance as a function of temperature for Nb_3Sn compared to niobium at 1.3 GHz [Hal70b]. R_{res} of 2.7 n Ω was assumed. T_c is indicated by a dashed line, and R_s of normal conducting copper is shown for comparison.

[Gal14, HGT13]. In Figure 2.5, Equation 2.9 was used to calculate the power dissipated in the helium bath as a function of operating temperature for R_s calculated above. The AC power required by the cryogenic plant in order to remove a watt of power dissipated in the helium bath depends on the efficiency of the plant at the operating temperature. Typical inverse coefficient of performance (COP^{-1} is the ratio of input power required to cooling power provided) as a function of temperature is plotted in Figure 2.6. This factor includes both the Carnot COP ($\text{COP}_{carnot} = T_{He}/(T_{rm} - T_{He})$, where T_{He} is the helium bath temperature and T_{rm} is room temperature [PKH08]) and typical figure of merit, which takes into account deviation of a realistic plant from the Carnot COP ($\text{FOM} = \text{COP}/\text{COP}_{carnot}$). Typical FOM values were found in [SKR03]. Taking efficiency into account, the AC power required ($P_{AC} = \text{COP}^{-1} P_{diss}$) per cavity of this type is shown in Figure 2.5 as a function of temperature for both Nb and Nb_3Sn . Not only is the AC power smaller for Nb_3Sn than for Nb at a given tem-

perature, but also it is very small at high temperatures, allowing for a further cost reduction by simplifying the cryogenic plant¹⁰.

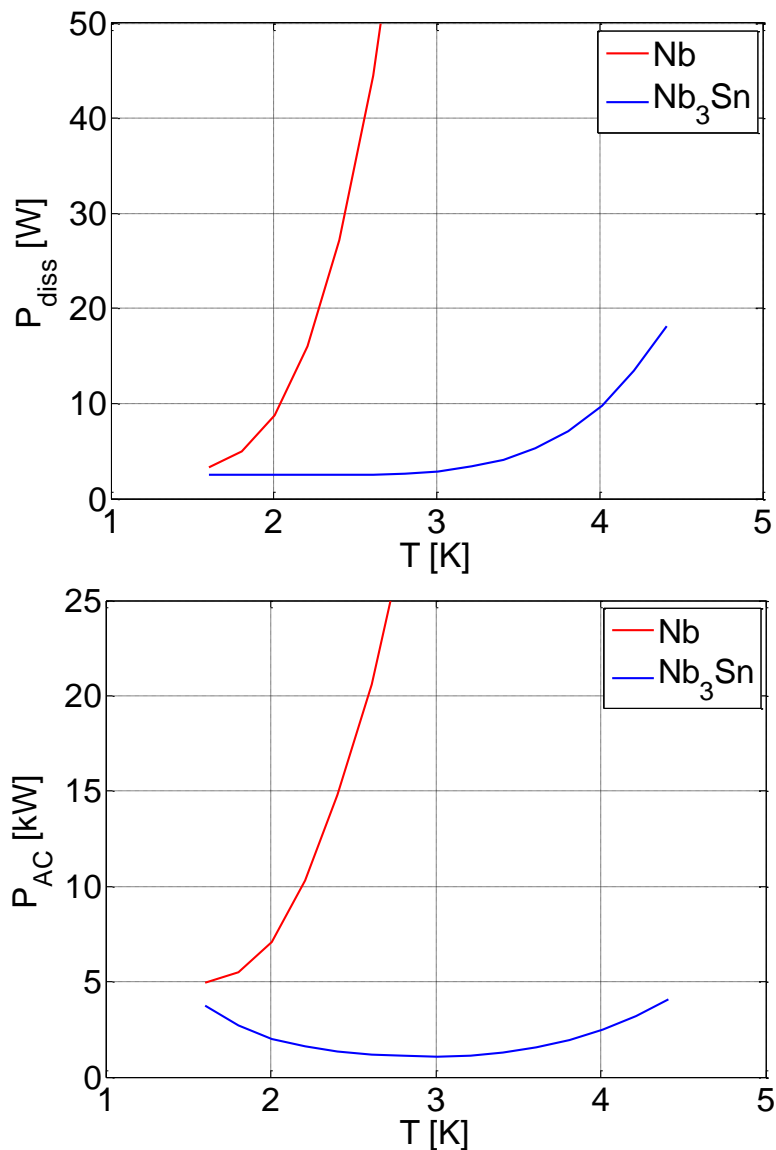


Figure 2.5: Power dissipated in the walls of a 1.3 GHz TeSLA cavity at 16 MV (top) and AC power required to cool this cavity taking into account the cryogenic plant efficiency (bottom) as a function of temperature. Niobium is compared to Nb₃Sn, showing the strong reduction in power required to cool the Nb₃Sn cavity.

For high energy applications, it is important to be able to operate as high as

¹⁰Note that this is only a qualitative comparison, as the numbers are sensitive to material parameters and R_{res} .

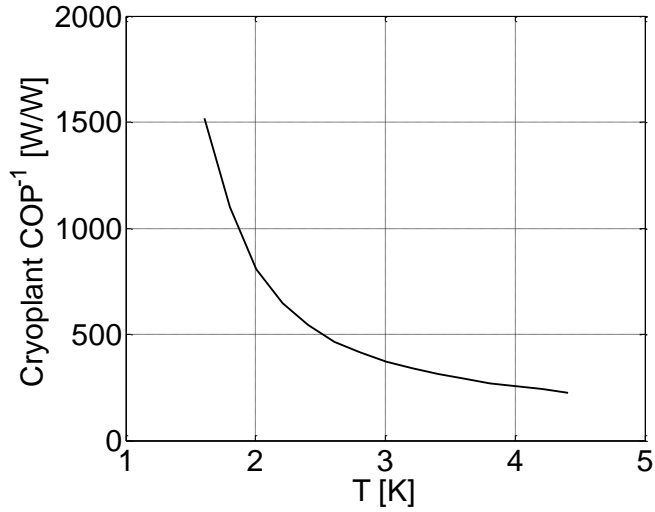


Figure 2.6: Overall efficiency as a function of helium temperature for a large cryogenic plant. Calculated using data from [SKR03].

possible in E_{acc} , and currently cavities are limited by H_{sh} of niobium. Nb₃Sn is predicted to have a low temperature $\mu_0 H_{sh}$ of ~ 400 mT [TCS11], approximately twice that of niobium. At $B_{pk}=400$ mT, an ILC-style cavity would reach $E_{acc} \approx 100$ MV/m, compared to the maximum field for a niobium cavity, ~ 50 MV/m.

These dramatic increases in both Q_0 at a given temperature and H_{sh} illustrate the potential of Nb₃Sn to improve large SRF linacs. On a smaller scale, Nb₃Sn cavities could be used in low energy industrial applications. In these situations, it may not be cost-effective to have a supply of superfluid liquid helium to keep Nb cavities in the $Q_0 \sim 10^{10}$ regime. The higher T_c of Nb₃Sn would allow low-loss operation with atmospheric liquid helium at 4.2 K or perhaps gas or supercritical helium at higher temperatures. This could have applications in flue gas and wastewater treatment, isotope production, and border security [HS10, Sab13].

2.8 Other SRF Materials

There are superconductors other than Nb_3Sn that have high H_{sh} and large Δ , but not all of them are options for SRF applications. To be a viable SRF material, a superconductor must fulfill certain criteria:

- It must have a relatively large ξ compared to the size of defects in the material to avoid nucleation of flux penetration.
- It must be possible to fabricate it in a way that it conforms to a complex geometry over large area.
- It must have decent thermal conductivity for cooling to avoid thermal runaway.
- It must have minimal surface roughness to avoid field enhancement.
- It must be able to be made clean (for example, it cannot release potentially field emitting dust, and there must be a method to clean surface contaminants without affecting quality).
- After surface processing, it must have a reasonably small secondary electron yield (SEY). SEY predicts the average number of electrons produced per electron impact at the surface at a given energy. If SEY is well above 1, there is a risk of resonant electron buildup (multipacting).

Some of the most promising alternative SRF materials and relevant properties are shown in [Table 2.2](#), along with those of niobium. Experimental references for these properties were chosen to try to display realistic properties for polycrystalline films. However, material parameters vary depending on how

Material	$\lambda(T = 0)$ [nm]	$\xi(T = 0)$ [nm]	$\mu_0 H_{sh}$ [mT]	T_c [K]	$\Delta/k_B T_c$
Nb	50	22	219	9.2	1.8
Nb ₃ Sn	111	4.2	425	18	2.2
MgB ₂	185	4.9	170	37	0.6-2.1
NbN	375	2.9	214	16	2.2

Table 2.2: Measured material properties of niobium and three promising alternative SRF materials. For Nb a RRR of 10 was assumed. For MgB₂, λ and ξ are not calculated, as the experimental values are given in the reference. H_{sh} for Nb is found from [DDD97] and for others calculated from Equation 2.5. Nb data from [MM65, NM75], Nb₃Sn data from [Hei99], NbN data from [OAC⁺91], and MgB₂ data from [WPJ01]. Note that the two gap nature of MgB₂ may require more careful analysis than is shown here.

the superconductor is fabricated, and some improvement in SRF qualities can be expected with R&D.

Of these materials, Nb₃Sn has the highest predicted H_{sh} by far, giving it the most potential for high field applications. It also has among the highest T_c and $\Delta/k_b T_c$, making it extremely promising for high duty factor applications as well. It is stable with exposure to water (which for example is not true for MgB₂ [ZCZ⁺01]); furthermore, no evidence of damage has been observed after cleaning using one of the standard methods for niobium, high pressure water rinsing. In addition, as is discussed in section 5.3, SEY measurements indicate that the probability for multipacting is not significantly worse than with niobium. For these reasons, it was chosen as the material to pursue in this research program.

2.9 Enhancing Understanding of RF Superconductivity

The advantages of Nb₃Sn for accelerator applications have been discussed, but there is also strong scientific motivation for studying this material. Nb₃Sn research can help scientists better understand how superconductors interact with magnetic fields. This includes a better understanding of flux penetration for a defect free surface, flux penetration for a surface with defects, sources of spurious surface resistance, and the optimal geometry for maintaining the Meissner state.

2.9.1 Flux Penetration for a Defect Free Surface

H_{sh} is a critical field that is not easily measurable under most circumstances. 4-wire probe measurements in magnetic fields measure the field at which flux in the superconductor becomes depinned and starts to flow. Measurements of magnetization curves can be used to obtain H_{sh} , but it can be complicated by the influence of demagnetization and pinning. On the other hand, measurements of the quench field of a cavity coated with that superconductor unambiguously provide a lower bound for H_{sh} . In a cavity in which surface defects are small compared to ξ , and non-fundamental limitations are prevented, the quench field will be a direct measurement of H_{sh} . In this way, measurements of H_{sh} of niobium have been made in cavities prepared with state-of-the-art techniques, agreeing well with theory [Val14].

Theoretical predictions have been made for the scaling of H_{sh} with κ for high- κ superconductors such as Nb₃Sn [TCS11]. Previous researchers have per-

formed pulsed measurements of maximum fields of Nb₃Sn cavities [Cam85, HPS97], which agree with predictions at temperatures close to T_c , but are significantly lower than H_{sh} at lower temperatures (see chapter 8). Additional studies are needed to understand if the predictions are incorrect, or if another mechanism prevents cavities made from this material from reaching H_{sh} . Defect-free Nb₃Sn cavities would provide an ideal method for exploring this. One of the goals of this research is to make steps towards cavities that could be used for such an experiment.

2.9.2 Flux Penetration for a Surface With Defects

It may not be possible to reach H_{sh} in Nb₃Sn cavities because of its relatively small ξ . Even small defects could act as nucleation sites for flux penetration. However, it is difficult to predict what size of defect will result in flux penetration at a given field. Correlating quench fields to defect size can lead to a better understanding of the scaling laws relevant for defects on RF superconductors. Such scaling laws could be used to guide the development of preparation methods for low- ξ SRF materials in order to avoid dangerous defects.

At the start of this research, it was also not clear if bulk flux penetration would be inevitable above the first critical field for a small ξ material. Below H_{c1} , even if flux penetrated at defects, it would be more energetically favorable for it to be close to the surface than deep in the bulk; however, the opposite would be true above H_{c1} . It had been hypothesized that the metastable state would be unreliable for Nb₃Sn, and that a fundamental loss mechanism such as vortex dissipation would occur above H_{c1} when the most energetically favorable

position for flux would be in the bulk [BKM⁺97, Gur06]. One of the goals of this research program is to prove or disprove this idea.

2.9.3 Sources of Spurious Surface Resistance

Even after decades of studying niobium cavities, there are phenomena that are not well understood. One of these is a decrease in Q_0 as E_{acc} is increased, which can be a gradual drop in the case of medium field Q -slope (MFQS), or sharp in the case of high field Q -slope (HFQS). Many theories have been postulated for the causes of these degradations (a few examples are [RP10, PZC⁺08, Cio06, KGLP99]—see [Pad09] for a review of some of these mechanisms), but none have been proven. If high quality Nb₃Sn cavities can be produced, it can provide more information about MFQS and HFQS. Its strength in this material with strongly different BCS material parameters may support one of the proposed theories, or suggest a mechanism that has not been thought of before.

There are also experiments in which spurious surface resistance is observed in high- κ materials that is not observed in niobium. For example, previous experimenters have observed Nb₃Sn cavities that show very low R_s at low fields, but as the magnetic field is increased, R_s increases sharply. The cause of this extra resistance might be regions of incorrect stoichiometry, but there may also be more fundamental behavior occurring. In-depth studies of high- κ materials can point to the mechanisms that cause these losses and lead to a better understanding of how superconductors interact with large RF magnetic fields.

2.9.4 Closing of the Quasiparticle Spectral Gap

One possible limit for SRF cavities was discussed by Lin and Gurevich in [LG12]. They show that as the surface magnetic field in an SRF cavity approaches H_{sh} , it becomes easier to generate quasiparticles, excitations of Cooper pairs out of the superconducting state. As H/H_{sh} approaches unity, the currents in the superconductor become significant, and the momentum of the electrons changes the density of quasiparticle energy states $\nu(\epsilon)$, causing the energy gap ϵ_g in the quasiparticle spectrum to shrink. This is shown in Figure 2.7, a reproduction of a figure in [LG12] based on their formalism in the high- κ limit. As the magnetic field is increased (represented by the increase of a parameter u proportional to the superfluid velocity towards its value at the superheating field u_s), the quasiparticle energy gap (which is given by the lowest energy state in the density of states as a function of quasiparticle energy ϵ) becomes smaller.

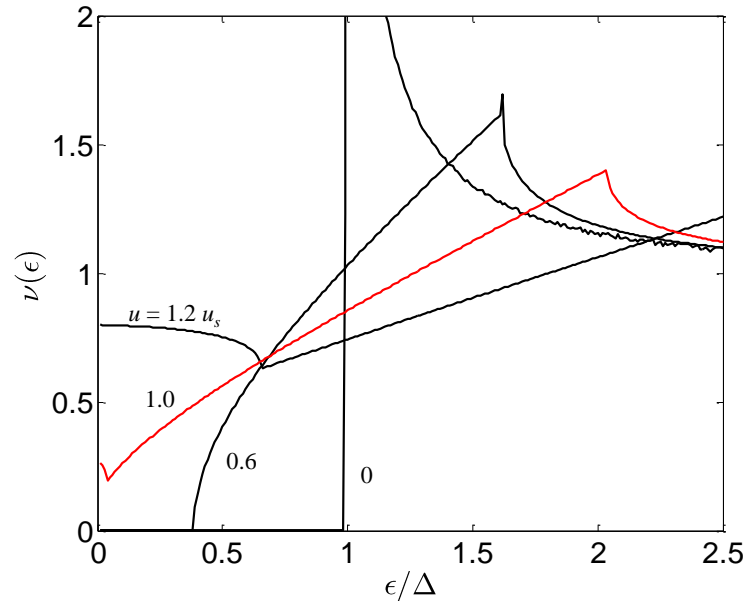


Figure 2.7: Density of states in the clean limit for various values of u , which reaches u_s when $H = H_{sh}$; reproduction of a figure from [LG12].

The quasiparticle energy gap as a function of $H/H_{sh} = u/u_s$ was solved for numerically using Lin and Gurevich's formalism. It is shown in Figure 2.8, normalized to the energy gap at zero field and zero temperature Δ . The calculations is performed for $\alpha = 0, 3.6$, and 20 , where α is a measure of the dirtiness of the superconductor given by $\alpha = \pi\xi_0/l$. These three values of α represent, respectively, the clean limit, a moderately dirty superconductor, and a very dirty superconductor.

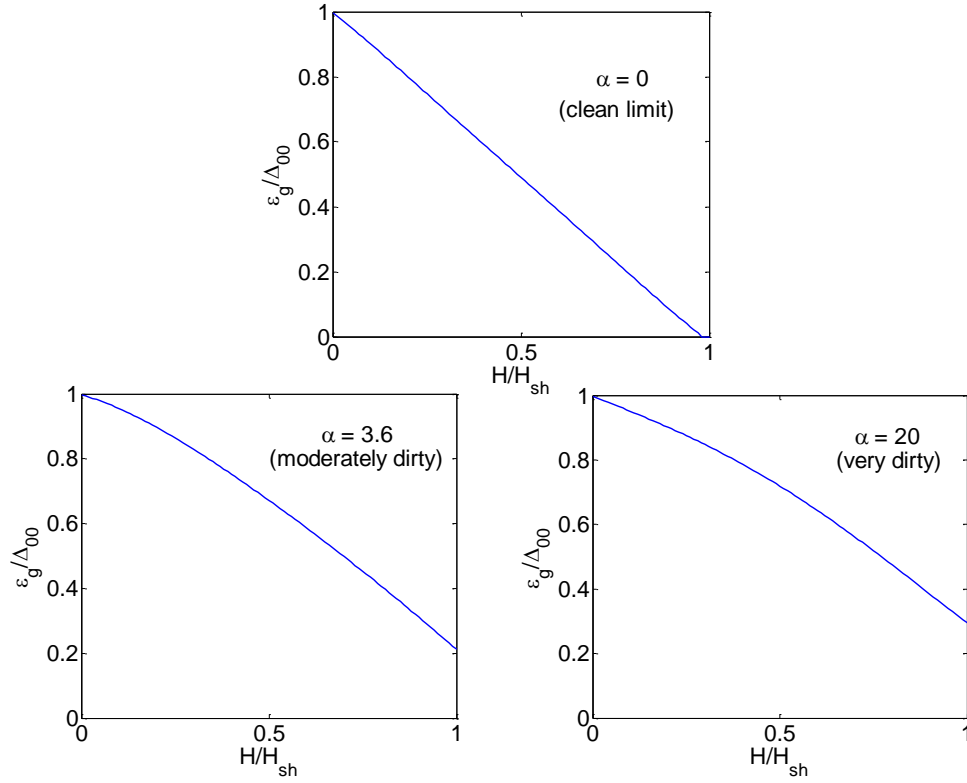


Figure 2.8: Results of the calculation of the quasiparticle gap as a function of field for three different levels of dirt α .

As observed by Lin and Gurevich, in the clean limit, the gap closes at $0.97H/H_{sh}$. As the level of dirt increases, H_{sh} is reached without the gap closing, and the size of the gap at H_{sh} increases as the level of dirt increases. The gap closes in a more or less linear fashion with field. The change in the BCS resistance can be estimated by replacing the energy gap Δ at zero field in Equa-

tion 2.2 with $\epsilon_g(H)$ [LG12]. This can be used to approximate the expected effect on the Q vs E curve, using SRIMP¹¹. Except for the modified gap, the parameters input to SRIMP are the same as those in Figure 2.4, including R_{res} of 3 n Ω . An operating temperature of 4.2 K was assumed.

The 4.2 K Q vs E curves show that for a modest amount of dirt, the Q_0 stays in the 10^{10} range until near $\mu_0 H_{sh}$ of niobium, approximately 200 mT. As a result, it does not seem likely to interfere with applications until very high fields. On the other hand, even at modestly high fields around 100 mT, the gap closing should be large enough to be observed if R_{res} can be kept small. It would be a very interesting to compare a measurement of the magnitude of its effect on Q_0 with these predictions.

At 2.0 K, the Q vs E curves with a modest amount of dirt maintain Q_0 above 10^{10} up to B_{pk} higher than 300 mT. Therefore, even with the closing of the gap, Nb₃Sn can still offer extremely high field performance with high Q_0 .

2.9.5 Optimal Geometry for Maintaining the Meissner State

State-of-the-art cavities are either made of formed niobium sheets or another material coated with a bulk niobium film (bulk meaning many penetration depths thick). This geometry provides excellent screening, but it is possible that another configuration may allow for larger amplitude RF fields to be screened. Is it possible for superconductors to be arranged as a series of thin films such that they can screen fields significantly larger than their H_{sh} in bulk form? In the

¹¹For this calculation, $H = B_{pk}/\mu_0$ is used when finding $\epsilon_g(H)$. Only the part of the cavity surface in the high magnetic field is close to B_{pk} , but calculating $Q_0 = G/R_s$ in this way assumes the whole cavity is at B_{pk} . Therefore this is an overestimate of the degradation of Q_0 caused by the gap closing

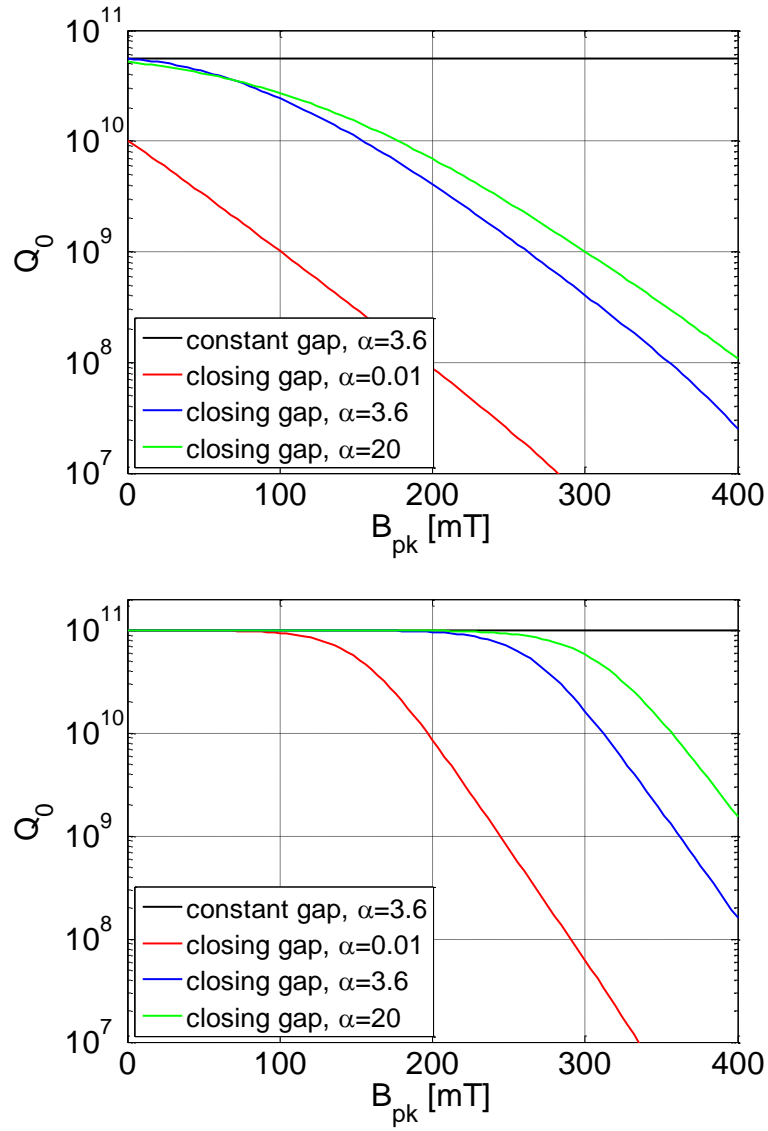


Figure 2.9: Calculated Q_{BCS} vs H curves for a Nb_3Sn cavity ($G = 270 \Omega$) at 4.2 K (top) and 2.0 K (bottom) found using the decreasing quasiparticle gap with field.

next chapter, the SIS' geometry is considered and a discussion is presented of whether it might be a better implementation of Nb_3Sn than a bulk film.

CHAPTER 3

THEORETICAL INVESTIGATION OF THE SIS' GEOMETRY

The following¹ is a study of the SIS' structure, a thin superconducting film (or series of thin films) on a bulk superconductor with a thin insulating film between them. Citing the enhancement of the first critical field B_{c1} in thin superconducting films, this structure was proposed as a method to protect alternative SRF materials from flux penetration [Gur06, Gur05]. In this chapter, this structure is compared to bulk films, to determine if it is a viable tool for increasing the maximum magnetic field that can be screened by an SRF cavity.

The study begins with a derivation of the Gibbs free energy for a vortex in a superconductor. The calculation is then applied to a bulk structure, an isolated thin film, and a SIS' structure, and an explanation is presented for why the enhancement seen in the isolated film does not directly transfer to the SIS' structure. Comparison plots are presented showing that the maximum screenable field can be enhanced slightly in the SIS' structure compared to a bulk, but only for a small range of film thicknesses and only if the film and the bulk are different materials. They also show that using a multilayer instead of a single thick layer is detrimental, as this decreases H_{sh} of the film. Finally, it is concluded that the SIS' structure does not appear to offer a significant advantage compared to bulk superconductors².

¹Collaborators for this research were G. Catelani, M. Liepe, J. P. Sethna, and M. K. Transtrum. Some of the analysis in this chapter appears in [PCL+13], and other parts are planned to be included in a future publication.

²Note that in this chapter we consider only ideal (defect-free) surfaces. A thorough analysis would be required to determine whether the SIS' structure would provide a benefit if defects were significant, or if it would be limited by mechanisms such as buildup of vortices in the film.

It should be noted that an analysis of H_{sh} of the SIS' structure was performed concurrently to and published earlier than this study by Kubo, Iwashita, and Saeki [KIS13]. However, it did not include consideration of H_{c1} , and incorrect material parameters resulted in a considerable overestimate of the H_{sh} that the SIS' structure could provide.

3.1 Background: Maximum Fields

It is helpful to begin the discussion of the SIS' structure by providing some historical context. A. Gurevich presented the idea of using the SIS' structure in SRF cavities around 2005 [Gur05], at a time when it was becoming clear that niobium cavities were approaching fundamentally limiting fields, and that new technologies were needed to continue to improve performance. To help motivate the idea that thin superconducting layers could be used to enhance the critical fields of a cavity, Gurevich highlighted the enhancement of the lower critical field in an isolated film with thickness $d \ll \lambda$ compared to that of a bulk superconductor in a parallel magnetic field [Gur06]:

$$\mu_0 H_{c1} = \frac{2\phi_0}{\pi d^2} \left(\ln \frac{d}{\xi} + \gamma \right) \quad (3.1)$$

where ϕ_0 is the flux quantum and $\gamma = -0.07$.

In early presentations of the idea, Gurevich used as an example a SIS' structure with several layers of Nb₃Sn shielding a 2 T external field. 2 T is an extremely high field, 10 times higher than the highest fields obtained in niobium SRF cavities, and well above the metastable H_{sh} of bulk Nb₃Sn. Accompanying calculations showed that this field was below the H_{c1} of an isolated Nb₃Sn thin film, but no calculations were shown of the H_{c1} or H_{sh} of the actual geometry. In

a recent paper, Gurevich clarifies that the H_{c1} of an isolated film cannot predict the maximum field that a SIS' can screen, and that this situation was presented only as an illustration of the potential of thin films [Gur13]. However, a coating that can screen a 2 T field is extremely attractive, and at the time considerable excitement was generated for the potential of SIS' structures to far outperform bulk superconductors. Several advanced programs were developed to fabricate the coatings (see, for example, [Pro13, AVM13, VFEP+13, THC+12]), usually citing the enhancement of H_{c1} in an isolated film as motivation.

The calculations presented in this chapter are intended to remove confusion related to the SIS' structure by applying to it the formalism developed many years ago for calculating the critical fields in superconductors.

3.2 Critical fields in the London limit

The critical fields in a superconductor are determined by the behavior of magnetic flux. They can be found by calculating the Gibbs free energy \mathcal{G} of a magnetic vortex as a function of position and external field. The calculations are performed in the London limit; that is, it is assumed that both film and bulk superconductors are strongly type II materials, with penetration depths much longer than coherence lengths. The calculation neglects non-linearity, and is therefore only an estimate of the critical fields, but as shown elsewhere, the London limit results are close to those generated by a full Ginzburg-Landau numerical calculation [PCL+].

The geometry of an example SIS' structure is shown in Figure 3.1. The film material's penetration depth is denoted by λ_f and the coherence length by ξ_f ;

the thickness d of the film is assumed to be large compared to ξ_f . The film is separated from a bulk superconductor with penetration depth λ_b by an insulating film of thickness δ . The superconducting film is screening the bulk from a parallel magnetic field with amplitude B_0 . The screened field between the film and the bulk has amplitude B_i . In this geometry, the x -axis is perpendicular to the film, pointing into it, with origin at the interface with the exterior. The z -axis is aligned with the magnetic field.

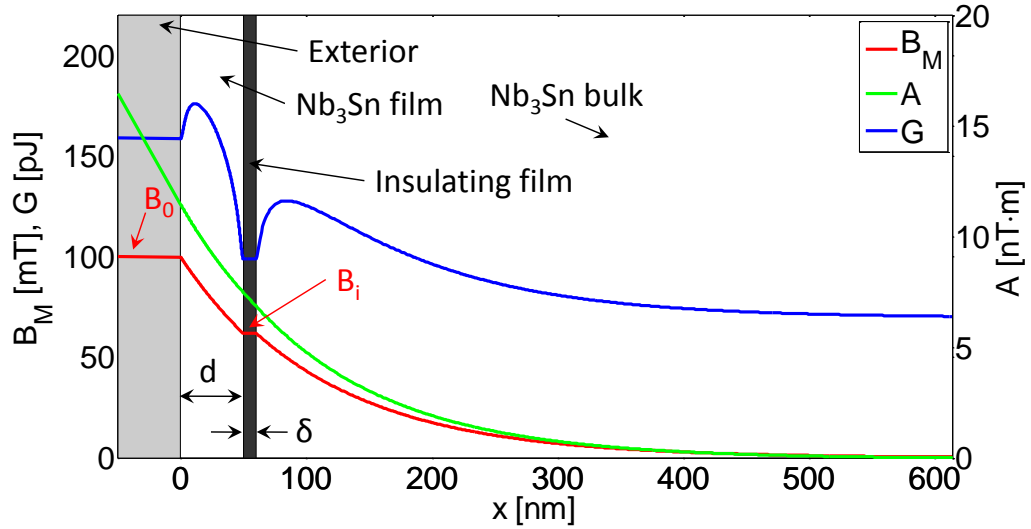


Figure 3.1: Example of a SIS' structure. The amplitudes of the magnetic field B_M , the corresponding vector potential A , and the Gibbs free energy are plotted as a function of distance into the structure.

The Gibbs free energy of a vortex in a superconductor can be determined from the value of two magnetic fields evaluated at the vortex location r_0 : the Meissner-screened external field B_M and the field generated by the vortex in the film B_V [SGKC94]:

$$\mathcal{G} = \frac{\phi_0}{\mu_0} (B_V(r_0)/2 + B_M(r_0)) , \quad (3.2)$$

where ϕ_0 is the flux quantum and μ_0 the magnetic constant. The field B_M can be

found by minimizing the free energy in the structure when no vortex is present.

This procedure gives:

$$B_M = \frac{B_0 + B_i}{2} \frac{\cosh \frac{x-d/2}{\lambda_f}}{\cosh \frac{d}{2\lambda_f}} - \frac{B_0 - B_i}{2} \frac{\sinh \frac{x-d/2}{\lambda_f}}{\sinh \frac{d}{2\lambda_f}}, \quad (3.3)$$

where B_i is given by

$$B_i = B_0 \left[\frac{\delta + \lambda_b}{\lambda_f} \sinh \frac{d}{\lambda_f} + \cosh \frac{d}{\lambda_f} \right]^{-1}. \quad (3.4)$$

Explicit formulas for B_V are available for thin ($d \ll \lambda_f$) and thick ($d \gg \lambda_f$) films. [SGKC94] To study the full range of thicknesses, the more general expression of [Shm72] is used (this expression assumes $r_0 = (x_0, 0)$):

$$B_V = \frac{2\phi_0}{\lambda^2 d} \sum_{n=1}^{\infty} \int_{-\infty}^{\infty} \frac{dk}{2\pi} e^{iky} \frac{\sin(\pi n x/d) \sin(\pi n x_0/d)}{k^2 + (\pi n/d)^2 + 1/\lambda^2} \quad (3.5)$$

Equation 3.3-Equation 3.5 give the fields in the structure, and Equation 3.2 gives the Gibbs free energy as shown in Figure 3.1. The barrier to flux penetration is due to the positive slope of \mathcal{G} inside the superconducting regions near the interfaces. To check this procedure, a film with $d \gg \lambda$ is studied, such that the film behaves as a bulk superconductor. This calculation is shown in the top plot of Figure 3.2. When the external field reaches the first critical field H_{c1} of the structure, the free energy outside the superconductor is equal to that when a vortex is deep in the bulk. Just above this field, it is energetically favorable for a vortex to be inside the superconductor, but an energy barrier prevents it from penetrating. When the external field reaches the superheating field H_{sh} , the barrier to flux penetration is reduced to zero and the vortex can enter. This plot is very similar to the one from Bean and Livingston's 1963 paper [BL64].

The calculation is performed for a single thin film (not in a SIS' structure) by setting $B_i = 0$ in Equation 3.3. This calculation is shown in the bottom plot of

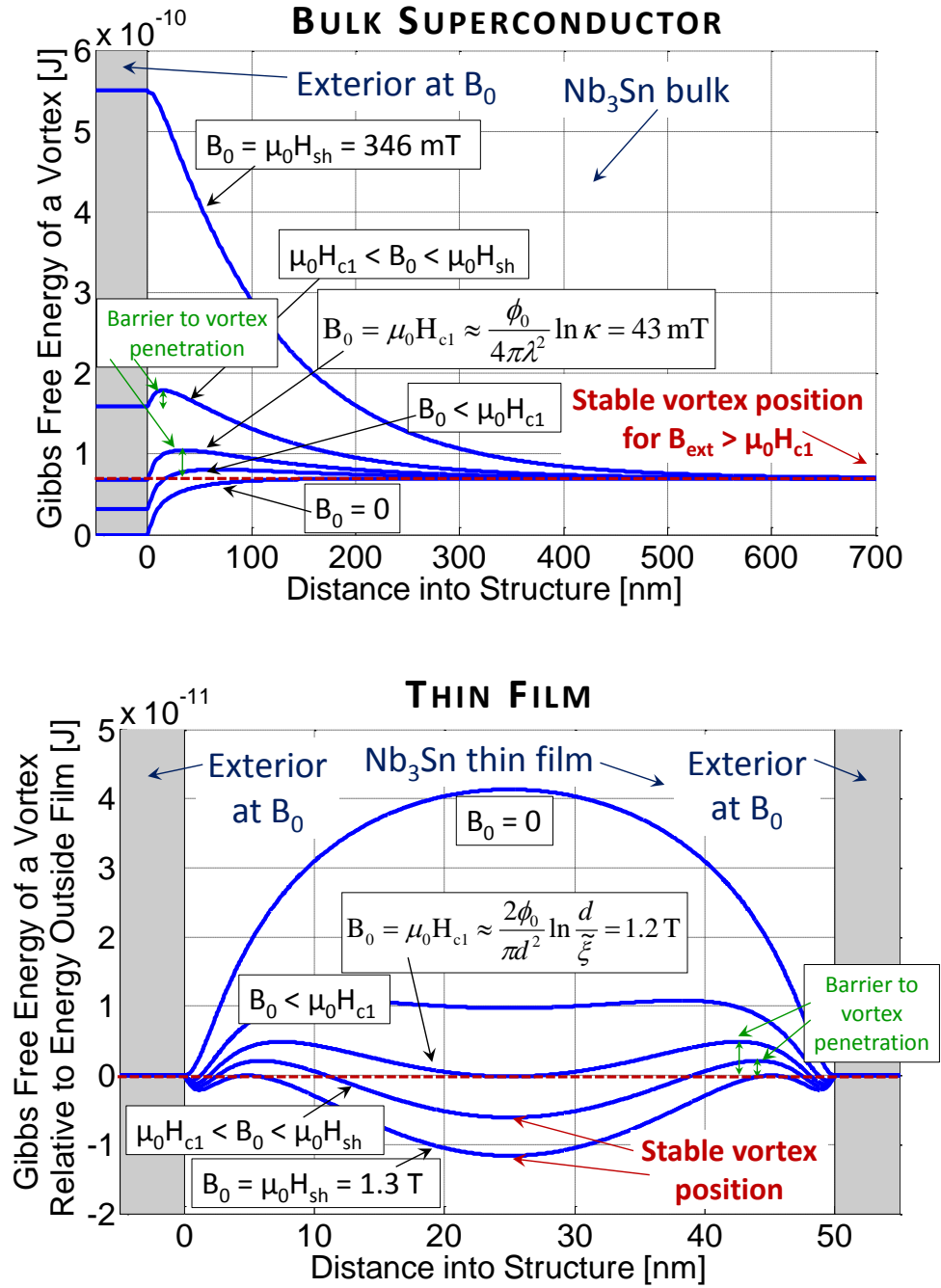


Figure 3.2: Gibbs free energy at various fields for a single vortex in (top) bulk Nb₃Sn, and (bottom) a 50 nm Nb₃Sn thin film. H_{c1} is the smallest field at which there is a position inside the structure where the free energy for a vortex is smaller than the value outside. H_{sh} is the field at which the energy barrier to vortex penetration disappears. These plots show the H_{c1} enhancement for a thin film compared to a bulk.

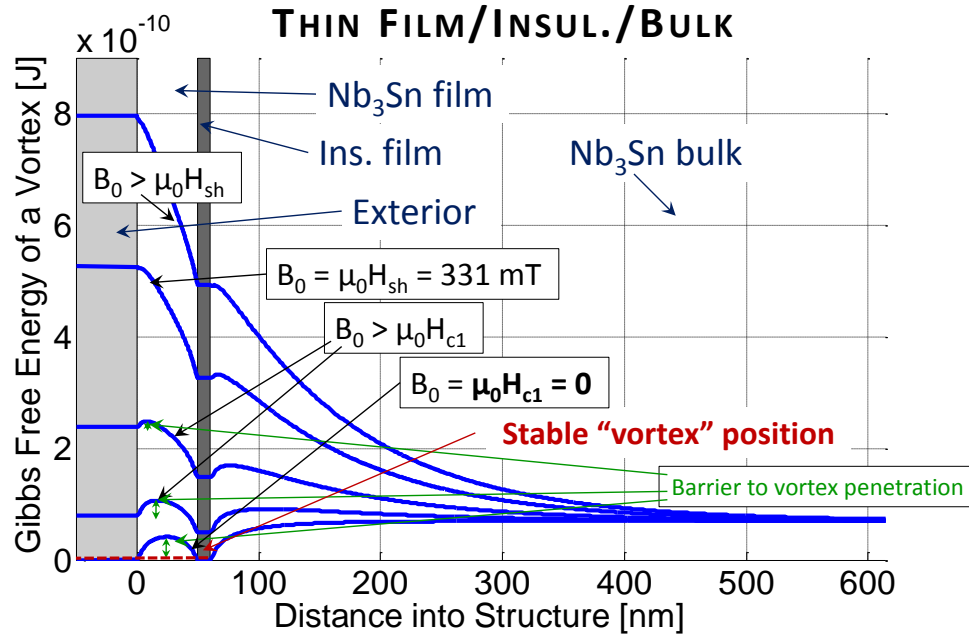


Figure 3.3: Gibbs free energy at various fields for a SIS' structure with a 50 nm Nb_3Sn film on a Nb_3Sn bulk. The plot shows that for a SIS' structure $H_{c1} = 0$ because at any field there is a stable position for flux inside the structure, on the side of the film adjacent to the insulating layer. Equation 3.1 for the thin film H_{c1} is not valid for the SIS' structure because it assumes that the first stable vortex position will be at the center of the film.

Figure 3.2 (the free energy outside the film is subtracted from each of the plots for clarity). In this case, there is no bulk, so the first location at which the free energy drops below the external value at high fields is in the center of the film. This would be the stable position for a single vortex above H_{c1} . Both H_{c1} and H_{sh} are much higher for the film than the bulk.

Finally, the free energy of vortex in a single layer SIS' structure is plotted in Figure 3.3. In contrast to the previous case, only one side of the thin film is exposed to the external magnetic field. The field at the other side is smaller due to screening by film. Since $B_V = 0$ at the edges of the film, Equation 3.2 shows

that the free energy in the insulating layer is lower than the free energy outside. The film provides screening at any finite B_0 below the second critical field, so for $B_0 > 0$, the energetically favorable configuration is for flux to be trapped in the insulating layer. This implies that in practice for the SIS' structure, H_{c1} is zero.

Why is [Equation 3.1](#) describing the enhancement of H_{c1} in a lone thin film not applicable for the SIS' structure? This expression assumes that the first stable vortex position will occur in the center of the film. It predicts when the free energy at the center of the film will dip below the value of the free energy in the exterior. However, for the SIS' structure, the free energy at the insulator side of the film will dip below the exterior value at fields much smaller than this.

[Figure 3.3](#) shows that at moderate fields, when B_i is below $\mu_0 H_{c1}$ of the bulk superconductor, there is no stable position for a vortex in either the bulk or the film. In effect, both superconductors are below their individual H_{c1} , so it is not immediately obvious if H_{c1} of the overall structure is important. Let us consider the implications of it being energetically favorable for a vortex to pass through the film, and have its flux trapped in the insulating layer. Once the flux is trapped in this way, it is non-dissipative under RF fields (unlike a vortex, which has a normal conducting core). However, as the vortex penetrates through the film to the insulator, dissipation occurs due to drag [[BS65](#)] that is too strong to be tolerable for SRF applications. Therefore it is the H_{c1} of the SIS' structure that is important, not that of the individual superconductors. Above H_{c1} , the structure is in a metastable state: only the energy barrier of the film prevents quench-inducing vortex penetration.

3.3 Evaluation of Field Limits

To calculate the maximum field without flux penetration, B_{max} , the lowest field is found at which the barrier is reduced to zero in any of the superconductors. In Figure 3.4, B_{max} is plotted as a function of superconducting film thickness for various SIS' structures. Various insulator thicknesses are considered, including the thin layer limit, for illustrative purposes as it gives the highest fields. The materials analyzed are the promising alternative RF superconductors from Table 2.2.

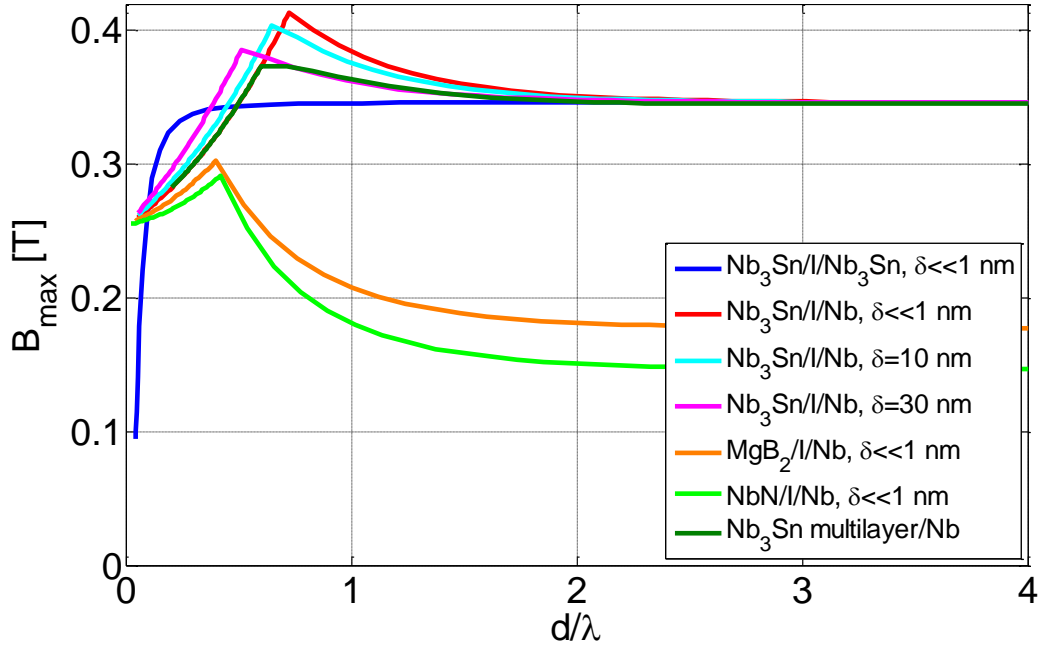


Figure 3.4: Maximum field below H_{sh} of both the film and the bulk as a function of film thickness for various film materials in a SIS' structure with Nb. The effect of varying the insulator thickness δ is shown for the Nb_3Sn film, as is the effect of splitting the film thickness d over 5 equally thick multilayers with thin separating insulators. All calculations done in the London limit.

The structures plotted in Figure 3.4 can be divided into two types: homolaminates, in which the film is the same material as the bulk, and heterolami-

nates, in which they are different. Calculations show that for a homolaminate like $\text{Nb}_3\text{Sn}/\text{insulator}/\text{Nb}_3\text{Sn}$, the film is the weak point: it always reaches its H_{sh} before the bulk, and the thinner the film, the lower its H_{sh} . Homolaminates with films that are so thick that they behave like a bulk superconductor have the highest B_{max} . To better understand this, consider the magnetic forces on a vortex, which can be derived from (Equation 3.2).

B_M is approximately exponential decay with a slight perturbation from the thin insulating film, as shown in Figure Figure 3.1. B_V is more difficult to conceptualize from the equations, but the effective force it creates is equivalent to a series of image antivortices [BL64], which attract the vortex, pulling it out of the film. There will be an image antivortex opposite the interface of the film with the exterior vacuum and another opposite the interface with the insulating film. These will be the leading order terms and have the strongest effect, each pulling in opposite directions. As the film thickness is reduced, the image on the insulator side of the film has a stronger effect, as shown in Figure 3.5. This lowers the barrier to penetration.

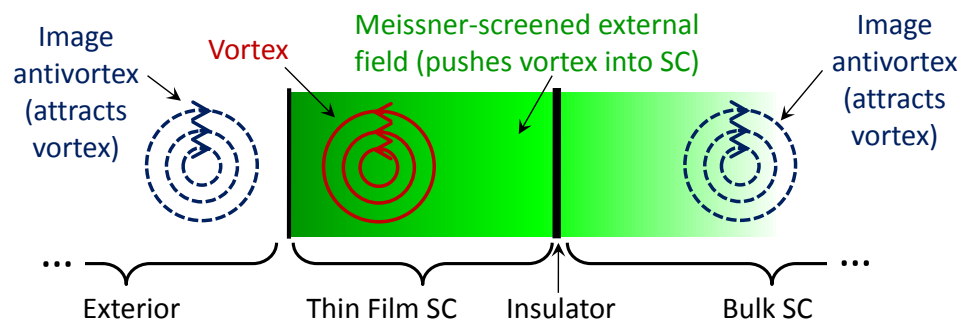


Figure 3.5: Forces on a vortex in a homolaminate. As the film is made thinner, the image antivortex to the right of the film has a stronger pull on the vortex, lowering the barrier to vortex penetration.

The differing penetration depths in the layers of a heterolaminate cause it

to behave differently than a homolaminate. Here only structures in which the bulk has a smaller penetration depth than the film are considered. For such structures, if the film is very thin, it does not provide much screening for the bulk, and B_i reaches the bulk's superheating field before the thin film barrier disappears. As with a homolaminate, a very thick film behaves like a bulk, and reaches that material's bulk H_{sh} while B_i is still relatively small. However, between these two extremes, there is a situation in which the film provides some screening, so that B_i is large but still smaller than B_0 . In this case, a benefit can be realized – the small penetration depth of the material in the bulk causes B_i to be larger than it would be in that location with the exponential decay expected for a thick film (Equation 3.4). This in turn reduces the magnitude of the negative gradient in B_M , bolstering the barrier to flux penetration (Equation 3.2). This increase in the barrier is depicted in Figure 3.6. The dark curves show B_M , B_V , and \mathcal{G} for a Nb₃Sn thin film/insulator/Nb bulk SIS structure with 10 nm thick insulator and $d/\lambda = 0.64$ (the peak of the cyan curve in Figure 3.4). The light curves show calculations for a bulk Nb₃Sn film (for this case, the dark shaded region representing the insulator does not apply). In this example, $B_0 = 300$ mT. The Gibbs free energy of the SIS' structure is still sharply peaked, showing a relatively robust energy barrier, but that of the bulk film is almost flat, showing that flux penetration is likely to occur at slightly higher fields.

The impact of this is a modest increase in B_{max} for these structures compared to the bulk value of the film material. However, the range of film thicknesses over which the increase is appreciable (\gtrsim few %) is relatively small, and the gain decreases as the thickness of the insulating layer increases.

The gain in B_{max} cannot be multiplied by adding more films of the same

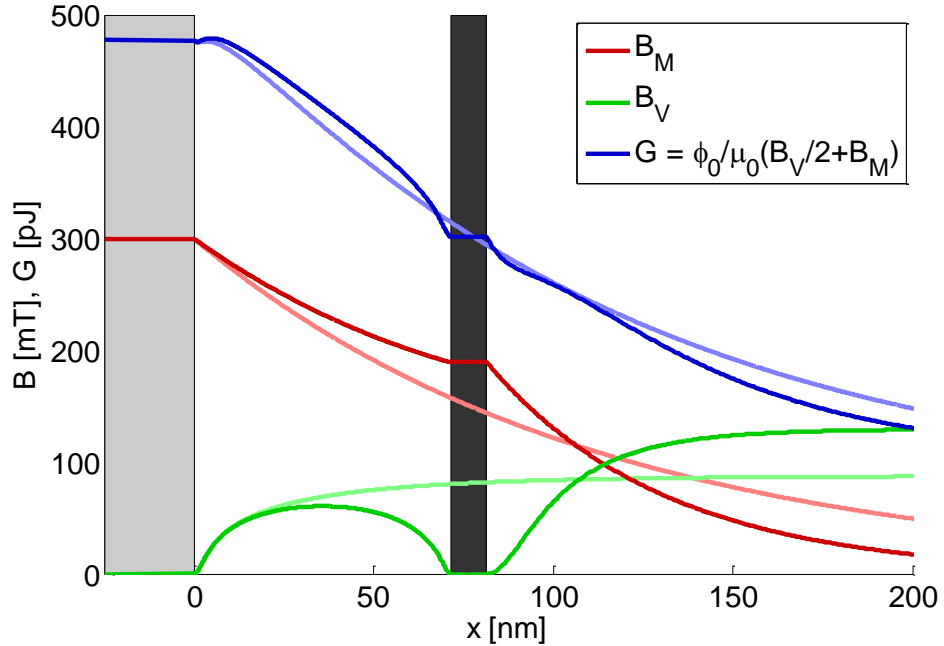


Figure 3.6: Comparison of a SIS' film with near-optimal parameters (dark curves) to a bulk film (light curves). The slower decay of B_M in the large- λ thin film influences \mathcal{G} , bolstering the barrier to flux penetration. Note that the dark shaded region representing the insulating region of the SIS' can be ignored for the bulk film.

material. As with the homolaminate, B_M will be unchanged by splitting up the superconducting film into separate layers with thin insulators between them, but B_V will have a stronger influence on the vortex, pulling it into the film.

3.4 Conclusions: Optimal Geometry for SRF Coatings

The analysis in this chapter has shown that contrary to suggestions that SIS' structures enhance H_{c1} , in fact they reduce it to zero. In addition, it was shown that the H_{sh} of an SIS' structure is only marginally larger than the bulk value and only for a small parameter space. Therefore, for a defect-free superconductor, the SIS' structure offers only minimal advantage compared to a bulk, but it is

much more difficult to fabricate with the right parameters over a complicated geometry with a large surface area.

A realistic superconductor can have defects which can make the metastable state vulnerable to flux penetration. For niobium, it appears possible to overcome defects, and reach³ fields very close to H_{sh} . For materials with smaller ξ , such as Nb₃Sn, defects may be more problematic, but it is too early in the development of the material to understand if this is the case. Preliminary indications suggest that the level of defects in a realistic cavity is tolerable: in [chapter 7](#), results will be shown of Nb₃Sn cavities reaching fields well above the onset of metastability with high quality factors. If defects were in fact problematic for this material, to the author's knowledge, there has been no study investigating the ability of the SIS' structure to ameliorate the problems associated with defects.

As a result of these considerations, one can conclude that currently, bulk ($d \gg \lambda$) superconductors are the most promising geometry for SRF cavities. The remainder of this thesis concentrates on bulk Nb₃Sn films.

³See, for example, experiments from N. Valles [[Val14](#)]. Based on the measured $\kappa = 3.49 \pm 0.16$, the cavity reached fields very close to the calculated H_{sh} and far above the calculated onset of metastability H_{c1} , approximately $0.4H_{sh}$

CHAPTER 4

NB₃SN BACKGROUND

This chapter presents the background of Nb₃Sn relevant to fabricating films for SRF cavities. It begins with general properties of the material and highlighting properties that are important specifically for SRF applications. For more in depth descriptions of the properties of Nb₃Sn and of superconductivity in the material, please see, for example, the works of Godeke [God06a, God05], Dew-Hughes [DH75] and Devantay et al. [DJD⁺81], which were drawn on in this discussion. Then various published methods are discussed for fabricating Nb₃Sn, and the choice to use the vapor deposition method is justified. Then a brief review is given of the development of the vapor diffusion process for SRF cavities at Siemens, University of Wuppertal, and other labs, with a focus on results that affected the direction of the research for this dissertation. Therefore, many important and well-designed Nb₃Sn SRF experiments are not included, such as: a five-cell cavity produced by University of Wuppertal [PHK⁺88]; a 500 MHz cavity produced by CERN [AMC86]; experiments at KfK using very high reaction temperatures that produced very large grains (85 microns after 1850°C reaction) [KKSH78]; and pulsed experiments at Cornell [HPS97] and SLAC [CF84], which will be discussed later with relation to new results. For very helpful reviews of Nb₃Sn SRF applications, please see, for example, Kneisel [Kne12], Sharma [Sha06], and Godeke [God06b].

4.1 General Properties of Nb₃Sn

Nb₃Sn is an alloy with composition ranging from approximately 18 to 25 atomic percent tin. It has an A15 crystal structure, shown in [Figure 4.1](#), in which chains

of niobium atoms pass through the faces of body center cubic (BCC) tin. It has a lattice parameter of approximately 0.529 nm, and as the unit cell in [Figure 4.1](#) shows, the spacing between niobium atoms is nominally half of this, approximately 0.265 nm. This is significantly closer than the nearest neighbor distance of approximately 0.286 nm in BCC niobium with lattice parameter 0.330 nm [[SZ70](#)]. The proximity of the niobium atoms is proposed as a reason for enhanced superconducting properties in Nb₃Sn compared to Nb [[God06a](#), [DH75](#)].

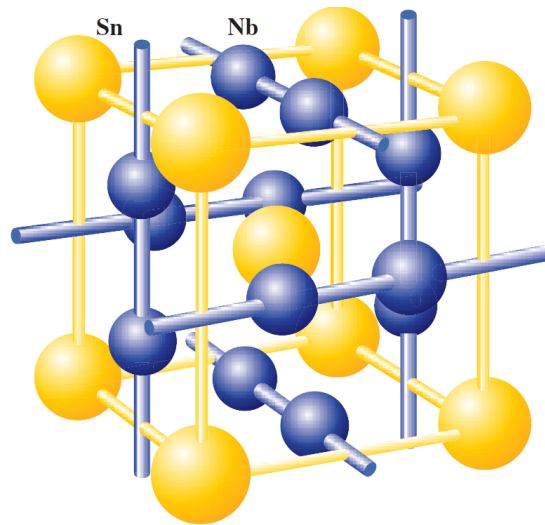


Figure 4.1: The A15 crystal structure of Nb₃Sn. Image from [[God06a](#)].

The phase diagram of the Nb-Sn binary system is shown in [Figure 4.2](#)¹. The critical temperatures of the different possible phases are given in [Table 4.1](#), showing that Nb₃Sn has the highest critical temperature by far. In order to obtain high quality surfaces for SRF applications, it is important to minimize the formation of undesired low- T_c phases. As a result, when fabricating Nb₃Sn by high temperature reaction of niobium and tin, it is important to choose a reaction temperature above 930°C. The phase diagram has the favorable feature that

¹The phase diagram presented here likely overestimates the span of the Nb₃Sn phase at lower temperatures, based on recent investigations [[TSGS02](#), [Oka03](#)], but it should convey the qualitative aspects of the system well.

Nb_3Sn is stable at this temperature, but the undesired phases Nb_6Sn_5 and NbSn_2 are not. Another favorable feature of the phase diagram is that if the tin concentration is below $\sim 25\%$ after high temperature formation of Nb_3Sn , it remains the only thermodynamically stable phase during cooldown to room temperature. It should be noted that only the binary system was considered here. If the application allows it, the addition of copper to form a ternary system can lower the reaction temperature required to avoid spurious tin-rich phases [God06b].

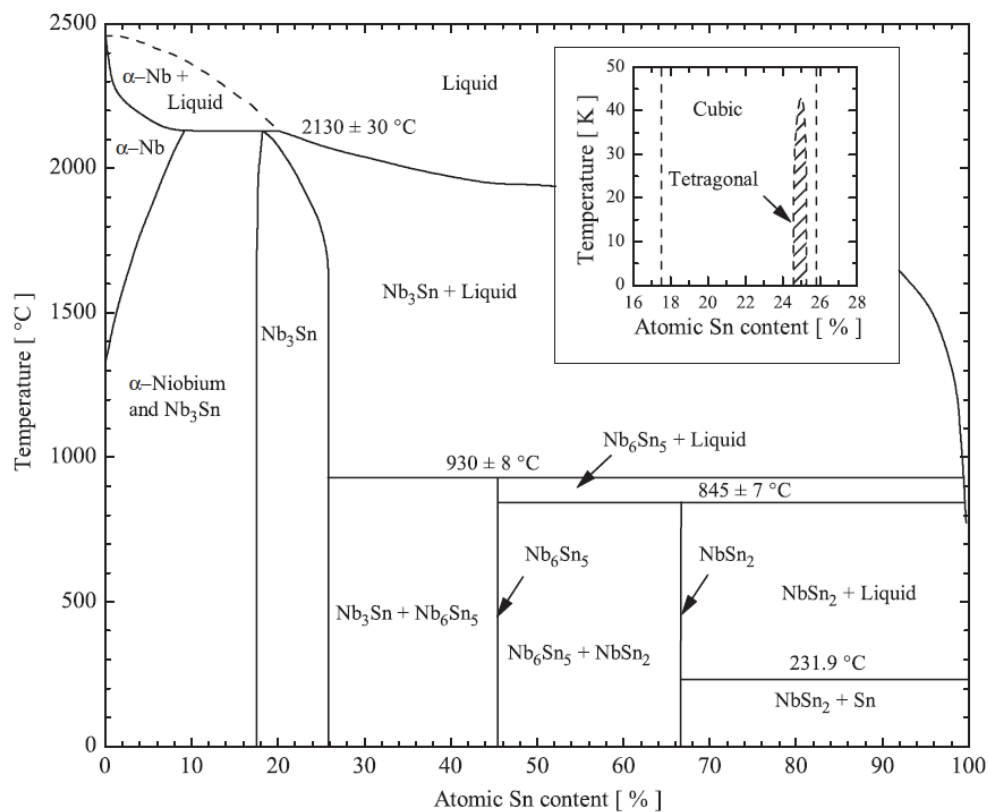


Figure 4.2: Phase diagram of the binary Nb-Sn systems. The A15 Nb_3Sn phase is favored between 18 and 25 atomic percent tin. Inset shows an observed change in crystal structure observed at low temperature and high tin content. Image adapted from [God06a], in turn adapted from [CMM70].

The inset of Figure 4.2 shows that at cryogenic temperatures, for tin contents close to 25 atomic percent tin, a shift of the crystal structure from cubic to

Table 4.1: Maximum critical temperatures of Nb-Sn phases. Data from [God06a, MGC63].

Phase	Maximum T_c
Nb	9.2 K
Nb ₃ Sn	18.3 K
Nb ₆ Sn ₅	2.8 K
NbSn ₂	2.7 K
Sn	3.7 K

tetragonal has been observed to occur, which has been correlated to increased strain and decreased superconducting qualities [God06a, God06b, DJD⁺81]. As a result, Godeke suggests that a composition below approximately 24.5 atomic percent tin may be preferred for SRF applications.

Nb₃Sn is a brittle material (for illustration, see cracks formed in material after bending in Figure 4.8), and as a result, shaping for applications is generally done before reaction. For manufacturing superconducting cables, brittleness prevents drawing after the alloy is formed, so generally niobium and tin are combined as wires or powders in their intended shape, then reacted in place at high temperatures [Sha87]. For manufacturing SRF cavities, deep drawing of sheets into shape is likely not an option—the niobium and tin should be reacted in the desired shape to avoid fracture.

The thermal conductivity k of Nb₃Sn is significantly smaller than that of niobium at a given temperature. Figure 4.3 shows example datasets for k of Nb [Sch95] with RRR~300 and of Nb₃Sn [Wan13], which show that at a given temperature, niobium has k approximately 2 orders of magnitude higher. Niobium cavities can sustain surface heat loads on the order of 400 W/m² (B_{pk} of 200 mT with R_s of 30 nΩ) at 2 K without thermal runaway, showing that the thermal impedance through the cavity wall can be made sufficiently small. If

the surface heat load would be similar for a Nb₃Sn cavity, to obtain a similar conductive thermal impedance, the Nb₃Sn layer would have to be significantly thinner than the niobium layer. As a result, Nb₃Sn SRF layers are generally deposited as films with thickness on the order of a few μm ($d \gg \lambda$), approximately 3 orders of magnitude smaller than bulk niobium cavity walls, which have thickness on the order of a few mm. Nb₃Sn cavities also have the option of operating at higher temperatures, where k is larger.

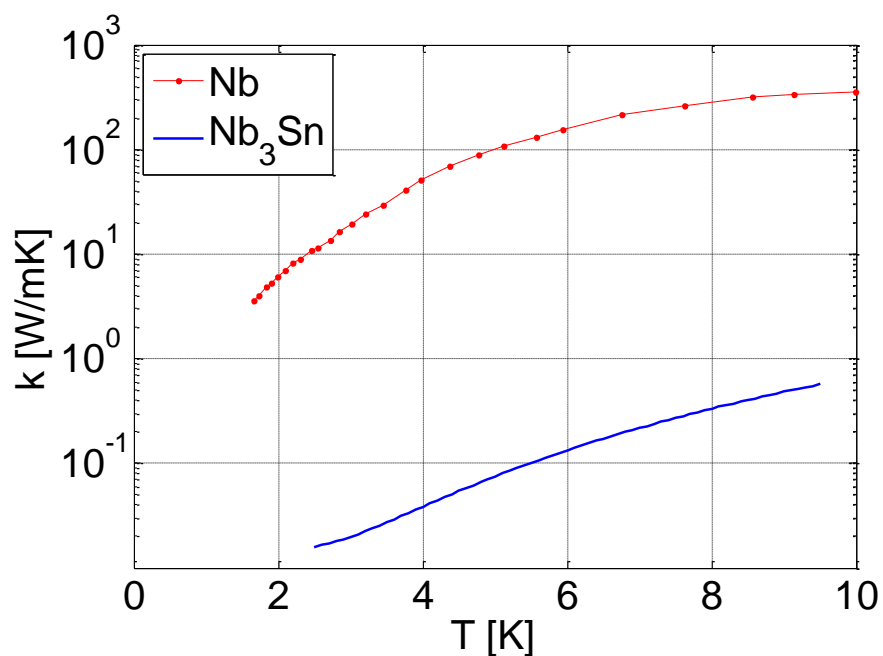


Figure 4.3: Typical thermal conductivity data for Nb with RRR~300 and Nb₃Sn at cryogenic temperatures. Data from [Sch95, Wan13].

4.2 Coating Method

A method had to be chosen for creating Nb₃Sn layers at Cornell, so a literature review was performed of fabrication methods. Many methods have been developed, but in many cases issues have been observed that would be problematic

for SRF applications, such as incorrect stoichiometry, a non-uniform surface, or poor adherence of the coating.

The fabrication of Nb_3Sn is well established in the area of very high field magnets. Sophisticated methods have been developed, such as the restacked rod and powder in tube processes [Sha87, AAA⁺07]. These processes are optimized for magnet applications, so they produce many pinning sites (e.g. voids) for flux, and often involve copper in the alloy. However these properties are undesirable for RF applications, so these methods would not be appropriate.

Various methods have been developed specifically for Nb_3Sn layers on SRF cavities, several of which are described briefly in the following. In general, these methods produce layers as thin films over a substrate rather than as a bulk structure due to the brittleness of the material and its poor thermal conductivity. The cavity substrate is usually niobium or sapphire, due to the high temperatures often involved in the coating process. In multilayer sputtering, niobium and tin are alternatively coated onto a substrate, and then annealing is performed [RDS]. Liquid tin dipping involves dipping a niobium cavity into a pool of tin in a furnace followed by annealing, but it can result in tin droplets on the surface and undesirable tin-rich phases [Dea08]. In mechanical plating, a niobium substrate is tumbled in a container with powdered tin and other media, after which it is annealed, but adhesion has been a difficulty [DK07]. Electron beam coevaporation uses two electron beams to vaporize niobium and tin targets; this process may be vulnerable to structural inhomogeneities [ABHT83]. A bronze process involves the use of copper in the reaction, though it is not yet clear if high quality factors can be achieved by this method [Hak88]. Chemical vapor deposition uses vaporized precursors of niobium and tin to chemically

coat a substrate [CRZC,Sti78]. So far, to the author's knowledge, only somewhat low CW accelerating gradients have been obtained from the above treatments, but relatively little development has been devoted to these methods.

There is one Nb_3Sn coating method that has in past experiments shown both high quality factors and relatively high surface magnetic fields, called vapor diffusion. In this method, developed by Saur and Wurm [SW62], a niobium substrate is heated in a furnace with tin, such that tin vapor coats the substrate and alloys with it, as sketched in Figure 4.4. The vapor diffusion method was chosen for the research presented in this thesis because of the promising results shown previously, which are the subject of the next section.

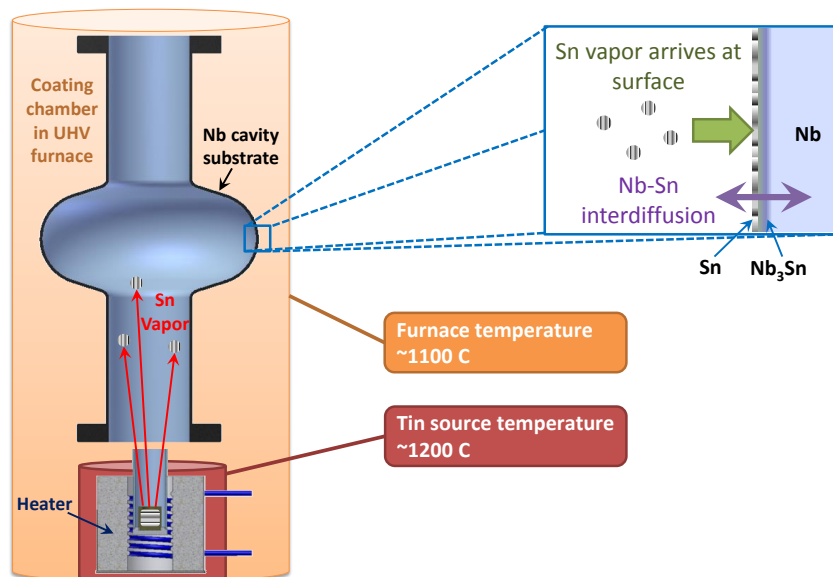


Figure 4.4: In the vapor diffusion coating method, tin vapor coats and alloys with a niobium substrate in a furnace to form Nb_3Sn .

4.3 Previous Results

Pioneering work into developing vapor diffusion of Nb₃Sn for SRF applications was performed in the 1970s to 1990s by Siemens AG [HMP⁺77], Kernforschungszentrum Karlsruhe (KfK) [KSH79], University of Wuppertal [AP77], Cornell University [Sti78], Jefferson Lab [MKM96], CERN [AMC86], and SLAC [CF84].

Siemens researchers developed a Nb₃Sn coating process with 10 GHz TM and TE cavities. They would place a niobium reaction chamber in a UHV furnace with a tin source. They would react at ~1050°C for approximately 3-4 hours to produce a coating 1-2 micron thick. Sometimes the reaction produced uncoated regions, but researchers found that this could be avoided by nucleating the surface with tin sites. In early experiments, nucleation was accomplished by anodizing the surface to create a thick oxide layer on the niobium, then using a temperature gradient in the furnace to bring the tin source to high temperature before the cavity [Hil80]. It is thought that this would create a significant vapor pressure of tin in the cavity so that tin sites would be deposited on the oxide, nucleating uniform coverage of tin as the oxide dissolved at high temperatures [Kne12]. Later, nucleation was accomplished using tin compounds SnCl₂ or SnF₂ with high vapor pressure at relatively low temperature, as shown in Figure 4.5 [Kne12, Gmea, Gmeb, LB]. This would avoid the temperature gradient, as well as the potential RRR degradation resulting from dissolving a thick oxide into the cavity bulk. After nucleation, growth is accomplished by diffusion of atoms through the Nb₃Sn layer. It is generally assumed in the literature that the primary method of diffusion in this case is migration of tin atoms through the grain boundaries to the Nb bulk below, growing the film at the

interface [Kne12,Hil80,Far74]. However, the process is not well understood.

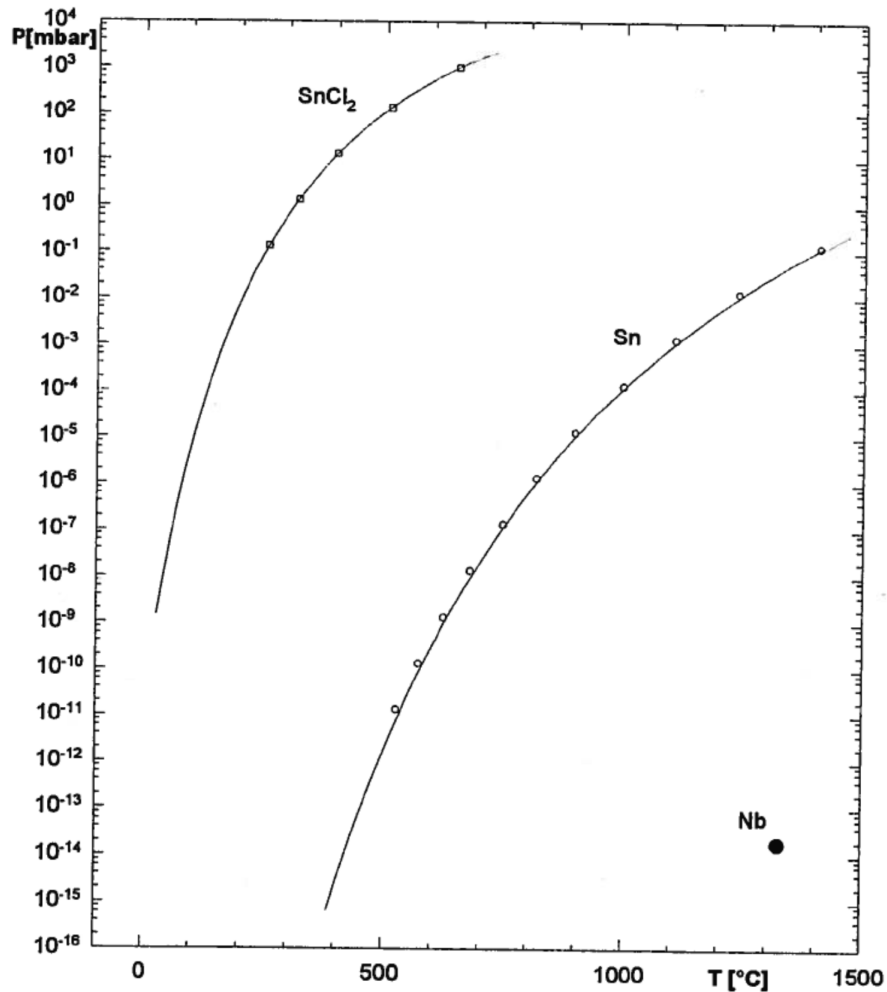


Figure 4.5: Vapor pressure of Sn and SnCl_2 . The SnCl_2 vapor pressure is relatively high at temperatures $\sim 500^\circ\text{C}$, allowing it to be used as a nucleation agent. Figure from [Kne12], who cites [Gmea, Gmeb, LB].

Siemens experiments demonstrated the high gradient potential of Nb_3Sn coatings, achieving very high surface magnetic fields—even at 4.2 K—in 10 GHz cavities. Results of several different high performing cavities given somewhat different preparations are summarized in Figure 4.6 (for ease of comparison, the R_s shown is the weighted average given by G/Q_0).

Researchers at the University of Wuppertal obtained very small R_s values

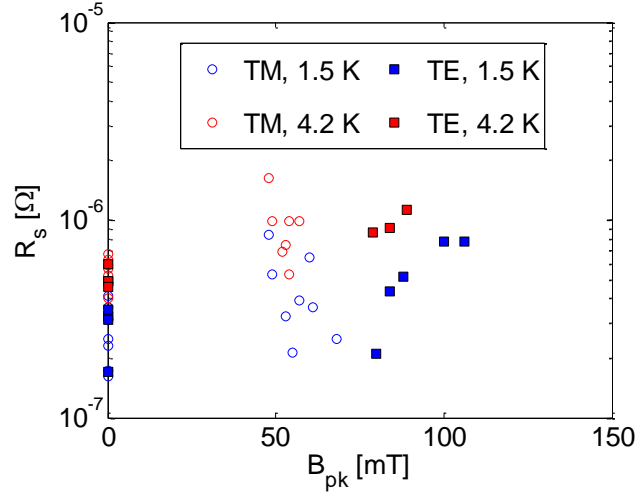


Figure 4.6: 1.5 K and 4.2 K data for some of the best Nb₃Sn TM and TE 10 GHz cavities produced by Siemens AG [Hil80] [HKP⁺81]. Only the Q_0 at zero field and at the maximum field were reported.

in Nb₃Sn cavities with shapes and frequencies appropriate for particle accelerators. The graph of quality factor Q_0 vs accelerating gradient E_{acc} of two of the best cavities produced by University of Wuppertal is shown in Figure 4.7 [MPP⁺00]. They are 1.5 GHz single-cell cavities of the CEBAF shape tested at Jefferson Lab. At 4.2 K, at small accelerating gradients, the cavities had Q_0 on the order of 10^{10} , more than an order of magnitude higher than would be achieved in an uncoated Nb cavity. For small E_{acc} at 2.0 K, one of the cavities achieved Q_0 of 10^{11} , again far higher than would be possible with Nb (though it should be noted that Wuppertal reports higher R_{res} for most of their cavities [MKM96]). However, these high Q_0 values did not continue as the field was increased. The cavities showed strong Q -slope (increasing R_s with B_{pk}), such that at fields that were useful for applications, Q_0 was prohibitively low. Neither field emission nor quench was observed in these measurements; the limitation was available RF power.

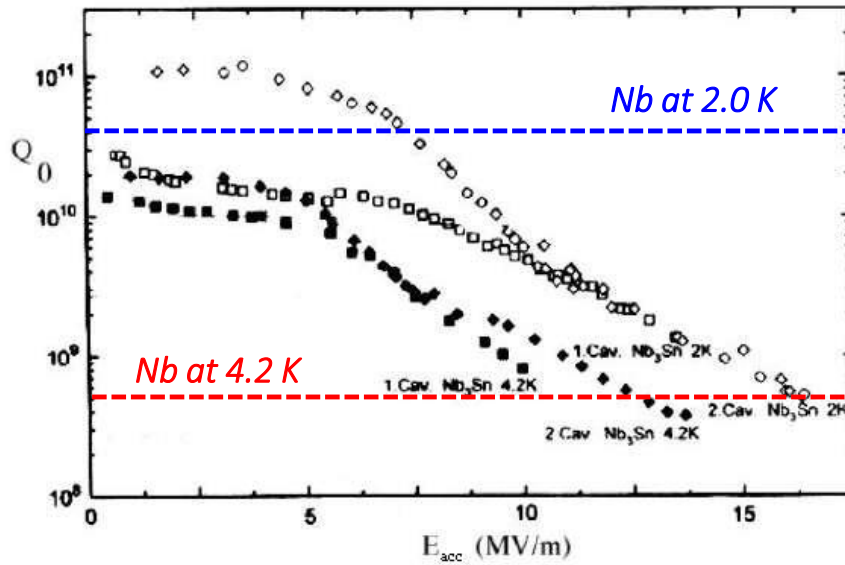


Figure 4.7: Performance curves at 2 K and 4.2 K for two of the best Nb₃Sn cavities produced by U. Wuppertal [MPP⁺00]. The approximate values that could be expected for an equivalent Nb cavity are shown for comparison.

In a later study, Wuppertal and JLab researchers tested three Nb₃Sn cavities, each of which exhibited strong Q -slope above an onset field, similar to what is shown in Figure 4.7. They used temperature mapping to study the distribution of heating over the surfaces. Though somewhat limited by saturation effects, they observed increased heating over broad regions after the onset of Q -slope consistent with the increased losses. They also observed a trend: a similar onset field for the strong Q -slope and increased heating in their cavities. Moreover, this onset field fell within the expected range for the lower critical field H_{c1} of Nb₃Sn. This led to speculation that the Q -slope was caused by a fundamental loss mechanism that occurred above H_{c1} , such as bulk vortex dissipation [BKM⁺97, Gur06]. If strong losses above H_{c1} were unavoidable, then not just Nb₃Sn, but bulk alternative SRF materials in general—which tend to have relatively small H_{c1} values—would be severely limited.

Another explanation for the cause of the Q-slope was that grain boundaries were acting as “weak links,” regions with high R_s . Even if R_s was small in the Nb₃Sn crystal grains, if lossy material were present in the grain boundary region, it could lower the overall Q_0 compared to what would be expected for high quality Nb₃Sn. Two reasons to suspect that this might be the case are that 1) a similar Q-slope has been observed in copper cavities sputtered with niobium, which is often attributed to intergrain losses [DWBM95, BS91, PKH08] (though other causes are also postulated [BCC⁺99, BCD⁺01]), and 2) R_{res} has been observed to follow an f^2 dependence, which is predicted in models of weak link grain boundaries [PHK⁺88, PKH08].

4.4 Weak Link Grain Boundaries

Researchers at the University of Wuppertal continued their investigations of Nb₃Sn, measuring films prepared on 1” diameter samples rather than full cavities. By varying the size of the Nb₃Sn grains, they could perform a systematic study of its effect on maximum sustainable RF field by testing their films in a 19 GHz resonator. They interpreted their results as showing a competition between two effects. At grain sizes above ~1.5 μm, they found that the field limitation could be explained by local thermal overheating². At smaller grain sizes, their analysis implicated weak link behavior as the cause for strong Q-slope, in which grain boundary regions would be driven normal conducting above a critical current density J_c . The dependence of the onset field on grain size was interpreted as being caused by an increase in J_c with increasing grain

²At 19 GHz, the Nb₃Sn is vulnerable to overheating due to the f^2 dependence of R_{BCS} . Overheating is not expected to be a problem at these fields for cavities at ~1 GHz.

size [PCH⁺99]. Another explanation is that with larger grains, there are fewer grain boundaries, which would be advantageous if they are lossy.

In their study, Wuppertal researchers controlled grain size by adjusting the thickness of the Nb₃Sn film³, but it should also be possible to grow larger grains via high temperature annealing of the Nb₃Sn film. If a method could be found to increase the grain size by annealing without negatively affecting the stoichiometry, it may be possible to increase the onset field of Q -slope in full cavities.

An annealing step after removing the tin source was investigated by researchers at Siemens. At these temperatures, atomic transport for the growth of the Nb₃Sn layer is assumed to be largely accomplished by diffusion of tin through the grain boundaries [Hil80, Far74], which can lead to compounds between grains with undesirable stoichiometry. With the addition of the annealing step, Siemens researchers hoped to prevent the formation of off-stoichiometric compounds that can act as weak links between grains. They observed a “cleaning” and strengthening of the grain boundaries—they found that when subjected to mechanical stress, cracking in the layer shifted from intergranular to intragranular, as shown in Figure 4.8—but found that there was no improvement in the microwave performance [Hil80]. However, unlike the Wuppertal cavities, the Siemens cavities were not afflicted with strong Q -slope even before adding the annealing step. One possible explanation is that unlike the Wuppertal cavities, which were coated with the tin source heated to ~1200°C and the cavity at ~1100°C, the Siemens cavities were coated with the tin source and the cavity both at ~1050°C [Hil80]. If the Siemens procedure resulted in grain

³For these experiments, Wuppertal researchers sputtered niobium onto sapphire samples, then converted the Nb film to Nb₃Sn via the vapor diffusion process. They found that the grain size was correlated to the original Nb film thickness, so they would use sputtering time to control the Nb₃Sn grain size.

boundaries that were satisfactorily clean immediately after coating not to produce weak links, then an additional anneal may not have improved the coating.

Wuppertal researchers also attempted an extra annealing step in at least one study. In hopes of increasing the size of the Nb₃Sn grains, they annealed at 1250°C for 24 hours. These preliminary studies produced an average grain size of 5 μm, but they also caused enhanced diffusion of tin into grain boundaries [MKM96].

The Nb₃Sn program at University of Wuppertal ended in the early 2000s, at a time when there was still significant room for improvement in Nb cavities, which were much easier to fabricate than Nb₃Sn cavities. However, Nb cavities are now approaching the fundamental limits of the material, and the demands of future particle accelerators continue to increase. In order to meet the needs of these future accelerators, it may be very rewarding to make progress now in the significant R&D work necessary to understanding—and if possible ameliorating—the mechanisms that have limited Q_0 and E_{acc} of Nb₃Sn cavities in the past.

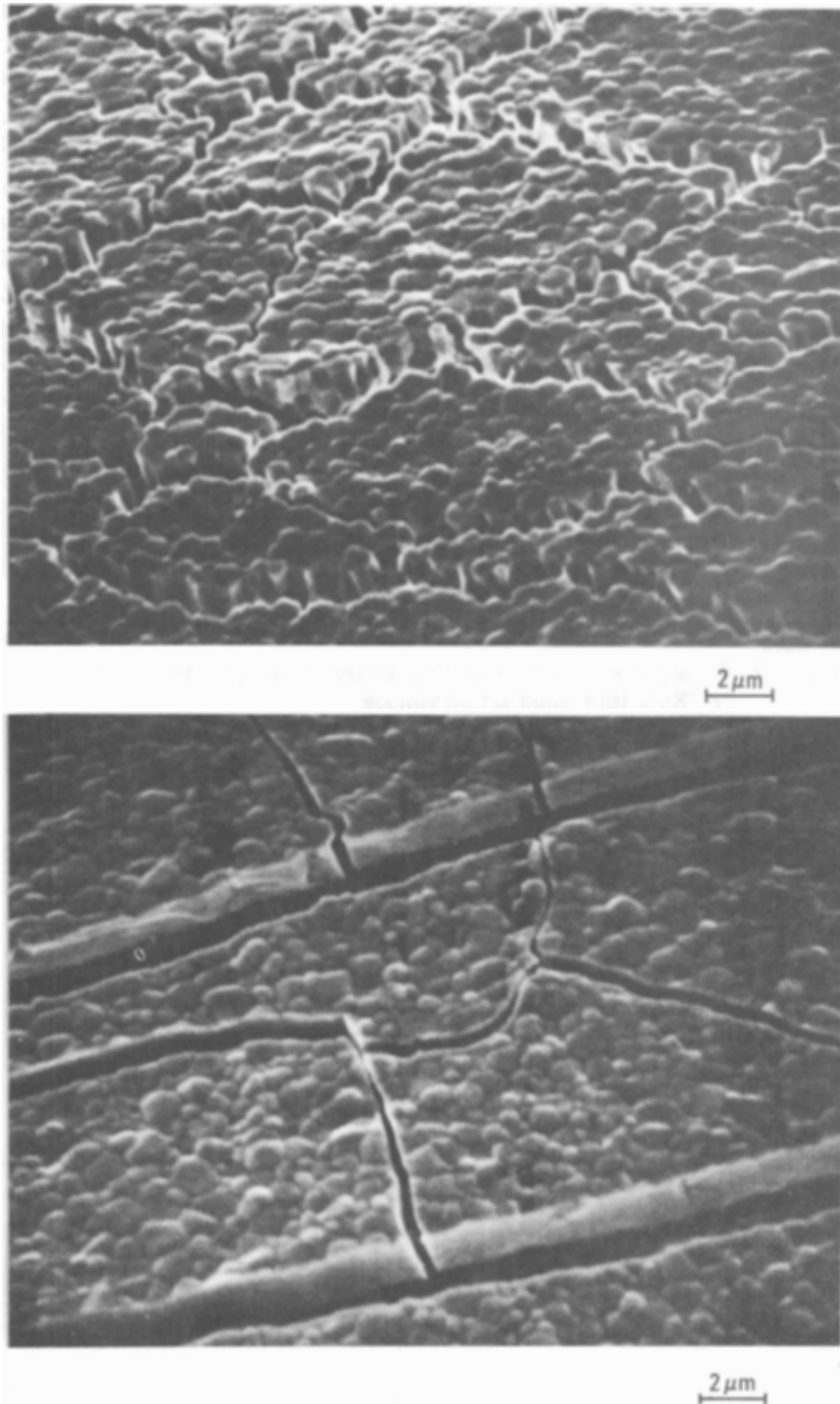


Figure 4.8: Siemens observed that increasing annealing time can strengthen grain boundaries. When a sample is mechanically bent, with short annealing times, the cracks that form are intergranular (top), but with long annealing time, they are intragranular (bottom). Images from [Hil80]

CHAPTER 5

CORNELL Nb_3Sn COATING APPARATUS

This chapter is devoted to the coating process: the coating chamber, the coating procedure, and initial evaluation of the coatings on small samples. Careful design of the coating process is extremely important, as it ultimately determines the properties of the deposited layer. The chapter starts with a description of how constraints on the facilities at Cornell affected the coating chamber design. Then the features of the constructed coating chamber and special precautions taken to minimize the risk of contamination are described. Then the steps of the coating procedure are outlined in detail. The last section describes the initial evaluation of the films on samples.

5.1 Design

Due to the success shown by previous researchers who used the vapor deposition technique, when the research program for this thesis started, we sought a method to develop a facility at Cornell that would coat cavities with Nb_3Sn using this method. We put together a scheme in which a coating chamber would be inserted into an existing ultra-high vacuum (UHV) furnace in the Cornell clean room, and it would share the furnace's vacuum pumps. The constraints on the coating chamber were as follows:

1. The chamber must fit in the UHV furnace, and interface with it via a 22.125" wire seal flange.
2. Below the stainless steel flange, the coating chamber must transition to a material that can withstand temperatures up to 1200°C or higher.

3. The UHV furnace and its pumps must not be contaminated with tin.
4. There is only one heated zone in the furnace, so having the tin source in a separate hot zone below the cavity is not an option (this had been done in previous furnaces [AM84]).

Because of constraints 1 and 2, the coating chamber was designed as being all niobium in the hot zone of the furnace, with a copper transition from niobium to stainless in the low temperature region, as can be seen in [Figure 5.1](#). Because of constraint 3, a valve was added between the chamber and the pumps so that it could be isolated during coating, when the tin was mobile. Constraint 4 led the addition of a small in-vacuum resistive heater, that would raise the temperature of the tin source to a higher temperature than the furnace. Power is supplied to the heater via molybdenum rods that extend through the heat shields.

Temperatures are measured by C-type thermocouples, shown in [Figure 5.2](#), two on the outside of the coating chamber to measure the cavity temperature, and two in the auxiliary heater to measure the tin source temperature. To understand the relationship between the temperature read by the thermocouples and the temperature in the coating chamber, a calibration run was performed without any tin or cavity, but with K-type thermocouples inside the coating chamber. The calibration was done as high as the maximum temperature of the K-type thermocouples, approximately 1100°C. It showed that for the cavity to be at 1100°C, the thermocouples outside the coating chamber should read just over 1150°C, and for the tin source to be at approximately 1200°C, the thermocouples in the tin source heater should read approximately 1300°C.

A number of special precautions were taken to ensure that the coating chamber would produce contamination-free Nb₃Sn films. These precautions are out-

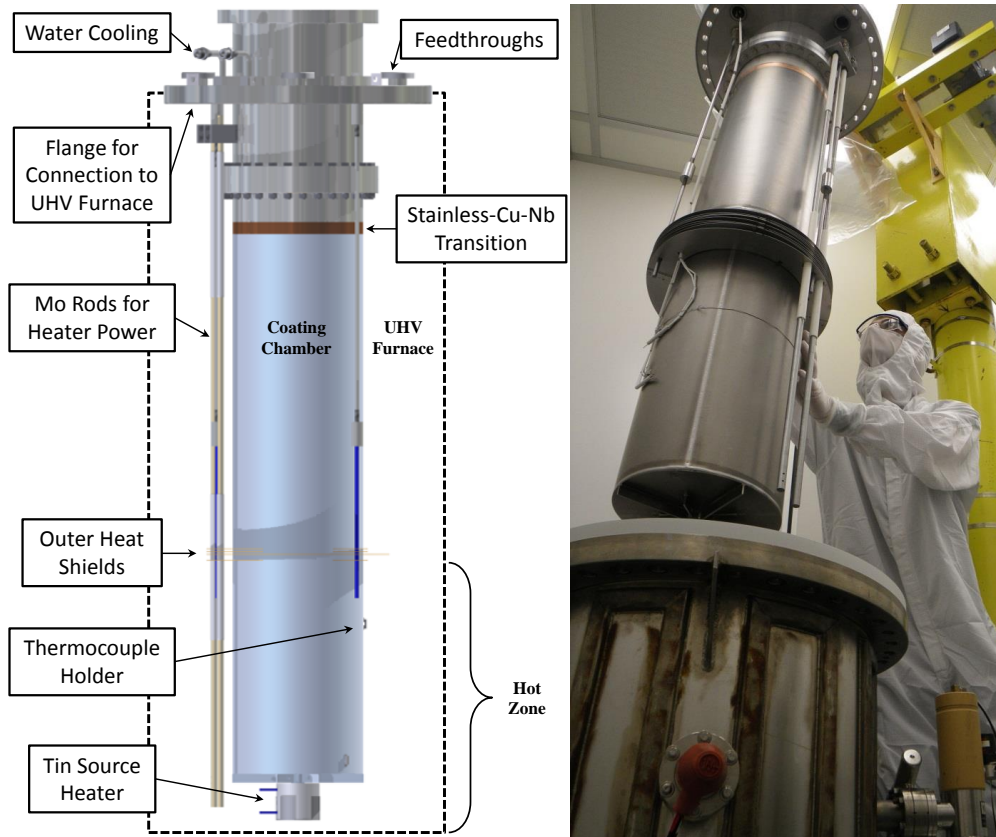


Figure 5.1: Cornell Nb₃Sn coating chamber. Left: computer model of coating chamber with UHV furnace dotted outline shown. Right: coating chamber after fabrication, being lowered into the UHV furnace.



Figure 5.2: Thermocouples measuring the cavity temperature (left) and the tin source temperature (right).

lined below:

- Niobium was chosen as the material for the coating chamber itself, rather than another material which could contaminate the Nb₃Sn layer.
- The cavities that were coated were fully niobium, including the flanges, which use indium gasket seals, rather than using NbTi flanges for aluminum gasket seals. NbTi flanges could have caused contamination from titanium, as has been observed previously [GR13].
- The tin crucible, the SnCl₂ holder, and any other non-niobium parts in the hot zone of the coating chamber were made of tungsten, which has a very low vapor pressure at these temperatures, so it should not cause contamination.
- Before coating, cavities were given BCP inside and out to remove any possible source of contamination, as shown in Figure 5.3. If an EP surface was desired, the cavity was given BCP inside and out then given EP inside afterwards.
- The coating chamber is quite tall, and it would be helpful to be able to use a crane to lower cavities into it. However, there was concern that operating a crane above the chamber could cause contamination from its moving parts. Instead, a system involving niobium wires and hooks was developed to lift by hand the cavity and other parts into and out of the chamber.
- The heater for the tin source was located outside of the coating chamber to avoid potential contamination. The only materials regularly placed inside the hot zone of the coating chamber are niobium, tin, SnCl₂, and tungsten.

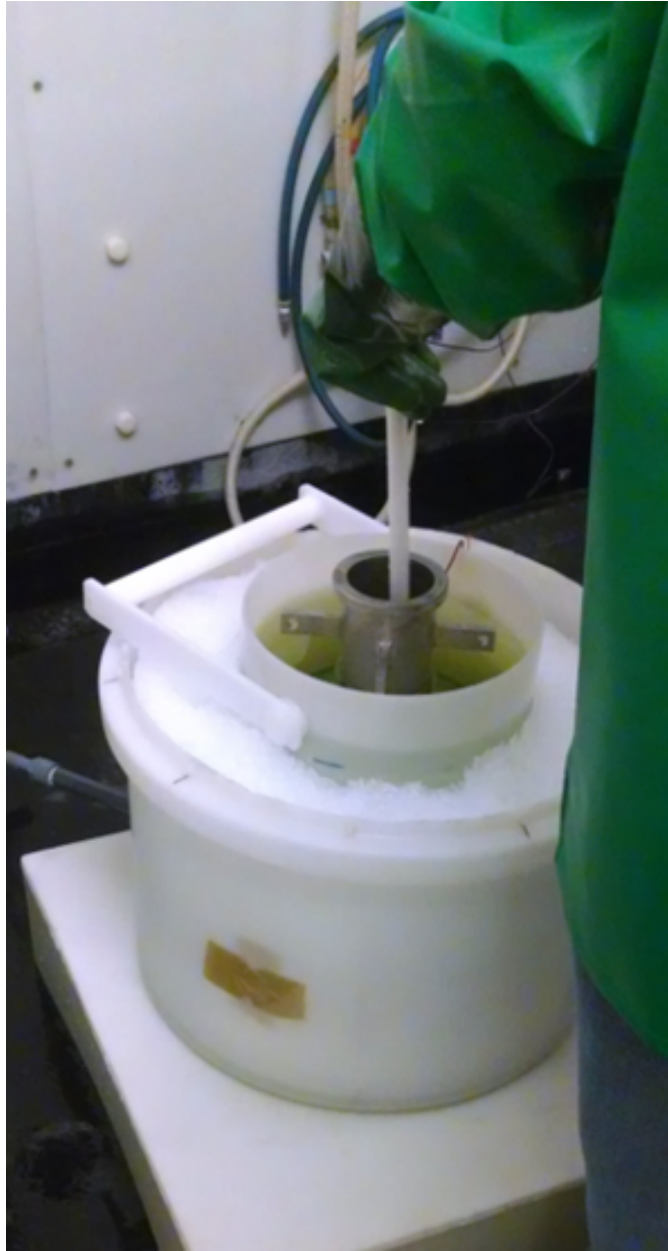


Figure 5.3: BCP of inside and outside of cavity to remove any contamination before Nb_3Sn coating.

In addition to the cavity, several other parts have to be lowered into the coating chamber before a coating, as shown in [Figure 5.4](#). A tungsten crucible containing pellets of 99.999% pure tin is lowered into a small niobium tube that extended below the main bottom plate of the chamber into the auxiliary heater. Another tungsten container for the SnCl_2 nucleation agent is lowered into a spot inside the diameter of the cavity beamtube, next to two niobium witness samples. The witness samples are necessary for performing Nb_3Sn surface analyses without cutting apart the cavity. The niobium for the witness samples is carefully chosen to be from the same batch as the cavities for accurate comparison. The cavity itself is lowered onto three tungsten feet to prevent it from seizing to the niobium bottom plate at high temperatures. After the cavity is lowered in, the inner niobium heat shields are lowered into place.

5.2 Coating Procedure

The coating recipe used at Cornell was based on the temperatures and times specified by University of Wuppertal in [\[MKM96\]](#), with some modifications. The process is shown in the plot in [Figure 5.5](#). It starts with a degassing step at 200°C to prevent RRR degradation of the niobium bulk from absorption of gases, in order to preserve its thermal conductivity. Degassing takes approximately 24 hours, after which the valves to the pumps are closed to prevent their being contaminated with tin. This is different than the Wuppertal procedure, in which a plate is lowered onto the cavity after initial degassing to contain the tin, and the pumps continue to run on the coating chamber. The Cornell simplification affects the containment of the tin vapor, but it eliminates the need for a rotary motion feedthrough and the need holes in the heat shields to accommo-

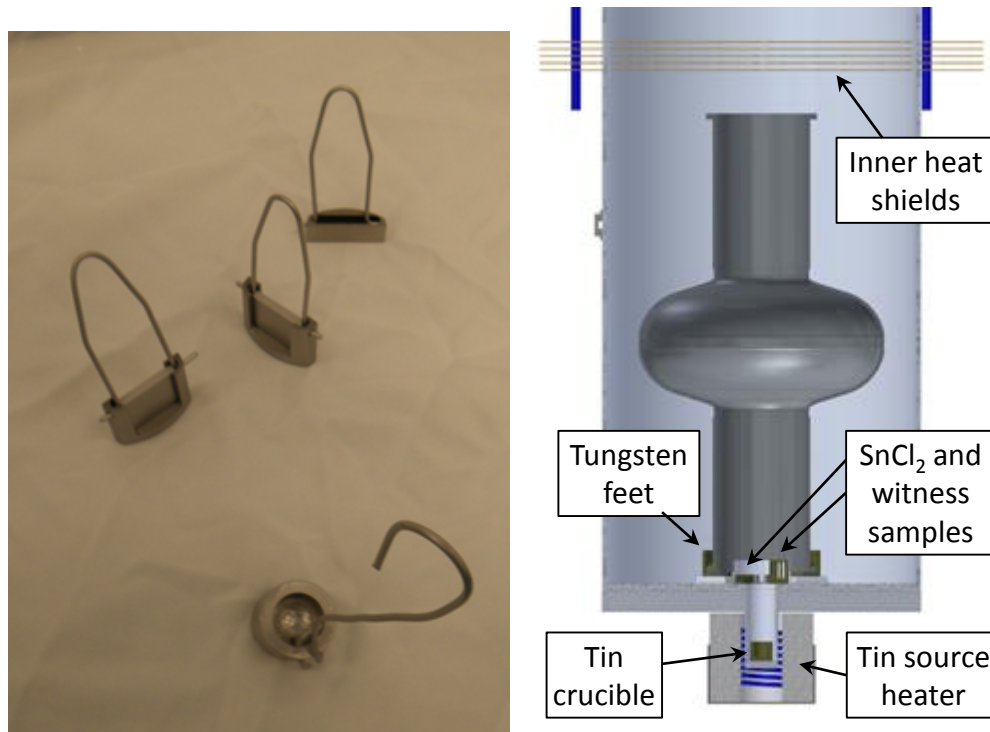


Figure 5.4: From bottom to top, crucible for high purity tin pellets, niobium witness samples, and container for nucleation agent SnCl_2 (left); computer drawing of coating chamber cross-section with cavity and coating accessories (right).

date the moveable plate.

After degassing and closing the valves to the pumps, the temperature is raised to 500°C for nucleation. At this temperature, the SnCl_2 has a high vapor pressure, which creates tin sites on the surface of the cavity. The nucleation step lasts for 5 hours, after which the temperature is increased for the coating step. Coating lasts 3 hours, with the cavity at 1100°C and the tin source at 1200°C . The temperature of the tin source controls the tin vapor pressure and therefore the rate at which tin arrives at the cavity surface. The cavity temperature controls the rate of interdiffusion of niobium and tin. By controlling the two temperatures independently during the coating step, these two rates can be balanced so

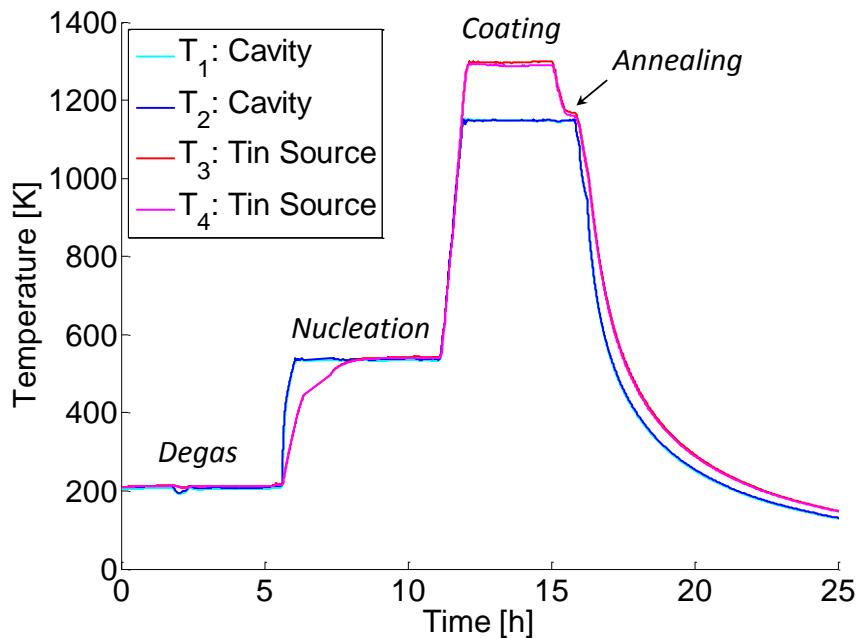


Figure 5.5: Nb₃Sn coating process, with recipe based on [MKM96].

that the desired stoichiometry can be achieved.

After the coating step is completed, the tin heater power is ramped down to zero, and the furnace is left on for another 0.5 hours to give residual tin on the surface time to diffuse into the surface and react before turning off the furnace. This final step is included to prevent the presence of unreacted tin on the surface, which can be lossy under RF. Drawings of the Wuppertal furnaces show the tin source in a separate hot zone from the cavity, so that its temperature is independent of the furnace temperature. In the Cornell furnace, the tin source is in the cavity hot zone, so the tin source temperature is at least as high as the cavity temperature, even when the heater is turned off. This did not appear to cause residual tin to be present on the surface after coating, possibly because the tin vapor pressure was sufficiently small with the source temperature at 1100°C.

Once the furnace is cool, it is vented with nitrogen, then opened, and the

cavity is carefully removed, given a high pressure rinse (HPR), then mounted to a test stand for RF evaluation. Images of a cavity after coating are shown in Figures [Figure 5.6](#) and [Figure 5.7](#). Alternatively, instead of using a cavity substrate, this procedure can be carried out with small niobium sample substrates, hung from the heat shields.



Figure 5.6: A Nb_3Sn cavity (left) stands next to an uncoated cavity.

5.3 Coating Evaluation

Before coating cavities, several small samples were run through the coating process, and many studies were performed to evaluate the quality of the material.

A first test was anodization to test surface composition and uniformity. In

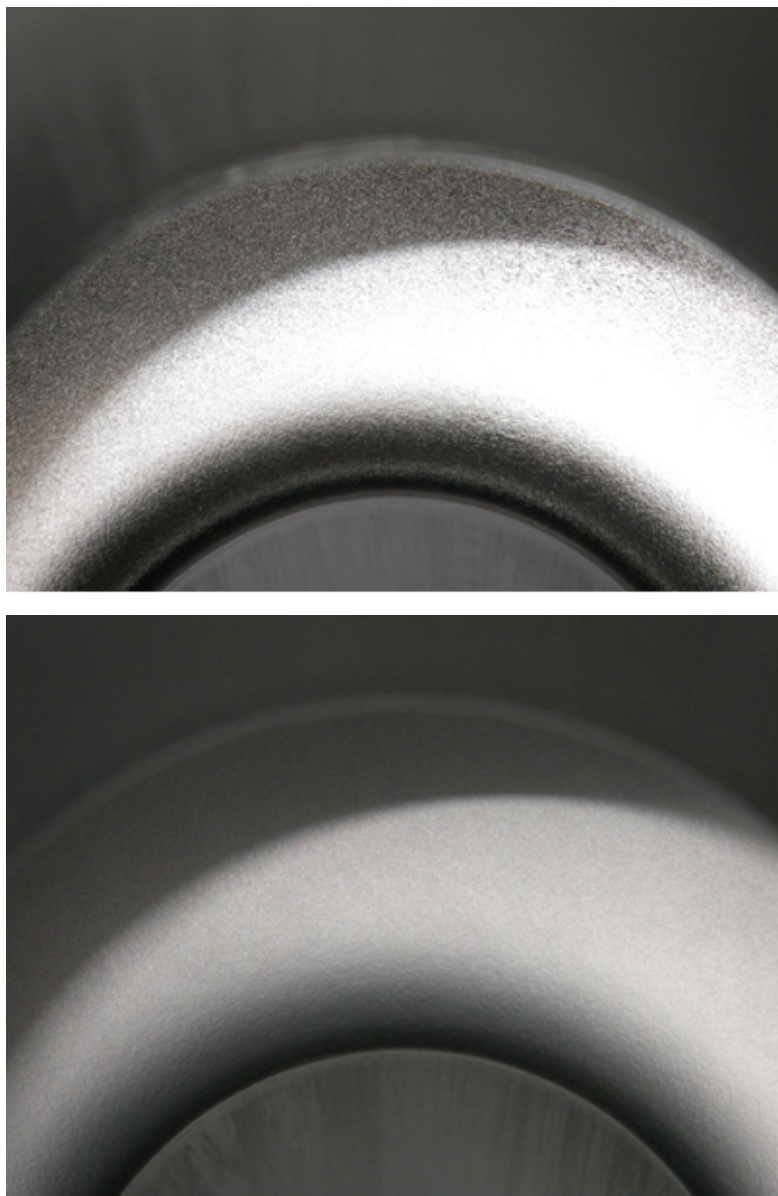


Figure 5.7: Pictures taken looking down the beamtube of a cavity at the inner surface of one of the half cells. Top: shiny niobium surface before coating. Bottom: typical matte gray Nb₃Sn surface.

this procedure, the sample is placed in 10% NH₄OH and a 75 V potential is applied between it and an aluminum anode. The thickness of the oxide that grows gives it a color that is characteristic of the material on the surface. Any unreacted tin will turn yellow, niobium will turn blue, and Nb₃Sn will turn pink-purple [Sti78]. The color of the sample, shown in Figure 5.8, indicates that

the material on the surface is Nb_3Sn . The lack of other colors shows that the coating is uniform, with no residual tin on the surface.

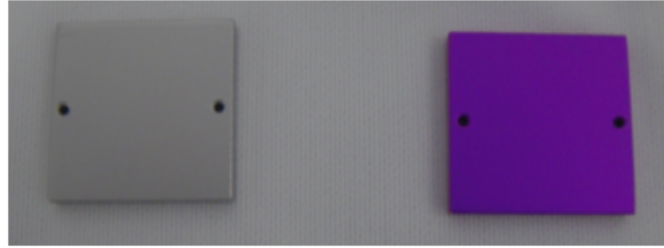


Figure 5.8: Nb_3Sn -coated sample (left) and an identical sample after anodization in NH_4OH at 75 V (right). The pink-purple color indicates Nb_3Sn phase on surface.

SEM (scanning electron microscope) images obtained using of the first samples coated are shown in Figure 5.9. Micron-sized grain growth was observed similar to that in images published by the group at University of Wuppertal.

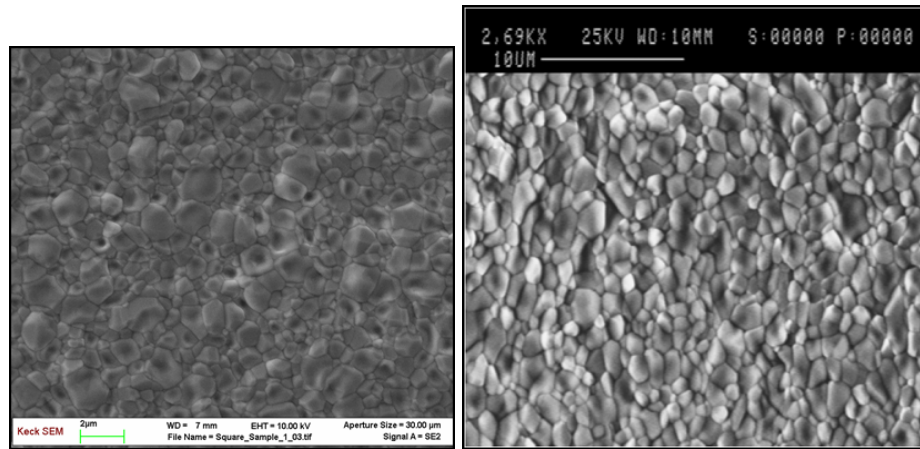


Figure 5.9: SEM images of Nb_3Sn produced at Wuppertal in 1996 (left) and at Cornell in 2011 (right).

To quantify the composition of the Nb_3Sn layer, an energy dispersive x-ray (EDX) analyzer connected to the SEM was used. Firing 10 keV electrons at the sample and measuring the spectrum of x-rays emitted (shown in Figure 5.10), it probes the relative abundance of Nb and Sn up to approximately 0.5 microns into the surface. An abundance of 24.2 ± 0.5 atomic percent tin ($\text{atm}\% \text{Sn}$) was

measured.

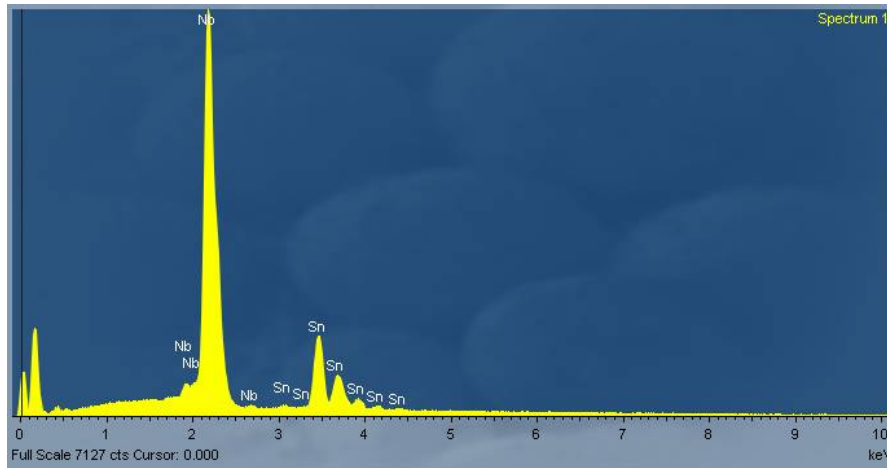


Figure 5.10: EDX spectrum of Nb_3Sn sample indicates composition 24.2 atm%Sn.

Nb_3Sn is the name given to the A15 phase of the Nb-Sn system, which has a composition ranging from approximately 18 to 25 atm%Sn. A. Godeke has reviewed the strong variation in the properties of the alloy with composition [God06a]. The variation of T_c with composition is shown in Figure 5.11. The data indicate that higher Sn content will yield a higher T_c , which is desirable to reduce the BCS resistance. However, as noted in section 4.1, above 24.5 atm%Sn the alloy will undergo a spontaneous lattice distortion at low temperatures which can lead to strain and, Godeke suggests, reduced RF performance [God06b]. The composition measured in EDX is in the desired range to achieve a high T_c without lattice distortion at low temperatures.

X-ray photoelectron spectroscopy has a much shallower scan depth than EDX, on the order of 10 nm. By alternatively performing an XPS scan and sputtering the sample with Ar^+ ions, the variation in composition with depth could be studied. The results in Figure 5.12 show that the Nb_3Sn layer has approximately uniform composition up to a depth of $\sim 1.5 \mu\text{m}$. The first surface scan

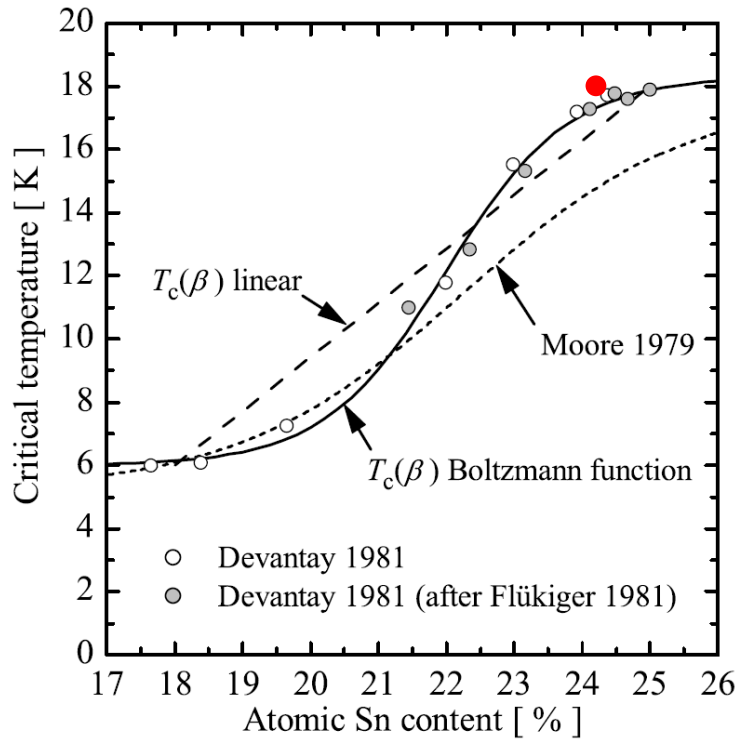


Figure 5.11: Literature data for T_c versus composition. From [God06a]. The measured composition and T_c (from Figure 5.14) is plotted in red.

is not shown as it showed foreign elements, likely from handling outside the clean room. The composition is normalized to the scan after the first etch, as differential sputtering rates give the absolute composition large uncertainty.

The sample thickness was also measured using a focused ion beam (FIB), during preparation of a sample for transmission electron microscopy (TEM results are presented in a later chapter). A gallium ion beam was used to make a steep trench in the sample, so that SEM could be used to look at the layers in profile. A distinct change in appearance is visible in Figure 5.13 at a depth of 2-3 μm , which was interpreted as being the division between the A15 phase of Nb_3Sn and the cubic phase of niobium.

The critical temperature of the layer was measured by induction [Sti78], us-

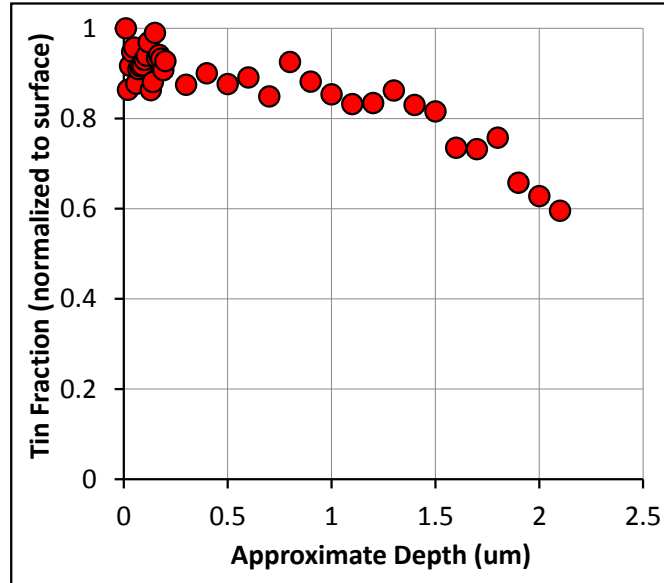


Figure 5.12: Alternately sputtering sample and performing XPS scans shows composition versus depth.

ing coupled coils on either side of the sample to determine the temperature at which the sample expels magnetic flux due to the Meissner effect. An apparatus was manufactured to perform this measurement, shown in Figure 5.14. The measurement gave a clear signal, a sharp transition at 18.0 ± 0.1 K, close to the highest measurement for this material from the literature [God06a]. The measurement is plotted with the measured composition from EDX in Figure 5.11, fitting well with the trend.

The RRR of the niobium substrate after coating was measured via a 4-wire measurement during cooldown. A low-frequency AC current was passed through the sample while measuring the induced voltage with a lock-in amplifier. The resistance of the sample was monitored from the transition up to room temperature, as plotted in Figure 5.15. RRR is defined as the ratio of the 300 K resistance to the normal 4.2 K resistance. The normal resistance at 4.2 K could not be measured, but a lower bound for the RRR of 210 could be obtained using the

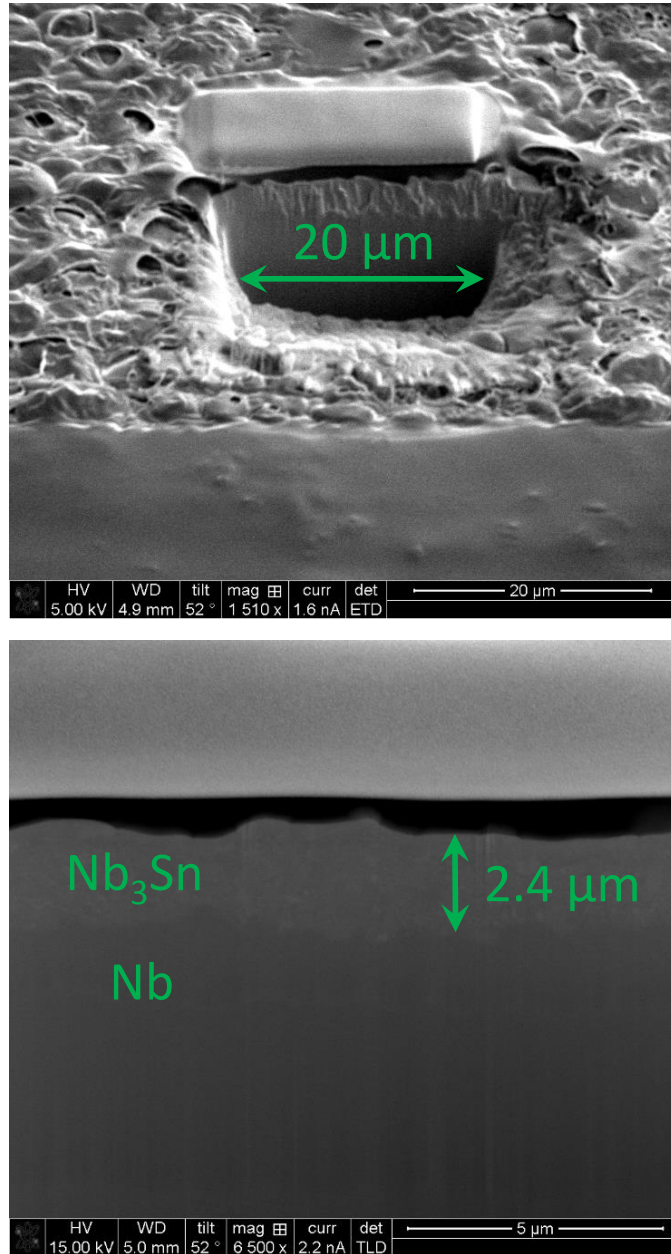


Figure 5.13: Trench made by ion beam (top) and profile of layers made visible by ion beam (bottom).

resistance just above the transition. Since the starting RRR was approximately 300, this shows that the RRR degradation during coating is minimal, and therefore the thermal conductivity of the substrate should be minimally affected by the coating process.

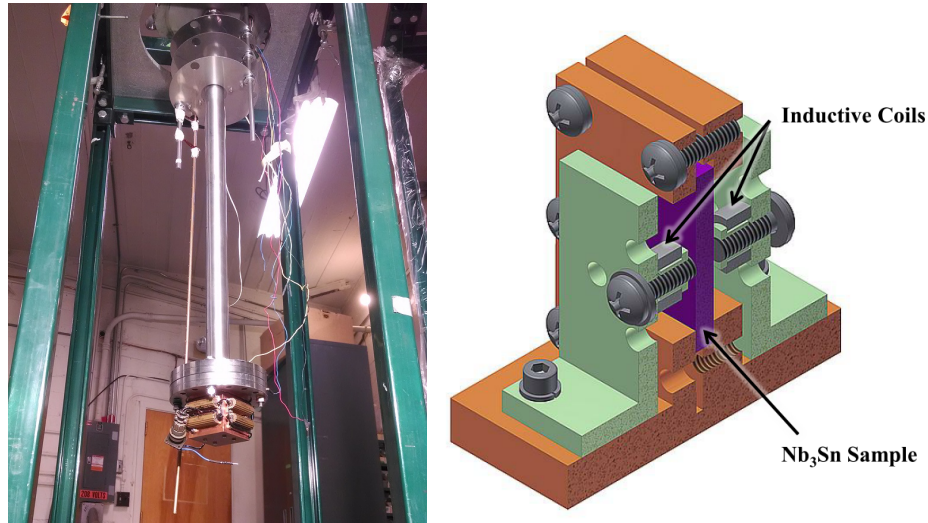


Figure 5.14: Inductive T_c measurement stand (top left), computer model of sample holder contained in stand's temperature controlled box (top right), and measurement of Nb₃Sn sample (two different cooldowns are shown) indicating a T_c of 18.0 ± 0.1 K (bottom).

Secondary electron yield (SEY) measurements were performed by S. Aull at CERN on a Nb₃Sn sample provided by Cornell. The maximum SEY was found to be 2.5, very similar to niobium, suggesting that multipacting in Nb₃Sn cavities should be comparable to that normally observed in Nb cavities [Aul14]. The SEY curve is shown in Figure 5.16.

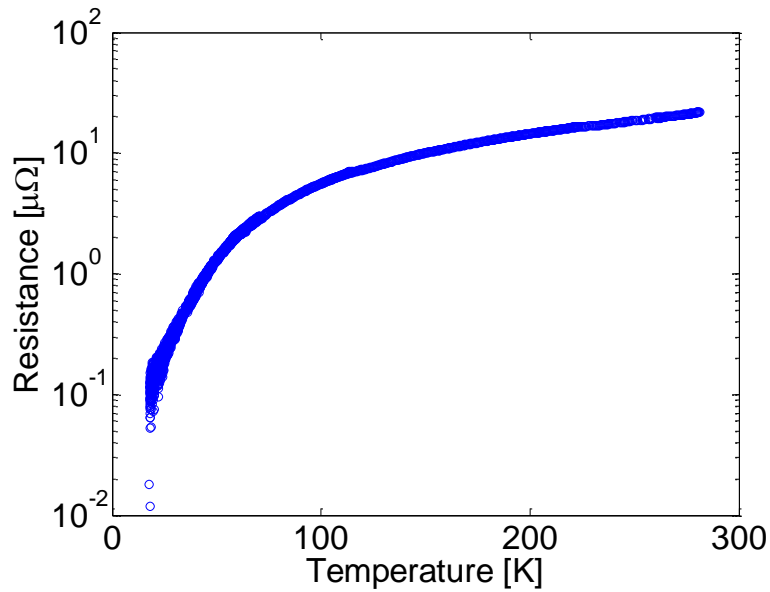


Figure 5.15: Resistance of sample versus temperature shows that minimal RRR degradation occurred during coating process.

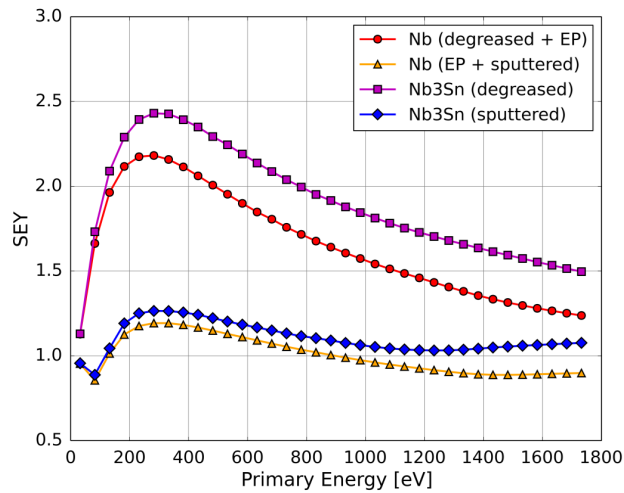


Figure 5.16: Measurements of SEY suggest that multipacting in Nb_3Sn cavities should be comparable to that normally observed in Nb cavities [Aul14].

Point contact tunneling (PCT) measurements [OZG98, PZC⁺08] were performed by T. Proslir at Argonne on a Nb_3Sn sample provided by Cornell. PCT curves show a nice, sharp gap at low temperatures. Correlations with temperatures gave an energy gap Δ at zero temperature of approximately 2.89 meV

with a T_c of 16 K ($\Delta/k_B T_c = 2.1$). These values (combined with composition from EDX) appear to follow correlations found in the literature for PCT measurements [God06a], as shown in Figure 5.17. Note that the gap and T_c measured via PCT can be lower at the surface than in the bulk [God06a, GGB⁺04]. This may explain the lower T_c values in Figure 5.17, in which values were measured using PCT, compared to Figure 5.11 and Figure 5.14, in which T_c was measured inductively.

H_{c2} measurements were also performed by T. Proslir at Argonne on the same Cornell Nb₃Sn sample, using a 50% resistive criterion (where the transition is taken to occur when the resistance is half of the normal conducting value). As shown in Figure 5.18, the extrapolated value for H_{c2} at zero temperature of 17.9 T appears to follow correlations found in the literature¹ [God06a].

These measurements showed that the samples produced in the Cornell coating chamber had excellent T_c and PCT gap. In addition, they had a similar appearance under SEM to Nb₃Sn produced by previous researchers, and they showed minimal RRR degradation. Measurements of the thickness of the layer via FIB and XPS revealed a layer with thickness of 1-3 microns, which should be many times the λ at low temperatures, approximately 100 nm. Therefore RF fields on the surface should decay sufficiently in the Nb₃Sn layer that the Nb substrate has minimal effect. All of these results indicated that the Nb₃Sn produced is of high quality. The decision was made to move on to next phase of the experimental program, coating of single cell cavities. The next chapter reviews the methods used for preparing and performing RF measurements on cavities. [chapter 7](#) presents results from CW cavity testing, as well as a comparison of material parameters extracted from RF measurements to values measured on

¹PCT and H_{c2} appear in [PLP14], and are to be published in full elsewhere.

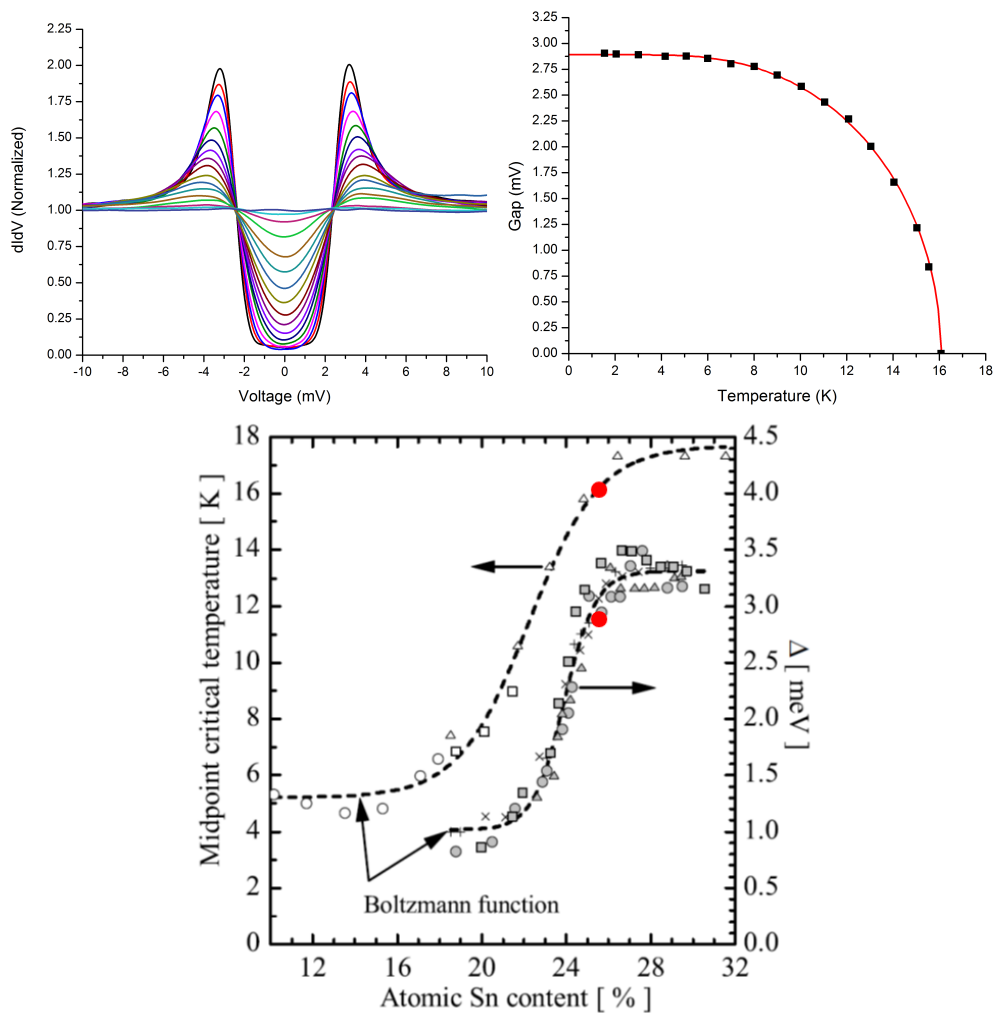


Figure 5.17: Top left: Point contact tunneling measurements by T. Proslir at Argonne at several different temperatures. Top right: extraction of T_c and Δ . Bottom: Comparison of extracted values (red) to literature with figure adapted from [God06a]. The uncertainty in the PCT data is unknown. Composition was measured using EDX.

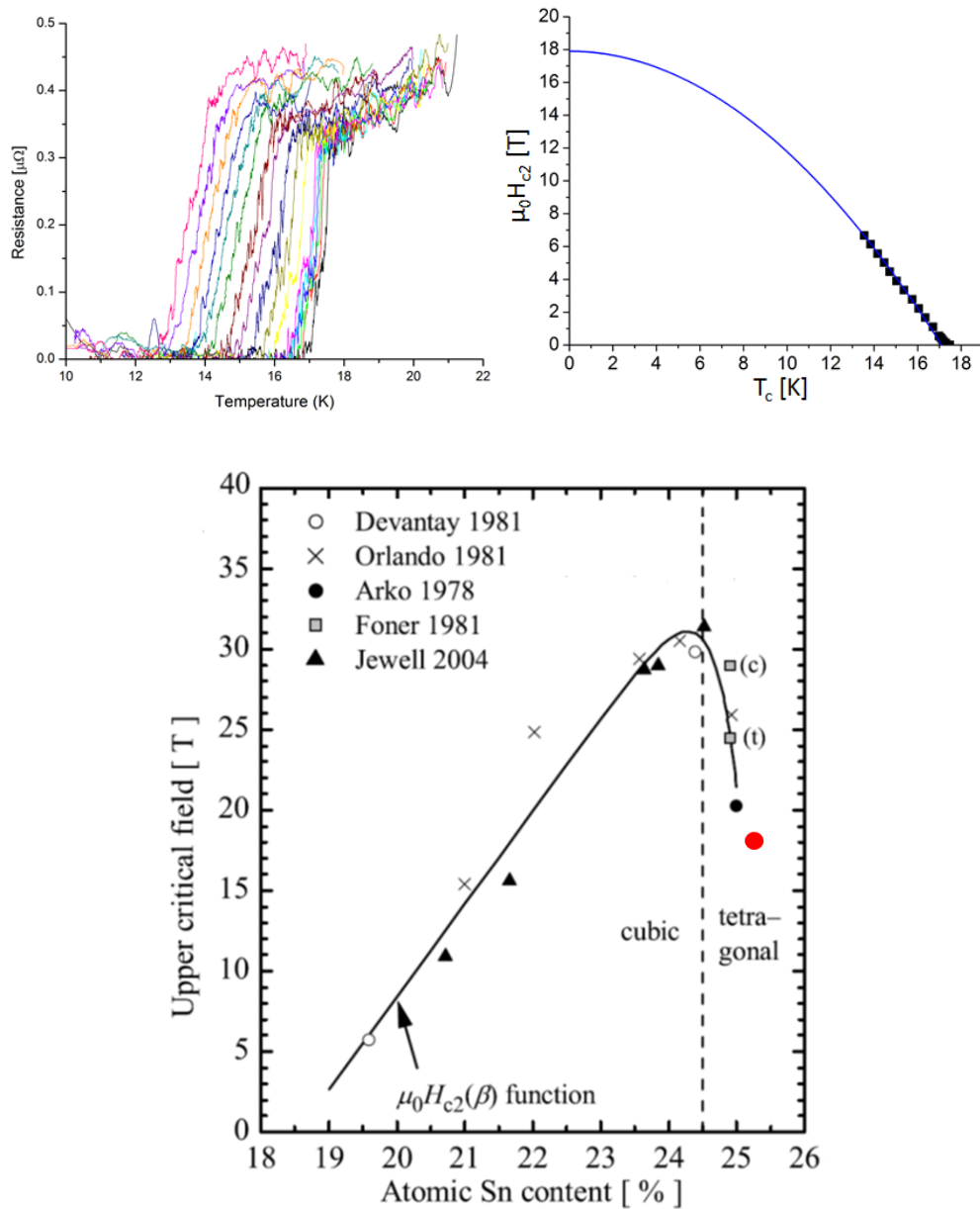


Figure 5.18: Top left: Resistive measurements performed at Argonne made at several different external fields. Top right: extraction of H_{c2} extrapolated to zero temperature with 50% resistive criterion. Bottom: Comparison of extracted value from H_{c2} measurements (red) to literature with figure adapted from [God06a]. The uncertainty in the H_{c2} data is unknown.

samples in this section.

CHAPTER 6

EXPERIMENTAL SRF FACILITIES

This chapter is devoted to the preparation and CW testing of SRF cavities. First an overview is given of how the cavities are prepared, including chemistry, cleaning, and mounting to test equipment. Then RF measurement methods are presented, using the formalism from [PKH08]. Next, the slow cool system is shown, used to prevent thermocurrent which can cause excess losses. Finally, the temperature mapping system is presented.

6.1 Preparation for Cavity Test

Niobium cavities are manufactured from purified niobium sheets that are formed into the desired shape and welded together. After manufacturing, the cavities are put through a deep chemical removal process to remove a layer of material about 100 μm thick which contains contamination and mechanical damage from the fabrication process. The removal process is generally either buffered chemical polish (BCP), in which the cavity is filled with an etching solution containing hydrofluoric acid (HF), nitric acid, and phosphoric acid, or electropolishing (EP), in which current is applied to the cavity through an electrolyte containing sulfuric acid and HF. EP generally produces a smoother surface than BCP, but it can lead to significant uptake of hydrogen into the niobium. If a cavity received bulk EP, it is degassed in a UHV furnace to remove hydrogen. Before going into the Nb_3Sn coating chamber, all cavities receive a light BCP inside and out to remove any contamination. If an EP surface is desired, it then receives a light EP. After chemistry, the cavity is cleaned in an ultrasonic

bath and then brought into a class 10 clean room. It is treated with HPR, in which deionized water at approximately 1000 PSI is sprayed from nozzles at the inside surface of the cavity to remove contaminants, as shown in [Figure 6.1](#). After drying, the cavity is placed into the coating chamber.



Figure 6.1: High pressure rinsing (left) and assembly of the cavity to the test stand (right).

After coating, the cavity is removed from the coating chamber, and a top plate is assembled to one of its beamtubes via an indium seal. The top plate contains a weakly coupled antenna to measure transmitted power (P_t). After this, the cavity is treated with HPR, and then its other beamtube is assembled to a test stand, as shown in [Figure 6.1](#) [Kno97]. The test stand contains a variable input coupler, an antenna with adjustable penetration into the cavity used to couple RF power into the cavity during test. The cavity is then slowly evacuated by a

pump stand with a scroll pump and oil-free turbomolecular pump that operate through a mass flow controller. The test stand is removed from the clean room, and, as shown in [Figure 6.2](#), instrumentation is added. This includes a helium level stick, a heater used to recover helium after testing, RF cables for the input and transmitted power couplers, cernox temperature sensors [lak], fluxgate magnetometers for measuring ambient magnetic fields during cooldown, and a temperature map (T-map). In addition, a helium transfer line is added, as well as a second helium transfer line which contains a slow cool system. The T-map and slow cool system are described later in this chapter.

The test stand is then sealed into a dewar. Liquid helium is transferred into the dewar, the temperature of which can be controlled via a pumping system connected to a helium recovery system. Once a radiation shielding block is moved into place over the dewar, RF testing can begin.

6.2 CW RF Cavity Testing

As discussed in [chapter 2](#), the two most important figures of merit for an SRF cavity are Q_0 and E_{acc} . Generally a Q vs E curve is used to characterize a cavity's performance. To obtain this curve, RF power is applied to a cavity close to its resonant frequency through the input power coupler. The forward power to the cavity P_f and the power reflected from the cavity P_r are sampled by directional couplers and measured using power meters¹. The fields in the cavity are sampled by the weakly coupled transmitted power coupler. P_t is also measured with a power meter. In addition, P_f and P_t are mixed together and used

¹Coupling constants and cable losses are taken into account during calibration to give the power at the cavity.

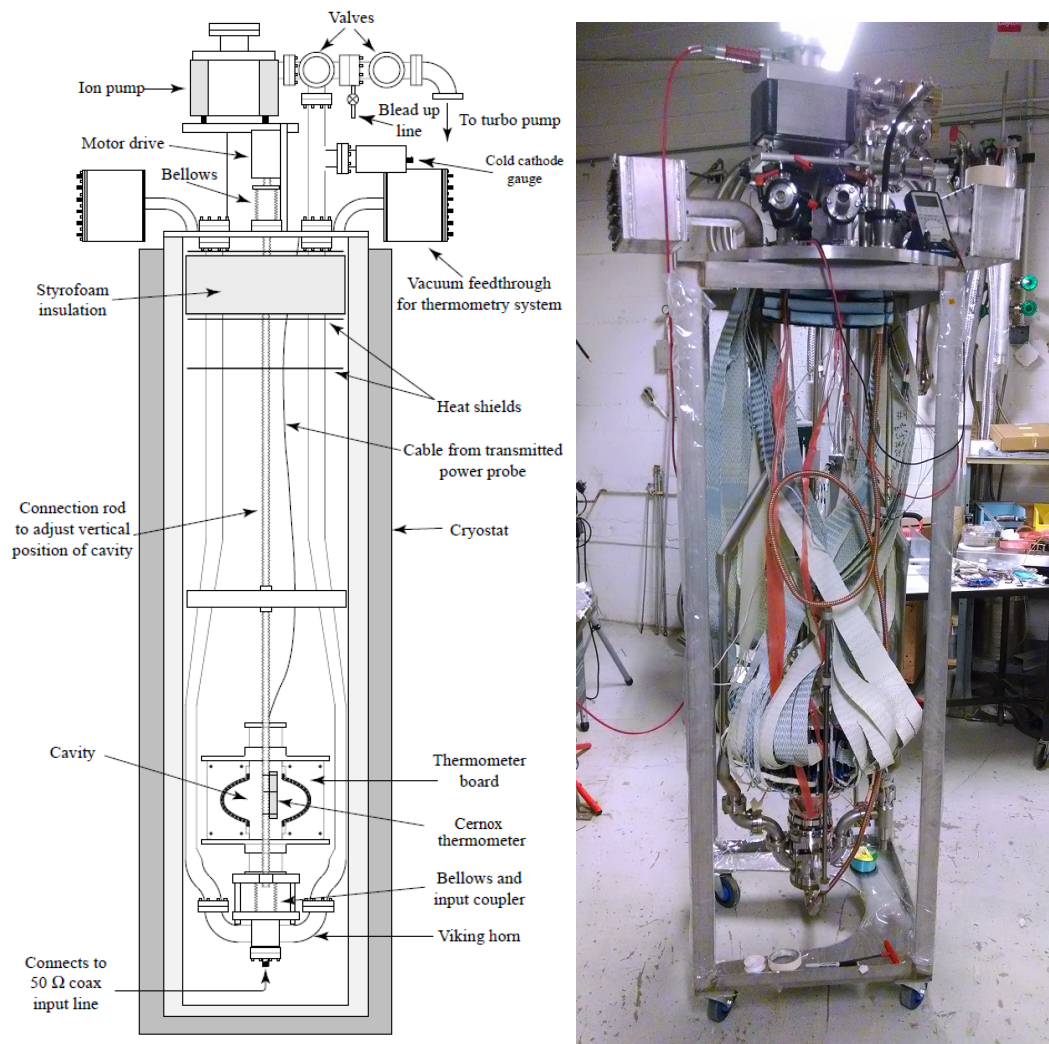


Figure 6.2: Testing stand for CW RF measurements. Left: schematic representation adapted from [Kno97]. Right: picture of test stand before insertion to the cryostat.

as phase feedback to the signal generator. This phase-locked loop (PLL) keeps the drive signal close to the cavity resonant frequency. A schematic of the PLL system is shown in Figure 6.3.

The intrinsic cavity quality factor Q_0 can be described in terms of the stored energy U , the angular frequency ω , and the power dissipated in the walls of the cavity P_{diss} as:

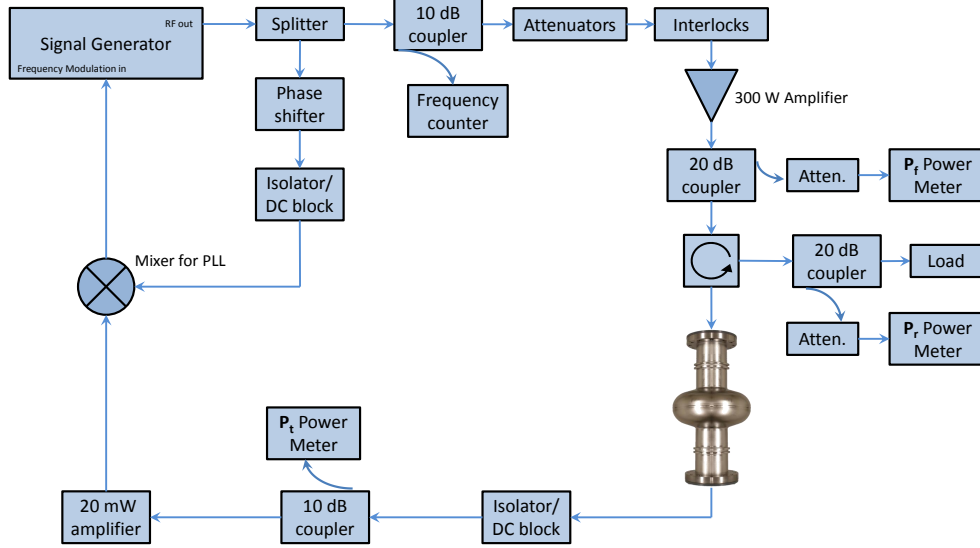


Figure 6.3: Block diagram of RF system.

$$Q_0 = \frac{\omega U}{P_{diss}} \quad (6.1)$$

In addition to the power dissipated in the walls of the cavity, some power leaves the cavity through the input power coupler P_e and through the transmitted power coupler P_t . Then the total power leaving the cavity is

$$P_{tot} = P_{diss} + P_e + P_t \quad (6.2)$$

We can also define a loaded quality factor Q_L :

$$Q_L = \frac{\omega U}{P_{tot}} \quad (6.3)$$

Using the definition of P_{tot} and defining similar quality factors for the couplers, the loaded quality factor can be separated: $Q_L^{-1} = Q_0^{-1} + Q_e^{-1} + Q_t^{-1}$. Since the transmitted power coupler is only weakly coupled, this is approximately:

$$\frac{1}{Q_L} = \frac{1}{Q_0} + \frac{1}{Q_e} = \frac{1}{Q_0} (1 + \beta) \quad (6.4)$$

where the coupling strength is defined as $\beta = Q_0/Q_e$

When the drive power to the cavity is turned off, the stored energy U decays according to:

$$\frac{dU}{dt} = -P_{tot} = -\frac{\omega U}{Q_L} \quad (6.5)$$

The solution to this is:

$$U = U_0 \exp\left(-\frac{t}{\tau_L}\right) \quad (6.6)$$

where

$$\tau_L = Q_L/\omega \quad (6.7)$$

For a cavity drive on resonance in steady state, one can write [PKH08]:

$$P_{diss} = \frac{4\beta}{(1+\beta)^2} P_f \quad (6.8)$$

During a cavity test, P_f , ω , τ_L , and β are measured. Using Equation 6.7 Q_L can be found using ω and τ_L . Then Equation 6.4 can be used to find Q_0 from Q_L and β . Following this, Equation 6.1 and Equation 6.8 can be used to find U using Q_0 , ω , P_f , and β . For a given cavity geometry, E_{acc}/\sqrt{U} is a constant that can be calculated using computer codes and then used to find E_{acc} .

In this way, Q_0 and E_{acc} can be determined using simple measurements. P_f is measured with the power meters as described above. τ_L can be measured by taking the derivative of a decay curve on the power meters for P_r or P_t . ω can be measured with a frequency counter. β is measured from the P_r power meter in the two ways.

A typical P_r trace is shown schematically in Figure 6.4 [Val14]. When the RF drive power is on but not locked to the cavity frequency (full reflection), $P_r = P_i$, and the incident power can be read from the power meter. After feedback is

turned on and the drive power locks to the cavity frequency, the cavity fills with energy and P_r settles into a steady state value, which is again read by the power meter. When the RF drive power is turned off, instantaneously, $P_r = P_e$; the emitted power is measured by the power meter. The power meter continues to read the P_r trace to measure the decay constant τ_L .

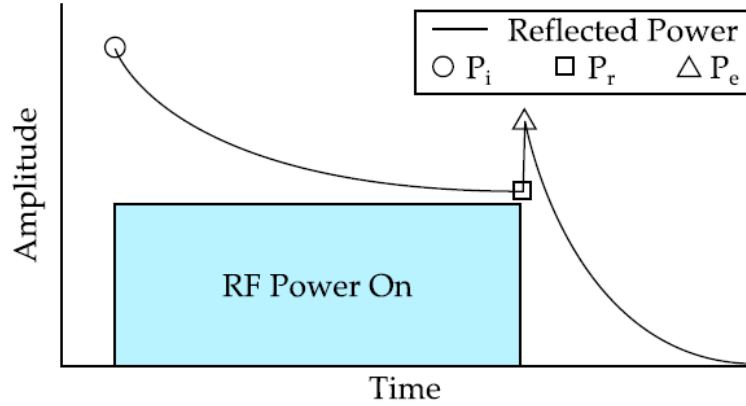


Figure 6.4: Typical trace from P_r power meter, shown schematically. The “RF Power On” box denotes when the forward drive power is on and locked to the cavity frequency on resonance. The incident power, steady state reflected power, and emitted power are highlighted. Image from [Val14].

From these measurements on the P_r power meter, β can be calculated in two ways. From the ratio of P_i to P_e , one can calculate [PKH08]:

$$\beta_e = \frac{1}{2\sqrt{\frac{P_i}{P_e}} - 1} \quad (6.9)$$

From the ratio of P_r to P_i , one can calculate [PKH08]:

$$\beta_r = \frac{1 \pm \sqrt{P_r/P_i}}{1 \mp \sqrt{P_r/P_i}} \quad (6.10)$$

where P_r here is the steady state value with the frequency locked. If the $\beta > 1$, the cavity is said to be overcoupled and the upper sign is used. Otherwise, the

cavity is undercoupled and the lower is used². Equation 6.9 is used to determine if the cavity was overcoupled or undercoupled. β_e and β_r are averaged to produce the β value used in the equations above³.

After a measurement of Q_0 and E_{acc} has been made at one field, the P_t value measured on the power meter can be used as a calibration for other fields in order to simplify the measurement process. In this case, the constants U/P_t and $E_{acc}/\sqrt{P_t}$ are used in conjunction with the steady state value of P_t to determine U and E_{acc} directly. Then U , P_f , and β are used to determine Q_0 . Measurement uncertainty in E_{acc} is approximately 10%, and uncertainty in Q_0 is approximately 10%.

6.3 Slow Cool System

Researchers at the University of Wuppertal discovered that the quality factors obtained in Nb cavities coated with Nb₃Sn were strongly dependent on the cooldown. They found that a uniform, slow (~1 K/5 min) cooldown would produce the best results. They interpreted this effect as being caused by thermocurrents. In effect, the interface between Nb and Nb₃Sn acts like a thermocouple, and temperature gradients over the surface can produce thermocurrents by the Seebeck effect. The currents produce magnetic flux, which gets trapped in the superconductor as it cools through T_c [PHK⁺88]. The trapped flux causes strong R_{res} as high as 40 nΩ or more, depending on the conditions (see [subsection 7.2.6](#)). Additionally, a similar decrease in Q_0 is observed after quench, likely

²To avoid having strong fields around the coupler that can cause excess losses, the coupler position is generally adjusted such that $\beta \approx 0.3$.

³A difference between β_e and β_r of more than ~ 20% is indicative of a problem with the measurement. Good agreement between the two gives confidence to the average β value.

due to strong local heating during quench, followed by rapid cooldown through T_c with strong temperature gradient.

The procedure used by Wuppertal researchers for slowly cooling through T_c involved producing a pool of liquid helium below the bath, evaporating it with a heater in the pool, and controlling temperature gradients on the cavity with heaters on its surface. For the research in this thesis, a different system was developed. To minimize temperature gradients, the system generates cold gas just below the cavity temperature, then slowly decreases the temperature of the gas as the dewar becomes colder. An apparatus was built consisting of a long narrow channel with a series of heaters along it, as shown in [Figure 6.5](#). The apparatus is connected on one side to a helium transfer stinger with a JT valve built in to further restrict the flow, and on the other side to a transfer tube to bring the cold gas to the bottom of the dewar. Liquid helium is transferred into the slow cool system from a large dewar with a valve that can be finely controlled with a computer setpoint. This setup allows temperature control of a steady stream of helium gas, so that the cavity can be uniformly cooled as slowly as desired. The temperature is monitored via three cernox sensors far apart from each other on the cell of the cavity. An example of the extremely slow cooldown rate achievable with the system ($\lesssim 1$ K/hour) is shown in [Figure 6.5](#).

6.4 Temperature Map

A temperature mapping system is an array of temperature sensors in good thermal contact with the outer surface of the cavity, used to map out the distribution of heating by RF fields inside the cavity over its surface [[LMN72](#), [Pie80](#), [Mu84](#),

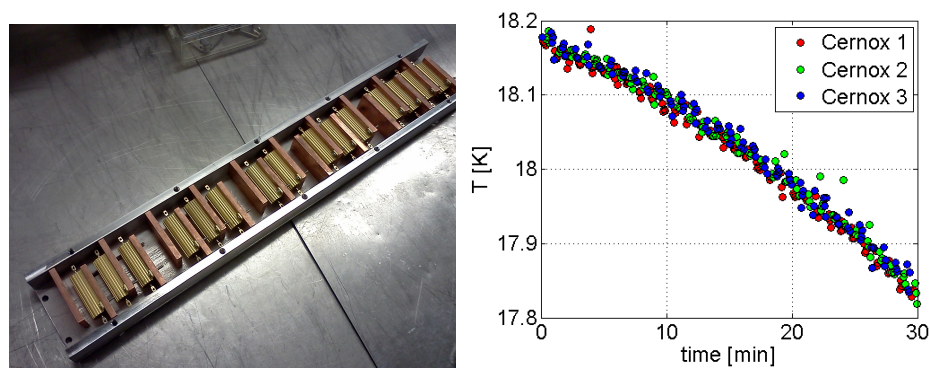


Figure 6.5: Left: apparatus used to slowly and uniformly cool cavities to avoid thermocurrents. With the cover removed, the helium channel with heaters is visible, which liquid enters and cold gas leaves. Right: an example of a very slow cooldown rate through $T_c = 18$ K, measured by 3 cernox sensors over the surface of the cavity.

[Kno97]. The T-mapping system from Cornell is shown in Figure 6.6. T-mapping is useful for localizing regions where quench occurs, or regions where the local R_s is high, both of which can be indicative of a defect. Alternatively, they can show global problems, such as high R_s is a over a large region of the cavity surface, indicative of a problem with the cavity preparation. If a local problem is found, optical inspection of that area can be performed using a telescope and mirror system; the T-map allows a correlation to be made between RF performance and any unusual features found during optical inspection.

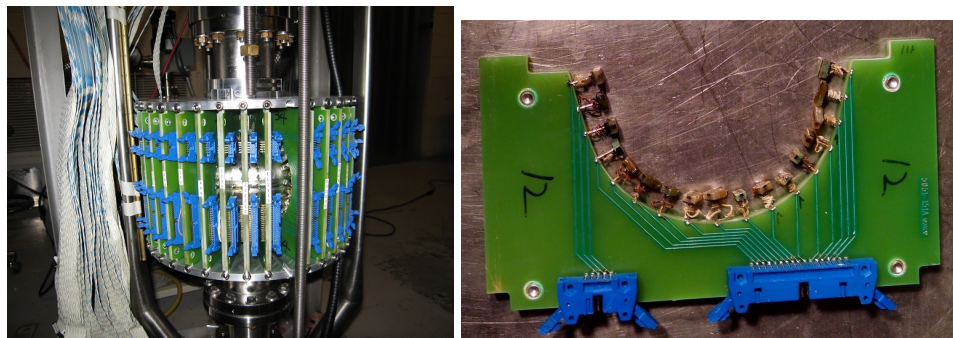


Figure 6.6: Temperature mapping system assembled to cavity (left) and one of the 38 T-map boards, each of which holds 17 RTDs (right).

The current Cornell T-map system was developed by J. Knobloch [Kno97] for 1.5 GHz CEBAF cavities, and was adapted to 1.3 GHz TeSLA and Cornell ERL cavities as a part of this research. It consists of 38 printed circuit boards that each hold 17 Allan-Bradley carbon resistors, which act as sensitive resistive thermal devices (RTDs). The resistors are mounted onto pogo sticks for good thermal contact with the cavity. The 646 resistors are driven by a 3 μ A current, and the voltage induced is read by a multiplexor. The Allan-Bradley resistors are calibrated using cernox sensors in the helium bath. T-map resistors are distributed such that there is a surface area of approximately 1 cm² per resistor in the high magnetic field region. The layout of the T-map on an ERL shape cavity is shown in Figure 6.7.

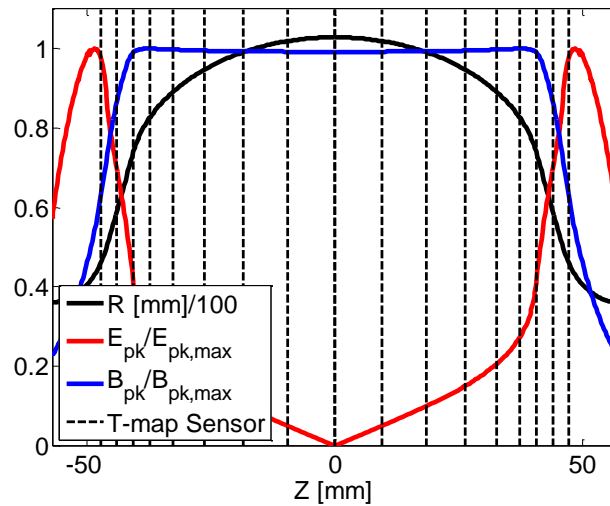


Figure 6.7: Distribution of the 17 T-map sensors per board compared to the ERL cavity shape and its surface fields. The TESLA shape and surface fields are similar.

The low R_s of Nb₃Sn at low temperature requires the T-map to be sensitive to very small signals. For maximum accuracy, the sensors are read into the analog-to-digital converter (ADC) one-by-one, with 1000 scans read per sensor. The T-map is read both with RF power on and with RF power off, and the RF

off reading is subtracted to remove any possible offsets. Allan-Bradley resistors in the bath are used as additional offset corrections (primarily for voltage drifts), and the readings are referenced to the helium temperature using the cernox sensors. Overall, the temperature resolution of the T-map is approximately 0.2 mK for a single measurement, and it can be further reduced by additional measurements. Each T-map measurement takes approximately 3 minutes. The spatial resolution of the T-map is given by the distance between resistors, approximately 1 cm. An example of a T-map measurement is shown in Figure 6.8. The channels that appear white in the figure are non-functional during the test.

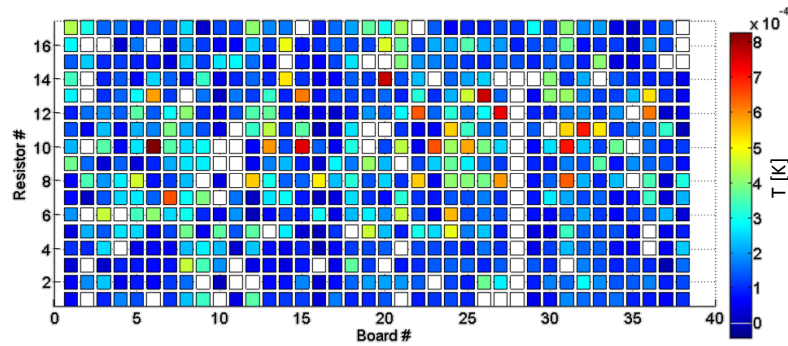


Figure 6.8: Example of a T-map plot. The boards wrap around the cavity (so that board 1 is next to board 38), and the resistors go from the top of the cavity to the bottom, with the equator at resistor 9. This 1.6 K T-map shows extremely high resolution with only ~ 0.16 W dissipated in walls of cavity. Average of 36 measurements shown.

CHAPTER 7

DEVELOPMENT OF Nb₃Sn SURFACE PREPARATION VIA CW TESTING

A number of different Nb₃Sn coating runs were carried out in the course of this research¹, in order to study the effects of different preparations. For each coating, a CW RF test was performed to evaluate it, and the results are presented in this chapter. First, an overview of the research program is presented, summarizing the tests performed. Next, several studies are presented in detail, comparing RF results within these tests based on the preparation parameters. After these studies, an analysis of Nb₃Sn material parameters is presented, which is used to show that several cavities have reach fields significantly higher than H_{c1} without strong Q -slope, proving that H_{c1} is not a fundamental limit for this material. A discussion is then presented of the weak link grain boundary model, with supporting RF and microscopy data, including TEM results that point to a possible cause of quench. In the last section, the potential for thermal instability in Nb₃Sn is evaluated.

7.1 Overview of CW Testing

Three cavities were used for experiments in this dissertation, all of which were 1.3 GHz single cells, made from fine grain niobium sheets. Each cavity had indium seal flanges and special fixtures for lowering into the coating chamber. Cavities 1 and 2 were the first made for this research, both Cornell ERL main linac shape, and they received BCP during preparation, similar to the cavities coated by previous researchers. Cavity 3 was fabricated in the final year of the

¹Collaborators for this research were M. Liepe, and D. Hall. Some of the analysis in this chapter and the next appears in [PL14], and other parts are planned to be included in a future publication.

research, with ILC shape, and it received bulk and final EP before coating.

An overview of selected Nb₃Sn CW tests performed for this dissertation is presented in [Table 7.1](#). Q vs E curves for each of the tests appear in [Figure 7.1](#)². In this section, a summary description of the results is presented. Detailed analysis comparing the different preparations used are presented in [section 7.2](#), along T-maps, microscopy images, and Q vs E curves.

Cavity #	Pre-Coat Chemistry	Anneal Time [h]	Post-Coat Treatment	Max 4.2 K B_{pk}	Q_0 at Max 4.2 K B_{pk}	Limit
1	BCP	0.5	HPR	33	5×10^8	RF power
1	—	—	oxypol.+HPR	—	—	—
1	BCP	0.5×2	HPR	56	4×10^8	RF power
2	BCP	6.5	HPR	55	1×10^{10}	quench
2	—	—	HF rinse+HPR	31	1×10^9	RF power
2	BCP	6.5	HPR	62	7×10^9	quench
2	—	—	CBP+HPR	23	2×10^8	RF power
2	BCP	16.5	HPR	56	8×10^9	quench
3	EP	6.5	HPR	49	9×10^9	quench
2	BCP	0.5	HPR	71	8×10^9	quench

Table 7.1: Table of CW Nb₃Sn cavity tests analyzed in this chapter. The tests are listed chronologically. The limitation at 4.2 K as well as the maximum B_{pk} and corresponding Q_0 are listed for each test (except test 2 of cavity 1, for which 4.2 K Q vs E was not measured). No field emission was observed in any of the tests.

For cavity 1, the recipe developed by Wuppertal researchers outlined in [chapter 5](#) was followed. After coating, the cavity showed the expected matte grey appearance in one half cell, but an unusually shiny appearance in the other. RF tests showed relatively high R_{res} on the order of $10^{-7} \Omega$, as well as strong Q -slope. T-maps showed that the half-cell with the matte gray appearance expected for high quality Nb₃Sn had minimal heating, but it was very strong in the other half-cell. By coating and testing in different orientations,

²Error bars are not shown on the plot for increased clarity, but as presented in [chapter 6](#), the measurement uncertainty in E_{acc} and Q_0 is approximately 10%.

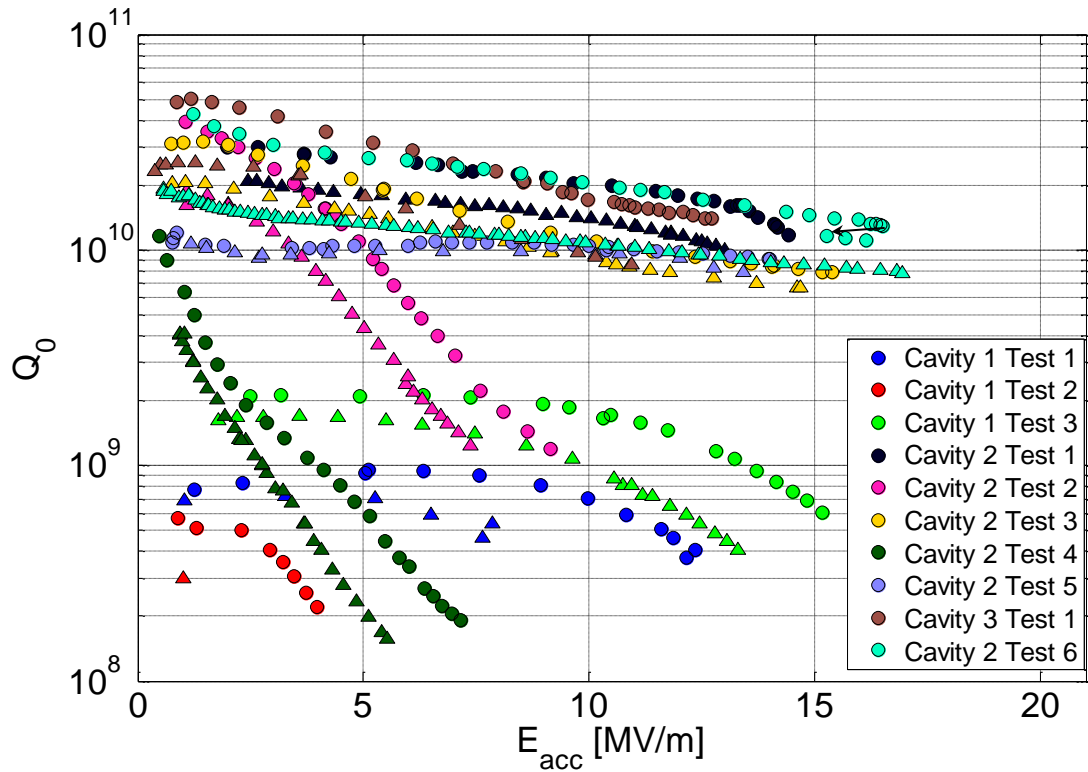


Figure 7.1: Q vs E curves for the cavity tests analyzed in this chapter. Circles represent measurements with a 2 K bath temperature and triangles represent 4.2 K. The preparations for each test are listed in order in [Table 7.1](#) and compared in the next section. The arrow in test 6 of cavity 2 indicates Q -switch.

it was concluded that there was likely a problem with the half-cell substrate that prevented proper coating with Nb_3Sn . Oxypolishing was attempted to improve performance, but instead a strong degradation was observed (see [subsection 7.2.1](#), Substrate Quality).

As detailed in [\[PCH⁺99\]](#), sample studies performed by U. Wuppertal researchers indicated that the onset field of Q -slope could be increased by increasing Nb_3Sn grain size. Whereas Wuppertal researchers increased grain sizes by controlling the thickness of a niobium film sputtered onto sapphire, at Cornell, a procedure was developed to increase grain size while maintaining the desired

stoichiometry by annealing for several hours at high temperatures. For the first coating of cavity 2, after the heater for the tin source was turned off, the cavity was left at 1100°C for 6.5 hours instead of 30 minutes. The cavity performed extremely well, reaching fields on the order of 12 MV/m with a Q_0 of 10^{10} at 4.2 K, limited by quench. No strong Q -slope was observed. The preparation with longer annealing time resulted in a cavity with minimal Q -slope, so the longer anneal was used in future tests while other parameters were varied to try to push performance further.

After the first test, cavity 2 was mounted to a waveguide insert and tested in pulsed mode, as detailed in the next chapter. It was then rinsed with hydrofluoric acid (HF) as a light material removal. It showed strong Q -slope in subsequent testing, so the coating was removed with BCP, and the cavity was recoated with the same extra-long anneal. Again it had a Q_0 above 10^{10} at 4.2 K and reached medium fields with minimal Q -slope, showing the reliability of the coating procedure. To see if chemistry-free material removal could have a benefit, the cavity was then treated with light centrifugal barrel polishing (CBP), which again resulted in strong Q -slope. The coating was removed and the cavity was recoated and tested, and then this process was repeated, in order to test the effect of different annealing times. In the first of these coatings, the annealing time was doubled, and in the second, only approximately 30 minutes of annealing was performed. The performance did not seem to depend strongly on the annealing time. The Q_0 and Q -slope were similar in all cases, and the quench field was also similar, though slightly higher for the shortest anneal (see [subsection 7.2.2, Annealing Time](#)). In the last of these cases, the recipe should be very similar to Wuppertal's, but the Q -slope is less severe for this cavity, and the quench field is somewhat lower. It is not yet clear why this is the case, but there

are preliminary indications that the ramp up to coating temperatures and low tin content regions play important roles. See additional discussion in [chapter 9](#).

Cavity 3 was used to evaluate the effect of having a smooth EP niobium surface as the substrate for coating. It showed a similar performance to cavity 2, which had a BCP niobium surface before coating. The 2 K Q_0 at very low fields was significantly higher than cavity 2, but the performance at the highest fields was approximately the same (see [subsection 7.2.5](#), Initial Chemistry).

After material removal in cavity 2, analysis was performed of Q vs E at different temperatures and of Q vs T , leading to two conclusions: 1) there appears to be a superconductor on the surface with relatively high R_s , and 2) there appears to be a material on the surface with T_c of 6 K. A hypothesis was developed, that low tin content Nb-Sn alloys were present in the grain boundaries, which would be consistent with these conclusions, as well as with the observations of Wuppertal regarding the dependence of Q -slope on grain size (see [subsection 7.2.4](#), Material Removal After Coating). Microscopic investigations of samples showed some indications of this mechanism, but also revealed another possible location for low tin content Nb-Sn alloys, which may be the cause of quench. Details of the microscopic analysis and conclusions are presented in [section 7.5](#).

Q -switch was observed in tests 1 and 6 of cavity 2. Before the cavity quenched, as the power to the cavity was increased close to the quench field, a sudden decrease in P_f was observed, and when Q_0 was measured, it had decreased (switched) from its high value. The switched Q_0 was maintained as the power to the cavity was increased, but the higher Q_0 could be recovered by bringing the cavity to a field somewhat below the Q -switch onset. The effect

was relatively small in test 1 and more significant in test 6, where it is indicated by an arrow in [Figure 7.1](#).

Not shown in [Table 7.1](#) are baseline tests for cavities 1 and 2 with niobium surfaces. Cavity 1 was tested before its first coating as an initial evaluation of the cavity, and cavity 2 was tested after removing its first coating, to ensure the removal process was sufficient to return the cavity to the performance of standard BCP niobium. In both cases, the cavities achieved fields above 20 MV/m at 2 K, with Q_0 above 10^{10} , limited by high field Q -slope between 20 and 30 MV/m. Since no limitations were observed up to the maximum fields reached in the Nb₃Sn tests, it is possible to rule out strong defects in the original niobium cavity carrying over after coating.

7.2 Effects of Preparation Parameters

There is a wide parameter space to explore to optimize the Nb₃Sn coatings, including:

- The niobium material used in the substrate (e.g. fine grain versus large grain) and the material removal process used to clean it
- The duration and temperature of various steps during the coating as well as the rate at which the temperature is changed between steps
- The method used to nucleate the niobium surface with tin sites at the beginning of the coating process (e.g. anodization of the substrate, enhanced tin source temperature, inclusion of SnCl₂ or SnF₂)

- The gases present during coating and those used for venting the furnace afterwards
- The chemical and cleaning treatments used on the cavity after coating
- The ambient magnetic field around the cavity during cooldown
- The spatial and temporal temperature gradient in the material during transition through T_c before test

A portion of the parameter space was explored in this research project, with a focus on areas that had not yet been explored. An emphasis was placed on exploring the influence of annealing time and of surface treatments not yet applied to Nb₃Sn cavities.

7.2.1 Substrate Quality

Cavity 1 had an unusual appearance after Nb₃Sn coating, as shown in [Figure 7.2](#). The top half cell had a matte gray appearance—which is typical for Nb₃Sn and was observed in both half-cells of each coating of cavities 2 and 3—but the bottom half cell had a shiny appearance, suggesting poor Nb₃Sn coverage. In test 1, immediately after coating, shown in [Figure 7.3](#), R_{res} was relatively high, giving a low field Q_0 around 1×10^9 at 2 K, and there was a strong Q -slope similar to that observed in the Wuppertal cavities. However, the 4.2 K curve still shows significantly higher Q_0 than a niobium cavity would have, indicating that the Nb₃Sn coating strongly improves the cavity's performance. T-maps showed strong heating on the half cell with the unusual appearance, as shown in [Figure 7.4](#).

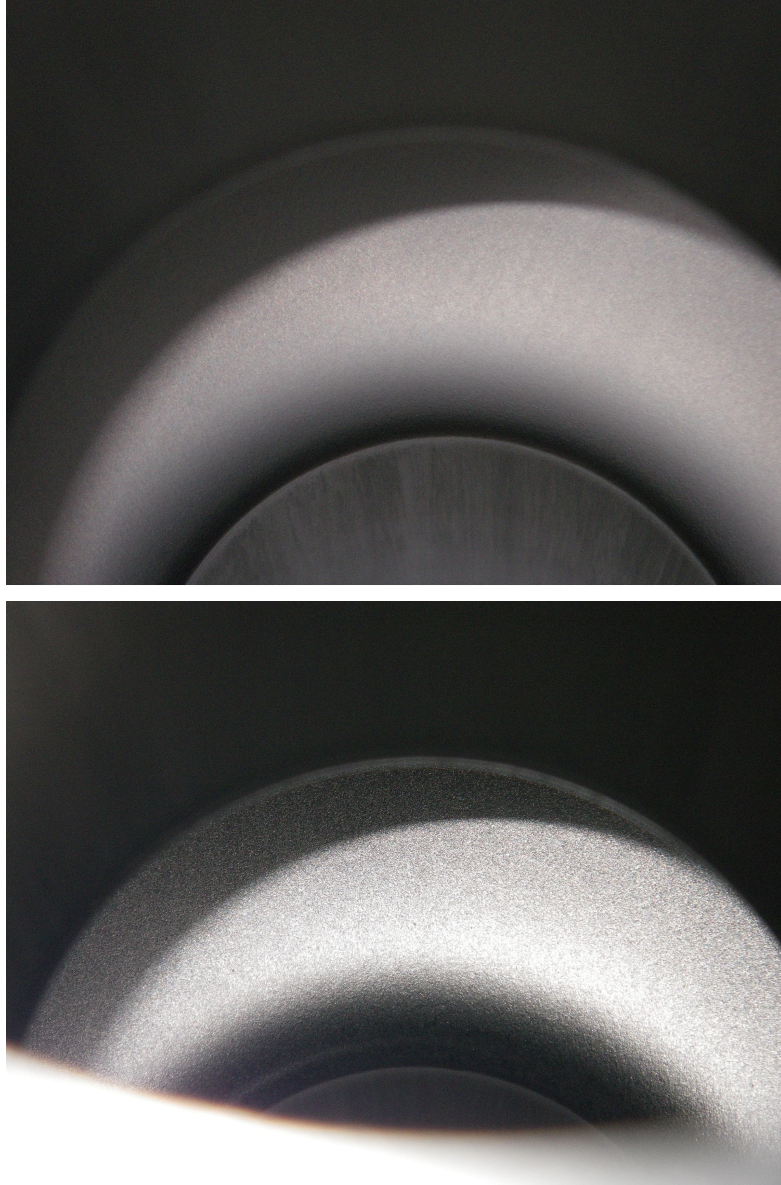


Figure 7.2: Top: Top half cell of cavity 1 after coating showing expected matte gray appearance. Bottom: Bottom half cell after coating showing unusually shiny appearance.

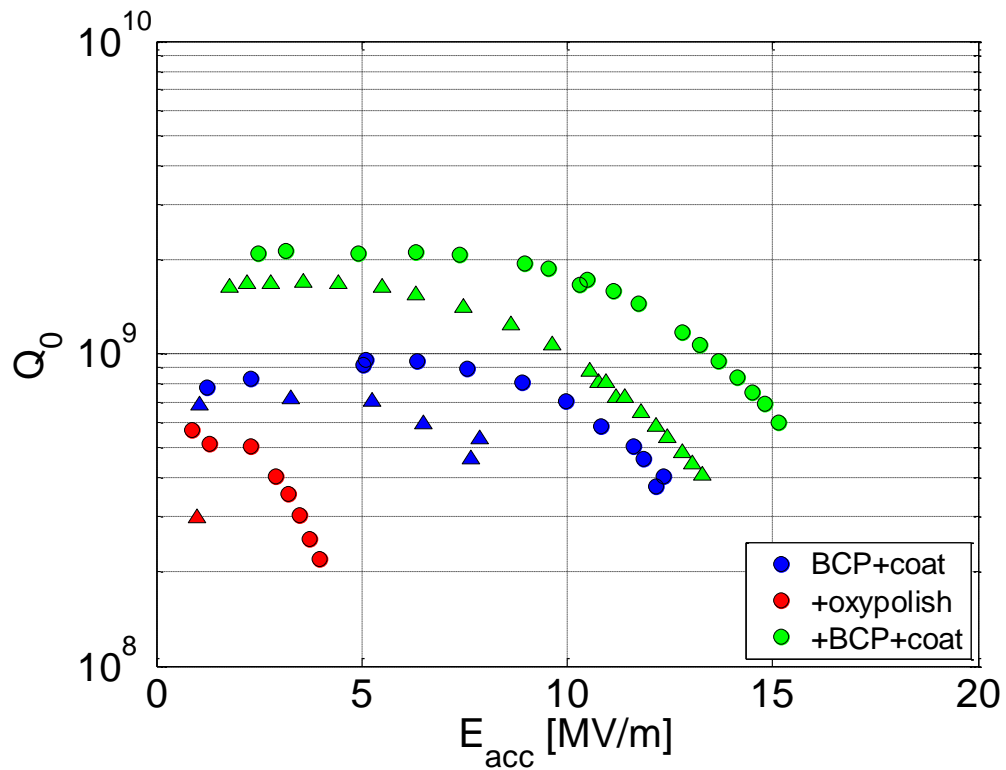


Figure 7.3: Q vs E curves for cavity 1, in which one of the half cell consistently showed bad regions after coating. Circles represent measurements with a 2 K bath temperature and triangles represent 4.2 K.

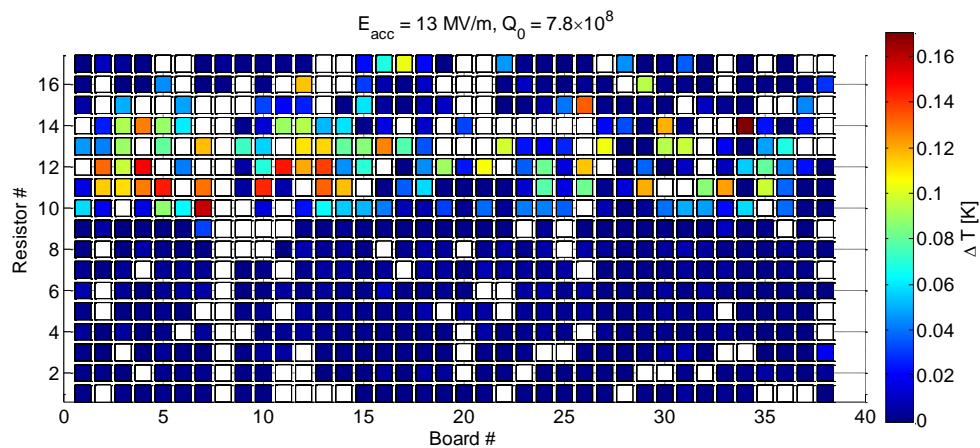


Figure 7.4: 2 K T-map of cavity 1 test 3, showing very strong heating on the half cell with unusual appearance.

Following the first test, the cavity was oxypolished using the recipe in [Sti78] in order to try to improve performance. If excess tin were present on the surface, which might be a cause for shiny areas, chemistry can remove it. Oxypolishing has been successfully employed to improve performance of Nb₃Sn cavities (see, for example, [HMP⁺77,KKS⁺77] and images in Figure 7.5). To oxypolish the cavity, it was anodized to 75 V to grow an oxide layer on the surface, and then a hydrofluoric acid (HF) rinse was applied to remove it. This process was applied twice. Using the thickness-voltage relation from [Sti78], 2.8 ± 0.2 nm/V, this gives a total removal of 0.41 ± 0.03 μ m. This should give a significant amount of removal while staying below 200 V of total removal, above which pitting has been reported to occur in the surface [Hil80]. Before the second HF rinse, the cavity interior was photographed using an optical inspection system, in which a mirror and lighting system mounted on a narrow tube gives a view of regions inside the cavity near the equator. Figure 7.6 shows that many parts of the cavity were purple, indicating Nb₃Sn, and many parts were blue, which indicates niobium. The distribution of colors did not suggest an obvious cause: the upper beam tube and lower half cell were mostly blue while the lower beam tube and upper half cell were mostly purple, with a transition region in the equator speckled with blue and purple regions that appeared to correspond to niobium grains. One possibility is that these different grains have different orientations, and that the thickness of the layer created by the diffusion process depends on the grain orientation. Siemens researchers have performed some investigations on single crystal samples that show that grain orientation does have an impact on the coating process. They observe that the grain orientation affects the fraction of the surface that is left uncoated when the coating is performed without any nucleation step [HUS80].

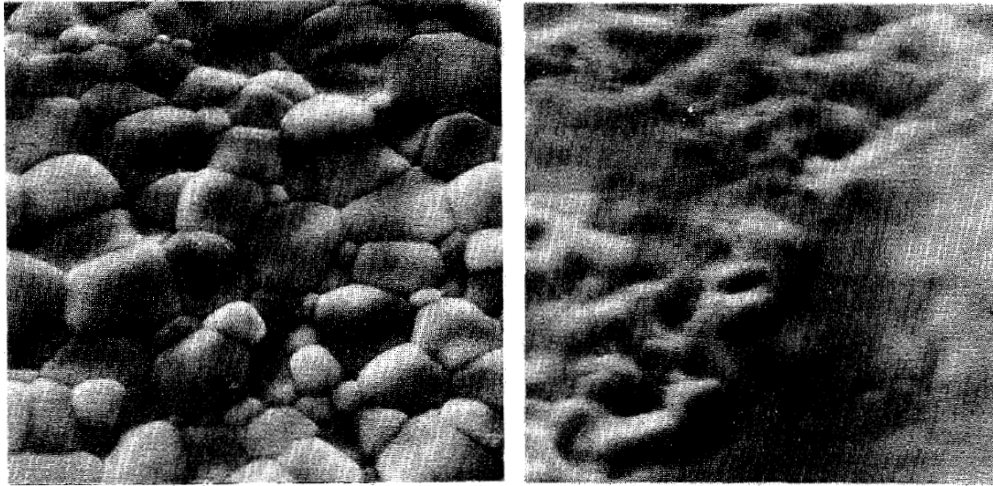


Figure 7.5: Nb₃Sn surface before (left) and after (right) oxipolishing. Images from [KKS⁺77].

The cavity was tested after oxipolishing, resulting in a further reduced Q_0 at low fields and an even stronger Q -slope that onset at lower fields. Next, the coating was removed with BCP and the cavity was recoated. Again the bottom half cell had an unusually shiny appearance. The previous anodization suggested that the problem might be uncovered areas, so the cavity was put through the coating process again to try to achieve better coverage, only this time, it was coated upside down. If there were a problem with the coating process (for example, if the tin pressure were too low at one half cell), then the flipped orientation should allow the process to proceed correctly. However, after coating the half cell was still shiny. The cavity was tested, showing similar performance and heating patterns in the T-map. It was tested again, in reverse orientation, to see if the problem might be connected to its orientation during cooldown, but the performance was again similar. Because the same half cell consistently had an unusual appearance and large heating on the T-map, it was concluded that there was likely an issue with the niobium substrate of that half cell that prevented proper coating. Therefore the cavity was put aside, and experiments

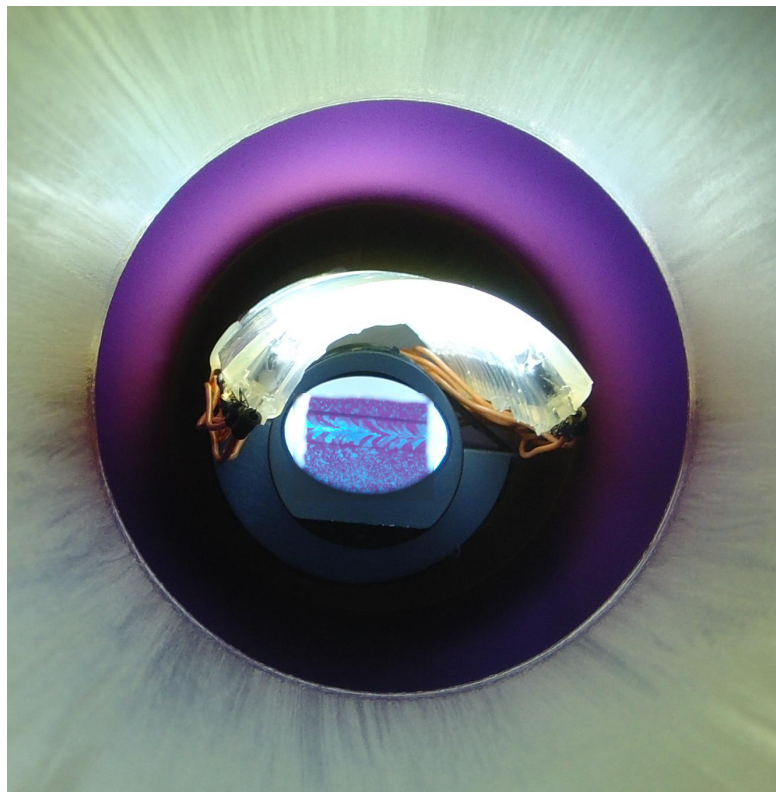
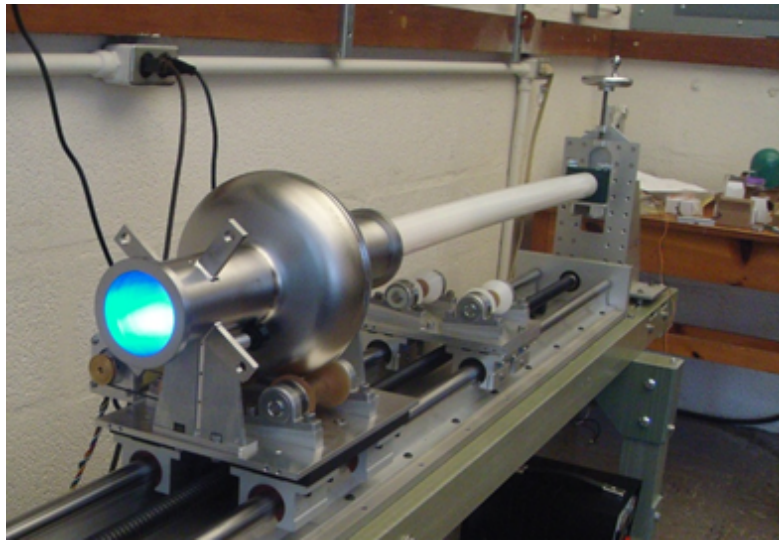


Figure 7.6: Top: anodized cavity on optical inspection showing blue beam tube. Bottom: optical inspection mirror shows equator of cavity speckled with blue and purple regions that appear to be correlated to niobium grains, especially in the weld bead.

continued with cavity 2.

7.2.2 Annealing Time

As discussed in [section 4.4](#), U. Wuppertal's experiments on samples suggested that weak link grain boundaries may be causing strong Q -slope, and that growing grains may help to prevent this problem. To attempt to increase the grain size, an investigation of annealing time was performed. An annealing step is performed immediately after coating, once the tin heater has been turned off, and the coating chamber is left at $\sim 1100^\circ\text{C}$. Three different annealing times were evaluated in the course of this research: a short 0.5-hour anneal (specified in the Wuppertal recipe), a medium 6.5-hour anneal, and a long 16.5-hour anneal. Witness samples from different coatings were studied under SEM, and images from coatings involving different annealing times can be seen in [Figure 7.7](#). By inspection, longer annealing times result in larger Nb_3Sn grains, up to $\sim 3\ \mu\text{m}$ in size. The images were analyzed to determine the approximate number of grain boundaries per unit length, as annotated in the figures³.

It is interesting that coating 1 of cavity 1 produced different grain sizes than those in coating 6 of cavity 2, even though both had 0.5 h of annealing. One possible influence is a change that was made to the coating procedure. It had been reported previously that having the tin source temperature higher than the cavity temperature could prevent uncovered niobium spots [[HMP⁺77](#)], likely by providing a high tin vapor pressure during the formation of the Nb_3Sn layer.

³Grain boundaries were traced, and then the traces were analyzed. Pixel by pixel, lines were scanned horizontally and vertically, determining the number of grain boundary crossings over the width and height of the picture. The number of grain boundaries per unit length was then determined by averaging.

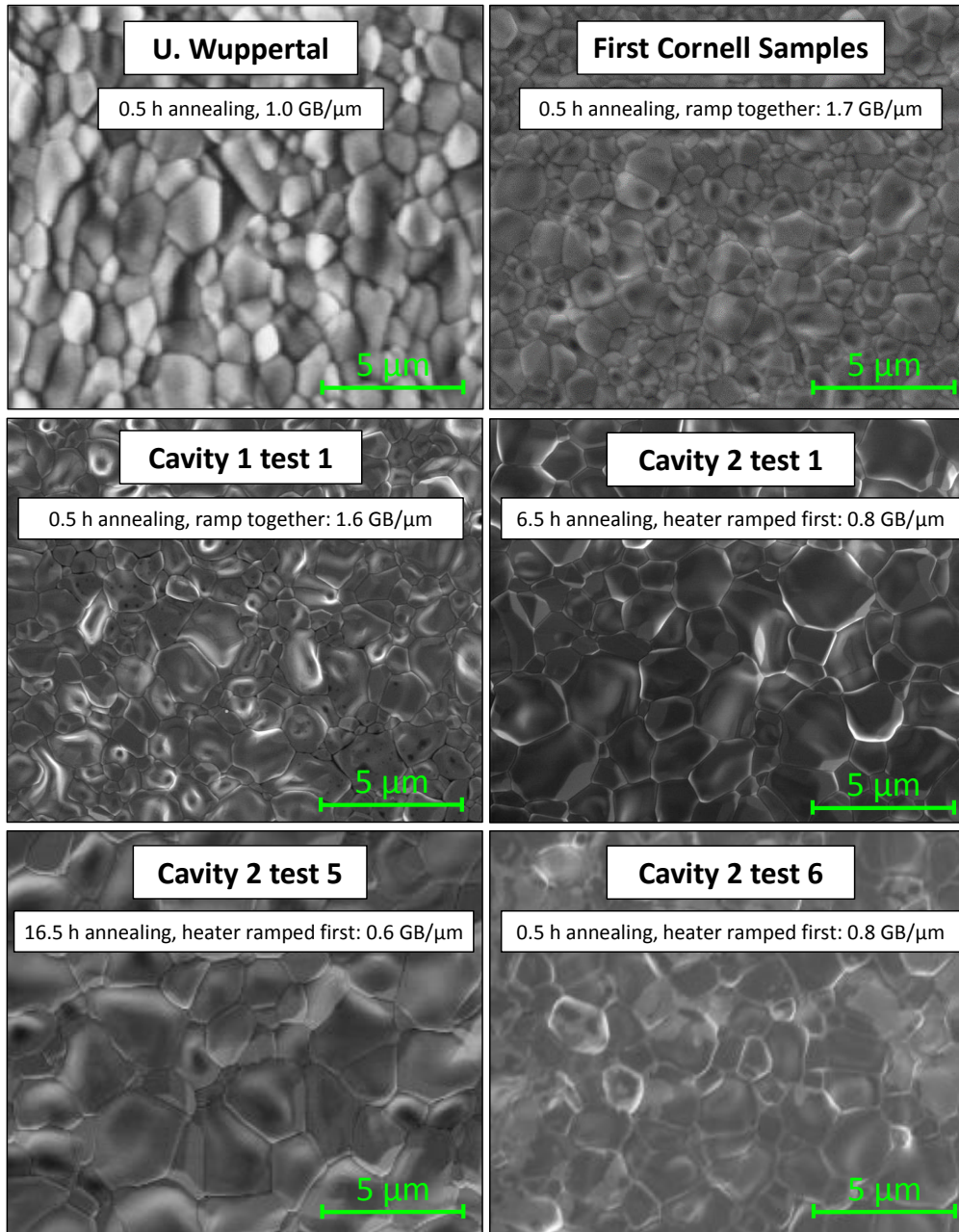


Figure 7.7: SEM images of Nb₃Sn surfaces in samples grown under various coating conditions. Annealing time, the number of grain boundaries per unit length, and the method for ramping up to coating temperature are noted where available. Wuppertal image from [MKM96].

For cavity 1 and for the first samples from [section 5.3](#), after initial nucleation, the furnace temperature was ramped up to coating temperature with minimal power to the tin source heater, so that the two ramped up at the approximately the same temperature. Because cavity 1 appeared to be having problems with Nb₃Sn coverage, for cavity 2, after nucleation, the tin source heater was powered on first. Only once it reached a ΔT of 100-150°C higher than the cavity was the furnace temperature increased. This difference is shown in [Figure 7.8](#).

It is possible that this modification would have prevented the poor performance of cavity 1, but it seems unlikely. The distribution of heating in the T-map and the distinct change in color observed at the equator of the cavity after anodization both strongly suggest that the problem is related to one half cell and not the other. However, it might be the case that this modification causes larger grains to grow, which would be consistent with the small grain sizes observed in cavity 1 and the first samples from [section 5.3](#). It appears that the annealing time also has impact on grain size, as the 16.5 h anneal appears to produce significantly larger grains than the shorter annealing times.

Q vs E curves from 4 coatings of cavity 2 are shown in [Figure 7.9](#), comparing different annealing times. It is difficult to determine from this graph if there is any correlation between annealing time and RF performance.

To analyze the data in greater detail, first R_s was calculated from the Q_0 data as shown in [Figure 7.10](#). Following this, the 2 K curves were fit with a polynomial, as shown in the figure. 2 K is much smaller than $T_c \approx 18$ K, meaning that R_{BCS} should be very small at this temperature. R_{res} should therefore be by far the dominant component, which is supported by saturation observed in Q vs T measurements (see for example [Figure 7.23](#), [Figure 7.28](#), and [Figure 7.31](#)).

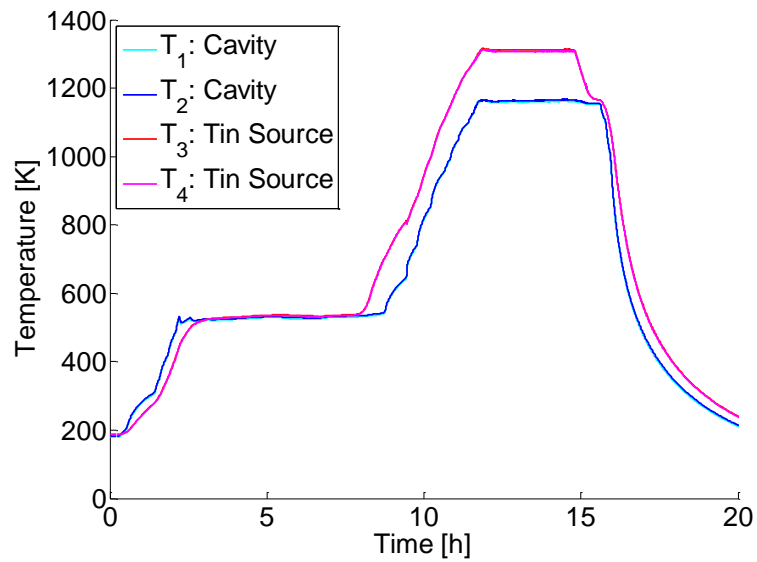
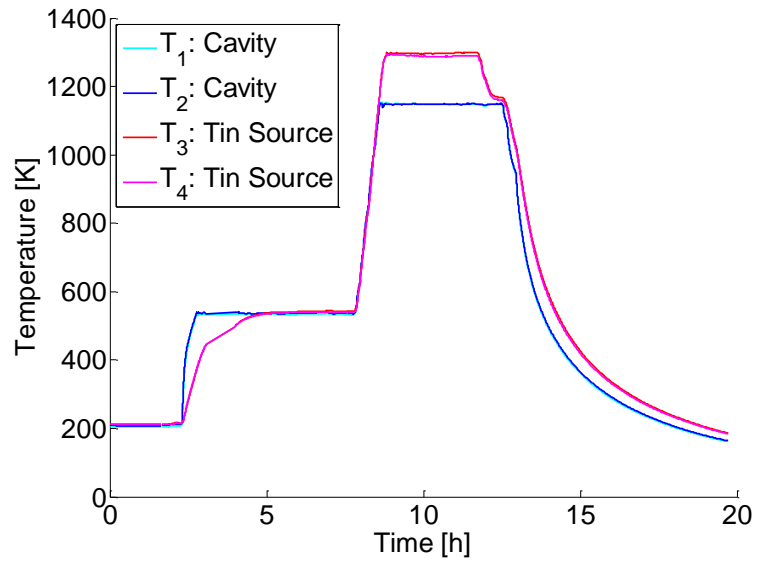


Figure 7.8: Left: original recipe with cavity and tin heater ramped at same rate after 500°C nucleation. Right: modified recipe with tin heater ramped at ~150°C higher than the cavity.

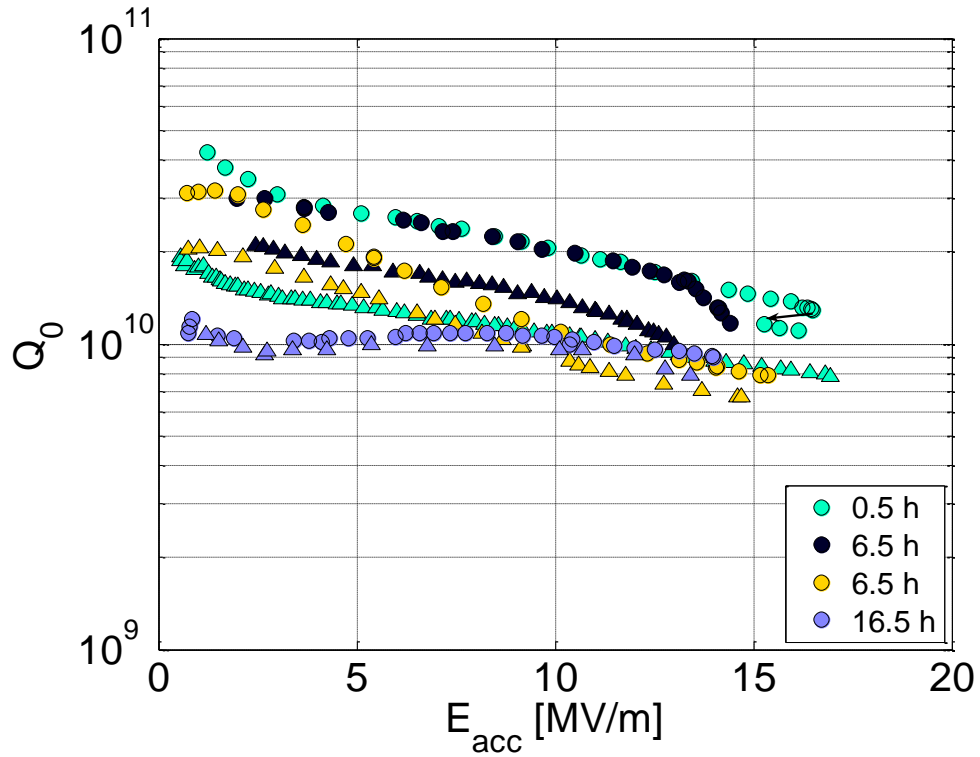


Figure 7.9: Q vs E curves for cavity 2, coated using different annealing times. Circles represent measurements with a 2 K bath temperature and triangles represent 4.2 K.

Therefore, the polynomial fit to the 2 K data should be a good approximation to R_{res} as a function of E_{acc} . Then the 4.2 K data curve can be separated into R_{res} and R_{BCS} components [RG13] using $R_{BCS} = R_s - R_{res}$. The result is shown in Figure 7.11.

It is interesting that R_{BCS} appears to be relatively constant with the modest Q -slope in these tests appearing to be caused primarily by R_{res} . There are several logical candidates for the cause of this increase in R_{res} with field, including weak link grain boundaries (see section 7.5 for discussion), flux trapped during cooldown (see subsection 7.2.6 for discussion), and the standard medium field Q -slope observed in niobium cavities. There appears to be a trend of decreasing R_{BCS} with increasing annealing time. To illustrate this, R_{BCS} was averaged up

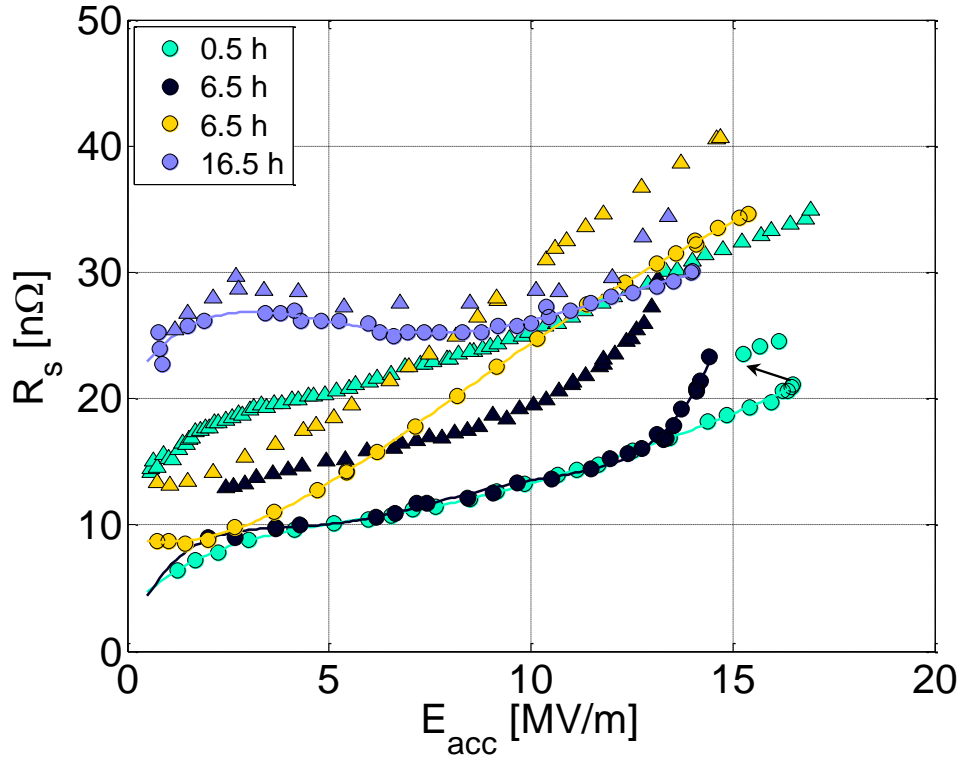


Figure 7.10: R_s vs E curves for cavity 2, coated using different annealing times. Circles represent measurements with a 2 K bath temperature and triangles represent 4.2 K. The 2 K curves were fit to determine R_{res} .

to 10 MV/m for each curve, and the result is plotted as a function of annealing time in Figure 7.12. There also appears to be a trend at low fields of increasing R_{res} with increasing annealing time. However, the magnitude of the modest Q -slope does not appear to depend on annealing time, and it dominates R_{res} above 10 MV/m.

Comparing Figure 7.9 to the corresponding grain sizes in Figure 7.7, it can be seen that the grain sizes from the coatings of cavity 2 are somewhat larger than those for cavity 1 or from U. Wuppertal. It is possible that this larger grain size is related to the lack of Q -slope in these tests, by the mechanisms discussed in section 4.4.

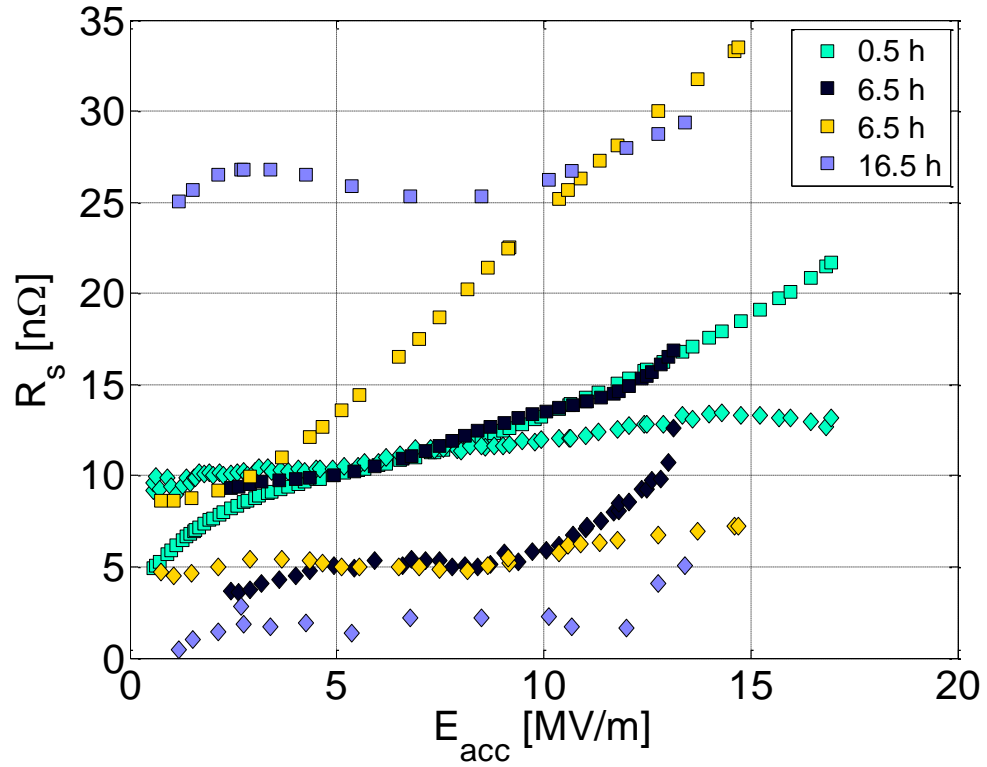


Figure 7.11: Decomposed 4.2 K R_s vs E curves for cavity 2, coated using different annealing times. Squares represent R_{res} and diamonds represent R_{BCS} .

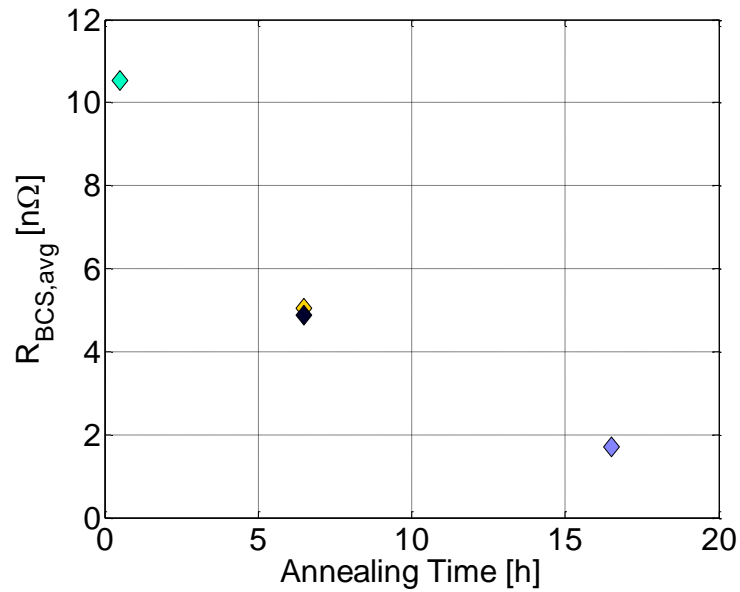


Figure 7.12: Decomposed 4.2 K R_s vs E curves for cavity 2, coated using different annealing times. Squares represent R_{res} and diamonds represent R_{BCS} .

7.2.3 Surface Defects

Several RF tests showed promising performance, reaching medium fields with high Q_0 at 4.2 K, but in each case, quench and modest Q -slope were encountered. In order to guide improvements to preparation, it is important to understand if these limitations are local problems due to surface defects, or if they are global problems over the whole surface.

T-maps are helpful tools for localizing problems, and they were recorded at various fields in most of the CW measurements. Generally, in tests of cavities 2 and 3 immediately after coating (no post-coating chemistry), pre-quench T-maps showed small levels of heating, with some regions showing slightly more heating than others, but with no strongly heating regions that might indicate a defect⁴. A typical example is shown in Figure 7.13.

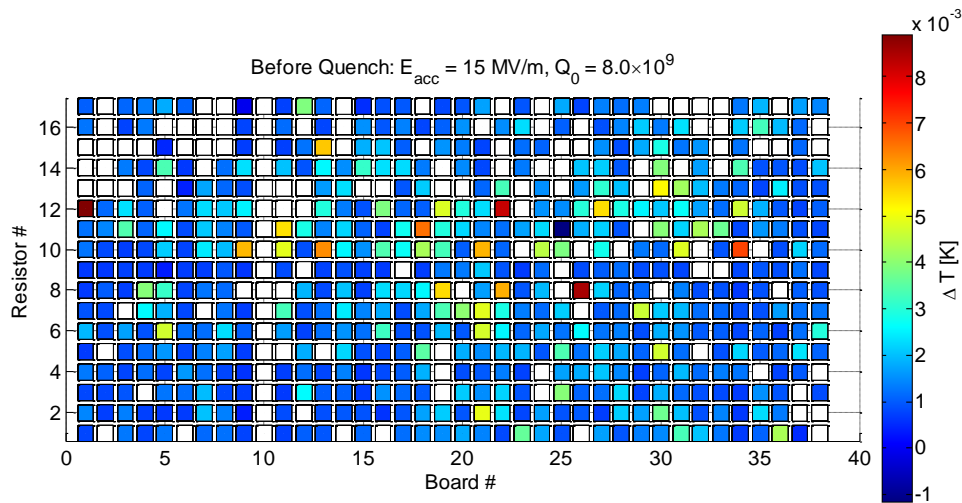


Figure 7.13: Typical T-map showing small levels of broadly distributed heating. Data measured during test 3 of cavity 2.

To study the modest Q -slope observed, T-maps could be compared at differ-

⁴The exceptions to this were the tests where Q -switch occurred at high fields as is discussed later.

ent fields. A T-map at a relatively small field near the maximum Q_0 could be compared to a high field T-map affected by the moderate Q_0 -slope observed in all these tests. [Figure 7.14](#) shows an example of this from cavity 2 test 6. The heating observed in each of the T-map sensors is plotted from a 11 MV/m T-map on the horizontal axis and from a 16 MV/m T-map on the vertical axis. The blue line on the plot shows $\Delta T(16\text{MV/m}) = A_1\Delta T(11\text{MV/m})$ and the red line shows $\Delta T(16\text{MV/m}) = A_1A_2\Delta T(11\text{MV/m})$, where $A_1 = \frac{E_{acc,2}^2}{E_{acc,1}^2}$, $A_2 = \frac{Q_{0,1}}{Q_{0,2}}$, $Q_{0,1}$ is the Q_0 at $E_{acc,1} = 11$ MV/m, and $Q_{0,2}$ is the Q_0 at $E_{acc,2} = 16$ MV/m. The A factors account for the expected ratio of dissipated power predicted by [Equation 2.9](#). Using A_1 alone accounts only for the quadratic dependence on field, and in conjunction with A_2 , it accounts for the change in R_s as well. Since the data seems to agree well with the red line, it seems that a good model for what is occurring is that R_s is changing over the entire T-map, rather than mostly in a few sensors. In other words, the indication is that the Q -slope is a global phenomenon, not one localized to defects.

No field emission was observed in any of the tests. In the tests where quench occurred, no change in the quench field was observed after up to an hour of repeated quenching. After quench, the quality factor would be reduced by a factor of approximately 3-5, likely due to thermocurrents: in the quench region, the temperature spikes to near or above T_c during quench. This creates large thermal gradients across the surface, which generate thermoelectric currents by the Seebeck effect (see [section 6.3](#)). As the quench region cools through T_c and becomes superconducting again, the flux from these currents becomes trapped, producing strong losses under RF fields. The original high Q_0 could be recovered by thermal cycling above T_c .

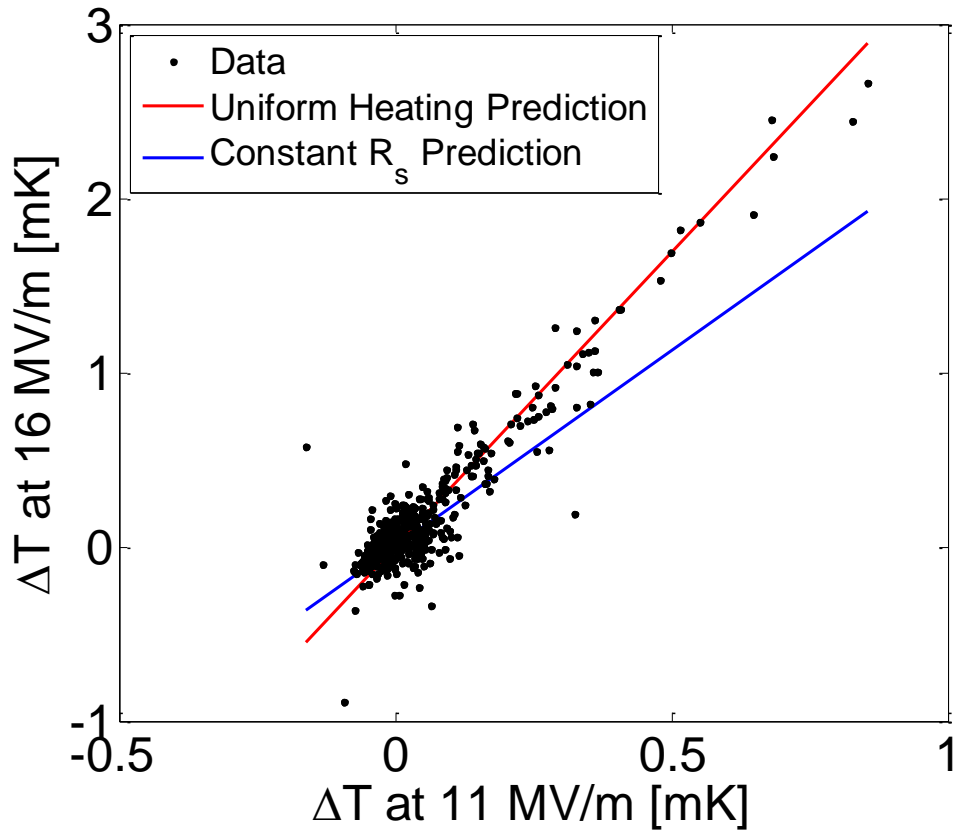


Figure 7.14: Comparison of heating in a T-map at 16 MV/m to a T-map at 11 MV/m. The blue line accounts only for changes in E_{acc}^2 between the two fields and the red line accounts for changes in R_s as well. Data from test 6 of cavity 2. Uncertainty in ΔT is approximately 0.2 mK.

After quench, T-maps would show strong heating in a localized area. An example of this is shown in Figure 7.15. To confirm that this area was the quench location, many readings from the T-map sensors were recorded during the quench, and the duration for which a given sensor had a resistance below a certain threshold—which indicates it had a very high temperature—was recorded (see inset in lower image). The duration that the sensor was warm should be related to its proximity to the quench spot where severe heating was occurring. An example of one of these “quench videos” is also shown in Figure 7.15.

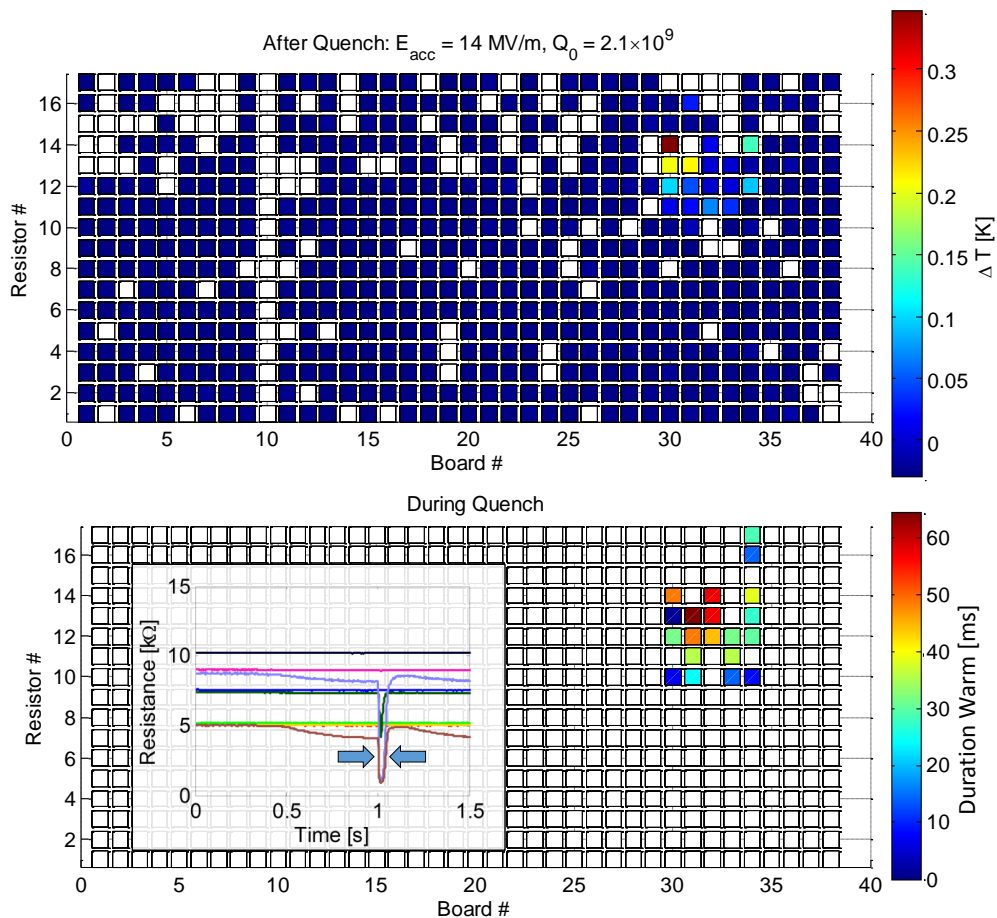


Figure 7.15: T-map after quench (top) and plot of the duration that a given T-map sensor was warmer than a certain threshold during quench (bottom). The inset in the lower image shows examples of data recorded from T-map resistors for a quench that starts at approximately 1 s. Resistors close the quench heat up dramatically, causing a spike in their resistance. The width of the spike is used to make the “video.” Data measured during test 3 of cavity 2.

The quench location was recorded in each test that the cavity was limited by quench. For cavity 2, which was coated multiple times, the quench did not occur in the same location each time, but changed from test to test, as shown in Figure 7.16. Data was recorded during tests 1, 3 and 6. Quench also occurred during test 5, but T-map was not available for that experiment. Quench consistently occurs in the high magnetic field region, showing that they are related to

the magnetic field (see [Figure 6.7](#) for a plot showing both T-map sensor locations and surface magnetic fields). However the quench location is different from test to test. If quench had occurred at the same location on cavity 2 in all the tests, one might suspect a defect in the substrate that remained on the surface even after several rounds of BCP. Instead, the quench location moved by several cm each time, making it more likely that the cause of quench is present in the Nb₃Sn coating.

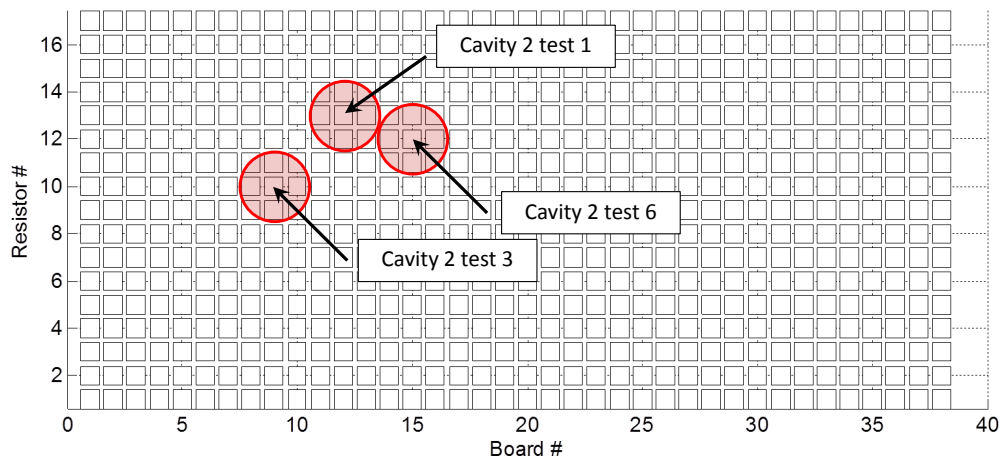


Figure 7.16: Quench locations for cavity 2, presented as an overlay on the temperature map for convenience (board number is arbitrary). The T-map pixels are approximately 1 cm apart.

As discussed in [chapter 2](#), the small ξ of Nb₃Sn makes it vulnerable to even small defects. Examples of possible defects include off-stoichiometric regions (as discussed in [section 7.5](#)) or strongly field-enhancing geometries—the associated grain structure shows significant three dimensional features, as shown in [Figure 7.17](#) (field enhancement factors of 2 or more are possible [SP08]). The T-map results point to defects on the surface as the cause for quench—a local problem, rather than a global problem with the Nb₃Sn layer. Defects would be expected to cause local flux penetration at fields smaller than the predicted H_{shr} as was observed. Additionally, Q -switch was observed just below quench in

tests 1 and 6 of cavity 2, and in test 1 it was accompanied by additional heating on the T-map in the region where quench would later occur. These observations suggest that the limitation is a defect that becomes normal conducting at sufficiently high field when Q_0 switch occurs, and triggers thermal breakdown at slightly higher fields.

This conclusion that the measured maximum fields are limited by defects, rather than reaching a fundamental limit, is supported by the pulsed measurements in [chapter 8](#). Furthermore, though they were operating with smaller Q_0 , both Wuppertal and Siemens cavities reached significantly higher CW fields on the order of 80-100 mT [[MPP+00](#), [Hil80](#)], so the quenches observed in this research program cannot be attributed to a fundamental problem with Nb₃Sn.

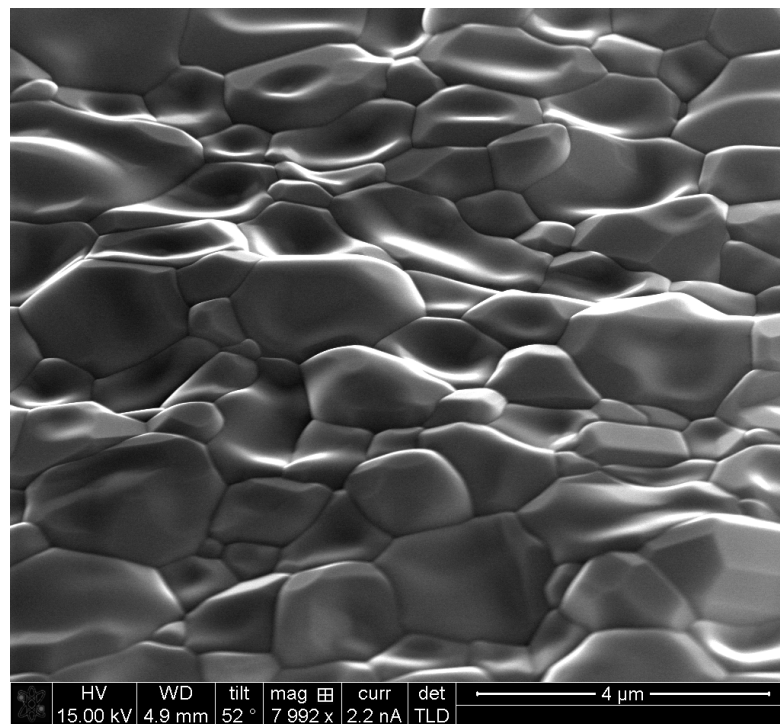


Figure 7.17: SEM image of witness sample tilted at 52° to show three-dimensional features. Some features may act as field-enhancing geometric defects.

This conclusion that the gradient is limited by defects is consistent with

observations by Siemens researchers. They concluded that defects limited the maximum field in their experiments based a statistical analysis of quench fields from many cavity tests, which they found followed a normal distribution [Hil80].

7.2.4 Material Removal After Coating

If a niobium cavity were suspected of having a performance-limiting defect, material removal might be used to try to remove it. The usual processes of BCP and EP would remove too much material for a Nb₃Sn cavity (as the layer is only a few microns thick), so the only option is light removal. The first light material removal process attempted was five cycles of HF rinsing, in which the cavity was immersed in hydrofluoric acid for 2 minutes to remove the oxide, then immersed in water for 5 minutes to regrow the oxide. Five cycles is expected to remove 30-50 nm of material. The desired outcome of this process would be an increase in maximum E_{acc} , Q_0 , or both. However, as Figure 7.18 shows, this resulted in a strong increase in Q -slope.

The action of hydrofluoric acid on Nb₃Sn may be more complicated than with Nb. When HF is applied to Nb, it reacts with the Nb₂O₅ oxide, removing it [Pad09]. However, the oxide of Nb₃Sn will be a different compound. It has been reported that Nb₃Sn is quite resistant against HF [KKS⁺77], but it is not obvious from the literature exactly how HF and the oxide of Nb₃Sn react, or how HF affects the material closest to the surface below the oxide. To investigate the action of the acid, SEM was used to examine samples after HF rinse. The images in Figure 7.19 show that some residue that was not present before HF

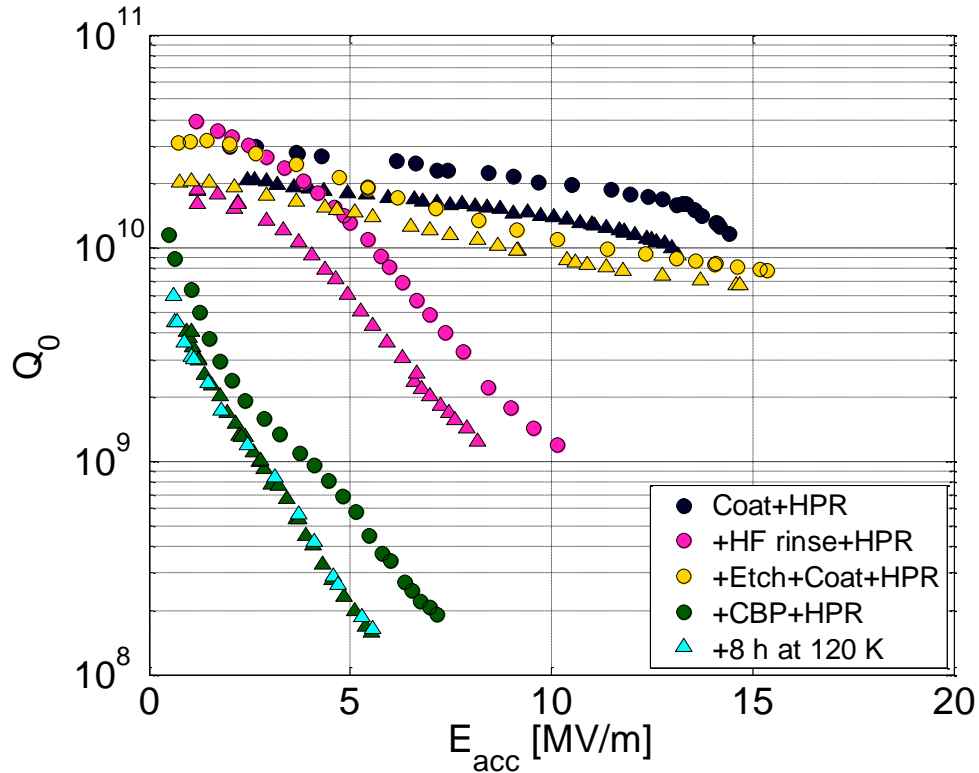


Figure 7.18: Q vs E curves for cavity 2, to which both hydrofluoric acid rinsing and centrifugal barrel polishing were applied after initial coating. Circles represent measurements with a 2 K bath temperature and triangles represent 4.2 K.

rinse appears afterwards. EDX was used to probe the structures, but no sign of contamination was measured, and no change in atomic percent composition of the elements normally observed on the surface (Nb, Sn, O, and a small amount of C). However, the resolution of the tool is on the μm scale, so if the residue is a very thin layer on the surface, EDX is likely unable to resolve it. Auger analysis is planned to achieve higher resolution. It is also not yet known if these residues would be removed by HPR. However, it is possible that they are lossy, and cause the Q -slope observed after HF rinse⁵. For example, there may be different removal rates for Nb and Sn under HF, in which case HF may create regions with relatively high or low tin content, or else it may react and create

⁵Another possible mechanism is discussed in [subsection 7.5.3](#)

for example SnF₂.

The cavity was given BCP to remove the Nb₃Sn layer and coated again and tested. After this test, a different method for light removal was attempted, as chemical removal seemed to be detrimental to performance. Cavity 2 showed strong Q -slope after HF rinse, cavity 1 showed a strong degradation after oxipolishing, and Wuppertal researchers reported a 50% degradation of low field Q_0 and the onset field for Q -slope after light oxipolishing [MKM96]. To try to avoid these problems, mechanical removal was used in this round of testing, via centrifugal barrel polishing. CBP is an industrial mechanical polishing technique in which an abrasive material is placed inside the cavity, and then it is rotated at high speeds. To perform a small amount of material removal, only the finest polishing step of the standard niobium recipe [CCG+13,PCB+13] was used. Figure 7.20 shows the 40 nm colloidal silica with wood blocks that were put into cavity 2 for the 4.5 hour process.

The performance degradation was even stronger after CBP than after HF rinse, as Figure 7.18 shows. An example of a T-map is shown in Figure 7.21, showing that the dissipation was not localized in only one or two areas, but rather was of the same order of magnitude at many different areas in the high magnetic field region. This suggests a global problem as a cause for the Q -slope rather than a defect. One possibility for the source of this Q -slope is Q -disease. It is known that CBP can cause the material on the surface of the cavity to absorb a significant quantity of hydrogen, and hydrogen can form lossy hydrides on the surface of the cavity [PKH08]. After initial testing, the cavity was left at ~120 K overnight to check for Q -disease (this procedure is known to exacerbate the problem in Nb cavities if Q -disease is present), but none was observed,

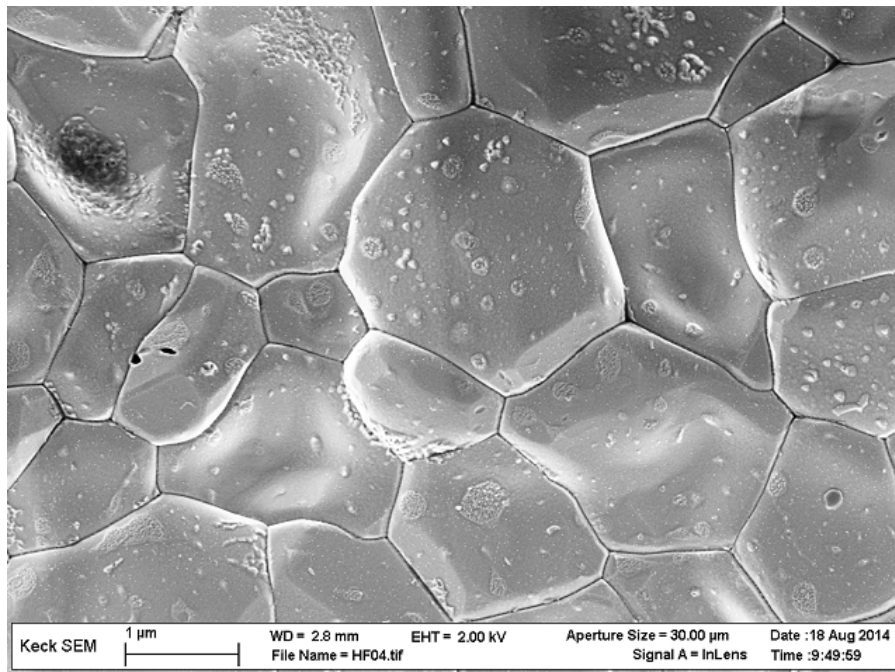
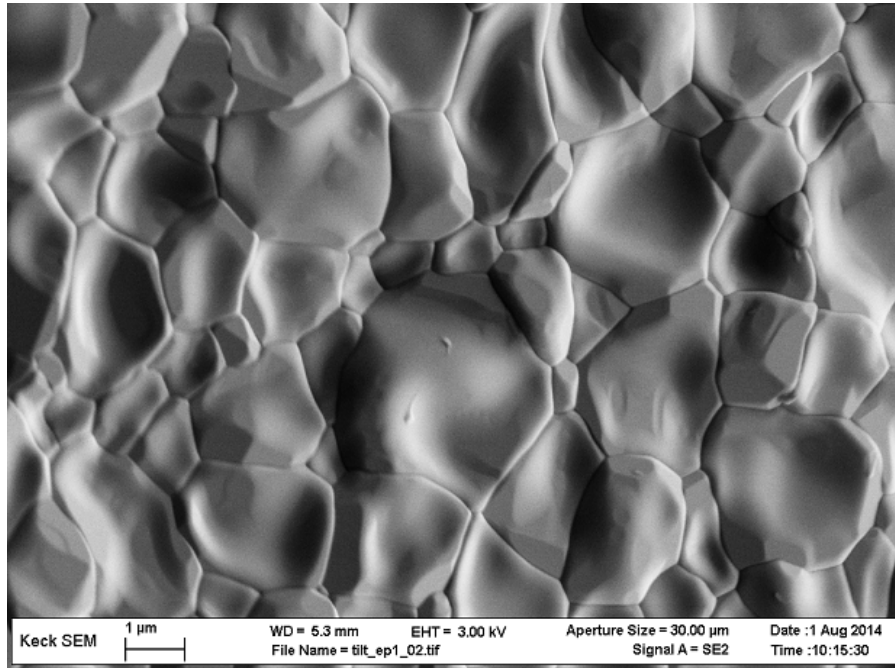


Figure 7.19: Nb₃Sn coated on an EP Nb surface before (top) and after (bottom) HF rinsing. Note the structures found after rinsing.



Figure 7.20: Centrifugal barrel polish machine loaded with Nb₃Sn cavity (left); and polishing media after 4.5 hours (right).

ruling hydrogen out as the cause for Q -slope.

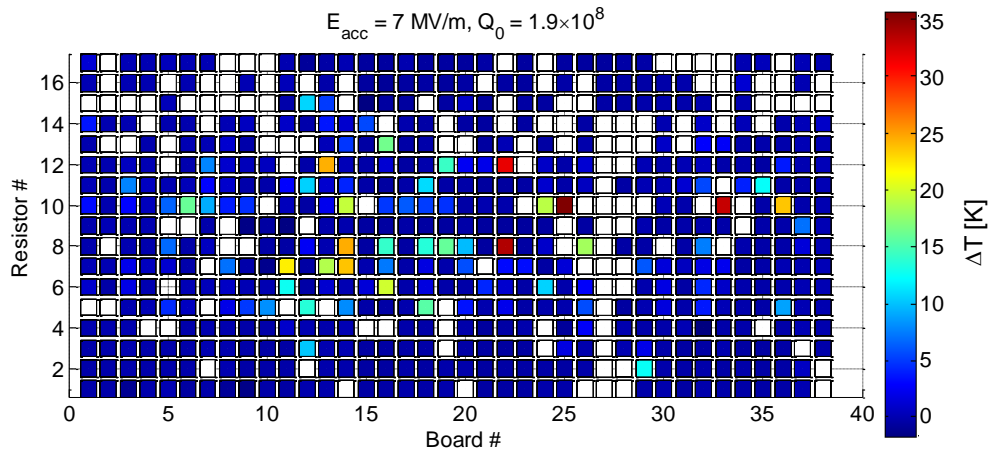


Figure 7.21: T-map after CBP showing heating at many locations in the high magnetic field region.

An unusual temperature dependence was observed in the post-HF rinse and post-CBP tests of cavity 2, so R_s vs E was measured at many different temperatures, as shown in Figure 7.22. There is a clear trend of increasing R_s as the temperature is increased at every field. Since R_{res} is not temperature dependent, one can conclude that it is not the only cause for R_s being higher than what is expected for high quality Nb₃Sn. If R_{res} were the only cause of the strong Q -slope, then one would expect that the higher temperature data would meet the low temperature data at higher fields where the slope is strongest⁶. The strong

⁶Note that some part of the Q -slope at higher fields likely comes from heating since the

temperature dependence even at higher fields suggests that there is a superconductor with poor superconducting qualities on the surface, rather than a normal conductor or a dielectric.

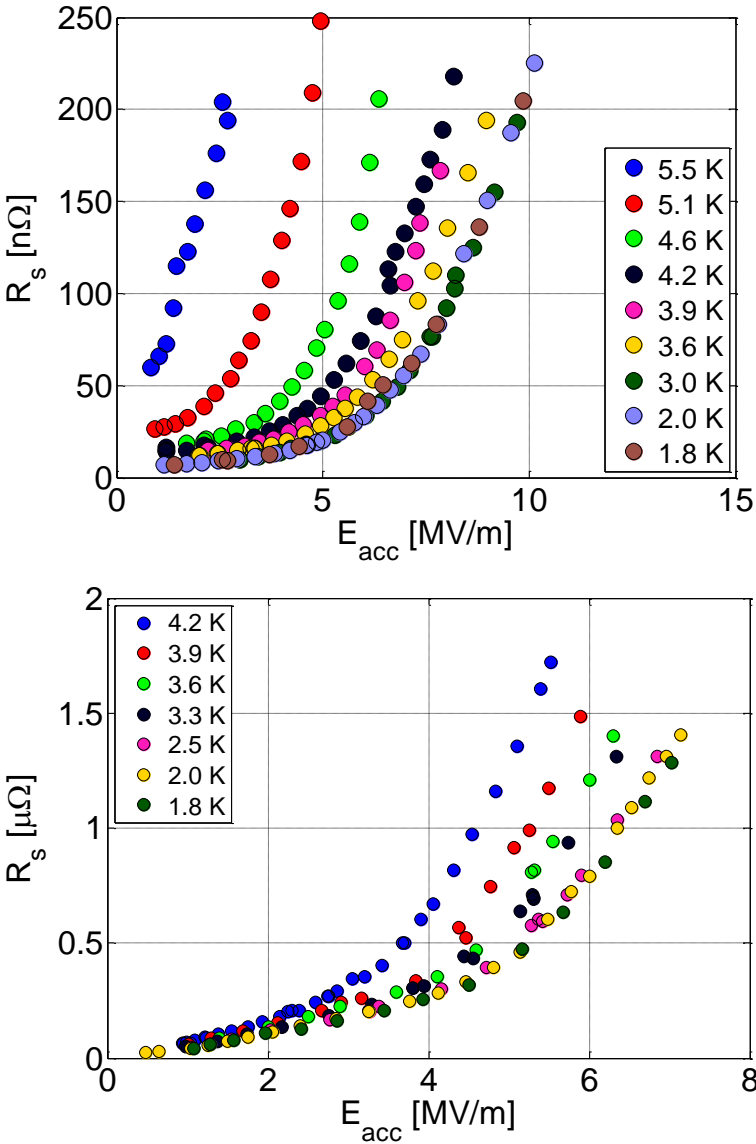


Figure 7.22: R_s vs E at various temperatures after HF rinse treatment (top) and centrifugal barrel polishing (bottom). The strong temperature dependence suggests that R_{res} cannot be the only cause for Q -slope.

Q vs T also changed dramatically after material removal, as shown in Fig-
dissipation is relatively large.

Figure 7.23. Immediately after coating and HPR, Q_0 increases strongly as the cavity is cooled, starting close to T_c (not shown as only PLL measurements are plotted, and it is difficult to lock when Q_0 is very low), and continuing steadily until it saturates as R_{res} begins to dominate over R_{BCS} . However, after HF rinse, the increase in Q_0 with decreasing temperature is significantly slower until approximately 6 K, when Q_0 increases sharply. This effect is even more pronounced after CBP. The sharp change in Q_0 at 6 K resembles a superconducting transition, suggesting that there may be a material in the RF layer with $T_c \approx 6$ K. In section 7.5, a discussion is presented as to what such a material might be.

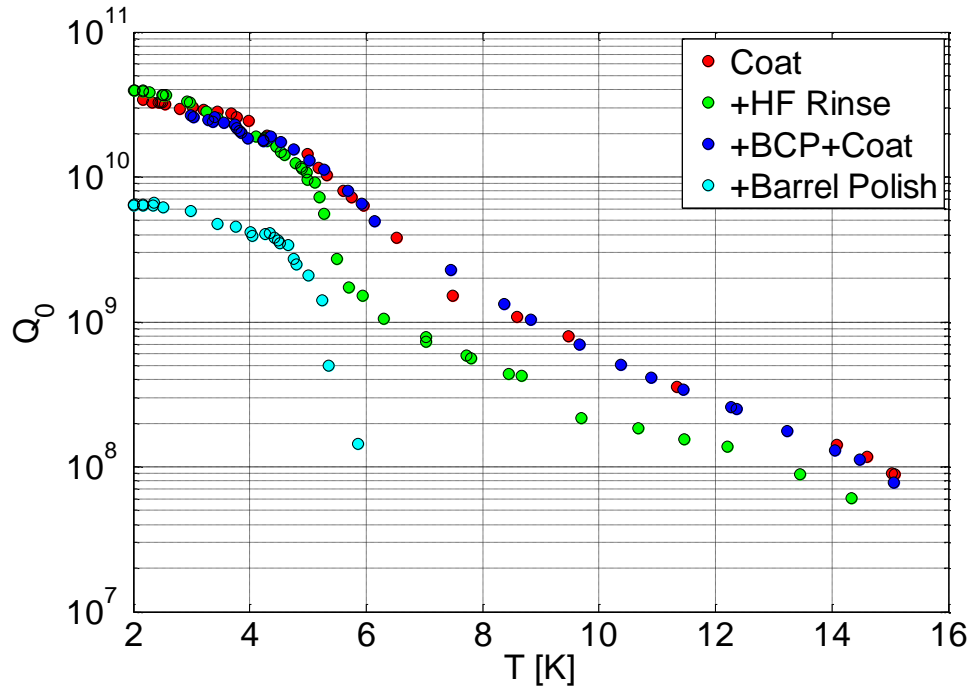


Figure 7.23: After material removal, Q vs T shows a sharp increase just below 6 K, possibly a superconducting transition. Shown are tests 1-4 of cavity 2.

It should be noted that it is unknown if reduction of quench-inducing defects was achieved after material removal from HF rinsing and CBP. The maximum E_{acc} in the post-removal tests was limited by available RF power to fields well below where quench occurred before removal.

7.2.5 Initial Chemistry

Since material removal after coating seemed to degrade performance, EP was used to give a smoother, more defect-free substrate surface before coating, in an attempt to improve the post-coating surface. Cavity 3 was given bulk EP, degas, and light EP, then coating with 6.5 hour anneal. Its performance can be seen in [Figure 7.24](#) compared to cavity 2 test 1, which had a BCP substrate. The low field Q was higher for the cavity with EP substrate, as high as 5×10^{10} at small fields at 2 K, with similar modest Q -slope. The maximum field was approximately the same as with the BCP cavity, around 13 MV/m. More statistics are needed to make conclusive comparisons between EP and BCP substrates, but there does not appear to be a strong effect on the RF performance above 10 MV/m.

Even though the substrate surface would be smoother after EP than a BCP surface, it is possible that the coating process would yield a surface with similar levels of defects regardless, resulting in a similar quench field. It is important to note that this is the first time that Nb₃Sn coating has been applied to a cavity with a surface prepared with modern EP techniques, and cavity 2 was the first Nb₃Sn cavity to be tested after centrifugal barrel polishing. Very little has been tried with Nb₃Sn cavities—it is still at the beginning of development.

7.2.6 Cooldown Rate

As discussed in [chapter 6](#), researchers at U. Wuppertal observed that a slow cooldown through T_c was necessary to achieve high Q_0 , likely due to thermocurrents. They specified a rate of approximately 5 min/K [[PHK⁺88](#)].

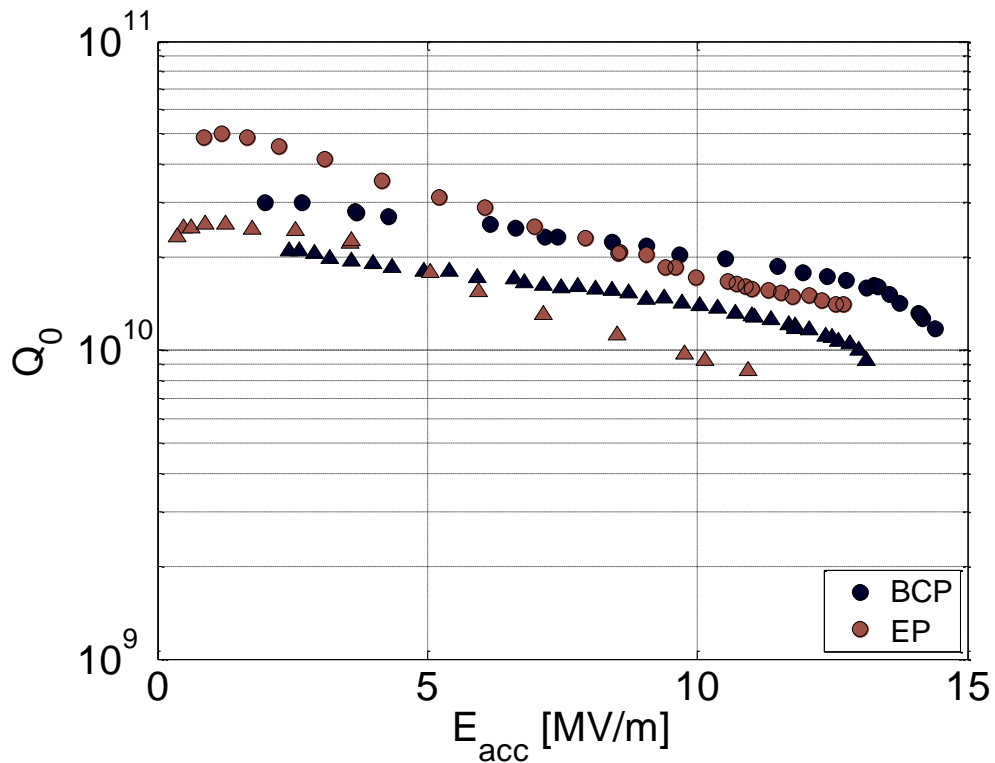


Figure 7.24: Q vs E curves for cavity 2 and cavity 3, both immediately after their first coating, comparing BCP and EP as the method for removal before coating. Circles represent measurements with a 2 K bath temperature and triangles represent 4.2 K.

The effect of cooldown rate was briefly investigated during test 3 of cavity 2. The three different cooldowns are shown in [Figure 7.25](#)-[Figure 7.27](#). Each temperature plot shows the readings from three cernox sensors, one located on the equator, one on the upper half cell, and one on the bottom half cell, each approximately 120° apart from the other two azimuthally. The temperature sensors are read sequentially by a Lakeshore 370 temperature bridge. Each magnetic field plot shows readings from two cryogenic fluxgate magnetometers located on the upper beam tube, one parallel to the cavity axis, the other perpendicular.

The cooling rates going through $T_c=18$ K in each plot are approximately 10 min/K, 2 min/K, and 0.2 min/K. The magnetic field measurements each show

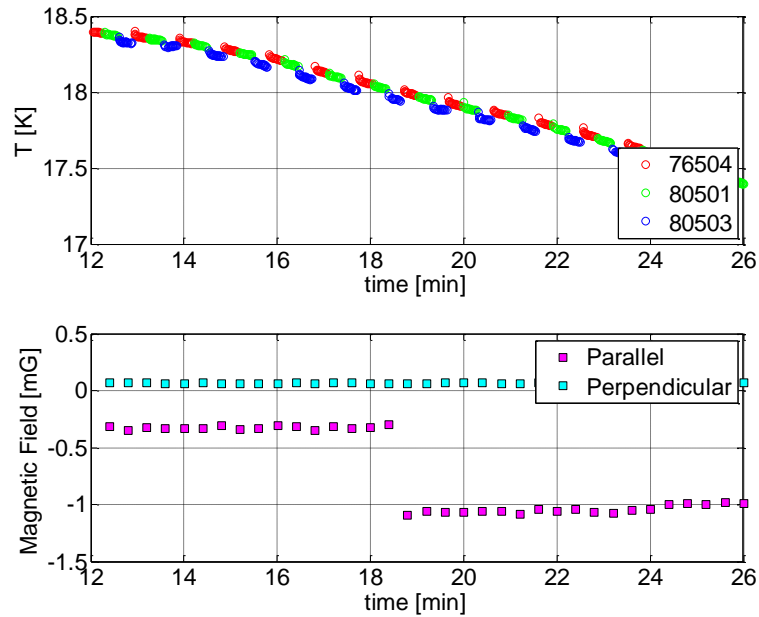


Figure 7.25: Investigation of different cooldown rates, showing measurements from both temperature sensors and magnetic field probes as a function of time. The cooling rate in this plot is approximately 10 min/K.

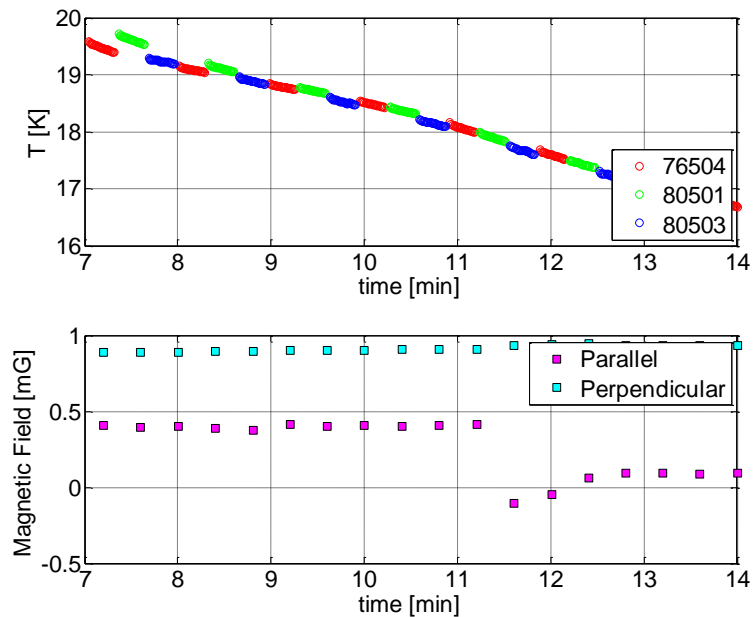


Figure 7.26: Investigation of different cooldown rates, showing measurements from both temperature sensors and magnetic field probes as a function of time. The cooling rate in this plot is approximately 2 min/K.

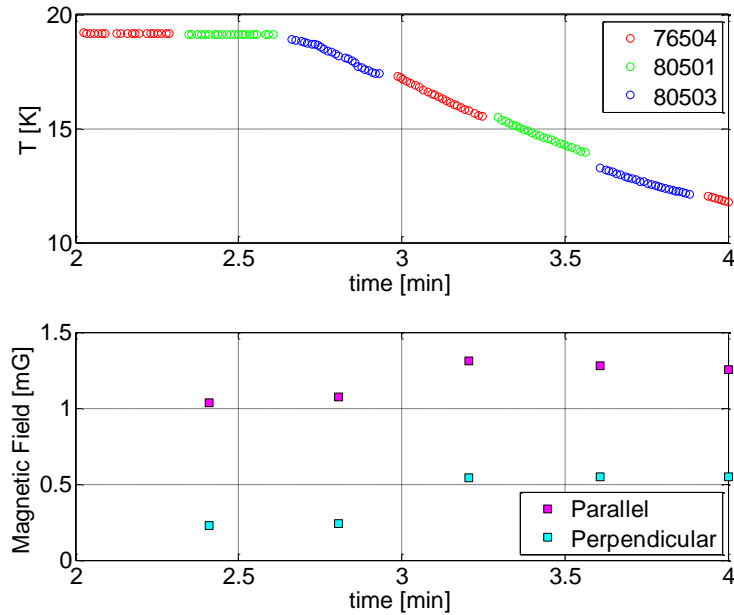


Figure 7.27: Investigation of different cooldown rates, showing measurements from both temperature sensors and magnetic field probes as a function of time. The cooling rate in this plot is approximately 0.2 min/K.

a jump due to expulsion of flux as the cavity becomes superconducting. Figure 7.28 compares R_s vs $1/T$ for each cooldown⁷. There is no significant difference between the 10 min/K and 2 min/K curves. However, the 0.2 min/K cooldown shows a significantly higher R_s at 4.2 K (the rate was maintained as much as possible throughout the cooldown, which was too fast to measure a full Q vs T curve). This cooldown was much faster, and less uniform, with temperature sensors showing a difference between them of approximately 0.5 K, compared with 0.05-0.1 K for the slower cooldowns.

Measurements of copper cavities coated with niobium—another situation involving a metallic film on metallic substrate—show that the spatial temperature gradient is likely the factor that strongly affects R_s , as opposed to the

⁷Here R_s is the weighted average given by G/Q_0 . The graph is presented this way instead of Q vs T to highlight the low temperature region where R_{res} dominates

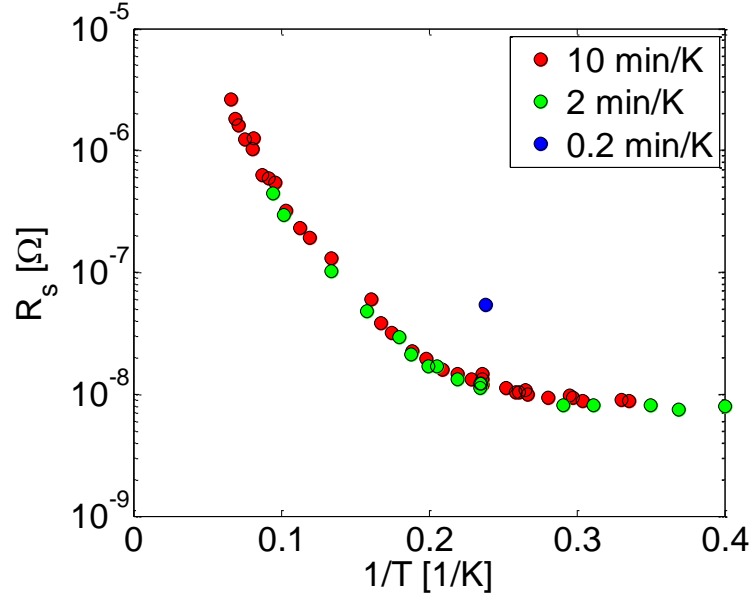


Figure 7.28: Comparison of R_s vs $1/T$ for different cooldown rates.

cooldown rate [Zha14]. This is expected to be the case, as spatial temperature gradients drive thermocurrents, which cause losses, as discussed in section 6.3. The studies on copper cavities reveal that these gradients affect not just the low field R_{res} value, but also the slope of an observed linear increase with field. Spatial temperature gradients during cooldown may also be the source of the linear slope in R_{res} observed in the Nb_3Sn cavity measurements in Figure 7.11. External magnetic fields during cooldown may also play a significant role (for example, [BCC⁺97, BCC⁺99] show how external fields can affect both the low field R_{res} value and the slope with RF field in niobium coated copper cavities). Further studies can determine what cooldown parameters are sufficient to minimize impact on R_s in Nb_3Sn cavities.

7.2.7 Substrate Grain Size

Another important parameter to study is the grain size of the niobium substrate. All of the cavities coated for this study were made from fine grain material (grains on the order of 10-100 μm), but some large grain samples (grains on the order of 1-10 cm) were fabricated for experimenting with different Nb_3Sn coating conditions (they were coated along with fine grain samples, separate from cavity coatings). After coating, these samples showed some structures not observed on fine grain niobium. SEM images show the 1-2 μm sized grains usually observed along with localized “clumps.” These regions, which appear as dark areas with size on the order of 10 μm , have a lower tin content, as measured by EDX, by up to 10 atomic percent. Two images taken from samples coated without the nucleation agent, SnCl_2 , are shown in [Figure 7.29](#) (these structures are also observed on LG samples when coating with SnCl_2).

The high temperature treatment causes significant growth of the Nb grains. Therefore, if relatively large grains in the niobium substrate caused low tin content areas to grow, it would be expected that such regions would occur in substrates that had been recoated after having previously received a coating and a BCP. [Figure 7.30](#) shows the surface of cavity 2 after its first coating was removed by BCP. Grains on the mm scale are visible, whereas the cavity was originally made from material with microscopic grains.

If low tin content areas were present on a recoated Nb_3Sn cavity, they would be expected to have significantly reduced T_c , as shown by [Figure 5.11](#). As a result, one would expect to see a quite poor RF performance. However, the high Q_0 s observed after recoating makes it seem unlikely that there was a significant amount of low- T_c material on the surface. In the future it would be interesting

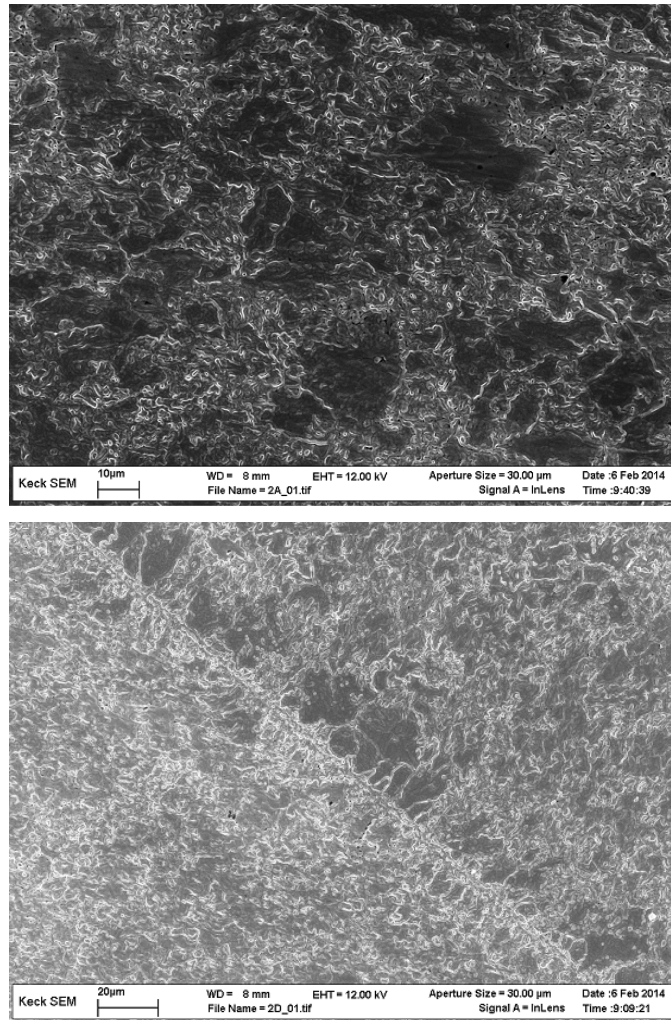


Figure 7.29: Large grain niobium coated with Nb_3Sn appears to have some regions with large “clumps” along with the usual grains. Shown is a sample coated without nucleation agent, both far from (top) and including (bottom) a grain boundary of the LG substrate. The niobium grain boundary’s influence on the grain structure of the Nb_3Sn is clearly observed.

to see if “clumps” appear on fine grain Nb samples that have been through high temperature treatment to grow its grains. It is also possible that some substrates produce a low quality coating for reasons that are not yet clear, as appeared to be the case in one half cell of cavity 1.

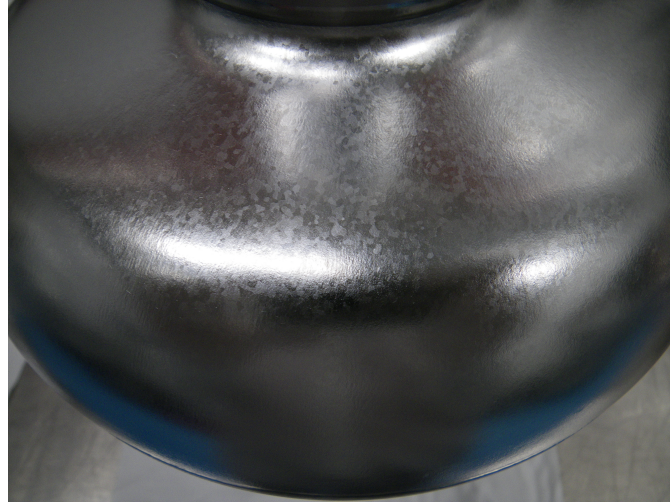


Figure 7.30: Grain growth was observed in the Nb substrate of cavity 2 after its first high temperature coating treatment. In this picture, the cavity had just received BCP inside and out in preparation for re-coating.

7.3 Material Parameters

Material parameters can be extracted from fits to measurements of Q vs T and f vs T (in this case measured at small values of E_{acc}). Q_0 is converted to $R_s = G/Q_0$ (assuming R_s is approximately uniform over the surface) and f is converted to λ using a calculation discussed elsewhere [Val14, Kne74, VCCR99, Cio04]. A program called SRIMP, developed by J. Halbritter [Hal70b, Hal70a], uses BCS theory to calculate R_s and λ as a function of temperature, for given inputs λ_L , ξ_0 , RRR (residual resistance ratio, which is converted to l), T_c , $\Delta/k_B T_c$, as well as a constant offset for each type of fit, λ_0 and R_{res} . To fit, R_s and λ are calculated using

SRIMP at the measured temperatures, then the input parameters are adjusted until the best polymorphic fit is obtained [Val14].

With so many input parameters, a high quality fit can be achieved with many different combinations of parameters; to minimize uncertainty, as many parameters were fixed as possible. T_c was measured in each cavity test, either from Q vs T or f vs T . A typical Q vs T curve highlighting the region near T_c is shown in Figure 7.31. The plot shows measurements from both network analyzer at high temperatures and PLL at lower temperatures, but only PLL measurements were used in fits. Typical values for the clean parameters λ_L and ξ_0 were found in the literature [Hei99].

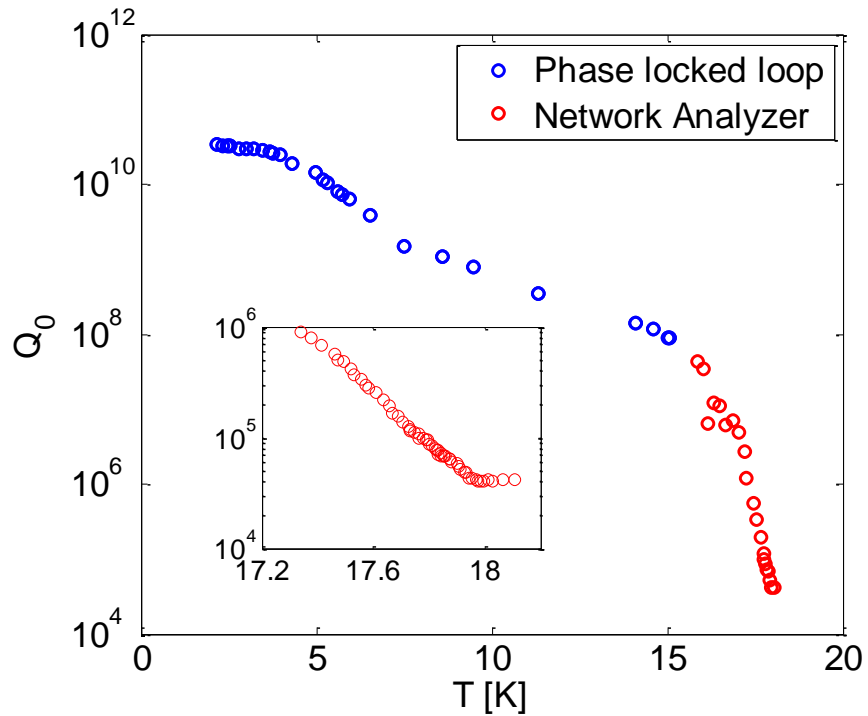


Figure 7.31: Typical Q vs T curve measured using a network analyzer at temperatures near T_c and a PLL at low temperatures.

The remaining parameters to fit are l , the energy gap, and the constant offsets. In order to predict the critical fields with small uncertainty, it is impor-

tant to maximize the reliability of the fit. Therefore a procedure was developed [MPL14] to fit l and energy gap for both sets of the data, then combine the two fits. For each set of data, l and energy gap are fixed at many different values in a reasonable range, and for each pair of fixed values, a fit is performed, varying only the constant offset λ_0 or R_{res} . The residual sum of squares (RSS) from the fit is recorded, as a measure of the fit quality. In this way, an array of RSS values is constructed, with size $N \times M$, where N is the number of fixed values used for l and M is the number of fixed values used for energy gap. Then contour plots are produced using these arrays, normalized to the minimum RSS, as shown in Figure 7.32 (test 6 of cavity 2 is used as an example in this illustration).

The contour plots show what range of values produce the best fits for Q vs T and for f vs T . Q vs T is very sensitive to the energy gap (see equation Equation 2.2) and f vs T is very sensitive to l , so combining the two results in a more reliable prediction of both. The contour plots are therefore averaged to produce a final fit, as shown in Figure 7.33.

The uncertainty in the fit can be determined approximately from the size of the region with small RSS (RSS with values up to 68% higher than the minimum were chosen for 1σ). The resulting fits to Q vs T and f vs T data are shown in Figure 7.34 for the example data set.

Material parameters for test 6 of cavity 2 are shown in Table 7.2, along with their derivation. Based on these parameters, the critical fields of the superconductor were also calculated and included in the table.

Parameters extracted this way from the five RF tests of cavities 2 and 3 without post-coating removal are shown in Table 7.3. There is some variation from

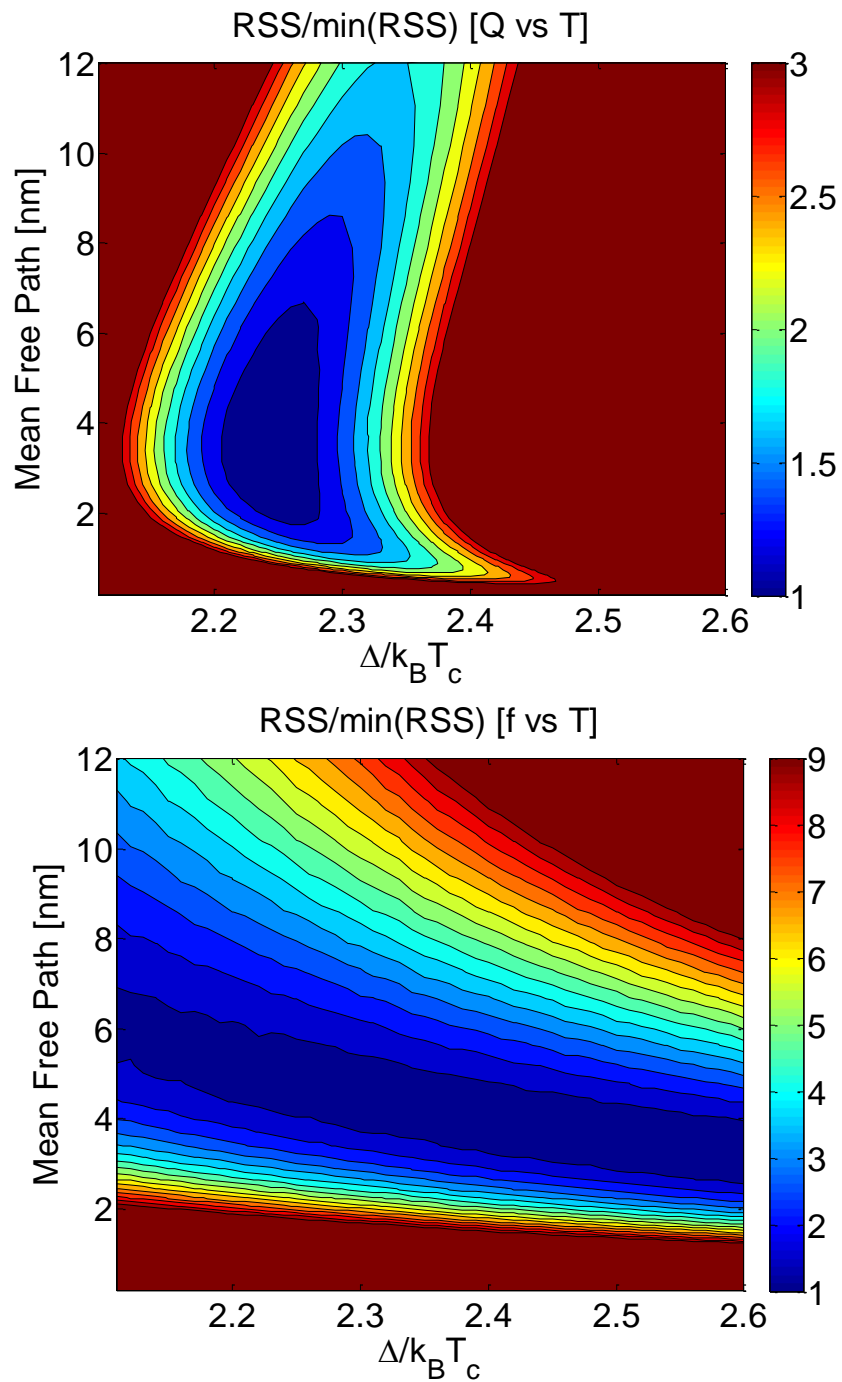


Figure 7.32: Contour plots of 1-parameter fits to Q vs T (top) and f vs T (bottom) measurements. The plots show how combining the two measurements can result in less uncertainty in extraction of $\Delta/k_B T_c$ and l . Data from cavity 2 test 6.

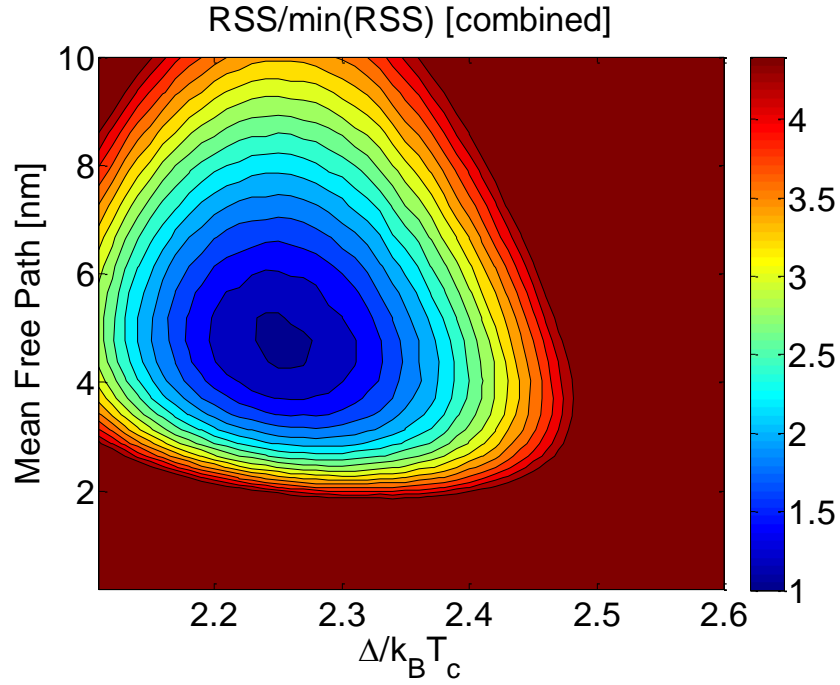


Figure 7.33: Combined contour plot isolating a far smaller region of parameter space than either Q vs T or f vs T alone.

Table 7.2: Measured and calculated properties of the Nb₃Sn film from cavity 2 test 6

Property	Value	Derivation
$\lambda_L(0)$ [nm]	89 ± 9	[Hei99], 10% uncertainty assumed
$\xi_0(0)$ [nm]	7.0 ± 0.7	[Hei99], 10% uncertainty assumed
T_c [K]	18.0 ± 0.1	observed from f vs T
$\Delta/k_B T_c$	2.25 ± 0.12	combined fit to Q vs T and f vs T
l [nm]	4.8 ± 2.0	combined fit to Q vs T and f vs T
R_{res} [n Ω]	8.5 ± 1.2	combined fit to Q vs T and f vs T
$\lambda(0)$ [nm]	139 ± 23	$\lambda_L \sqrt{1 + \frac{\xi_0}{l}}$ [Tin04]
$\xi(0)$ [nm]	3.4 ± 0.5	$0.739 \left[\xi_0^{-2} + \frac{0.882}{\xi_0 l} \right]^{-1/2}$ [OMFB79]
$\kappa(0)$	41 ± 9	λ/ξ [Tin04]
$\mu_0 H_c(0)$ [T]	0.49 ± 0.10	$\frac{\phi_0}{2\sqrt{2}\pi\lambda\xi}$ [Tin04]
$\mu_0 H_{c1}(0)$ [mT]	36 ± 3	$\frac{\phi_0}{4\pi\lambda^2} (\ln \kappa + 0.5)$ [Hei99]
$\mu_0 H_{c2}(0)$ [T]	28 ± 9	$\frac{\phi_0}{2\pi\xi^2}$ [Tin04]
$\mu_0 H_{sh}(0)$ [T]	0.41 ± 0.09	$\mu_0 H_c \left(\frac{\sqrt{20}}{6} + \frac{0.5448}{\sqrt{\kappa}} \right)$ [TCS11]

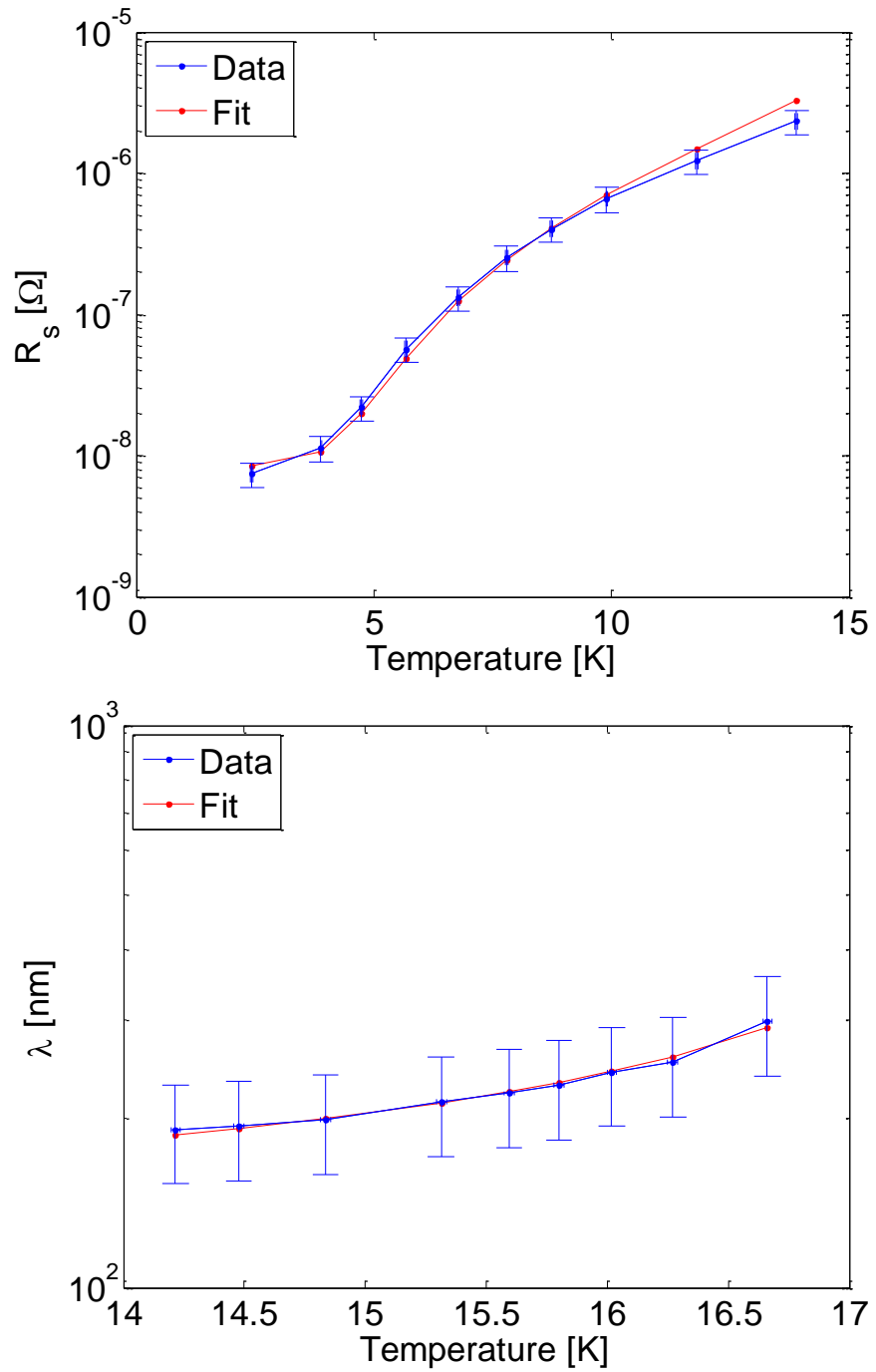


Figure 7.34: R_s vs T and λ vs T data from cavity 2 test 6 with best fit shown.

test to test in the parameters, but overall, they are fairly consistent, and they each give critical fields that are in the same range.

Table 7.3: Comparison of extracted parameters and critical fields from five cavity tests

Property	Cavity 2 Test 1	Cavity 2 Test 3	Cavity 2 Test 5	Cavity 2 Test 6	Cavity 3 Test 1
T_c [K]	18.0 ± 0.1				
$\Delta/k_B T_c$	2.5 ± 0.2	2.5 ± 0.2	2.6 ± 0.2	2.25 ± 0.12	2.5 ± 0.2
l [nm]	3.0 ± 1.0	1.7 ± 1.0	2.4 ± 1.0	4.8 ± 2.0	1.7 ± 1.0
R_{res} [n Ω]	9.5 ± 1.5	10.3 ± 1.2	21 ± 2	8.5 ± 1.2	7.2 ± 1.0
$\lambda(0)$ [nm]	161 ± 25	198 ± 50	174 ± 32	139 ± 23	198 ± 50
$\xi(0)$ [nm]	3.0 ± 0.4	2.4 ± 0.6	2.8 ± 0.4	3.4 ± 0.5	2.4 ± 0.6
$\kappa(0)$	54 ± 11	82 ± 28	63 ± 16	41 ± 9	82 ± 28
$\mu_0 H_c(0)$ [T]	0.49 ± 0.10	0.48 ± 0.17	0.49 ± 0.12	0.49 ± 0.10	0.48 ± 0.17
$\mu_0 H_{c1}(0)$ [mT]	29 ± 2	21 ± 2	25 ± 2	36 ± 3	21 ± 2
$E_{\text{acc}} _{B_{pk}=\mu_0 H_{c1}(0)}$ [MV/m]	6.8 ± 0.5	4.9 ± 0.5	6.0 ± 0.5	8.5 ± 0.7	4.9 ± 0.5
$\mu_0 H_{c2}(0)$ [T]	37 ± 11	56 ± 27	43 ± 15	28 ± 9	56 ± 27
$\mu_0 H_{sh}(0)$ [T]	0.40 ± 0.08	0.39 ± 0.13	0.40 ± 0.10	0.41 ± 0.09	0.39 ± 0.13
$E_{\text{acc}} _{B_{pk}=\mu_0 H_{sh}(0)}$ [MV/m]	95 ± 19	93 ± 32	94 ± 23	97 ± 21	93 ± 32

T_c , measured via f vs T or Q vs T , appears to be very reproducible from coating to coating and it is in agreement with the value measured on the sample in [section 5.3](#). l values also are close together, within uncertainty. These l values are considerably smaller than ξ_0 , indicating that the Nb₃Sn produced acts as a relatively dirty superconductor.

$\Delta/k_B T_c$ falls within a range from approximately 2.2 to 2.6, well above the minimum expected for strong coupling behavior [[God06a](#)]. Point contact tunneling measurements of the energy gap of high Sn content Nb₃Sn generally give values in the range of 2.0-2.3 [[MZR79](#), [RB84](#), [God06a](#), [GGB+04](#)], which agrees with the PCT sample measurement in [section 5.3](#), but is somewhat smaller than the values extracted from RF measurements. However, point contact tunneling is

expected to give a somewhat smaller gap at the interface than in the bulk, underestimating the bulk value [God06a, GGB⁺04]. It is interesting that the measured values agree well with the value of 2.45 ± 0.02 measured by Guritanu et al. [GGB⁺04], who postulate two gaps based on specific heat measurements.

λ , ξ , κ and the critical fields can vary from sample to sample, depending on the tin content and impurity content, so it is difficult to compare directly to literature. However, the values in this table are of the same order as those measured in other work (for example [Hei99, KKS⁺77, GGB⁺04, God05]).

Of particular interest of the derived values is H_{sh} , which has been measured to be the ultimate limit of SRF for niobium [Val14], and is predicted to be the ultimate limit for Nb₃Sn as well. The H_{sh} values extracted in the table are in each case approximately 400 mT, roughly twice that of niobium. This is very promising for high field applications. If these fields could be realized, it would allow linear accelerators to be significantly shorter to reach a given energy than they would be using niobium cavities.

In Figure 5.18, a measurement of H_{c2} of a sample was presented. The measured $\mu_0 H_{c2}(T = 0K) = 17.9$ T is somewhat lower than that predicted from RF test data. The correlation from Godeke [God06a] in the figure shows that in fact measured H_{c2} values increase quickly as tin content increases from 19%, then level off and drop as the tin content approaches 24.5%. As discussed in chapter 2, this drop is attributed to the shift of the lattice from cubic to tetragonal crystal structure at high tin content and low temperature. It is possible, however, that l and therefore ξ continues to decrease as the tin content increases, which would cause a large prediction for H_{c2} from Equation 2.6 (for example if ξ_0 changes with composition from the value used in calculations).

The fits to RF measurements yield $H_{c1}(T = 0\text{K})$ values in the range of 20-40 mT. To confirm that this range of values represents the H_{c1} of the material, this critical field was determined on samples using an alternative method. A Nb_3Sn sample was coated at Cornell using the same procedure used on cavities, and then sent to TRIUMF for measurements using muon spin rotation ($\mu\text{-SR}$) by R. Laxdal. In this measurement, spin-polarized muons are implanted approximately 200 μm deep into the coated sample. The sample sits in an applied magnetic field at a given temperature. At this temperature, if the magnetic field penetrates into the bulk of the sample where the muons are located, it will cause their spin to precess. Positron detectors located around the sample determine the distribution of the decay positrons. If there is a high degree of asymmetry in the decay positrons, it indicates that Meissner screening has prevented the magnetic fields from penetrating. If the asymmetry is close to zero, it indicates that the magnetic fields have caused the muon spins to precess [GBK⁺13]. This measurement gives an upper bound on H_{c1} (pinning and superheating can affect the result). Figure 7.35 shows an image of the sample measured (which is ellipsoidal with a known demagnetization factor), and Figure 7.36 shows the measurements performed at several different fields and temperatures⁸. The measured upper limit for $\mu_0 H_{c1}(T = 0\text{K})$ of the Nb_3Sn layer is approximately 31 mT, which agrees well with the values in Table 7.3 [Lax14].

⁸Only temperatures above expected T_c of niobium are shown. At low temperatures, Nb provides shielding to relatively high fields; at temperatures above T_c of niobium, Nb_3Sn shell provides shielding. Data to be published elsewhere.



Figure 7.35: Ellipsoidal sample used to measure H_{c1} of Nb_3Sn coating using μ -SR at TRIUMF.

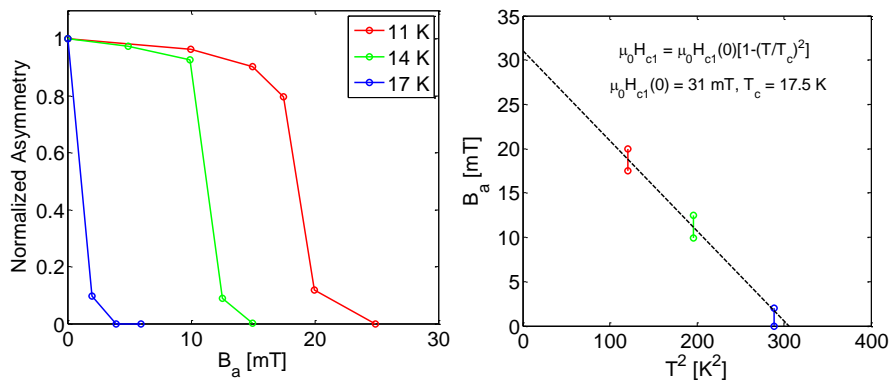


Figure 7.36: Left: μ -SR measurement showing corrected normalized asymmetry as a function of applied field. For asymmetry values close to 1, implanted muons are shielded from the external field; for values close to 0, the muons are exposed to penetrating fields. Right: Approximate fit to determine $H_{c1}(0)$ from fields at each temperature above and below flux penetration.

7.4 Flux Penetration at H_{c1}

As discussed in [chapter 4](#), there had been speculation that the strong Q -slope observed in previous 1.5 GHz Nb₃Sn cavities was caused by a fundamental loss mechanism that occurred above H_{c1} , such as bulk vortex dissipation [[BKM⁺97](#), [Gur06](#)]. This idea can be tested with the critical fields extracted from fits to material parameters in [Table 7.3](#), which are supported by direct measurement of H_{c1} from μ -SR. For each of the tests in the table, the cavity reached fields far above H_{c1} with no strong Q -slope (this takes into account uncertainty from measurement and fitting), and with no indication of degradation near the extracted H_{c1} other than the moderate Q -slope that was present at lower fields. For illustration of this, Q vs B is plotted for several cavities in [Figure 7.37](#), along with H_{c1} extracted with uncertainty.

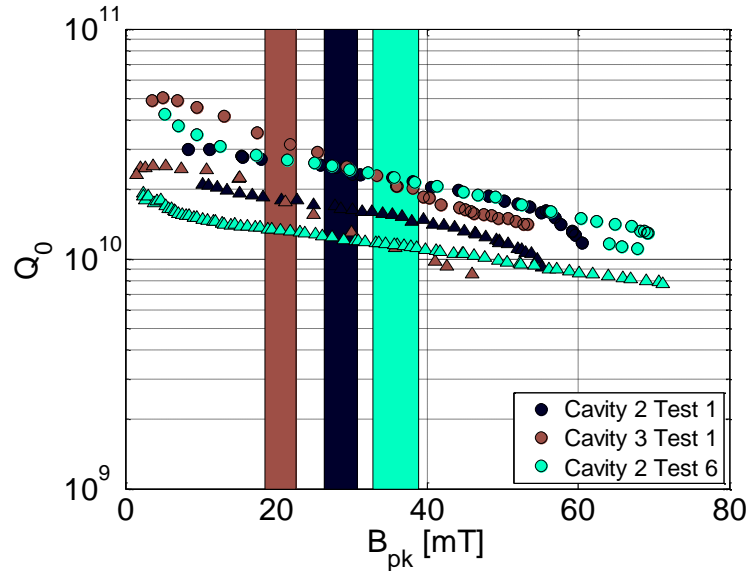


Figure 7.37: Q vs B for selected cavities from [Table 7.3](#). $\mu_0 H_{c1}$ is plotted by color using rectangles that cover the range given by value with uncertainty. In each test from the table, H_{c1} is significantly exceeded without strong Q -slope showing that it is not a fundamental limit.

This result shows that H_{c1} does not represent a fundamental limit for Nb₃Sn.

The energy barrier allows the material to operate in the metastable state even with its somewhat small ξ . This conclusion is extremely important not just for Nb₃Sn, but also for the field of alternative superconductors for SRF. As shown in [Table 2.2](#), these materials also have relatively small ξ , making them potentially vulnerable to flux penetration in the metastable state, and they also tend to have relatively small H_{c1} . This result is encouraging for operating SRF cavities coated with NbN, MgB₂, and other materials at useful fields above H_{c1} in the metastable state.

The small ξ may still be the cause for quench at fields below H_{sh} . However, so far only as-coated surfaces and surfaces degraded by material removal have been tested. Additional research can develop a preparation that produces a more defect free surface. Since H_{c1} is not a fundamental limit, a higher quality surface can be expected to reach higher fields in the metastable state.

7.5 Alloys with Low Tin Content

In [subsection 7.2.4](#), temperature dependence after material removal was studied, and it was shown that the measurements are consistent with there being a superconductor present in the RF layer with $T_c \approx 6$ K. [Figure 5.11](#) presents a plot of T_c vs tin content of Nb₃Sn, which at tin contents below approximately 20 atomic percent gives a T_c of approximately 6 K. This makes low tin content alloys in the RF layer a likely candidate for being the source of the unusual temperature dependence after material removal.

Material with a T_c of 6 K would be sensitive to overheating with increasing P_{diss} at higher B_{pk} . Additionally, a low quality superconductor would likely have

a lowered H_{shr} , making it more sensitive to flux penetration at lower fields. A combination of these two factors could cause volumes containing this material to be driven normal conducting at relatively small fields. If more and more of these regions became normal conducting while the rest of the cavity stayed superconducting and thermally stable, it could cause the Q -slope observed in tests.

7.5.1 Weak Link Grain Boundaries

If low tin content alloys were the cause of Q -slope, the next question would be where they are located. [chapter 4](#) presented a discussion of the hypothesis that weak link grain boundaries were the cause of Q -slope observed in U. Wuppertal's cavities, and showed a summary of their experiments with different grain sizes that showed results consistent with this hypothesis. One possibility is that the grain boundaries contain low tin content alloys. Transport of tin into the depth of the layer is primarily accomplished by grain boundary diffusion in certain regimes [[Far74](#), [Hil80](#)]. It might be possible for this process to cause tin to become depleted in the grain boundaries.

If this were the case, then one may expect altering the grain structure to alter RF performance. One example of such an alteration might be material removal by HF rinse or CBP. This might cause the grain boundary width to increase appreciably compared to ξ , increasing weak link behavior. An example of an alteration that might be beneficial is annealing to grow grains. This could have several effects: 1) it would decrease the number of grain boundaries, which should improve RF performance if these regions are lossy 2) the extra annealing

time could affect the tin content in the grain boundaries 3) the longer anneal was observed to cause strengthening of the grain boundaries at Siemens (see [Figure 4.8](#)).

In RF testing, the annealing time was varied by many hours, which changed the grain size appreciably (see [subsection 7.2.2](#) for details). There was no clear trend observed in the quench field, but [Figure 7.11](#) and [Figure 7.12](#) show that there is some trend of R_s with annealing time. In addition, there a linear increase in R_{res} with field, which is consistent with some models of weak link grain boundaries [[Mu89](#), [BS91](#), [PKH08](#)]. However, the strong Q -slope observed in U. Wuppertal's tests was not observed in any of the tests immediately after coating, in spite of using the times and temperatures specified by Wuppertal for the shortest annealing time. It is not clear why this is the case, and without a direct comparison, it is difficult to make any conclusions on the effect of annealing time on strong Q -slope. However, it is possible to use microscopic investigations to check for the presence of low tin content regions.

7.5.2 SEM/EDX

To check for the presence of low tin content alloys in grain boundaries, a line scan was performed using EDX to observe the change in composition across a grain boundary. The results are shown in [Figure 7.38](#). The counts measured for Nb and Sn are smaller in the grain boundary, but no significant change in the relative abundance is observed. However, the EDX excitation volume, on the order of 1 cubic micron, is relatively large compared to the size of the grain boundary, which is expected to have width on the order of the lattice parame-

ter, approximately 0.5 nm (see [section 4.1](#)). As a result, EDX may not have the resolution required for this measurement.

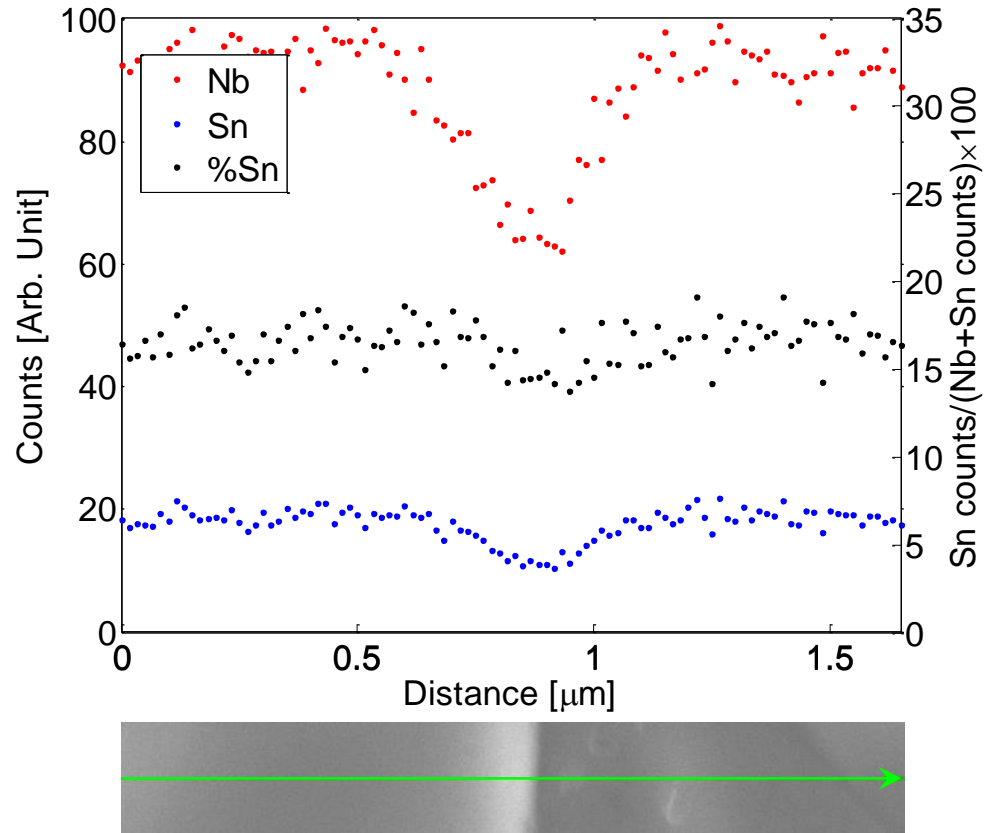


Figure 7.38: EDX line scan across a grain boundary. No significant change in the relative abundance is observed.

7.5.3 TEM

Transmission Electron Microscope (TEM) studies on a Cornell Nb₃Sn witness sample (witness for the first coating of cavity 2) were carried out by T. Proslie and R. E. Cook at Argonne National Lab. They were able to obtain electron-transparent samples many microns across, exposing the entire depth of the Nb₃Sn layer and part of the Nb layer beneath. They also performed high resolution elemental analysis with EDX. In [Figure 7.39](#) and [Figure 7.41](#), two regions

studied are shown under STEM bright field. The cross sectional view shows the exterior surface on one side of the image, and the Nb bulk on the other side, with the Nb₃Sn layer between. Figure 7.40 and Figure 7.42 show EDX area maps for Nb and Sn, measured using the x-ray L-edges. Brighter colors indicate a higher atomic concentration.

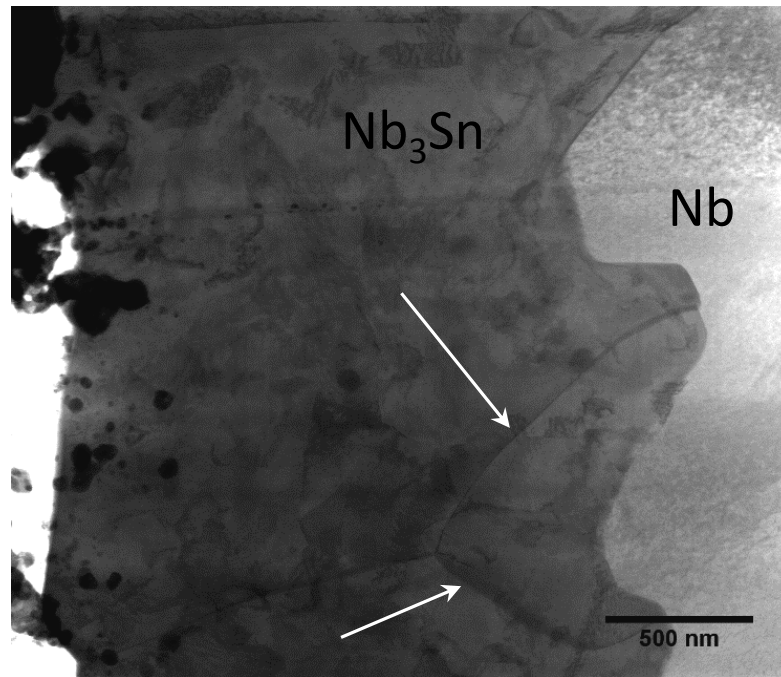


Figure 7.39: STEM bright field image of region A of the TEM sample measured at ANL. This is a cross section of the material, with exterior surface is the left and niobium bulk on the right. Grain boundaries are highlighted with arrows. The black spots near the surface are silver which was sputtered on the surface as part of the FIB process.

There are many interesting features in these images that provide useful information about the Nb₃Sn coatings produced at Cornell. The images resemble the FIB image from Figure 5.13, but with much better ability to resolve details. First, observe that there are several lines on each of the STEM images, some of which are highlighted with white arrows. These are most likely Nb₃Sn grain boundaries. Observe from the EDX area maps that close to the Nb bulk, these regions are tin depleted (darker green) compared to nearby areas, and niobium

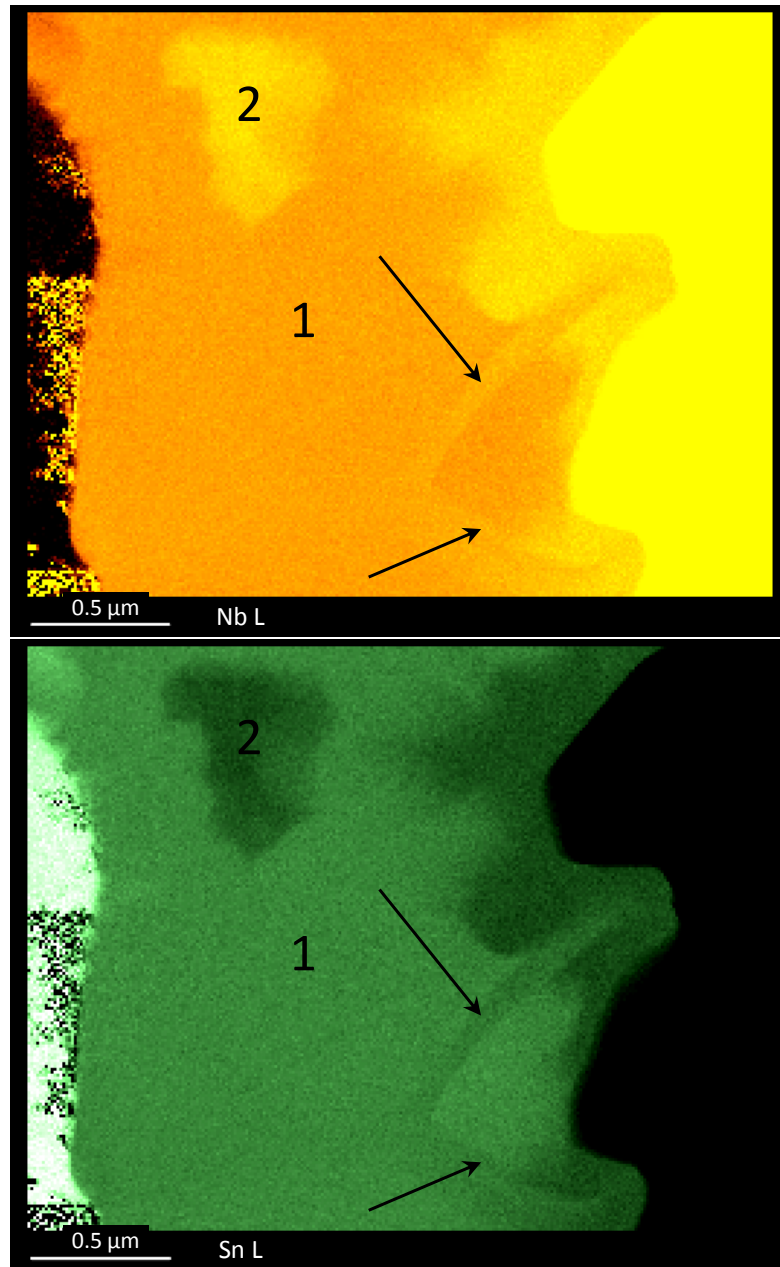


Figure 7.40: EDX area scans of region A, showing niobium concentration (top) and tin concentration (bottom). EDX of area 1 reveals a tin concentration of 24 atomic percent using the L edge. Area 2 gives 16 atomic percent.

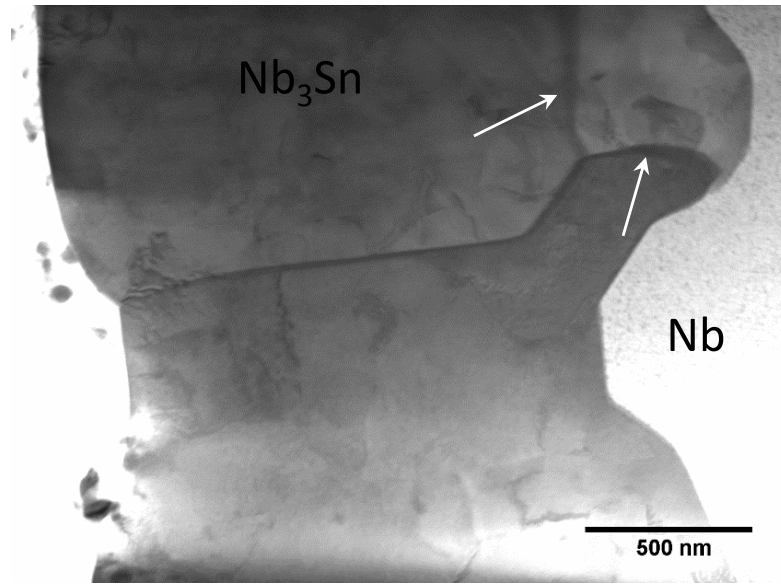


Figure 7.41: STEM bright field image of region B of the TEM sample measured at ANL. This is a cross section of the material, with exterior surface on the left and niobium bulk on the right. Grain boundaries are highlighted with arrows.

rich (brighter orange). This agrees with the previously discussed prediction. Furthermore, notice that close to the grain boundary, the Nb_3Sn phase penetrates deeper into the niobium bulk than in other regions, as expected if the grain boundaries are the primary transport mechanism for tin into the layer. However, for the grain boundaries close to the surface, no significant change is observed in the elemental composition compared to nearby areas. This may indicate that the grain boundaries in the RF layer ($\lambda \approx 100\text{-}200\text{ nm}$) are not tin depleted, and do not act as weak links.

On the other hand, there are prominent tin-depleted regions far from grain boundaries, but relatively close to the RF surface. Labeled with 2s in Figures [Figure 7.40](#) and [Figure 7.42](#), they appear as areas a few hundred nanometers in diameter, rather than the thin lines that would be expected for grain bound-

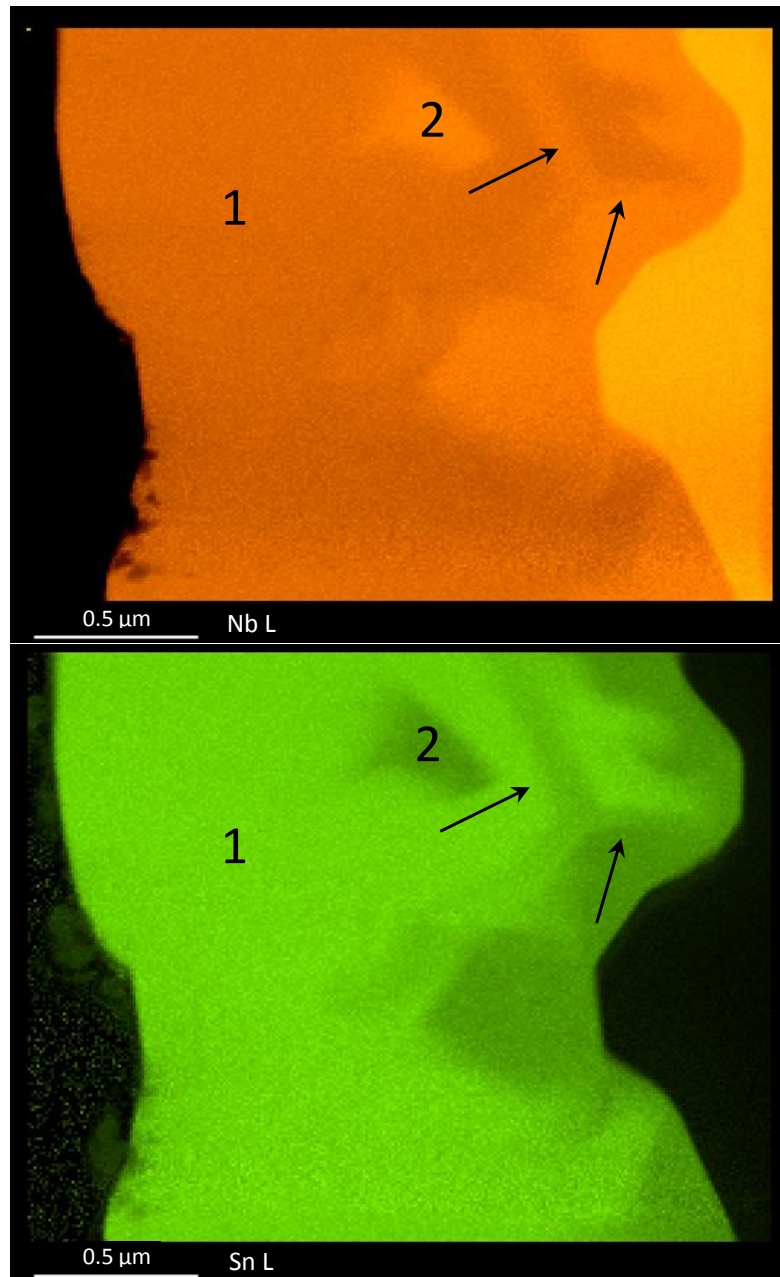


Figure 7.42: EDX area scans of region B, showing niobium concentration (top) and tin concentration (bottom). EDX of area 1 reveals a tin concentration of 25 atomic percent using the L edge. Area 2 gives 18 atomic percent.

aries⁹. These areas have compositions of 16-18 atomic percent tin, compared to surrounding areas with 24-25 atomic percent tin. The cause for the formation of these regions is not obvious. However, they may explain many features observed in RF tests. After material removal, the high quality Nb₃Sn screening these regions would be depleted, explaining the new temperature dependence observed. The composition is in the expected range for giving a $T_c \approx 6$ K. These regions also likely also have smaller critical fields, which could cause the Q -switch and quench observed during tests. This is explored further in the next section.

7.6 Thermal Stability

As discussed in [chapter 4](#), the thermal conductivity of Nb₃Sn is significantly smaller than that of Nb, making overheating a concern for Nb₃Sn coated cavities. Overheating can occur in both defect-free surfaces and at defects.

7.6.1 Thermal Instability for a Defect-Free Surface

In cavities that are relatively free of defects, thermal stability becomes a 1-dimensional conduction problem. The helium bath has a Kapitza thermal resistance to the wall of the cavity [[PKH08](#)], there are conductive impedances in the Nb and the Nb₃Sn (as well as a possible interface resistance between the two), and there is an RF heat load at the cavity surface.

⁹It is possible that these are grain boundaries that are grazed by the TEM cross section, but this seems unlikely, given that other grain boundaries far from the bulk show little change in elemental makeup compared to surrounding areas.

The additional thermal impedance from the Nb₃Sn layer is a concern, as it might lead to instability as more power is deposited in the walls of the cavity at high fields. However, in post-HF rinse and post-CBP tests, cavities operated stably with Q_0 more than an order of magnitude lower than tests immediately after coating, and as a result many watts of power were being dissipated in the cavity walls. Furthermore, the Wupperal cavities reached fields on the order of 70-80 mT even with $Q_0 < 10^9$ without thermal instability. Therefore global thermal instability is not expected to be a concern up to at least 100 mT if high Q_0 can be maintained. If these fields could be obtained in Nb₃Sn cavities with $R_{res} < 10 \text{ n}\Omega$ and minimal Q -slope at 4.2 K, they would be beneficial for a wide variety of applications. In the future, if higher fields are desired and thermal impedance becomes a concern, R&D efforts can concentrate on reducing the thickness of the deposited layer.

7.6.2 Thermal Instability at a Defect

The small thermal conductivity of Nb₃Sn may cause thermal runaway at a defect at heat fluxes that might be stable if it occurred in a niobium matrix. For illustration, let us consider a small volume of low tin content material embedded within the high quality Nb₃Sn layer as was observed in TEM. If this material is close enough to the surface, some RF currents will pass through it, causing it to dissipate, and if its low T_c gives it a high R_s , it will dissipate more strongly than the material around it. Because the thermal conductivity of Nb₃Sn is relatively poor, it will not transport the heat away effectively, and the temperature can build up locally. If the fields and temperatures were large enough, this material could become normal conducting, and dissipate even more strongly. This

could be the cause of the Q -switch observed in cavity 2 test 6. At some point, the heating will become so great that even the high quality material around the defect will be driven normal conducting, and thermal runaway will cause the cavity to quench. This mechanism could explain why the Nb_3Sn cavities appear to be sensitive to quench. In that case, finding preparation methods that prevent these tin depleted regions would be expected to increase the quench field.

CHAPTER 8

EXPERIMENTAL PROBE OF MAXIMUM FIELD LIMITS

In the CW tests discussed in the last chapter, it appeared that quenches observed were caused by defects. In this chapter, investigations are presented of cavity performance at high fields using powerful probes. The chapter is divided into two experiments. In the first, a Nb–3Sn cavity was driven with a klystron that provided RF pulses with approximately 1 MW of power. In the second, a superconducting solenoid positioned next to a Nb–3Sn cavity's exterior surface so that the DC flux penetration field could be measured.

8.1 Pulsed RF Cavity Testing

Following test 1 of cavity 2, it was mounted onto a waveguide test stand, shown in [Figure 8.1](#), and tested in high power pulsed (HPP) mode. Pulsed power was used to reach high fields in the cavity very quickly ($<100 \mu\text{s}$), in an effort to outpace any significant temperature increase of the inner wall, which would strongly impact the behavior of the cavity. If a defect were causing thermal runaway, it is expected that significantly higher fields could be reached in HPP testing compared to CW testing.

A typical pulse at 4.2 K is shown in [Figure 8.2](#). With the RF input coupler set to $Q_{ext} = 2 \times 10^6$, the cavity quenches in $\sim 60 \mu\text{s}$, reaching $B_{pk} \approx 110 \text{ mT}$. This is nearly twice the maximum field achieved in CW measurements, consistent with CW quench occurring due to defects.

[Figure 8.3](#) shows the effect of decreasing the forward power on the quench

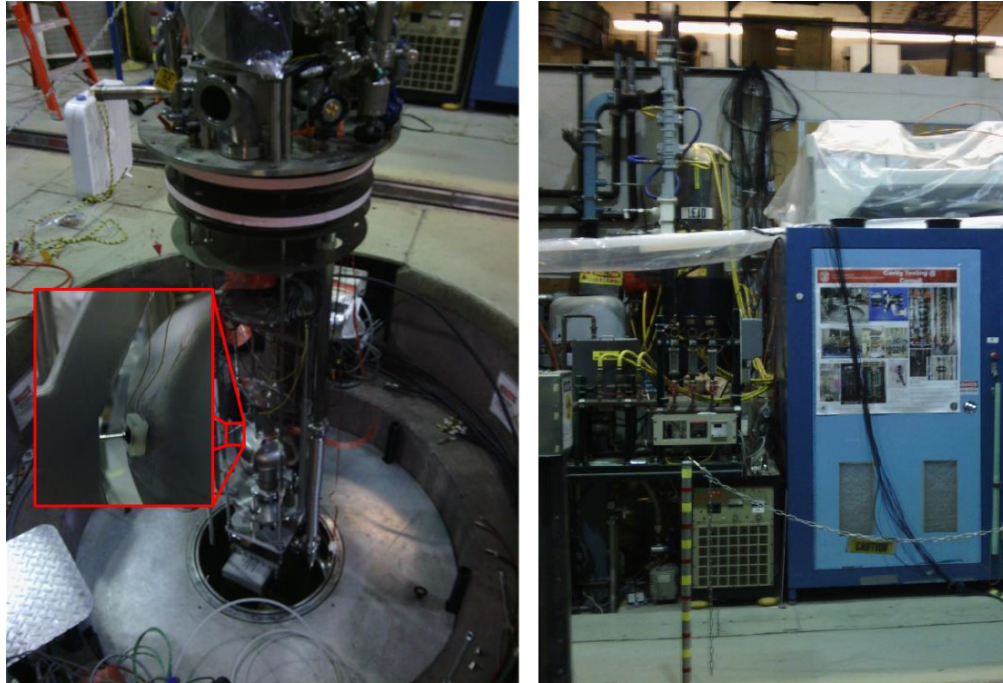


Figure 8.1: Cavity on waveguide insert being lowered into dewar (left), and 1.3 GHz 1 MW klystron (right). The inset shows one of the pogo sticks that keep good contact between the temperature sensors and the cavity.

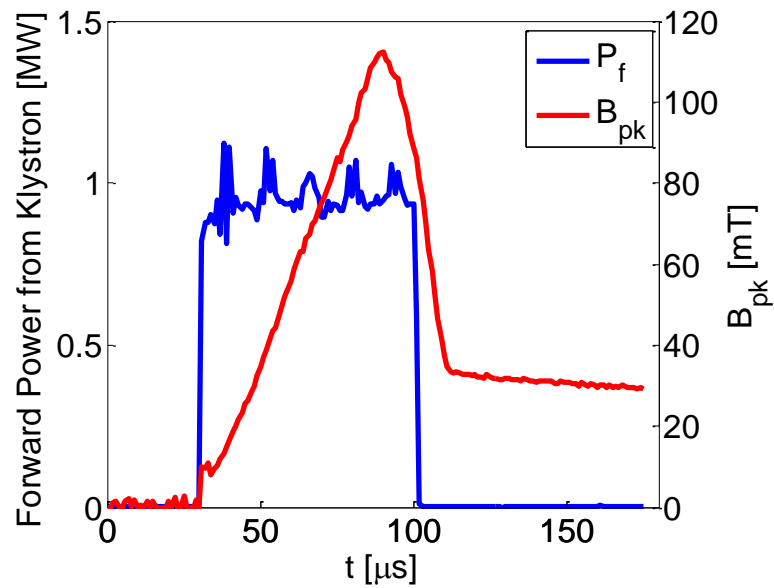


Figure 8.2: Nominally square forward power klystron pulse at 4.2 K and cavity response measured from transmitted power signal.

field at 4.2 K. As the klystron power decreases, it takes longer for the cavity to quench, and the quench field decreases due to thermal effects (heating of the inner cavity wall by the RF fields). If the cavity were reaching a fundamental magnetic field limit, then the pulse length should not matter—the cavity should always transition to into the normal conducting state at the same field at a given temperature. Our interpretation is that as the cavity fills with RF energy, the temperature of the inner wall of the cavity T_w becomes noticeably higher than the ambient temperature T , and quench occurs at $\mu_0 H_{sh}(T_w)$, which is significantly smaller than $\mu_0 H_{sh}(T)$. Assuming that the cavity quenches due to heating, a very simple thermal model was introduced and applied to the data with a one-parameter fit. It agrees well with the trend, supporting the conclusion that even with 1 MW of power, the cavity is not filling with RF energy fast enough to fully circumvent thermal effects at small defects.

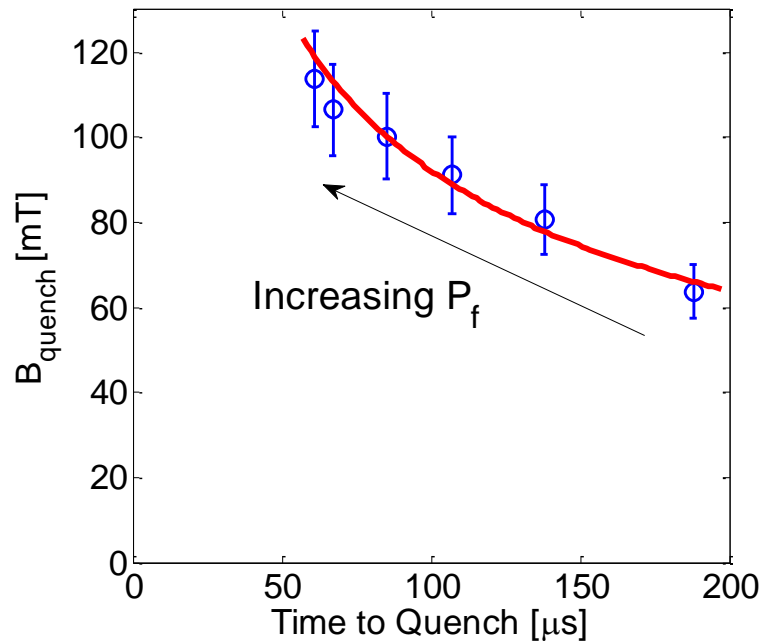


Figure 8.3: Reducing the forward power from the klystron increases the time to quench and decreases the quench field. The red curve is a one-parameter fit to the data based on a simple thermal model.

This measurement was repeated in helium gas, at constant forward power (as high as possible), at ambient temperatures T up to T_c . The method from [HPS97] was used to extract the quench field, determined by when the Q_0 had dropped to a value corresponding to 90% of the cavity still being superconducting. The result is shown in the Figure 8.4, along with $H_{sh}(T)$ and $H_{c1}(T)$ from Nb₃Sn coating parameters for this cavity as listed in Table 7.3¹. Results from measurements by Hays [HPS97] and Campisi [Cam85] on Nb₃Sn cavities are also shown.

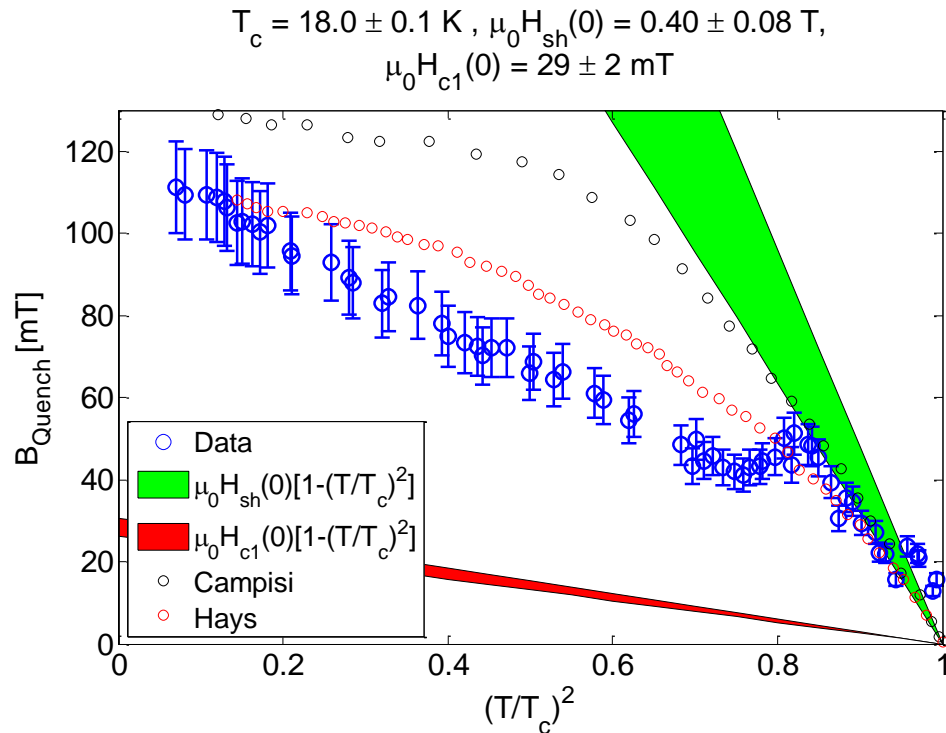


Figure 8.4: Pulsed quench field as a function of temperature at constant P_f . Data are compared to that of Campisi and Hays and to calculated H_{c1} and H_{sh} values.

Close to T_c , above $\sim 16 \text{ K}$, where $\mu_0 H_{sh}(T)$ is relatively small, B_{quench} follows the expected approximately $1 - \left(\frac{T}{T_c}\right)^2$ dependence², and indeed it approaches the

¹ $T = 0$ parameters are extrapolated to T_c with approximate $1 - (T/T_c)^2$ dependence.

²The temperature dependence is simplified here. The actual dependence will vary by ap-

superheating field. This is expected, as $\mu_0 H_{sh}(T)$ is the surface magnetic field at which flux is predicted to penetrate for an ideal surface at temperature T . The difference between $B_{quench}(T)$ and $\mu_0 H_{sh}(T)$ is likely due to some combination of the following effects: 1) heating from RF (surface resistance is quite large at these temperatures) 2) reduction in the energy barrier to flux penetration caused by surface defects with size on the order of the coherence length, and 3) magnetic field enhancement at sharp edges.

At low temperatures, the quench field is lower than the theoretical limit set by the superheating field, but in [Figure 8.3](#), it can be seen that near 4.2 K, it depends on the forward power. This clearly shows that the pulsed quench field is limited by thermal effects, rather than by a fundamentally limiting surface magnetic field.

At all temperatures, the quench field measured in this study is far higher than H_{c1} , further proving that it is not a fundamental limit.

At high temperatures, the plot of cavity 2 closely resembles those of Campisi and Hays, and all seem to follow H_{sh} . However, at lower temperatures, the data of these three plots are smaller than the predicted H_{sh} . This behavior is consistent with measurements of niobium cavities affected by high field Q -slope (HFQS). With the standard treatment to avoid HFQS of EP followed by 120°C bake, fields close to $\mu_0 H_{sh}^{Nb} \sim 200$ mT are observed, but without this treatment, pulsed measurements are limited to ~ 100 -150 mT [[HPS97](#), [Cam85](#), [VL11](#)], as shown in [Figure 8.5](#)³.

proximately an additional 10% over the temperature range [[CS08](#)].

³This comparison fits very well with the plots of Campisi and Hays, which also curve over then seem to plateau at some B_{quench} value at low temperatures. It is interesting that data measured on cavity 2 have an approximately quadratic dependence on T —the origin of which is not obvious—but as discussed earlier, [Figure 8.3](#) shows that the limiting field is not fundamental.

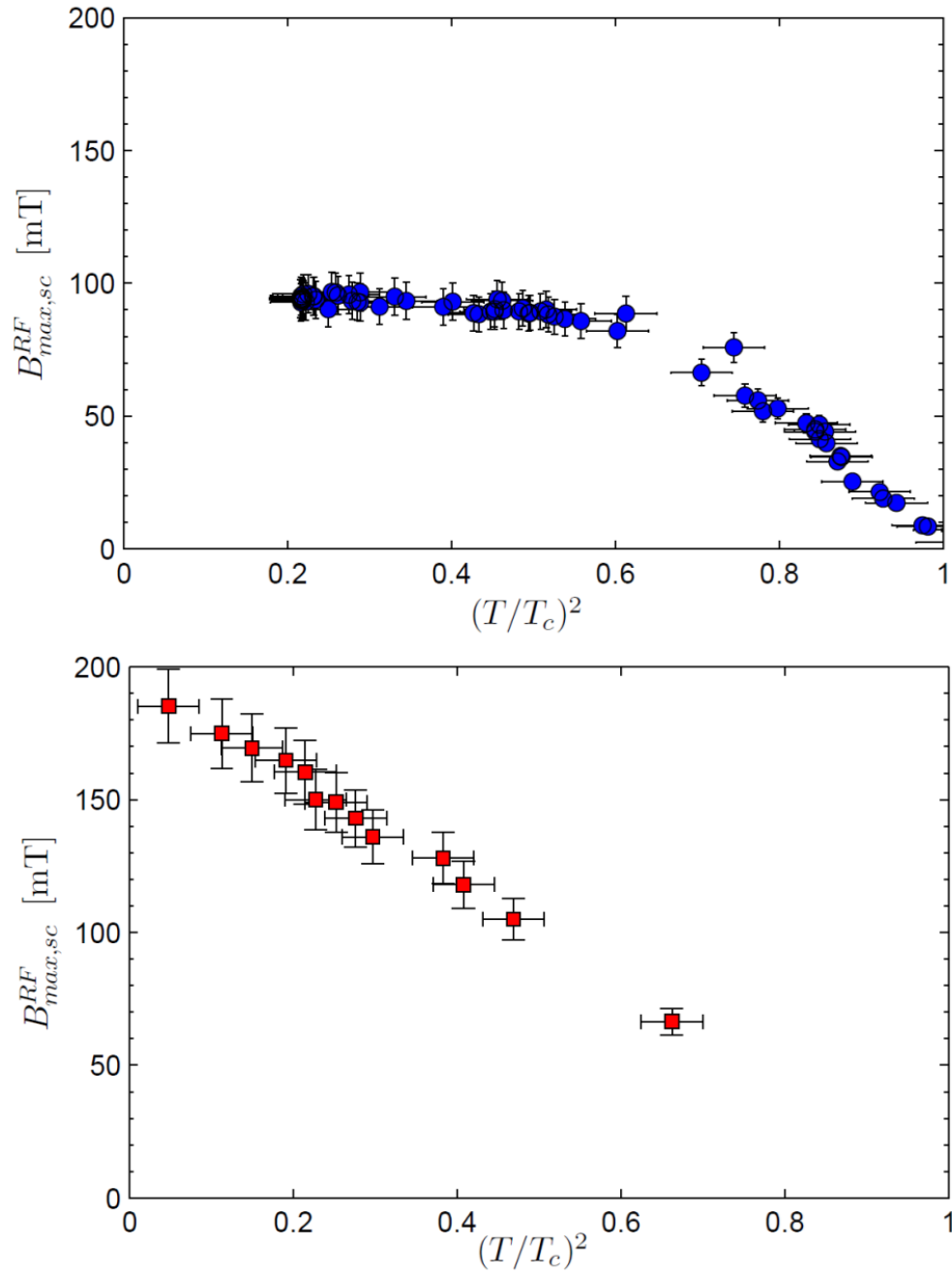


Figure 8.5: Pulsed quench field in a niobium cavity before high field treatment (top) and after (bottom). The trend of quench field with temperature observed in Nb₃Sn cavities is similar to the top plot, suggesting that a preventable mechanism may be limiting performance as HFQS does in Nb cavities. Figures adapted from [Val14].

This shows that a deviation of the pulsed quench field from H_{sh} , like is seen with Nb₃Sn, can be caused by a curable thermal overheating mechanism. If this were the case, then significantly higher fields could be reached at low temperatures. Figure 8.6 shows that if the trend in quench fields at high temperatures were extended to low temperatures, the quench field at 4.2 K would be approximately 250 mT.

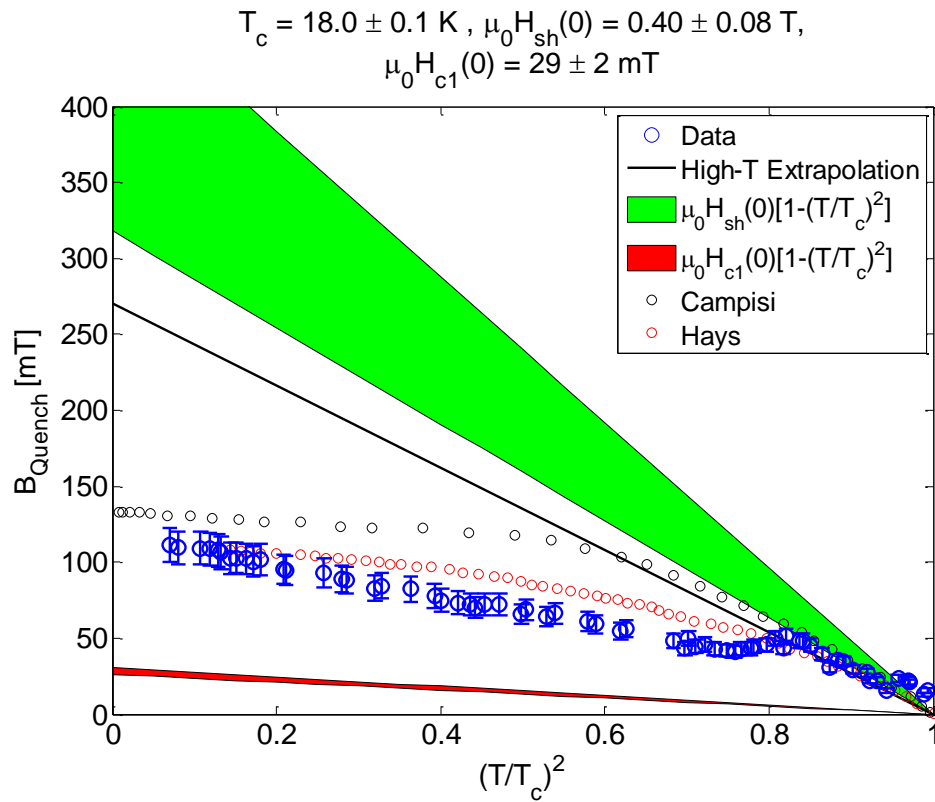


Figure 8.6: Extrapolated high temperature pulsed quench data shows promising maximum fields at useful temperatures.

8.2 DC Flux Penetration Field

A superconducting solenoid system developed for measuring the DC flux penetration field of niobium [Val14] was applied to cavity 2 after test 3, before removing it from the test stand. The main component is a NbTi magnet coil that is mounted rigidly to the beamtubes of a cavity, as shown in Figure 8.7. It is carefully fixed several mm away from the cavity surface, aligned with a Hall probe magnetometer that is mounted on the cavity surface prior to the magnet. Additionally, a cernox temperature sensor is mounted to the cavity nearby.

To measure the DC flux penetration field, first the cavity is maintained at a given temperature below T_c using cold gas from the slow cool system. Then the cavity is driven with a small amount of power from the PLL, enough to keep it at a few MV/m. Next, the current in the solenoid is ramped up slowly while recording the current, the field measured by the Hall probe, and the reflected power from the cavity, as shown in Figure 8.8. The field recorded by the Hall probe increases as the field applied by the solenoid ramps up. At some point, the magnetic field overcomes the ability of the superconductor to maintain the Meissner state, and flux penetrates in the cavity. Because the penetrating flux is extremely lossy under RF fields, the Q_0 of the cavity drops, and P_r increases significantly. When P_r jumps, flux has penetrated, and the magnetic field and current at penetration are noted. The cavity is then thermally cycled above T_c to remove trapped flux and the measurement is repeated again.

Figure 8.9 shows the DC flux penetration field as a function of temperature squared⁴. There are some stray points in the Hall probe measurement, but there

⁴In this graph, the magnetic field measured directly by the Hall probe has been converted to the field at the surface of the cavity using the procedure in [Val14].

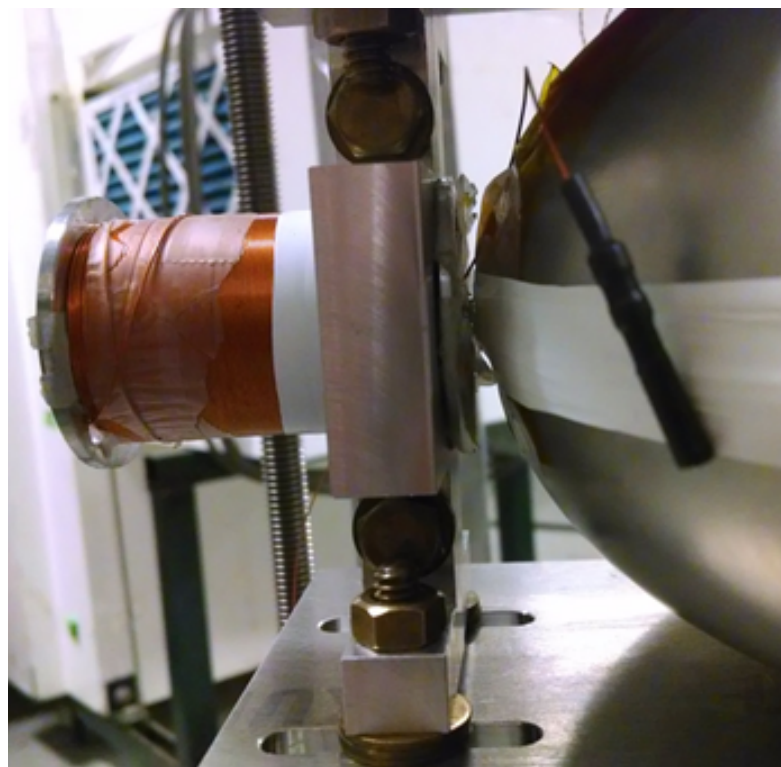
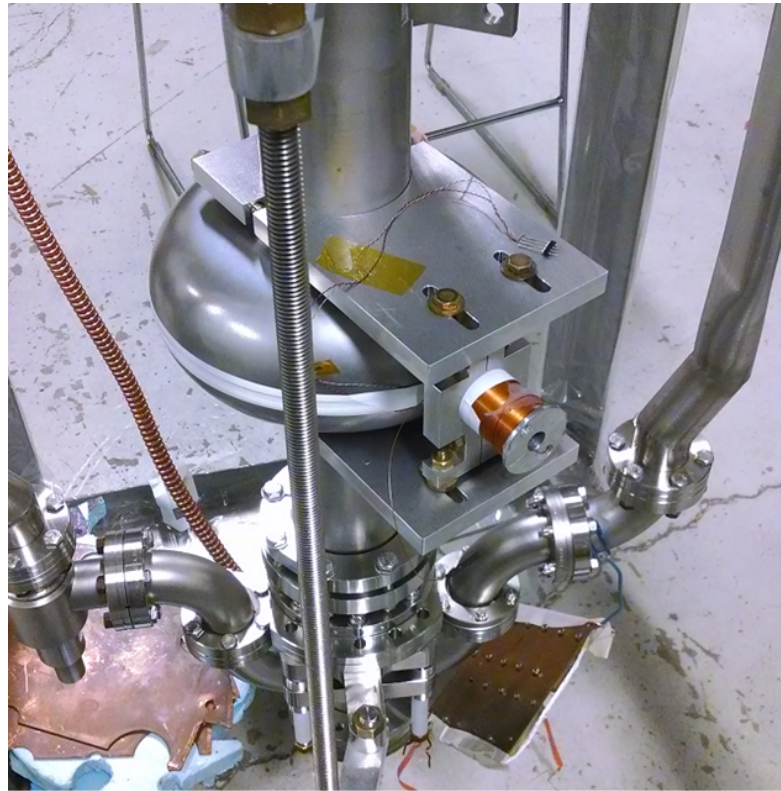


Figure 8.7: Top: solenoid connected to beamtubes of cavity. Bottom: the small gap between the solenoid and the cavity contains a Hall probe magnetometer and a cernox sensor.

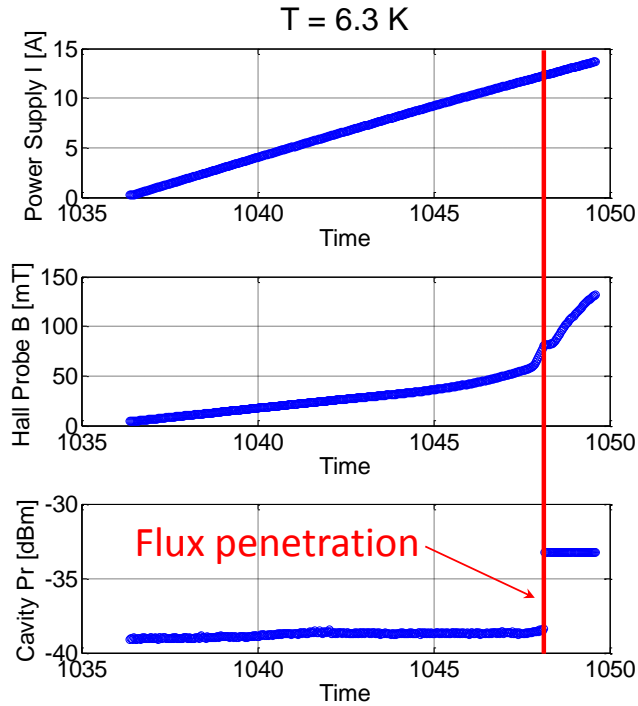


Figure 8.8: Example of a DC flux penetration field measurement performed at 6.3 K. The current in a superconducting solenoid is ramped up (top) while the magnetic field on a Hall probe (middle) and the reflected power in the cavity (bottom) are monitored. Flux penetration is determined to occur when the reflected power jumps.

is a clear overall trend. At low temperatures, the penetration field appears to be relatively high, and it agrees with the approximate⁵ expected curve (shown in black) for H_{sh} of clean niobium from the bulk, $\mu_0 H_{sh}(T) = \mu_0 H_{sh}(T = 0) \left(1 - \left(\frac{T}{T_c}\right)^2\right)$, where for niobium T_c is 9.2 K and $\mu_0 H_{sh}(T = 0)$ is approximately 240 mT [Val14]. Because the curve agrees well with $\mu_0 H_{sh}$ of niobium at low temperatures, it is expected that the low temperature DC flux penetration field $\mu_0 H_{pen}$ of the inner Nb₃Sn coating is smaller than this.

As the temperature increases and niobium approaches its T_c , it will go nor-

⁵The temperature dependence is simplified here. The actual dependence will vary by approximately an additional 10% over the temperature range [CS08].

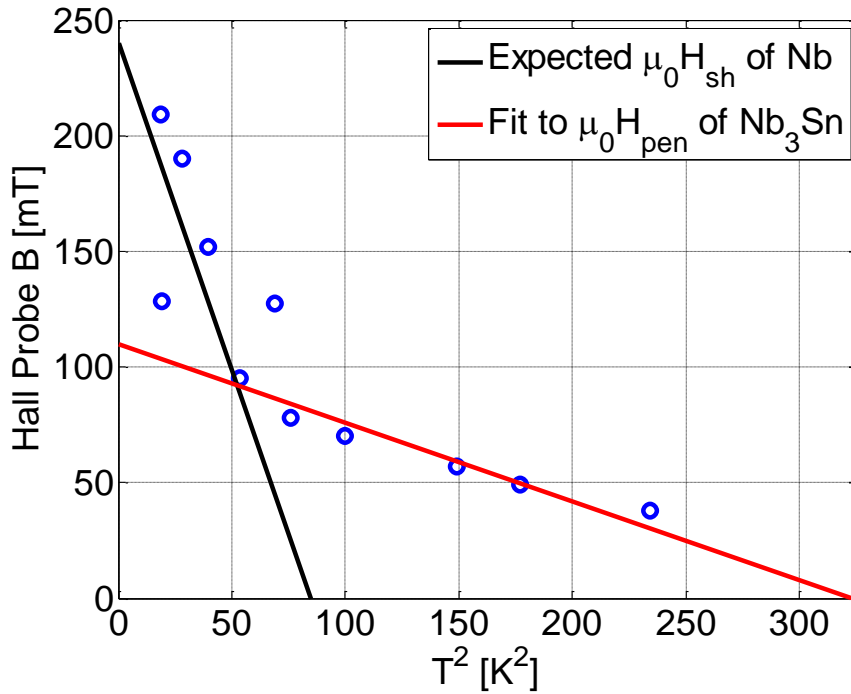


Figure 8.9: DC flux penetration field as a function of temperature. The low temperature data agrees well with $\mu_0 H_{sh}$ of clean niobium from the bulk. The high temperature data suggests that the DC flux penetration field of Nb₃Sn is lower than $\mu_0 H_{sh}$, possibly due to defects. Uncertainty in Hall probe measurements is approximately 20 mT and uncertainty in temperature is approximately 0.2 K.

mal conducting, and only the Nb₃Sn layer will be protecting the RF surface from flux penetration of the solenoid field. A second curve (shown in green) is plotted to model the flux penetration field of the Nb₃Sn layer, $\mu_0 H_{pen}(T) = \mu_0 H_{pen}(T = 0) \left(1 - \left(\frac{T}{T_c}\right)^2\right)$. Using the measured T_c of 18.0 K produces good agreement with the data, but the fitted $\mu_0 H_{pen}(T = 0)$ is approximately 110 mT, approximately 4 times smaller than $\mu_0 H_{sh}(T = 0)$ of Nb₃Sn (see calculated value for cavity 2 in [Table 7.2](#)). A possible explanation for this relatively small penetration field is that the magnet is applied not to the high quality Nb₃Sn material on the inner (vacuum) surface of the cavity, but to the other side of the layer, facing the Nb bulk. The calculation of H_{sh} assumes that there is vacuum above a supercon-

ductor surface, whereas in this case there will be a normal metal, transitioning over some depth from low Sn content Nb₃Sn to high quality Nb₃Sn. This will change the boundary conditions, and as a result it might be expected that the vortex-free limit would fall below H_{sh} .

In addition, defects may play a role in decreasing the barrier to flux penetration in these DC experiments, as they likely did in RF measurements.

CHAPTER 9

SUMMARY

This dissertation has presented research on Nb₃Sn SRF cavities, a promising technology for future accelerator applications that requires us to enhance our understanding of superconductivity. A coating chamber for single cell cavities was constructed, and building from the work of previous Nb₃Sn SRF researchers, modifications to existing coating procedures were studied. Progress resulting from this work includes far smaller surface resistances than has been achieved before at medium fields and temperatures close to 4.2 K. In addition, knowledge was gained of the SIS' structure and of RF superconductivity in granular materials with small coherence lengths. The results of this dissertation are summarized in this chapter, starting with progress in Nb₃Sn SRF research and a comparison to previous experimental programs. Then a brief overview is given of results of studies of different preparation parameters, as well as the advances in understanding made in the course of this research. The Nb₃Sn SRF state-of-the-art is evaluated, and then outlook and next steps are presented.

9.1 Progress and Comparison to Previous Research

The research performed in this dissertation benefited from the work of previous researchers, including those at U. Wuppertal, who were the first to study Nb₃Sn coatings on elliptical single cells at ~1 GHz. Incorporating their experiences into fabricating Nb₃Sn at Cornell, several coatings were produced. Five tests immediately after coating are compared to one of the best U. Wuppertal cavities in [Figure 9.1](#).

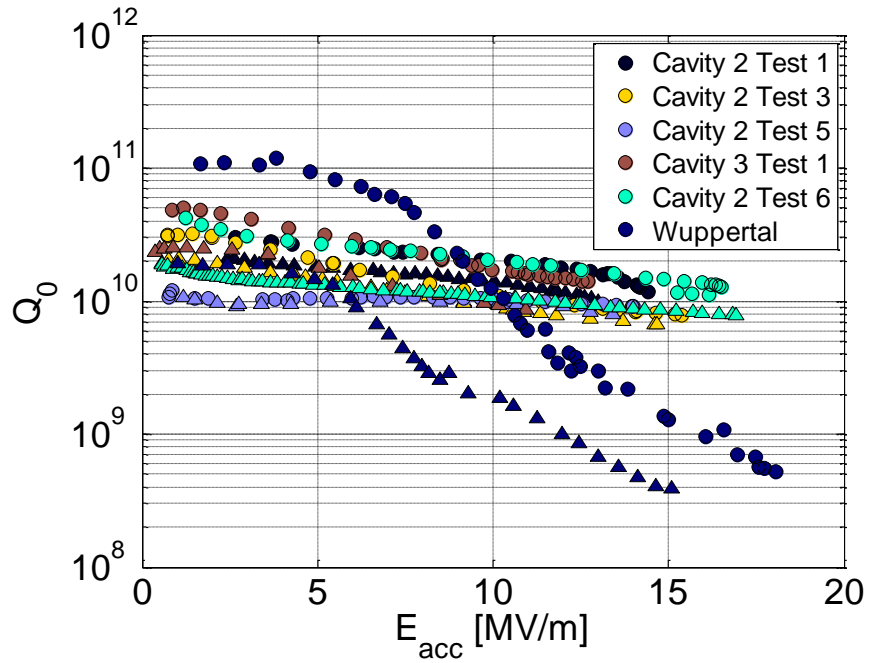


Figure 9.1: Five Cornell tests immediately after coating are compared to one of Wuppertal’s best cavities from Figure 4.7 [MPP⁺00]. Circles represent measurements with a 2 K bath temperature and triangles represent 4.2 K. The Cornell cavities reach significantly higher fields without strong Q -slope, especially at 4.2 K, though they have somewhat higher R_{res} .

The improvement in the Q at medium fields is evident in this picture. The strong Q -slope observed starting at ~ 5 MV/m in the Wuppertal cavities is not present in any of these tests. With Q_0 in the 10^{10} range at 4.2 K at fields above 10 MV/m, these performance levels are now useful for applications (see section 9.4). The maximum E_{acc} measured at 4.2 K and 2.0 K in these tests, about 13-17 MV/m, is similar to this best Wuppertal cavity. On the other hand, the Wuppertal cavity’s R_{res} at low fields was extremely small, approximately 3 n Ω . From the literature, it appears that this cavity had smaller R_{res} than others produced [MKM96,BKM⁺97,MPP⁺00], so it may be difficult to replicate, but it gives some indication of what might be possible with continued development. The quench fields of the cavities in this study can also be compared to those of

Siemens TM cavities in [Figure 4.6](#), and the maximum field of the other Wuppertal cavity from [Figure 4.7](#), which all reach similar maximum B_{pk} .

The comparison to Wuppertal is especially interesting, because the cavity substrates are very similar, and because the temperatures and times used for key steps of the procedure were based on Wuppertal's procedure described in [\[MKM96\]](#). The annealing time was varied for the Cornell tests, but it did not seem to have a strong effect on RF performance, and cavity 2 test 6 had approximately the same annealing time as was used at Wuppertal. Therefore it is not clear why there is such a striking difference in Q -slope.

One explanation might be that there is something special about Cornell's coating method, that the chamber is especially clean, or that the temperatures or times are different in a beneficial way. One factor that was noted in our experiments, which has been observed by previous researchers [\[HMP⁺77\]](#), is that the way in which the temperature is ramped up after initial nucleation of the surface appears to be very important. It may be, for example, that the nucleation step is longer, or that the ramp up to coating temperatures is faster, or that the temperature difference between the tin source and the cavity during that time is smaller. If any of these changes led to a difference in the surface coverage, grain size, or local composition, it could cause a drastic change in RF performance. The effect of the parameters chosen for this critical step would be a good topic to study next.

It is difficult to trace the cause of the differences in results between Cornell's cavities and Wuppertal's. However, several studies were performed in this work that allow for a direct comparison of several important parameters and lead to a better understanding of the microscopic structure of the Nb_3Sn

layers.

9.2 Comparisons between Coatings

As mentioned above, three different annealing times (0.5 h, 6.5 h, and 16.5 h) were attempted after the tin source heater was shut down after the coating step. No strong difference in RF performance was observed between these coatings.

Two different initial chemistry preparations were used before coating: BCP and EP. The cavity that received bulk and final EP had a higher Q_0 at low fields than the cavity that received bulk and final BCP. However, the quench field and Q_0 close to quench were very similar, approximately 10^{10} at 4.2 K at 13 MV/m.

After coating and testing, two different light material removal methods were tried, hydrofluoric acid rinse and centrifugal barrel polishing. Both resulted in strong Q -slope. The temperature dependence of the quality factor observed in these tests suggests that a material with T_c of 6 K is in the RF surface and responsible for the extra losses. One likely candidate for such a material is Nb_3Sn with low Sn content, possibly located in grain boundaries or in regions beneath the surface. After HF rinse of samples (with no HPR), structures were observed on the surface in SEM images that may also be a cause of increased losses.

In one test, three cooldowns were performed at different rates. 2 min/K and 10 min/K had very similar RF performances, but Q_0 was strongly reduced for a 0.2 min/K cooldown, which also had a significant temperature gradient over the cavity. This is consistent with measurements by Wuppertal in which they found that slowly cooling Nb_3Sn cavities would lead to higher Q_0 [PHK⁺88],

and with measurements of niobium-coated copper cavities.

One of the cavities coated showed an unusually shiny appearance in one half cell, which also showed very high heating on T-maps resulting in relatively low Q_0 . Anodization suggested that this half cell might have uncovered niobium areas, though the cavity did have a significantly higher Q_0 at 4.2 K than a niobium cavity would. The suspected cause for excess losses is niobium in one half cell that acted as a poor substrate for Nb_3Sn coating.

A number of small samples were cut from large grain niobium sheets and then coated in the furnace. These samples showed some “clumps,” regions with size of approximately $10\ \mu\text{m}$ with no obvious grain boundaries visible inside, and with tin content from EDX significantly smaller than in other regions, which is expected to cause a lowered T_c . Regions like this were not visible on fine grain samples also coated in the same run. It is not yet known if these regions occurred as a result of the particular niobium sheet used or if it is a consequence of using large grain material.

9.3 Advances in Understanding

One important question that was addressed was whether the SIS' structure could provide a higher maximum field for SRF applications than bulk superconductors. In [chapter 3](#), it was shown that for an ideal surface, a Nb_3Sn thin film/insulator/ Nb bulk SIS' sandwich provides at most a small increase in the maximum field compared to bulk Nb_3Sn , and only for a small range of film thicknesses. It was also shown that adding more Nb_3Sn thin film/insulator layers to build up a multilayer only decreases the maximum field.

At the start of this research, it wasn't clear if the metastable state would be reliable under RF fields in a small coherence length material like Nb₃Sn. The cavities produced by Wuppertal consistently showed strong Q -slope that began at approximately H_{c1} , bringing into question if flux were beginning to penetrate at this field. During the experiments performed for this dissertation, H_{c1} was extracted from fits to Q vs T and f vs T , as well as measured via μ -SR. In CW measurements, fields significantly above H_{c1} were reached without strong Q -slope, showing that the metastable flux-free state is reliable. This result was found in all five tests of cavities 2 and 3 immediately after coating, showing that the preparation method used produces high performing cavities in a repeatable manner.

By testing cavities both in CW and with HPP or DC flux penetration, further support was provided for defects being the cause of quench. Following test 1 of cavity 2, it was tested with pulsed power, reaching approximately twice the maximum field before quench as it did in CW testing. The suspected cause is that when the fields in the cavity are ramped up quickly, there is not as much time for thermal heating from defects, so it can reach higher fields before quench. Similarly, in DC flux penetration field measurements of cavity 2 after test 3, fields approximately twice as high as the CW quench field were reached before flux penetration. DC flux penetration measurements are expected to increase the maximum field by 1) not having the risk of thermal overheating posed by testing with strong RF fields, and 2) having strong fields only in a small area of the cavity, reducing the probability that a bad defect will experience strong fields. The increased maximum fields observed in both these measurements are consistent with defects being the cause of quench.

An ongoing question about Nb₃Sn is the causes of the observed field limitations, both Q -slope (where present) and quench. Wuppertal reported cavities that were limited by RF power after strong Q -slope rather than quench [MKM96], and Siemens reported quench fields with statistical distribution suggesting that defects were responsible [Hil80]. In chapter 7, clues were discovered that indicate what the causes of these limitation mechanisms might be. After material removal, strong Q -slope was observed accompanied by a temperature dependence that suggested the presence of a superconductor in the RF layer with T_c of approximately 6 K. This suggests that low tin content Nb-Sn alloys may be connected to the strong Q -slope observed. For the quenches that have been observed, one possible cause was revealed by microscopic analysis. TEM studies revealed the presence of sub-surface pockets of low tin content Nb-Sn alloys. These materials may have lower T_c and critical fields, making these regions vulnerable to overheating and flux penetration. Another mechanism that may play a role is weak link grain boundaries. Low tin content grain boundaries would also be consistent with the temperature dependence observed after material removal, and there was some trend of larger grain sizes (fewer grain boundaries) in cavities without strong Q -slope. Low Sn content grain boundaries were observed in TEM, near the niobium bulk, far from the surface. However, with extremely limited statistics, it is impossible to conclude whether or not some such structures may be close enough to the surface to affect RF performance. These clues are helpful, but further studies are needed to determine if either of these mechanisms is in fact the cause of the observed field limitations.

9.4 Evaluation of Nb₃Sn State-of-the-Art

In [chapter 2](#), a calculation was shown of the $R_s(T)$ comparing Nb and Nb₃Sn based on literature values. In [chapter 7](#), material parameters were extracted based on RF measurements. It is helpful to compare this to state-of-the-art high- Q_0 niobium prepared with nitrogen doping, for which material parameters can be found from the literature [[GEF⁺14](#)]. In [Figure 9.2](#), the dissipated power for a 1.3 GHz TeSLA cavity at 16 MV is compared for these two materials. Both the power dissipated in the walls and the AC power required to provide cooling at a given temperature are calculated, taking into account the cryoplant efficiency. Also shown is a calculation for the same Nb₃Sn material parameters, but with R_{res} of 3 n Ω , which has been obtained by previous researchers [[MPP⁺00](#)] on a 1.5 GHz cavity. The calculations based on material parameters are compared to Q_0 measurements of cavity tests presented in this dissertation, as well as the cavity tests from U. Wuppertal researchers shown in [Figure 4.7](#) [[MPP⁺00](#)]. Points are plotted at both 2 MV/m and 12 MV/m to show the level of Q reduction observed at high fields.

The plots show that within the liquid helium temperature range 1.6-4.4 K, Nb₃Sn at ~ 4 K with the measured material parameters offers the smallest power consumption, a factor of approximately 3 smaller than Nb at 2 K. Measurements at medium fields (squares in the figure) show an increased power consumption due to Q -slope, but it is still very close to niobium at 2 K. However, a 4.2 cryogenic plant for a Nb₃Sn linac would be simpler than a 2 K cryogenic plant for a Nb linac, reducing infrastructure costs. The dashed line shows that if R_{res} can be improved to 3 n Ω (as was demonstrated by Wuppertal) and if Q -slope could be reduced (as reported above, significant progress has been made on reducing Q -

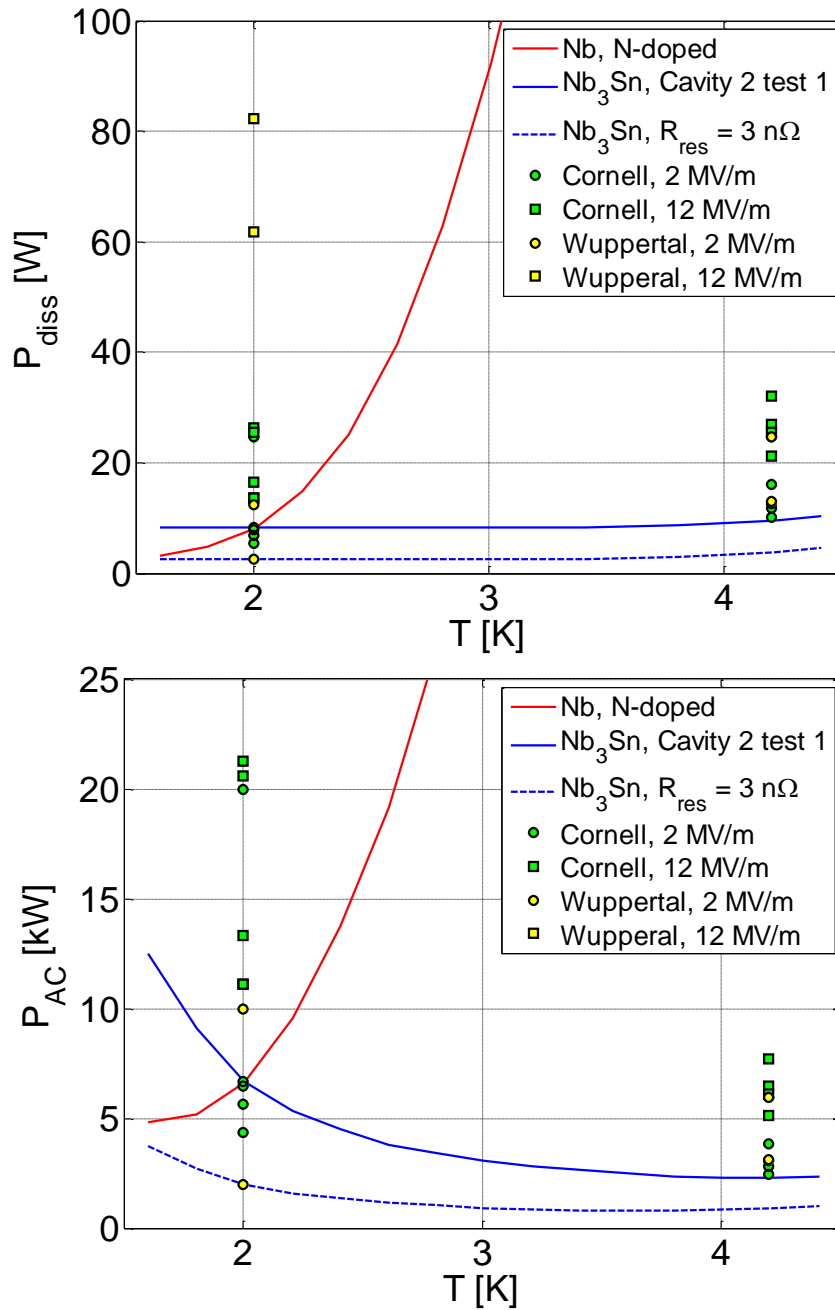


Figure 9.2: Power dissipated in the walls of a 1.3 GHz TeSLA cavity at 16 MV (top) and AC power required to cool this cavity (bottom) as a function of temperature, similar to Figure 2.5. Fitted data for N-doped niobium from [GEF⁺14] is compared to Nb_3Sn fit data from cavity 2 test 1, and the same data with smaller R_{res} . Also plotted are points based on Q_0 measurements of Cornell and Wuppertal 1.3-1.5 GHz Nb_3Sn cavities at 2 and 12 MV/m.

slope and it might be possible to reduce it further), then the power consumption of Nb₃Sn cavities could be reduced even more drastically.

Of all the CW tests in this research program, test 6 of cavity 2 showed the highest peak field. In [Figure 9.3](#), it is plotted in such a way that it can be compared against various benchmarks. To compare the fields in the cavity to other cavities with different B_{pk}/E_{acc} , the horizontal axis plots B_{pk} (top axis), and it is multiplied by $B_{pk}/E_{acc} = 4.3 \text{ mT}/(\text{MV}/\text{m})$ for a TeSLA or ERL shaped cavity (bottom axis) for ease of comparison with the plots in [chapter 7](#). On the vertical axis is Q_0 adjusted for cryoplant efficiency relative to 2.0 K by multiplying it by $\text{COP}^{-1}(2.0\text{K})/\text{COP}^{-1}(T)$, where COP^{-1} is the cryogenic plant efficiency from [Figure 2.6](#). This adjustment allows a fair comparison of the AC power required to cool the cavity, so that Q vs E points for cavities at different temperatures can be plotted in the same figure¹.

The cavity clearly exceeds H_{c1} without strong Q -slope, proving that H_{c1} is not a fundamental limit for RF superconductivity. The pulsed quench field and DC flux penetration field measured during other coatings of the same cavity show that additional improvement in the maximum field can be expected by reducing the influence of defects. The highest quench field of a Siemens TE cavity at 1.5 K reported in [\[Hil80\]](#) also shows that B_{pk} on the order of 100 mT can be achieved in CW RF tests, even with the small coherence length and small thermal conductivity of Nb₃Sn, even at 10 GHz. The comparison to one of the best cavities produced by U. Wuppertal [\[MPP⁺00\]](#) shows that the Q -slope observed in their tests is not a fundamental problem for Nb₃Sn, and it can be avoided. Finally, the comparison to the specs for the main linear accelerators of LCLS-II [\[Gal14\]](#)

¹If $Q_{0,adj} = Q_0 \frac{\text{COP}^{-1}(2.0\text{K})}{\text{COP}^{-1}(T)}$, then P_{ac} can be calculated for any T from $P_{ac} = \frac{\text{COP}^{-1}(2.0\text{K})V^2}{Q_0 Q_{0,adj}}$

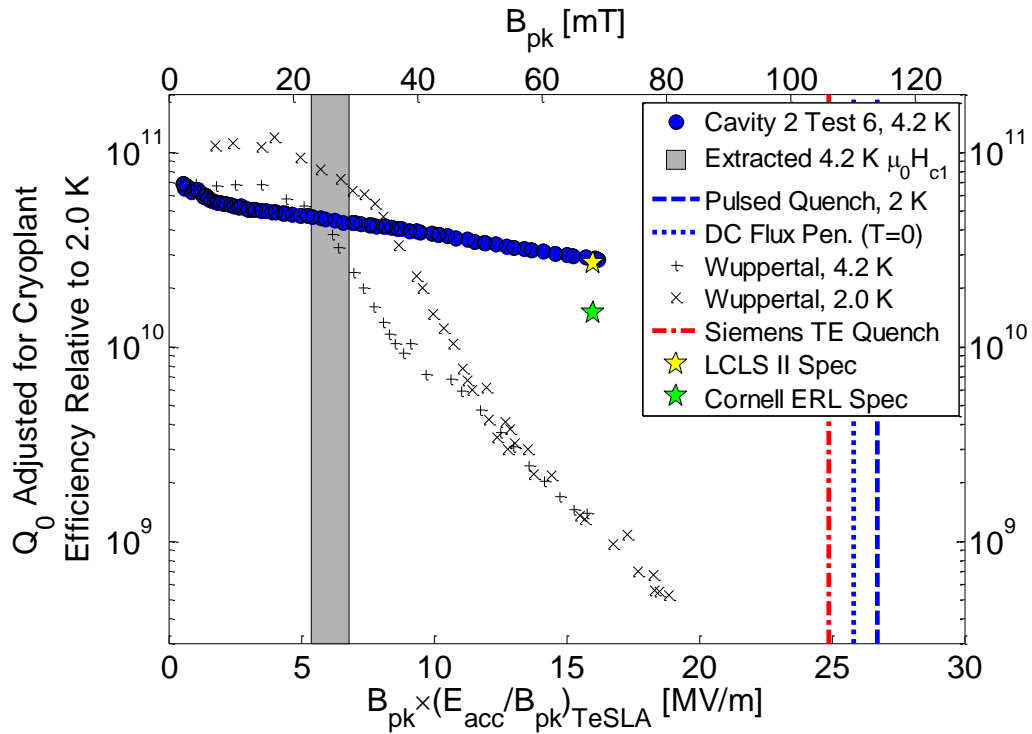


Figure 9.3: 4.2 K Q vs E curve of cavity 2 test 6 adjusted to 2 K by multiplying Q_0 by the ratio of the cryoplant efficiency at 4.2 K vs 2 K. Also plotted are the measured pulsed 2 K quench field and the DC flux penetration field extrapolated to $T=0$. These measurements are compared to the Q vs E curves from one of the best Wuppertal cavities [MPP⁺00], the highest quench reported by Siemens in [Hil80], and the operating specifications for LCLS-II [Gal14] and the Cornell ERL [HGT13]. All Q_0 values are adjusted to 2 K according to cryogenic efficiency.

and the Cornell ERL [HGT13] show that R&D-scale Nb_3Sn cavities operating at 4.2 K are now at the point where they meet the P_{AC} and E_{acc} specifications of state-of-the-art high- Q_0 SRF linacs.

9.5 Outlook and Next Steps

At the start of this research, the primary concern was the strong Q -slope that affected Nb_3Sn cavities at ~ 1 GHz in the past. Now that we are producing cavi-

ties that seem to reliably avoid this strong Q -slope, the next important things to address are 1) the quench field and 2) the residual resistance.

Quench fields as high as 17 MV/m have been obtained in this research, which is already sufficient for many applications, but it is still below the ultimate potential of the material. Continued studies can lead to a better understanding of the diffusion process, which in turn can determine what coating parameters will prevent the formation of tin depleted regions that are suspected to be the cause of quench. TEM studies have produced a unique insight into the Nb₃Sn coatings, and they may prove to be a powerful tool in the future for understanding how to tailor the layers on a microscopic level. With additional research, Nb₃Sn cavities may reach fields higher than H_{sh} of niobium, reducing the cost of future high energy linacs.

R_{res} values on the order of 10 n Ω were achieved at medium fields in the Nb₃Sn cavities tested for this dissertation. Figure [Figure 9.2](#) shows that this performance allows these cavities to approximately match the AC power efficiency of N-doped Nb cavities at 2 K, but if R_{res} could be reduced even further, the cryogenic power savings would be significant. This would be very beneficial for high duty factor applications. Next steps should focus on finding the dominant sources of R_{res} and improving the Nb₃Sn preparation protocol accordingly. These may include investigating weak link grain boundaries, cooldown procedures, and coating parameters.

Already the performances shown by the five tests in [Figure 9.1](#) are promising for low field applications at temperatures ~ 4.2 K or higher. Exploring the potential of Nb₃Sn in these applications could also be a rewarding next step.

BIBLIOGRAPHY

- [AAA⁺07] G Ambrosio, N Andreev, M Anerella, E. Barzi, R. Bossert, D. Dieterich, S. Feher, P Ferracin, A. Ghosh, S. Gourlay, V. V. Kashikhin, A. Lietzke, A. McInturff, J. Muratore, F. Nobrega, G. L. Sabbi, J. Schmalzle, P. Wanderer, and A. V. Zlobin. Design of Nb₃Sn Coils for LARP Long Magnets. *IEEE Trans. Appl. Supercond.*, 17(2):1035–1038, June 2007.
- [ABHT83] L. Allen, M. Beasley, R. Hammond, and J. Turneaure. RF surface resistance of high-T_c superconducting A15 thin films. *IEEE Trans. Magn.*, 19(3):1003–1006, May 1983.
- [Aea12] G. Aad et al. Observation of a new particle in the search for the Standard Model Higgs boson with the ATLAS detector at the LHC. *Phys. Lett. B*, 716(1):1–29, September 2012.
- [Alt07] Massimo Altarelli et al. (eds.). TESLA XFEL: First Stage of the X-ray Laser Laboratory; Technical Design Report. Technical Report July, DESY, Hamburg, 2007.
- [AM84] G Arnolds-Mayer. A15 surfaces in Nb cavities. In *Proc. Second Work. RF Supercond.*, Geneva, 1984.
- [AMC86] G Arnolds-Mayer and E Chiaveri. On a 500 MHz single cell cavity with Nb₃Sn surface. In *Proc. Third Work. RF Supercond.*, Chicago, 1986.
- [AP77] G. Arnolds and D. Proch. Measurement on a Nb₃Sn structure for linear accelerator application. *IEEE Trans. Magn.*, 13(1):500–503, January 1977.
- [Aul14] Sarah Aull. Secondary Electron Yield for SRF Materials. *Proc. Sixth Int. Work. Thin Film. New Ideas RF Supercond.*, 2014.
- [AVM13] C. Z. Antoine, J.-C. Villegier, and G. Martinet. Study of nanometric superconducting multilayers for RF field screening applications. *Appl. Phys. Lett.*, 102(10):102603, 2013.
- [BBF92] P Bernard, D Bloess, and T Flynn. Superconducting niobium sputter-coated copper cavities at 1500 MHz. *Proc. Third Eur. Part. Accel. Conf.*, pages 1269–1271, 1992.

- [BCC⁺97] C. Benvenuti, S. Calatroni, I. E. Campisi, P. Darriulat, C. Durand, M.A Peck, R. Russo, and A.M. Valente. Magnetic flux trapping in superconducting niobium. Technical Report October 1997, CERN EST/97-08 (SM), 1997.
- [BCC⁺99] C Benvenuti, S Calatroni, I.E. Campisi, P Darriulat, M.A. Peck, R. Russo, and A.-M. Valente. Study of the surface resistance of superconducting niobium films at 1.5 GHz. *Phys. C Supercond.*, 316(3-4):153–188, May 1999.
- [BCD⁺01] C Benvenuti, S Calatroni, P Darriulat, M.A. Peck, A.-M. Valente, and C.A.Vant Hof. Study of the residual surface resistance of niobium films at 1.5 GHz. *Phys. C Supercond.*, 351(4):421–428, April 2001.
- [BCS57] J. Bardeen, L. N. Cooper, and J. R. Schrieffer. Theory of Superconductivity. *Phys. Rev.*, 108(5):1175–1204, December 1957.
- [Beh13] Ties Behnke et al. (eds.). The International Linear Collider. Technical report, Technical Design Report, 2013.
- [Ben91] C Benvenuti. Superconducting coatings for accelerating RF cavities: past, present, future. *Proc. Fifth Work. RF Supercond.*, 1991.
- [BEW05] Donald H Bilderback, Pascal Elleaume, and Edgar Weckert. Review of third and next generation synchrotron light sources. *J. Phys. B At. Mol. Opt. Phys.*, 38(9):S773–S797, May 2005.
- [BKM⁺97] P Boccard, P Kneisel, G. Müller, J. Pouryamout, and H. Piel. Results from some temperature mapping experiments on Nb₃Sn RF cavities. In *Proc. Eighth Work. RF Supercond.*, Padova, 1997.
- [BL64] CP Bean and JD Livingston. Surface barrier in type-II superconductors. *Phys. Rev. Lett.*, 12(1):4–6, 1964.
- [BS65] John Bardeen and M. Stephen. Theory of the Motion of Vortices in Superconductors. *Phys. Rev.*, 140(4A):A1197–A1207, November 1965.
- [BS91] B Bonin and H Safa. Power dissipation at high fields in granular RF superconductivity. *Supercond. Sci. Technol.*, 257, 1991.

- [Cam85] I. Campisi. High field RF superconductivity: To pulse or not to pulse? *IEEE Trans. Magn.*, 21(2):134–141, March 1985.
- [CCG⁺13] C A Cooper, A C Crawford, C Ginsburg, A Grassellino, R Kephart, O S Melnychuk, A Rowe, and D A Sergatskov. Acid free extended mechanical polishing R&D. *Proc. Sixt. Conf. RF Supercond.*, pages 564–566, 2013.
- [Cea12] S. Chatrchyan et al. Observation of a new boson at a mass of 125 GeV with the CMS experiment at the LHC. *Phys. Lett. B*, 716(1):30–61, September 2012.
- [CF84] I. E. Campisi and Z. D. Farkas. Pulsed rf superconductivity program at SLAC. In *Proc. Second Work. RF Supercond.*, Geneva, August 1984.
- [Cio04] Gianluigi Ciovati. Effect of low-temperature baking on the radio-frequency properties of niobium superconducting cavities for particle accelerators. *J. Appl. Phys.*, 96(3):1591, 2004.
- [Cio06] Gianluigi Ciovati. Improved oxygen diffusion model to explain the effect of low-temperature baking on high field losses in niobium superconducting cavities. *Appl. Phys. Lett.*, 89(2):022507, 2006.
- [CMM70] J. P. Charlesworth, I. Macphail, and P. E. Madsen. Experimental work on the niobium-tin constitution diagram and related studies. *J. Mater. Sci.*, 5(7):580–603, July 1970.
- [CRZC] Giovanni Carta, Gilberto Rossetto, Pierino Zanella, and Laura Crociani. Attempts To deposit Nb₃Sn by MOCVD. *Int.infn.it*, (1):3–6.
- [CS08] G. Catelani and J. P. Sethna. Temperature dependence of the superheating field for superconductors in the high- κ London limit. *Phys. Rev. B*, 78(22):224509, December 2008.
- [DDD97] Andrew Dolgert, S. Di Bartolo, and Alan Dorsey. Erratum: Superheating fields of superconductors: Asymptotic analysis and numerical results [Phys. Rev. B 53, 5650 (1996)]. *Phys. Rev. B*, 56(5):2883–2883, August 1997.
- [De 99] P. G. De Gennes. *Superconductivity of Metals and Alloys*. Westview Press, Boulder, 1999.

- [Dea08] SM Deambrosis. *6 GHz cavities: a method to test A15 intermetallic compounds RF properties*. PhD thesis, 2008.
- [DH75] D. Dew-Hughes. Superconducting A-15 compounds: A review. *Cryogenics (Guildf.)*, 15(8):435–454, August 1975.
- [DJD⁺81] H. Devantay, J. L. Jorda, M. Decroux, J. Muller, and R. Flkiger. The physical and structural properties of superconducting A15-type Nb-Sn alloys. *J. Mater. Sci.*, 16(8):2145–2153, August 1981.
- [DK07] SM Deambrosis and G Keppel. The progress on Nb₃Sn and V₃Si. *Proc. 13th Work. RF Supercond.*, pages 392–399, 2007.
- [DWBM95] C. Durand, W. Weingarten, P. Bosland, and J Mayer. Non quadratic RF losses in niobium sputter coated accelerating structures. *IEEE Trans. Appiled Supercond.*, 5(2):1107–1110, June 1995.
- [Edw95] D. A. Edwards. TESLA Test Facility Linac Design Report. Technical report, DESY, Hamburg, 1995.
- [ET67] U. Essmann and H. Träuble. The direct observation of individual flux lines in type II superconductors. *Phys. Lett. A*, 24(10):526–527, May 1967.
- [Far74] H. H. Farrell. Grain boundary diffusion and growth of intermetallic layers: Nb₃Sn. *J. Appl. Phys.*, 45(9):4025, 1974.
- [Gal14] John N Galayda. The linac coherent light source-II project. *Proc. Fifth Int. Part. Accel. Conf.*, 2014.
- [GBK⁺13] a. Grassellino, C. Beard, P. Kolb, R. Laxdal, N. S. Lockyer, D. Longuevergne, and J. E. Sonier. Muon spin rotation studies of niobium for superconducting rf applications. *Phys. Rev. Spec. Top. - Accel. Beams*, 16(6):062002, June 2013.
- [GC34] C.J Gorter and H Casimir. On supraconductivity I. *Physica*, 1(1-6):306–320, January 1934.
- [GEF⁺14] Dan Gonnella, Ralf Eichhorn, Fumio Furuta, Mingqi Ge, Vivian Ho Daniel Hall, Georg Hoffstaetter, Matthias Liepe, Tim O’Connell, Sam Pose, James Sears, Vadim Veshcherevich, Anna Grassellino, Alexander Romanenko, and Dmitri Sergatskov. Nitrogen-Doped

9-Cell Cavity Performance in a Test Cryomodule for LCLS-II. *arXiv:1411.1659*, 2014.

- [GGB⁺04] V. Guritanu, W. Goldacker, F. Bouquet, Y. Wang, R. Lortz, G. Goll, and a. Junod. Specific heat of Nb₃Sn: The case for a second energy gap. *Phys. Rev. B*, 70(18):184526, November 2004.
- [Gmea] *Gmelins Handbuch der Anorganischen Chemie*. Verlag Chemie, Weinheim, Band 46Sn.
- [Gmeb] *Gmelins Handbuch der Anorganischen Chemie*. Verlag Chemie, Weinheim, Band 49Nb.
- [God05] A Godeke. *Performance boundaries in Nb₃Sn superconductors*. PhD thesis, University of Twente, Enschede, The Netherlands, 2005.
- [God06a] A Godeke. A review of the properties of Nb₃Sn and their variation with A15 composition, morphology and strain state. *Supercond. Sci. Technol.*, 19(8):R68–R80, August 2006.
- [God06b] A Godeke. Nb₃Sn for Radio Frequency Cavities. In *First Int. Work. Thin Film. New Ideas Push. Limits RF Supercond.*, Padova, 2006.
- [GR13] A Grassellino and A Romanenko. A pathway to SRF niobium cavities processing simplification and quality factor improvement via elimination of the post-annealing chemical treatment. *arXiv:1305.2182*, 2013.
- [GRS⁺13] a Grassellino, a Romanenko, D Sergatskov, O Melnychuk, Y Trenikhina, a Crawford, a Rowe, M Wong, T Khabiboulline, and F Barkov. Nitrogen and argon doping of niobium for superconducting radio frequency cavities: a pathway to highly efficient accelerating structures. *Supercond. Sci. Technol.*, 26(10):102001, October 2013.
- [Gur05] Alex Gurevich. RF breakdown in multilayer coatings: a possibility to break the Nb monopoly. *Proc. Second Int. Work. Thin Film. New Ideas RF Supercond.*, 2005.
- [Gur06] A. Gurevich. Enhancement of rf breakdown field of superconductors by multilayer coating. *Appl. Phys. Lett.*, 88(1):012511, 2006.

- [Gur13] Alex Gurevich. On the theoretical RF field limits of multilayer coating structures of superconducting resonator cavities. *arXiv Prepr. arXiv1309.5626*, pages 1–5, 2013.
- [HA63] J.L Harden and V Arp. The lower critical field in the Ginzburg-Landau theory of superconductivity. *Cryogenics (Guildf.)*, 3(2):105–108, June 1963.
- [Hak88] M Hakimi. Bronze-processed Nb₃Sn for RF applications. *J. Less Common Met.*, 139:159–165, 1988.
- [Hal70a] J. Halbritter. Comparison between measured and calculated RF losses in the superconducting state. *Zeitschrift fr Phys.*, 238(5):466–476, October 1970.
- [Hal70b] J. Halbritter. FORTRAN-program for the computation of the surface impedance of superconductors. *Intern. Note KFZ Karlsruhe 3/70-6*, 1970.
- [Hei99] Matthias Hein. *High-Temperature-Superconductor Thin Films at Microwave Frequencies*. Springer, New York, 1999.
- [HGT13] Georg H. Hoffstaetter, Sol M. Gruner, and Maury Tigner (eds.). Cornell Energy Recovery Linac Science Case and Project Definition Design Report. Technical report, Cornell University Laboratory for Accelerator-based Sciences and Education, 2013.
- [Hil80] B Hillenbrand. The Preparation of Superconducting Nb₃Sn Surfaces for RF applications. In *Proc. First Work. RF Supercond.*, Karlsruhe, 1980.
- [HKP⁺81] B. Hillenbrand, N. Krause, H. Pfister, K. Schnitzke, and Y. Uzel. Supraleitende Nb₃Sn Resonatoren. Technical report, Siemens AG, 1981.
- [HMP⁺77] B. Hillenbrand, H. Martens, H. Pfister, K. Schnitzke, and Y. Uzel. Superconducting Nb₃Sn cavities with high microwave qualities. *IEEE Trans. Magn.*, 13(1):491–495, January 1977.
- [HMS92] E. Haebel, A. Mosnier, and J. Sekutowicz. Cavity shape optimization for a superconducting linear collider. In *Proc. Fifteenth Conf. High energy Accel.*, volume 2, pages 957–959, Hamburg, 1992.

- [HPS97] T Hays, H Padamsee, and Nuclear Studies. Measuring the RF Critical Field of Pb, Nb, and Nb₃Sn. In *Proc. Eighth Work. RF Supercond.*, pages 789–794, Padova, 1997.
- [HS10] Walter Henning and Charles Shank. Accelerators for Americas Future. Technical report, US Department of Energy Office of Science, 2010.
- [HUS80] B Hillenbrand, Y Uzel, and K Schnitzke. On the preparation of Nb₃Sn-layers on monocrystalline Nb-substrates. *Appl. Phys.*, 23(3):237–240, November 1980.
- [JTS⁺80] J. E. Jensen, W. A. Tuttle, R. B. Stewart, H. Brechna, and A. G. Prodell. Brookhaven National Laboratory selected cryogenic data notebook. Technical report, BNL 10200-R, 1980.
- [KAK⁺85] P. Kneisel, J. Amato, J. Kirchgessner, K. Nakajima, H Padamsee, H. Phillips, C Reece, R. Sundelin, and M. Tigner. Performance of superconducting storage ring cavities at 1500 MHz. *IEEE Trans. Magn.*, 21(2):1000–1003, March 1985.
- [KGLP99] J Knobloch, RL Geng, M Liepe, and H Padamsee. High-field Q slope in superconducting cavities due to magnetic field enhancement at grain boundaries. *Proc. Ninth Work. RF Supercond.*, pages 77–91, 1999.
- [KIS13] Takayuki Kubo, Yoshihisa Iwashita, and Takayuki Saeki. RF electromagnetic field and vortex penetration in multilayered superconductors. *arXiv:1304.6876v1*, 2013.
- [KKS⁺77] P Kneisel, H Kupfer, W. Schwarz, O. Stoltz, and J. Halbritter. On properties of superconducting Nb₃Sn used as coatings in RF cavities. *IEEE Trans. Magn.*, 13(1):496–499, January 1977.
- [KKSH78] P. Kneisel, H. Küpfer, O. Stoltz, and J. Halbritter. Properties of Superconducting Nb₃Sn Layers Used in RF Cavities. *Adv. Cryog. Eng.*, 24:442–448, 1978.
- [KLT93] P Kneisel, B Lewis, and L Turlington. Experience with high pressure ultrapure water rinsing of niobium cavities. *Proc. Sixth Work. RF Supercond.*, 1993.

- [Kne74] P. Kneisel. On surface preparation and measurement of niobium used in high-frequency cavities. *J. Appl. Phys.*, 45(5):2296, 1974.
- [Kne99] P Kneisel. Preliminary experience with “in-situ” baking of niobium cavities. *Proc. Ninth Work. RF Supercond.*, pages 328–335, 1999.
- [Kne12] P Kneisel. History of Nb₃Sn Developments for Superconducting RF Cavities - A Review. Technical Report April, Jefferson Lab, 2012.
- [Kno97] J Knobloch. *Advanced thermometry studies of superconducting RF cavities*. PhD thesis, Cornell University, 1997.
- [KSH79] P. Kneisel, O. Stoltz, and J. Halbritter. Measurements of superconducting Nb₃Sn cavities in the GHz range. *IEEE Trans. Magn.*, 15(1):21–24, January 1979.
- [lak] www.lakeshore.com.
- [Lax14] R. Laxdal. Personal Communication. 2014.
- [LB] Landolt-Boerstein. *Zahlenwerte und Funktionen aus Physi, Chemie, Astronomie, Geophysik und Technik*. Auflage 6, Band II, Teil2, Bandteil:a.
- [LG12] F. Pei-Jen Lin and a. Gurevich. Effect of impurities on the superheating field of type-II superconductors. *Phys. Rev. B*, 85(5):054513, February 2012.
- [Lie09] Matthias Liepe. Overall SRF System Optimization for ERLs. In *Proc. Third Work. Energy Recover. Linacs*, Ithaca, 2009.
- [LMN72] C Lyneis, M Mcashan, and V Nguyen. Recent Measurements of S-Band and L-Band Cavities at Stanford. *Proc. 1972 Prot. Linear Accel. Conf.*, pages 98–102, 1972.
- [MGC63] B. Matthias, T. Geballe, and V. Compton. Superconductivity. *Rev. Mod. Phys.*, 35(1):1–22, January 1963.
- [MKM96] G Müller, P Kneisel, and D Mansen. Nb₃Sn layers on high-purity Nb cavities with very high quality factors and accelerating gradients. In *Proc. Fifth Eur. Part. Accel. Conf.*, Sitges, 1996.

- [MM65] B. Maxfield and W. McLean. Superconducting Penetration Depth of Niobium. *Phys. Rev.*, 139(5A):A1515–A1522, August 1965.
- [MPL14] S Meyers, S Posen, and M Liepe. Analysis of systematic and random error in SRF material parameter calculations. *Proc. 27th Linear Accel. Conf.*, 2014.
- [MPP⁺00] G. Müller, H. Piel, J. Pouryamout, P. Boccard, and P. Kneisel. Status and Prospects of Nb₃Sn Cavities for Superconducting Linacs. In D. Proch, editor, *Proc. Work. Thin Film Coat. Methods Supercond. Accel. Cavities*, Hamburg, 2000. TESLA Report 2000-15.
- [MSJ67] J. Matricon and D. Saint-James. Superheating fields in superconductors. *Phys. Lett. A*, 24(5):241–242, February 1967.
- [Mu84] G. Muller. Diagnostic techniques and defect classification. *Proc. Second Work. RF Supercond.*, pages 377–408, 1984.
- [Mu89] G. Muller. Microwave properties of high-T_c oxide superconductors. *Proc. 4th Work. RF Supercond.*, 1989.
- [MZRB79] D. Moore, R. Zubeck, J. Rowell, and M. Beasley. Energy gaps of the A-15 superconductors Nb₃Sn, V₃Si, and Nb₃Ge measured by tunneling. *Phys. Rev. B*, 20(7):2721–2738, October 1979.
- [Nat] National Institute of Standards and Technology. 2010 CODATA recommended values.
- [NM75] V. Novotny and P. P. M. Meincke. Single superconducting energy gap in pure niobium. *J. Low Temp. Phys.*, 18(1-2):147–157, January 1975.
- [OAC⁺91] D. Oates, Alfredo Anderson, C. Chin, J. Derov, G. Dresselhaus, and M. Dresselhaus. Surface-impedance measurements of superconducting NbN films. *Phys. Rev. B*, 43(10):7655–7663, April 1991.
- [Oka03] H. Okamoto. Nb-Sn (Niobium-Tin). *J. Phase Equilibria*, 24(4):380–380, July 2003.
- [OMFB79] T. P. Orlando, E. J. McNiff, S. Foner, and M. R. Beasley. Critical fields, Pauli paramagnetic limiting, and material parameters of Nb₃Sn and V₃Si. *Phys. Rev. B*, 19(9):4545–4561, May 1979.

- [Onn11] H. Kamerlingh Onnes. Further experiments with liquid helium. C. On the change of electric resistance of pure metals at very low temperatures etc. IV. The resistance of pure mercury at helium temperatures. *Commun. Phys. Lab. Univ. Leiden*, 12(120), 1911.
- [OZG98] L. Ozyuzer, J.F. Zasadzinski, and K.E. Gray. Point contact tunnelling apparatus with temperature and magnetic field control. *Cryogenics (Guildf.)*, 38(9):911–915, September 1998.
- [Pad09] H. Padamsee. *RF Superconductivity: Volume II: Science, Technology and Applications*. Wiley-VCH, Weinheim, 2009.
- [PCB⁺13] A D Palczewski, C A Cooper, B Bullock, S Joshi, A A Rossi, and A Navitski. R&D Progress in SRF Surface Preparation With Centrifugal Barrel Polishing (CBP) for both Nb and Cu. In *Proc. Sixth Conf. RF Supercond.*, pages 395–400, Paris, 2013.
- [PCH⁺99] M Perpeet, A Cassinese, M.A. Hein, T Kaiser, G Muller, H Piel, and J Pouryamout. Nb₃Sn films on sapphire. A promising alternative for superconductive microwave technology. *IEEE Trans. Appl. Supercond.*, 9(2):2496–2499, June 1999.
- [PCL⁺] S Posen, G Catelani, M Liepe, J. P. Sethna, and Mark K. Transtrum. To be published.
- [PCL⁺13] S Posen, G Catelani, M Liepe, J. P. Sethna, and Mark K. Transtrum. Theoretical field limits for multi-layer superconductors. In *Proc. Sixth Conf. RF Supercond.*, Paris, 2013.
- [PHK⁺88] M. Peiniger, M Hein, N Klein, G Müller, H Piel, and P. Thuns. Work on Nb₃Sn cavities at Wuppertal. In *Proc. Third Work. RF Supercond.*, Argonne National Laboratory, 1988.
- [Pie80] H Piel. Diagnostic methods of superconducting cavities and identification of phenomena. *Proc. First Work. RF Supercond.*, pages 85–118, 1980.
- [PKH08] Hasan Padamsee, Jens Knobloch, and Tom Hays. *RF superconductivity for accelerators*. Wiley-VCH, New York, 2008.
- [PL14] Sam Posen and Matthias Liepe. Advances in development of Nb₃Sn

- superconducting radio-frequency cavities. *Phys. Rev. Spec. Top. - Accel. Beams*, 17(11):112001, November 2014.
- [PLP14] S Posen, M Liepe, and T. Proslie. Nb₃Sn Materials Studies. *Proc. 27th Linear Accel. Conf.*, 2014.
- [Pow13] T Powers. Cost Optimization Models for SRF Linacs. In *Proc. Sixt. Conf. RF Supercond.*, Paris, 2013.
- [Pro13] Thomas Proslie. Atomic Layer Deposition of Thin Superconducting Films and Multilayers : Coupons and Cavity Tests. *Proc. Sixt. Conf. RF Supercond.*, 2013.
- [PZC⁺08] T. Proslie, J. F. Zasadzinski, L. Cooley, C. Antoine, J. Moore, J. Norem, M. Pellin, and K. E. Gray. Tunneling study of cavity grade Nb: Possible magnetic scattering at the surface. *Appl. Phys. Lett.*, 92(21):212505, 2008.
- [RB84] D. Rudman and M. Beasley. Microscopic superconducting parameters from tunneling in A15 Nb-Sn. *Phys. Rev. B*, 30(5):2590–2594, September 1984.
- [RDS] AA Rossi, SM Deambrosis, and S Stark. Nb₃Sn films by multilayer sputtering. *accelconf.web.cern.ch*, pages 149–154.
- [RG13] a. Romanenko and a. Grassellino. Dependence of the microwave surface resistance of superconducting niobium on the magnitude of the rf field. *Appl. Phys. Lett.*, 102(25):252603, 2013.
- [RP10] A Romanenko and H Padamsee. The role of near-surface dislocations in the high magnetic field performance of superconducting niobium cavities. *Supercond. Sci. Technol.*, 23(4):045008, April 2010.
- [Sab13] Sunil Sabharwal. Electron beam irradiation applications. *Proc. 25th North Am. Part. Accel. Conf.*, pages 745–748, 2013.
- [Sch95] Thomas Schilcher. *Wärmeleitvermögen von Niob bei kryogenischen Temperaturen*. PhD thesis, Universität Regensburg/DESY, 1995.
- [SGKC94] G Stejic, A Gurevich, E Kadyrov, and D Christen. Effect of geometry on the critical currents of thin films. *Phys. Rev. B*, 49(2), 1994.

- [Sha87] R.G. Sharma. Review on the fabrication techniques of A-15 superconductors. *Cryogenics (Guildf.)*, 27(7):361–378, July 1987.
- [Sha06] RG Sharma. A Review on A-15 Superconductors for RF Cavity Applications. . . *Ideas Push. Limits RF Supercond.*, 2006.
- [Shm72] VV Shmidt. Critical Current of an Ideal Type II Superconductor in the Mixed State. *Sov. Phys. JETP*, 34(1), 1972.
- [SK89] Kenji Saito and Yuzo Kojima. R&D of superconducting cavities at KEK. *Proc. Fourth Work. RF Supercond.*, 1989.
- [SKR03] W. J. Schneider, P. Kneisel, and C. H. Rode. Gradient optimization for SC CW accelerators. *Proc. Part. Accel. Conf. 2003*, pages 2863–2865, 2003.
- [SML04] R.M. Scanlan, A.P. Malozemoff, and D.C. Larbalestier. Superconducting materials for large scale applications. *Proc. IEEE*, 92(10):1639–1654, October 2004.
- [SP08] Valery Shemelin and Hasan Padamsee. Magnetic field enhancement at pits and bumps on the surface of superconducting cavities. *Telsa Technol. Collab. Rep. 2008-07*, 2008.
- [Sti78] JB Stimmell. *Microwave superconductivity of Nb₃Sn*. PhD thesis, Cornell University, 1978.
- [SW62] E. Saur and J. Wurm. Preparation und Supraleitungseigenschaften von Niobdrahtproben mit Nb₃Sn-Uberzug. *Naturwissenschaften*, 49(6):127–128, 1962.
- [SZ70] M. E. Straumanis and S. Zyszczyński. Lattice parameters, thermal expansion coefficients and densities of Nb, and of solid solutions NbO and NbNO and their defect structure. *J. Appl. Crystallogr.*, 3(1):1–6, February 1970.
- [TCS11] Mark K. Transtrum, Gianluigi Catelani, and James P. Sethna. Superheating field of superconductors within Ginzburg-Landau theory. *Phys. Rev. B*, 83(9):094505, March 2011.
- [THC⁺12] T. Tajima, N. F. Haberkorn, L. Civale, R. K. Schulze, H. Inoue, J. Guo, V. a. Dolgashev, D. Martin, S. Tantawi, C. Yoneda, B. Moeckly,

- C. Yung, T. Proslie, M. Pellin, A. Matsumoto, and E. Watanabe. Studies on thin film MgB₂ for applications to RF structures for particle accelerators. *AIP Conf. Proc.*, 297(2012):297–304, 2012.
- [Tin04] Michael Tinkham. *Introduction to Superconductivity*. Dover Publications, New York, 2004.
- [TSGS02] C Toffolon, C Servant, J C Gachon, and B Sundman. Reassessment of the Nb-Sn system. *J. Phase Equilibria*, 23(2):134–139, March 2002.
- [TT96] D. R. Tilley and J. Tilley. *Superfluidity and Superconductivity*. Institute of Physics Publishing, Bristol, 1996.
- [Val14] Nicholas R.A. Valles. *Pushing the Frontiers of Superconducting Radio Frequency Science: From the Temperature Dependence of the Superheating Field of Niobium to Higher-Order Mode Damping in Very High Quality Factor Accelerating Structures*. PhD thesis, Cornell University, 2014.
- [VCCR99] B Visentin, JP Charrier, B. Coadou, and D. Roudier. Cavity baking: A cure for the high accelerator field Q₀ drop. *Proc. Ninth Work. RF Supercond.*, pages 198–202, 1999.
- [Vea14] N. Valles et al. The main linac cavity for Cornell’s energy recovery linac: Cavity design through horizontal cryomodule prototype test. *Nucl. Instruments Methods Phys. Res. Sect. A Accel. Spectrometers, Detect. Assoc. Equip.*, 734:23–31, January 2014.
- [VFEP⁺13] A M Valente-Feliciano, G Ereemeev, H L Phillips, C E Reece, J K Spradlin, Q Yang, D Batchelor, and R A Lukaszew. NbTiN based SIS multilayer structures for SRF applications. *Proc. Sixt. Conf. RF Supercond.*, pages 670–673, 2013.
- [Vis98] B. Visentin. R&D issues in Superconducting Cavities. *TESLA Meet. DESY 98-05*, 1998.
- [VL11] N Valles and M Liepe. The Superheating Field of Niobium: Theory and Experiment. In *Proc. Fifteenth Conf. RF Supercond.*, number 4, Chicago, 2011.
- [Wan13] Y Wang. *Fundamental elements of applied superconductivity in electrical engineering*. John Wiley and Sons, Singapore, 2013.

- [WPJ01] Yuxing Wang, Tomasz Plackowski, and Alain Junod. Specific heat in the superconducting and normal state (2300 K, 016 T), and magnetic susceptibility of the 38 K superconductor MgB₂: evidence for a multicomponent gap. *Phys. C Supercond.*, 355(3-4):179–193, June 2001.
- [ZCZ⁺01] H Y Zhai, H M Christen, L Zhang, M Paranthaman, P H Fleming, and D H Lowndes. Degradation of superconducting properties in MgB₂ films by exposure to water. *Supercond. Sci. Technol.*, 14(7):425–428, July 2001.
- [Zha14] Pei Zhang. The influence of cooldown conditions at transition temperature on the quality factor of niobium sputtered quarter-wave resonators. In *Sixth Int. Work. Thin Film. New Ideas RF Supercond.*, 2014.